



ΑΡΙΣΤΟΤΕΛΕΙΟ ΠΑΝΕΠΙΣΤΗΜΙΟ ΘΕΣΣΑΛΟΝΙΚΗΣ  
ΣΧΟΛΗ ΘΕΤΙΚΩΝ ΕΠΙΣΤΗΜΩΝ  
ΤΜΗΜΑ ΓΕΩΛΟΓΙΑΣ



ΙΩΑΝΝΗΣ Α. ΣΟΦΙΑΔΗΣ  
Μαθηματικός  
M.Sc. Μετεωρολογία, Κλιματολογία & Ατμοσφαιρικό Περιβάλλον

ΜΕΛΕΤΗ ΤΩΝ ΕΠΙΠΤΩΣΕΩΝ ΤΗΣ ΑΛΛΑΓΗΣ ΚΑΛΥΨΗΣ ΓΗΣ ΣΤΟ  
ΚΛΙΜΑ ΤΗΣ ΕΥΡΩΠΗΣ ΜΕ ΧΡΗΣΗ ΠΕΡΙΟΧΙΚΟΥ ΚΛΙΜΑΤΙΚΟΥ  
ΜΟΝΤΕΛΟΥ

ΔΙΔΑΚΤΟΡΙΚΗ ΔΙΑΤΡΙΒΗ

ΘΕΣΣΑΛΟΝΙΚΗ  
2022



This work is licensed under a Creative Commons “Attribution-ShareAlike 4.0 International” license.





ARISTOTLE UNIVERSITY OF THESSALONIKI  
FACULTY OF SCIENCES  
SCHOOL OF GEOLOGY

IOANNIS A. SOFIADIS  
Mathematician  
M.Sc. Meteorology, Climatology & Atmospheric Environment

INVESTIGATING THE IMPACT OF LAND COVER CHANGES ON  
EUROPEAN CLIMATE WITH REGIONAL CLIMATE MODEL  
SIMULATIONS

DISSERTATION THESIS

THESSALONIKI  
2022



(λευκή σελίδα)



ΙΩΑΝΝΗΣ Α. ΣΟΦΙΑΔΗΣ  
MSc Μαθηματικός

## ΜΕΛΕΤΗ ΤΩΝ ΕΠΙΠΤΩΣΕΩΝ ΤΗΣ ΑΛΛΑΓΗΣ ΚΑΛΥΨΗΣ ΓΗΣ ΣΤΟ ΚΛΙΜΑ ΤΗΣ ΕΥΡΩΠΗΣ ΜΕ ΧΡΗΣΗ ΠΕΡΙΟΧΙΚΟΥ ΚΛΙΜΑΤΙΚΟΥ ΜΟΝΤΕΛΟΥ

Εκπονήθηκε στον Τομέα Μετεωρολογίας & Κλιματολογίας του Τμήματος Γεωλογίας Α.Π.Θ.  
Υποβλήθηκε στο Τμήμα Γεωλογίας Α.Π.Θ. τον Δεκέμβριο του 2022

Ημερομηνία Προφορικής Εξέτασης: 21/12/2022

Αριθμός Παραρτήματος Επιστημονικής Επετηρίδας Τμήματος Γεωλογίας Ν<sup>ο</sup>: 234

### **Τριμελής Συμβουλευτική Επιτροπή**

Αν. Καθηγήτρια Κατράγκου Ελένη, Επιβλέπουσα  
Καθηγητής Edouard L. Davin, Μέλος Τριμελούς Συμβουλευτικής Επιτροπής  
κύρια Ερευνήτρια Diana Rechid, Μέλος Τριμελούς Συμβουλευτικής Επιτροπής

### **Εξεταστική Επιτροπή**

Αν. Καθηγήτρια Κατράγκου Ελένη  
Καθηγητής Edouard L. Davin  
κύρια Ερευνήτρια Diana Rechid  
Αν. Καθηγητής Πάνος Χατζηνικολάου  
Ομ. Καθηγητής Θεόδωρος Καρακώστας  
Καθηγητής Πρόδρομος Ζάνης  
Καθηγητής Δημήτρης Μελάς



© Ιωάννης Α. Σοφιάδης, MSc Μαθηματικός, 2022

Με επιφύλαξη παντός δικαιώματος.

ΜΕΛΕΤΗ ΤΩΝ ΕΠΙΠΤΩΣΕΩΝ ΤΗΣ ΑΛΛΑΓΗΣ ΚΑΛΥΨΗΣ ΓΗΣ ΣΤΟ ΚΛΙΜΑ ΤΗΣ ΕΥΡΩΠΗΣ ΜΕ ΧΡΗΣΗ ΠΕΡΙΟΧΙΚΟΥ ΚΛΙΜΑΤΙΚΟΥ ΜΟΝΤΕΛΟΥ – Διδακτορική Διατριβή

Το έργο παρέχεται υπό τους όρους Creative Commons CC BY-NC-SA 4.0.

© Ioannis A. Sofiadis, 2022

All rights reserved.

INVESTIGATING THE IMPACT OF LAND COVER CHANGES ON EUROPEAN CLIMATE WITH REGIONAL CLIMATE MODEL SIMULATIONS – *Ph.D. Thesis*

The work is provided under the terms of Creative Commons CC BY-NC-SA 4.0.

#### Citation:

Σοφιάδης Ι., 2022. – Μελέτη των επιπτώσεων της αλλαγής κάλυψης Γης στο κλίμα της Ευρώπης με χρήση περιοχικού κλιματικού μοντέλου. Διδακτορική Διατριβή, Τμήμα Γεωλογίας Α.Π.Θ., Αριθμός

Παραρτήματος Επιστημονικής Επετηρίδας Τμ. Γεωλογίας Νο 234, 200 σελ.

Sofiadis I., 2022. – Investigating the impact of land cover changes on European climate with regional climate model simulations. Ph.D. Thesis, School of Geology, Aristotle University of Thessaloniki, Annex Number of Scientific Annals of the School of Geology No 234, 200 pp.

Απαγορεύεται η αντιγραφή, αποθήκευση και διανομή της παρούσας εργασίας, εξ ολοκλήρου ή τμήματος αυτής, για εμπορικό σκοπό. Επιτρέπεται η ανατύπωση, αποθήκευση και διανομή για σκοπό μη κερδοσκοπικό, εκπαιδευτικής ή ερευνητικής φύσης, υπό την προϋπόθεση να αναφέρεται η πηγή προέλευσης και να διατηρείται το παρόν μήνυμα. Ερωτήματα που αφορούν τη χρήση της εργασίας για κερδοσκοπικό σκοπό πρέπει να απευθύνονται προς το συγγραφέα.

Οι απόψεις και τα συμπεράσματα που περιέχονται σε αυτό το έγγραφο εκφράζουν το συγγραφέα και δεν πρέπει να ερμηνευτεί ότι εκφράζουν τις επίσημες θέσεις του Α.Π.Θ.



## Προλογικό σημείωμα

Η κάλυψη του εδάφους ρυθμίζει σε μεγάλο βαθμό τις τοπικές κλιματικές συνθήκες μιας περιοχής. Οι αλλαγές στις χρήσεις γης και στην κάλυψη του εδάφους διαταράσσουν τον βιομημικό και βιοφυσικό κύκλο διεργασιών που συμβαίνουν μεταξύ εδάφους και βιόσφαιρας, με αποτέλεσμα να επιφέρουν αλλαγές στο κλιματικό σύστημα. Πρόσφατα στοιχεία από την επιστημονική κοινότητα αναφέρουν ότι οι αλλαγές στις χρήσεις γης είναι υπεύθυνες για σχεδόν το ένα τρίτο των εκπομπών θερμοκηπικών αερίων από την προ-βιομηχανική περίοδο έως σήμερα.

Σκοπός της παρούσης διδακτορικής διατριβής είναι να αναδείξει τις βιοφυσικές συνέπειες των αλλαγών κάλυψης του εδάφους πάνω στο κλίμα της Ευρώπης, χρησιμοποιώντας προσομοιώσεις κλιματικών μοντέλων περιοχικής κλίμακας. Συγκεκριμένα, χρησιμοποιείται το κλιματικό μοντέλο WRF, σε χωρική ανάλυση πενήντα χιλιομέτρων και οδηγούμενο από τα δεδομένα επανάλυσης ERA-Interim για την περίοδο 1986-2015. Προκειμένου να ενισχυθεί η αξιοπιστία των αποτελεσμάτων που μεταφέρονται από το WRF, η ανάλυση περιλαμβάνει δεδομένα και από άλλα μοντελικά συστήματα, τα οποία εφάρμοσαν το ίδιο πειραματικό σχέδιο.

Η πρώτη ερώτηση στην οποία απαντά η εργασία είναι πόσο αξιόπιστη είναι η προσομοίωση από το WRF και ποιες είναι οι πηγές της αβεβαιότητας στο μοντέλο. Για τον σκοπό αυτό, στο κεφάλαιο 2, το σύστημα WRF-CLM μαζί με άλλες τρεις προσομοιώσεις με WRF με διαφορετικά ατμοσφαιρικά και εδαφικά σχήματα, συγκρίνονται με δεδομένα παρατήρησης για τη θερμοκρασία, τον υετό, τη νέφωση, την ακτινοβολία, τις ροές θερμότητας και την υγρασία εδάφους.

Το κεφάλαιο 3 απαντά στο ερώτημα για τις συνέπειες της μετάβασης από τις εκτάσεις ανοικτής γης σε δάση πάνω στη θερμοκρασία του εδάφους στην Ευρώπη. Στο πλαίσιο της ανάλυσης, χρησιμοποιούνται δεδομένα από το σύστημα WRF-CLM και τα υπόλοιπα μοντέλα που συμμετέχουν στη δράση Land Use Change Across Scales in Europe FPS, τα οποία εφαρμόζουν δύο ιδεατά σενάρια. Στο ένα σενάριο, η Ευρώπη είναι πλήρως καλυμμένη από δάση και στο άλλο καλυμμένη με γρασίδι. Οι συνέπειες των αλλαγών κάλυψης του εδάφους πάνω στη θερμοκρασία του εδάφους εξετάζονται υπό το πρίσμα των αλλαγών στο ενεργειακό ισοζύγιο στην επιφάνεια του εδάφους και την υγρασία του



εδάφους. Επιπρόσθετα, χρησιμοποιούνται δεδομένα θερμοκρασίας εδάφους από το δίκτυο σταθμών FLUXNET, ώστε να αξιολογηθεί η πληροφορία που μεταφέρεται από τα κλιματικά μοντέλα.

Στο κεφάλαιο 4, συγκρίνονται δύο προσομοιώσεις με WRF, όπου στη μία εφαρμόζεται ένας πραγματικός χάρτης κάλυψης γης για το έτος 1950 και στην άλλη ο χάρτης κάλυψης του εδάφους για το 2015. Ο σκοπός της σύγκρισης των δύο προσομοιώσεων είναι να απαντήσει στο ερώτημα για το πως οι πρόσφατες αλλαγές στην κάλυψη του εδάφους θα μπορούσαν να επηρεάσουν το κλίμα της Ευρώπης σε περιοχική κλίμακα. Εξετάζονται οι επιπτώσεις στη θερμοκρασία, τον υετό και τις ροές ενέργειας στην επιφάνεια του εδάφους.

Τέλος, στο πέμπτο κεφάλαιο γίνεται συζήτηση των αποτελεσμάτων από τα παραπάνω τρία κεφάλαια και αναφέρονται τα κομβικά συμπεράσματα της εργασίας.

Η καινοτομία αυτής της διδακτορικής διατριβής είναι το γεγονός ότι για πρώτη φορά μεταφέρεται κλιματική πληροφορία για τις βιοφυσικές συνέπειες των αλλαγών κάλυψης του εδάφους στην Ευρώπη, από σμήνος κλιματικών μοντέλων περιοχικής κλίμακας. Η πληροφορία αυτή μπορεί να βοηθήσει τους αρμόδιους για την πολιτική αντιμετώπισης της κλιματικής αλλαγής, σε μία εποχή που η αναδάσωση προτείνεται ως μία στρατηγική μετριασμού των ανθρωπογενών θερμοκηπικών αερίων στην ατμόσφαιρα.

Θα ήθελα να ευχαριστήσω όλους τους ανθρώπους που συνεισέφεραν στη διαμόρφωση και πρόοδο αυτής της εργασίας, την τριμελή συμβουλευτική επιτροπή και ιδιαίτερος την επιβλέπουσα καθηγήτρια κ. Κατράγκου Ελένη. Ιδιαίτερες ευχαριστίες δίνονται στην ενότητα Acknowledgements στο τέλος του κειμένου.



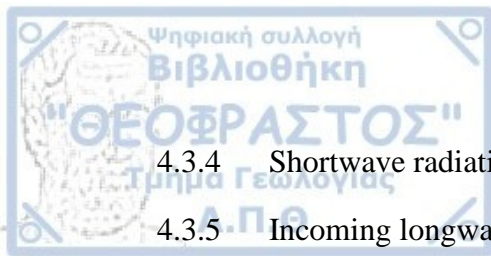


## Table of Contents

1	Introduction.....	1
1.1	Forest-climate relationships .....	1
1.2	Biophysical processes .....	2
1.3	Observations and satellite approaches.....	3
1.4	Climate models.....	4
1.4.1	Earth System Models (ESMs).....	4
1.4.2	Regional Climate Models (RCMs) .....	5
1.5	LUCAS initiative.....	5
1.6	Outline.....	6
2	Regional climate simulations within LUCAS FPS- Evaluation of a WRF multi-physics ensemble .....	7
2.1	Introduction .....	7
2.2	Data & Methods .....	7
2.2.1	WRF ensemble.....	7
2.2.2	Observational datasets .....	9
2.3	Results .....	10
2.3.1	Temperature .....	10
2.3.2	Precipitation .....	18
2.3.3	Radiation and clouds.....	25
2.3.4	Cloud cover.....	32
2.3.5	Seasonal cycles .....	34
2.3.6	Surface heat fluxes.....	38
2.3.7	Soil moisture .....	44
2.3.8	Model performances .....	46



2.4	Summary .....	48
3	Afforestation impact on soil temperature in regional climate simulations over Europe	
	51	
3.1	Introduction .....	51
3.2	Data & Methods .....	52
3.2.1	Regional climate model ensemble .....	52
3.2.2	Experimental design.....	53
3.2.3	FLUXNET observational data .....	55
3.3	Results .....	57
3.3.1	Soil temperature response .....	57
3.3.2	Surface energy input .....	62
3.3.3	Soil moisture .....	67
3.3.4	The origin of inter-model spread in AAST.....	70
3.3.5	FLUXNET paired sites .....	71
3.4	Summary .....	72
4	Recent land cover changes over Europe could increase the diurnal range of summer temperature at regional scale .....	75
4.1	Introduction .....	75
4.2	Data & Methodology.....	76
4.2.1	Model set-up .....	76
4.2.2	Land cover maps .....	77
4.2.3	Surface temperature decomposition.....	78
4.3	Results .....	79
4.3.1	Land cover changes in Europe.....	79
4.3.2	Land surface properties.....	81
4.3.3	Surface temperature .....	82



4.3.4	Shortwave radiation .....	85
4.3.5	Incoming longwave radiation .....	87
4.3.6	Sensible heat .....	88
4.3.7	Latent heat.....	88
4.3.8	Precipitation .....	89
4.3.9	2m temperature .....	91
4.4	Summary .....	92
5	Conclusions.....	94
5.1	Evaluation of WRF simulations .....	94
5.2	Afforestation impact on soil temperature in Europe .....	96
5.3	The effect of recent land cover changes on regional climate in Europe .....	97
5.4	Key remarks .....	99
	Abstract.....	101
	Περίληψη .....	102
	Acknowledgements.....	104
	References.....	105
	Appendix.....	117
	List of Abbreviations .....	117
	Supplementary maps and plots .....	118
	Supplementary tables .....	134



# 1 Introduction

Land cover is the natural material that covers the land surface and constitutes an essential factor in formulating the local and regional climate conditions. Land use is distinct from land cover and describes the activities through which people interact with terrestrial ecosystems (Meyfroidt et al., 2018). Land use includes recreational, agricultural or commercial purposes, such as the installation of city parks, the tillage and irrigation of farmlands, the construction of shopping districts etc.

Deforestation is a common anthropogenic land cover change in the industrial era in order to meet the increasing living needs. In the period 2000-2012, approximately 2.3 million km<sup>2</sup> of forest area lost on a global scale, mainly due to increased deforestation in tropical latitudes (Hansen et al., 2013). In Brazil, which owns most of the Amazon natural ecosystem, forest losses of over 40,000 km<sup>2</sup> were recorded for 2003. In Indonesia, the mean annual rate of forest loss for the period 2000-2012 was about 1000 km<sup>2</sup>/year. Deforestation also takes place in the boreal zone mainly due to fires which occur more frequently due to anthropogenic climate change (Potapov et al., 2008). On the other hand, forest areas tend to increase in the temperate zone of the northern hemisphere. In China, national targets for extensive reforestation have increased total forest area by 5.5% since the 1990s with the ultimate goal of forests covering 30% of China's land by 2050 (Zhang et al., 2016). In addition, Europe has seen a trend of forest regrowth in the period 1950-2010, mainly in eastern Europe at the expense of abandoned crops due to social, economic and political factors, such as the collapse of the Soviet Union (Alcantara et al., 2013; Huang et al., 2020; Kuemmerle et al., 2016; Fuchs et al., 2013).

In the future, changes to the land surface will continue. Recent evidence from modelling approaches suggests that the magnitude of global anthropogenic warming may worsen by as much as 1 °C over areas converted from forest to cropland (Bukovsky et al., 2021). Deforestation in the Amazon region could lead up to 0.5 °C warmer mean annual temperatures and drier than present conditions (Lejeune et al., 2015).

According to the Intergovernmental Panel for Climate Change (IPCC) special report on climate change and land, all land-use activities contributed to about a quarter of greenhouse gases emissions to the atmosphere over the 2007-2016 period (IPCC, 2019). The deployment of a broad range of land-based applications has been identified that have multiple benefits for a sustainable future climate. Afforestation or reforestation has a high estimated potential for carbon sequestration which amounts to 0.5 - 10 GtCO<sub>2</sub> per year (IPCC, 2019), thus it has emerged as a key land-based strategy in order to achieve the goals of Paris-Agreement towards the greenhouse gases mitigation (Grassi et al., 2017).

## 1.1 Forest-climate relationships

An estimated 3 trillion trees cover almost 42 million km<sup>2</sup> or the 30% of global land surface, with most of them inhabiting across the tropical latitudes (Pan et al., 2013; Crowther et al., 2015). The presence of forests provides

several benefits for natural systems and humankind, including refuges for biodiversity, protection of soil resources and provision of food and medicinal products (Bonan, 2008; Hassan et al., 2005). In addition, forests act as an important climate factor as they affect the carbon cycle in the climate system and modify the energy fluxes between ground and atmosphere.

The efficiency of forests in absorbing carbon from the atmosphere is the best-known reason why afforestation is promoted as a strategy to mitigate climate change. Recent studies which employed various land cover change scenarios showed that large-scale afforestation could store up to 25% of the current atmospheric carbon pool (Bastin et al., 2019, Veldman et al., 2019; Lewis et al., 2019). Arora and Montenegro, 2011 suggested that gradual planting of trees on areas occupied at present by crops could attenuate the global warming up to 0.45 °C in 2100 due to GHG mitigation potential of afforestation.

## 1.2 Biophysical processes

Apart from biogeochemical forcing, forests affect climate through modifications of biophysical processes. In the context of land cover change, as biophysical impact is considered any alteration of the water and energy redistribution at the land surface and the resulting consequences in components of climate system.

Prominent biophysical effects of afforestation include changes in albedo, the latent heat flux and the surface roughness (**Figure 1.1**). Forests have generally lower albedo than open lands (**Figure 1.1a**), especially in seasons and regions where the ground is snow-covered (Betts, 2000). The latter is associated with the fact that the trees remain exposed to solar radiation and mask the high reflectance of snow underneath whereas the open lands can become entirely snow-covered (Bonan et al., 1992). Thus, the transition from open lands to forests decreases the surface albedo leading to an increase of absorption of solar radiation at the surface and thus increasing surface temperature. The albedo-induced warming of surface temperature following forestation can be offset by cooling effects resulting from an increase in surface roughness and latent heat flux. The surface of trees is generally rougher than open lands and therefore creates more turbulence in the surface layer facilitating the turbulent exchange of energy and water vapor between the land surface and the overlying atmosphere (**Figure 1.1b**). Therefore, the surface roughness change has a cooling effect at surface. This cooling could be further amplified by an increase in evapotranspiration with forestation (**Figure 1.1c**). Forests have greater potential for evapotranspiration than grasses due to their transpiration-facilitating characteristics such as their big leaf area and deep rooting system, through which they have access to larger groundwater reserves. A potential increase of evapotranspiration could reduce the surface temperature and increase water input to atmosphere, which may enhance precipitation.

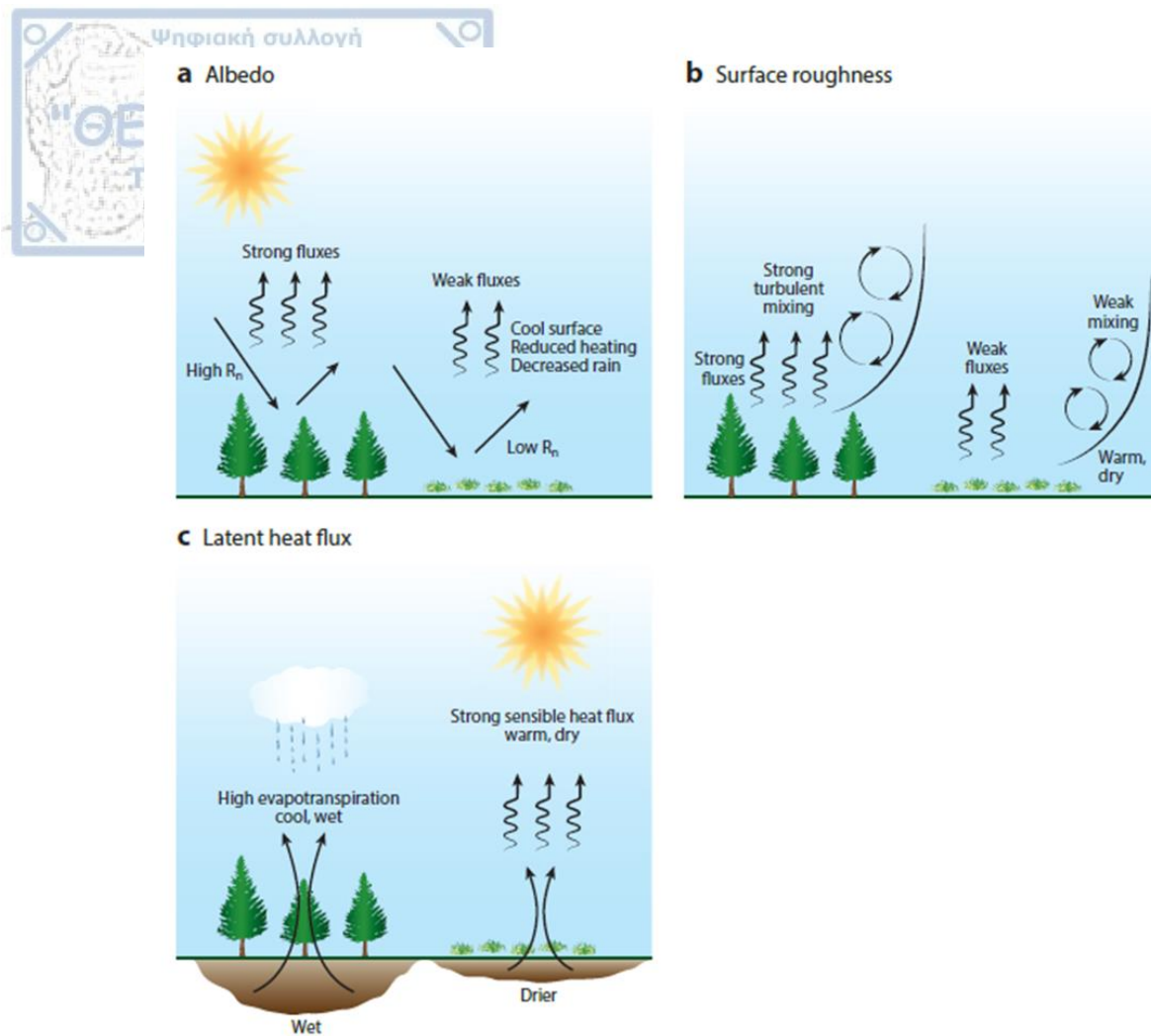


**Figure 1.1: Forest-climate biophysical feedbacks through modifications in a) surface albedo, b) surface roughness and c) latent heat flux. Figure was retrieved from Bonan, 2016.**

### 1.3 Observations and satellite approaches

Recent analyses based on in-situ observations adopted the space-for-time analogy to assess the biophysical impact arising from spatial patterns of different terrestrial ecosystems on local climate. The observational method concerns the difference in measurements between flux towers located in forests and nearby ground stations located in open lands. Their differences can be interpreted as the climate signal of hypothetical land cover change over time, assuming that the adjacent forests and open lands share the same background climate. Applying the space-for-time analogy over North-America, Lee et al., 2011 reported that the open lands have a lower mean annual temperature than forests. Following a similar approach, Zhang et al., 2014 reported contrasting results for temperate zone, as they found that the mean annual air temperature at open lands is 0.67 °C warmer than adjacent forests, which was mostly associated with daytime climate processes. In the boreal zone, open lands were 0.95 °C cooler than forests owing to cooler minimum temperatures throughout the year, in line with results from Lee et al., 2011. Pairing FLUXNET sites, Chen et al., 2018 reported that open lands have less net radiation amounts and turbulent fluxes at surface in summer with respect to forests. In the same context but focused on Europe,

Broucke et al., 2015 showed that open lands are cooler than forests at night, mostly in winter, whereas the daytime temperatures are higher in open lands in summer and lower in winter.

Satellite products for albedo, evapotranspiration (ET) and land surface temperature (LST) have also assisted in assessing the biophysical forcing of vegetation replacements across the world. Comparing satellite-retrieved albedo, ET and LST between adjacent vegetation types in North America, Zhao and Jackson, 2014 confirmed the general consensus that forests are darker than open lands, especially in locations with snow. Also, they found greater evaporation amounts over forests with respect to croplands during the growing season. Furthermore, forests had a smaller daily LST range in summer because of their warmer nighttime and cooler daytime temperatures than open lands. In a similar context, Alkama and Cescatti, 2016 reported that forest loss amplifies the diurnal LST range in summer, mostly increasing the maximum temperatures over arid zones. Conducting a global-scale study, Li et al., 2015 showed that the biophysical impact of forests depends largely on latitude. In the tropics, forests are cooler than open lands in all seasons, the temperate forests are cooler in summer and warmer in winter compared to open lands, while over boreal zone the forests are much warmer in winter due to snow-masking effect and slightly cooler in summer.

## **1.4 Climate models**

The observation-driven assessment of biophysical forcing of forest cover change reflects only the local effects on climate of specific small areas. Satellite analyses are also subject to restrictions as the data are retrieved only for clear-sky conditions (Bonan, 2016).

### **1.4.1 Earth System Models (ESMs)**

The most modern and comprehensive tool for exploring the underlying mechanisms behind the land cover changes relies on Earth System Models (ESMs). These complex models use mathematical equations to represent and quantify the processes which take place between the atmosphere, land surface, ocean and sea ice.

The most robust information about the biophysical effects of land cover changes on climate has been delivered from ensembles of ESMs so far. A multi-model approach applied in the context of LUCID project to investigate the impact of historical deforestation over North America and Eurasia between the period 1870-1992 (Pitman et al., 2009; Noblet-Ducoudré et al., 2012). Among the robust model responses to deforestation were a systematic increase of surface albedo and a decrease of total turbulent heat energy. However, significant uncertainties emerged for the surface temperature response to deforestation, linked to diverging results for turbulent heat fluxes partitioning. Divergent climate responses to historical land cover change in Northern America also emerged in CMIP5 simulations (Kumar et al., 2013). Also, LUCID and CMIP5 models were not able to reproduce correctly the changes in the diurnal temperature cycle identified in present-day observations of the effect of deforestation over temperate regions (Lejeune et al., 2017). The wide divergence on the turbulent heat fluxes partitioning is

present even in more recent model intercomparison projects (CMIP6), producing a large spread in the sign of global and regional temperature response to forest cover changes (Boysen et al., 2020; Pongratz et al., 2021).

ESMs have been also used individually to assess the global and regional temperature response to various forest cover change experiments. Davin and Noblet-Ducoudré, 2010 showed that the net biophysical impact of deforestation varies with latitude and depends on the competition between albedo, roughness and evapotranspiration effects. In the tropics, deforestation causes a warming because the surface roughness and evapotranspiration effects counteract the albedo-induced cooling. In temperate and boreal zone, deforestation induces a cooling because the decreased albedo dominates over the warming effects of non-radiative processes. Li et al., 2016 concluded that the temperature response to deforestation largely depends on the spatial extent of deforestation and on background climate conditions. Winckler et al., 2019 suggested that non-local effects of deforestation (impact on neighboring or remote regions from deforested area) have higher importance on global mean temperature than local effects (impact on deforested regions), regardless of geographical area and the spatial extent of deforestation.

#### **1.4.2 Regional Climate Models (RCMs)**

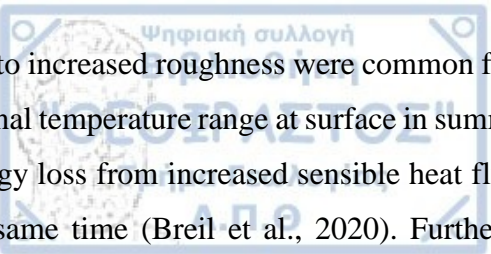
RCMs have also contributed to the understanding of land cover change impact at regional scale. RCMs downscale global reanalysis or GCM results to simulate climate variability over limited-area domains accounting for high-resolution topographical data (Rummukainen, 2016). Land cover change experiments over Europe with single RCM showed that the frequency of cold extremes in winter could be reduced with afforestation (Cherubini et al., 2018). Also, the increase in evapotranspiration efficiency due to maximum afforestation could reduce the summer temperature mostly in regions with available soil water for evapotranspiration (Strandberg and Kjellström, 2019). Moreover, precipitation extremes would be reduced in winter and mean summer precipitation would be likely increased in southern Europe owing to larger evapotranspiration amounts with afforestation (Belušić et al., 2019).

#### **1.5 LUCAS initiative**

Until now, climate information about land cover change impact has been delivered either from GMCs at global scale or single RCM studies which apply different experimental setups. The Land Use and Climate Across Scales (LUCAS) initiative is the first model intercomparison project designed with the ultimate goal to assess the biophysical impact of land cover changes on regional climate in Europe under a common experimental protocol. In the first phase, an ensemble of ten RCMs undertakes two idealized experiments, which represent Europe as fully covered by trees and grass respectively, in order to quantify the climate response to extreme land cover change.

LUCAS ensemble produced a large spread in temperature response to forestation in summer, associated with diverging results for turbulent heat fluxes partitioning, similar to previous intercomparison projects (Davin et al., 2020). On the other hand, the increase in net radiation due to decreased albedo and the increase in sensible heat





due to increased roughness were common features in almost all LUCAS models. Forestation induced a decreased diurnal temperature range at surface in summer because the increased net radiation amounts counteract the surface energy loss from increased sensible heat flux, which amplified the diurnal range of overlying air temperature at the same time (Breil et al., 2020). Furthermore, LUCAS models showed that forestation enhance snowmelt, however the forestation effects during the snow-melt period emerged as the greatest challenge for the RCMs (Mooney et al., 2021).

## 1.6 Outline

This study is focused on land cover changes impact on regional climate in Europe, as represented by WRF regional climate model within the framework of LUCAS FPS. Four different WRF simulations are performed under the common LUCAS experimental protocol, which combine different atmospheric and land surface schemes for the representation of physical processes.

The main part of this analysis is divided into three sections. In the first part, the ability of WRF ensemble in reproducing adequately the near-surface climate processes is evaluated. WRF simulations are compared to various observational, reanalysis and satellite products for temperature, precipitation, cloudiness, radiation and heat surface fluxes, in order to identify systematic biases and sources of uncertainty in model.

In the second part, the WRF configurations undertake the two idealized LUCAS experiments, FOREST and GRASS, in order to investigate the impact of extreme land cover change on soil temperature profile across Europe. Although the air and surface temperature responses to extreme forestation have been investigated in previous LUCAS studies, the soil temperature sensitivity remains unexplored. According to MacDougall and Beltrami, 2017 a warming effect on subsurface temperature remains present even by 500 years after deforestation. In this part, the analysis includes results from all LUCAS models.

In the third part, two WRF simulations which integrate realistic land cover maps for 1950 and 2015 respectively are compared, in order to assess the effect of recent land cover changes over Europe on regional climate of the reference period 1986-2015.

In summary, the questions that this dissertation intends to answer are:

- Is WRF RCM able to reproduce adequately the observed physical processes at surface, and what are the sources of uncertainty in model simulation?
- What is the afforestation impact on soil temperature profile across Europe?
- How recent changes in land cover would affect regional climate in Europe for the period 1986-2015?



## 2 Regional climate simulations within LUCAS FPS- Evaluation of a WRF multi-physics ensemble

### 2.1 Introduction

In the framework of FPS LUCAS Phase 1, ten climate simulations are performed for the time period 1986-2015 following the Euro-CORDEX intercomparison protocol for hindcast runs, in order to study the sensitivity of regional climate to idealized scenarios of land cover change. Prior to this phase, the RCM ensemble should be evaluated for its ability to correctly simulate the observed climate processes and not produce systematic errors that will reduce the reliability of results of land cover change experiments. This chapter is focused on the performance of a WRF mini ensemble included in LUCAS, which consists of four WRF simulations that share different atmospheric and land surface schemes. The multi-physics ensemble around WRF model helps to identify the role of land and atmospheric processes on the origin of model uncertainties.

The WRF performance has been assessed in the frame of multi-physics and multi-model intercomparison studies within Euro-CORDEX. García-Díez et al., 2015 found that a multi-physics ensemble of the WRF RCM can produce a similar spread as a multi-model ensemble within EURO-CORDEX, and García-Díez et al., 2013 confirm that no parameterization combination performs best for all applications. Precipitation overestimation has been reported as a typical WRF behavior, which remains the same or worsens at higher spatial resolutions (Kotlarski et al., 2014). In Kotlarski et al., 2014, the winter wet bias was closely related to the distinct negative bias of mean sea-level pressure, indicating a too-high intensity of low pressure systems passing the continent. Katragkou et al., 2015 suggested that WRF captures winter precipitation better than summer precipitation and related the summer overestimation to the weakness of cumulus schemes to reproduce correctly the convection processes on regional scale. Another common WRF feature was a winter cold bias over snow-covered areas in north-eastern Europe, which has been related to longwave component in Mooney et al., 2013 and problematic calculation of surface temperature over snow in Katragkou et al., 2015. The common WRF deficiencies should be considered when interpreting the results of model experiments.

Below, the WRF simulations are evaluated against various reference products for 2-meter temperature, precipitation, cloudiness, soil moisture, surface radiation and heat fluxes.

### 2.2 Data & Methods

#### 2.2.1 WRF ensemble

Four WRF reanalysis-driven simulations performed as part of the LUCAS FPS. **Table 1** depicts the model set-up for each participating WRF simulation. The simulations share the same atmospheric configuration with different land surface scheme or the same land component with different atmospheric schemes. WRFa-NoahMP and WRFb-NoahMP share the same LSM but differ in cumulus and microphysics scheme. WRFb-NoahMP and

WRFc-NoahMP differ only in PBL and surface layer schemes, while WRFb-NoahMP and WRFb-CLM4.0 have the same atmospheric set-up coupled with different LSMs.

**Table 1: The characteristics of WRF multi-physics ensemble.**

<i>Simulation name</i>	<i>WRFa-NoahMP</i>	<i>WRFb-NoahMP</i>	<i>WRFc-NoahMP</i>	<i>WRFb-CLM4.0</i>
<i>Institute ID</i>	IDL	UHOH	BCCR	AUTH
<i>RCM</i>	WRFv3.8.1(Skamarock et al., 2008)	WRFv3.8.1	WRFv3.8.1	WRFv3.8.1
<i>LSM</i>	NoahMP (Niu et al., 2011)	NoahMP	NoahMP	CLM4.0 (Oleson et al., 2010a)
<i>PBL</i>	MYNN Level 2.5 (Nakanishi and Niino, 2006)	MYNN Level 2.5	YSU (Hong et al., 2006)	MYNN Level 2.5
<i>Surface layer scheme</i>	MYNN (Nakanishi and Niino, 2009)	MYNN	MM5 (Jiménez et al., 2012)	MYNN
<i>Cumulus scheme</i>	(Grell and Freitas, 2014) for cumulus convection and GRIMS Scheme (Hong et al., 2013) for shallow convection.	Kain and Fritsch (Kain, 2004)	Kain and Fritsch	Kain and Fritsch
<i>Radiation</i>	RRTMG (Iacono et al., 2008)	RRTMG	RRTMG	RRTMG
<i>Microphysics</i>	Two-moment 6-class scheme (Lim and Hong, 2010)	(Thompson et al., 2004)	(Thompson et al., 2004)	(Thompson et al., 2004)
<i>Aerosols</i>	(Tegen et al., 1997)	(Tegen et al., 1997)	(Tegen et al., 1997)	(Tegen et al., 1997)

All simulations are performed over the EURO-CORDEX domain (Jacob et al., 2020) with a spatial resolution of 0.44° (~50 km), forced by ERA-Interim reanalysis data (Dee et al., 2011) at their lateral boundaries and at the lower boundary over the sea. The analysis covers the 30-year period of 1986–2015 and focuses on the following eight European subregions as described in Christensen and Christensen, 2007: the Alps (AL), the British Isles

(BI), eastern Europe (EA), France (FR), the Iberian Peninsula (IP), the Mediterranean (MD), mid-Europe (ME) and Scandinavia (SC) (Figure 2.1).

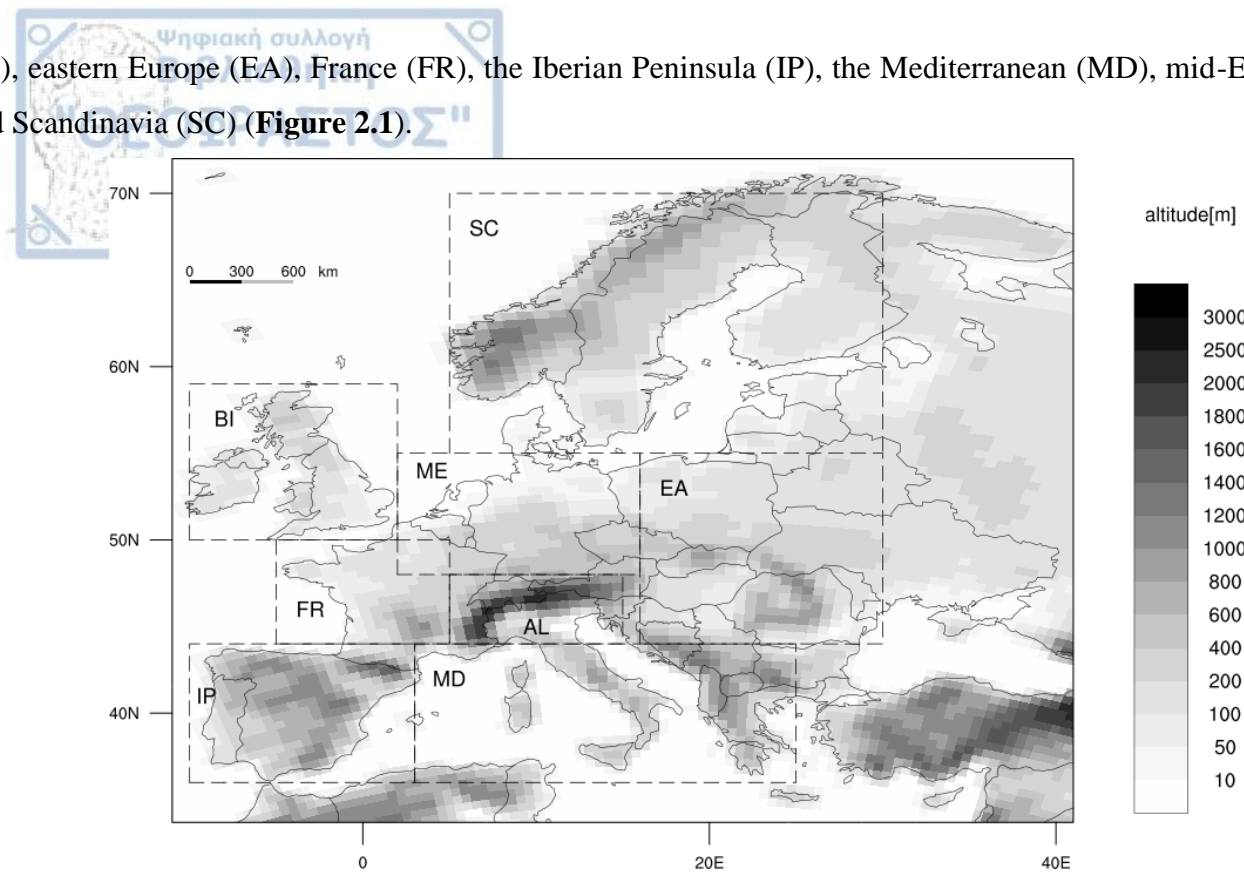


**Figure 2.1: Topography of the model domain. The outlined boxes with dashed lines correspond to the eight regions on which the analysis focused: AL (Alps), BI (British Isles), EA (Eastern Europe), FR (France), IP (Iberian Peninsula), MD (Mediterranean), ME (Mid-Europe), SC (Scandinavia).**

### 2.2.2 Observational datasets

The various reference products used for evaluation are described in **Table 2**. The monthly averaged data of gridded products used, which cover the full simulation period 1986-2015 for temperature, precipitation, cloud fraction, surface radiation fluxes, heat fluxes and soil moisture. Data were regridded, using bilinear interpolation, to model grid of  $0.44^\circ$ . When possible, different products are considered for a given variable in order to account for uncertainties in observation-based datasets.

**Table 2: Reference gridded datasets used for evaluation of WRF simulations.**

Dataset	Variables	Spatial resolution	Time period	Reference
E-OBS v25	2m temperature, precipitation	$0.1^\circ \times 0.1^\circ$	1986-2015	(Cornes et al., 2018)
CRU TS v. 4.06	2m temperature, precipitation, cloud fraction	$0.5^\circ \times 0.5^\circ$	1986-2015	(Harris et al., 2020)
CLARA-A2.1	Shortwave & longwave radiation, cloud fraction	$0.25^\circ \times 0.25^\circ$	1986-2015	(Karlsson et al., 2017)
ERA5-Land	Shortwave & longwave radiation, Latent heat flux, sensible heat flux, soil moisture	$0.1^\circ \times 0.1^\circ$	1986-2015	(Muñoz-Sabater et al., 2021)

Measured monthly data of latent and sensible heat flux are used from FLUXNET2015 Tier 2 dataset (Pastorello et al., 2020) to complement the evaluation of simulations for evaporation fraction. In the search for FLUXNET sites, the following criteria were defined: the sites 1) must be located inside the simulation domain, 2) have available long-period measurements within the simulation time period 1986-2015 and 3) be geographically dispersed to cover a large part of Europe. In total, 8 sites were found and their characteristics are described in **Table 3**. For comparison with simulations, the observed mean monthly evaporation fraction over a site is compared to the simulated evaporation fraction of the nearest model grid.

**Table 3: Characteristics of the sites selected from FLUXNET2015 dataset.**

FLUXNET site ID	Latitude, Longitude	Elevation(m)	Land cover	Time period
BE-Vie	(50.30,5.99)	493	Mixed Forest	1996-2014
CH-Fru	(47.11,8.53)	982	Grassland	2005-2014
DE-Geb	(51.09,10.91)	161	Cropland	2001-2014
ES-LJu	(36.92, -2.75)	1600	Open shrubland	2004-2013
FI-Hyy	(61.84,24.29)	181	Evergreen Needleleaf	1996-2014
FR-Gri	(48.84,1.95)	125	Cropland	2004-2014
FR-LBr	(44.71, -0.76)	61	Evergreen Needleleaf	1996-2008
IT-Col	(41,84, 13.58)	1560	Deciduous Broadleaf	1996-2014

## 2.3 Results

### 2.3.1 Temperature

In this section, the simulated 2-meter temperature from four WRF simulations is evaluated using the E-OBS gridded dataset for the 1986-2015 time period in Europe.

#### 2.3.1.1 Mean winter temperature

**Figure 2.2** depicts the mean 2-meter temperature bias (models minus observations) for winter, while the averaged model bias over the sub-regions of this analysis is presented in **Table 4**. In maps and tables, MMM represents the LUCAS multi-model ensemble mean including all simulations except WRF.

In winter, the sign of temperature bias among WRF configurations is mixed. WRFb-CLM4.0 and WRFb-NoahMP share the same atmospheric component but different land surface models (LSMs). They exhibit a similar spatial pattern of temperature bias in winter, indicating the minor contribution of LSMs on the simulation of winter temperature. Their major difference is the colder bias of WRFb-CLM4.0 over the Alps region ( $-1\text{ }^{\circ}\text{C}$  vs  $-0.2\text{ }^{\circ}\text{C}$ ). The atmospheric set-up selected for WRFc-NoahMP produces a large winter cold bias over Scandinavia ( $-2\text{ }^{\circ}\text{C}$ ) and Eastern Europe ( $-1.3\text{ }^{\circ}\text{C}$ ), while this is not the case for WRFb-NoahMP. The cold bias over North-Eastern Europe is a well-known deficiency which has been reported in previous WRF inter-comparison studies (Katragkou et al., 2015; García-Díez et al., 2015; Mooney et al., 2013). In a recent research conducted in the

context of LUCAS FPS (Daloz et al., 2021), the current WRF-NoahMP configurations were found to represent reasonably the snow-cover climatology and the incoming shortwave radiation at surface over the northern-eastern regions, implying also the realistic representation of cloud cover, when compared to satellite and reanalysis data. Since WRFb-NoahMP and WRFc-NoahMP differ only in parameterization options for PBL and surface layer, it could be suggested that the pronounced cold bias is related to problematic computation of skin temperature over snow-covered grounds in MM5 surface layer scheme, as reported in Mass, 2013. Last, the atmospheric settings selected for WRFa-NoahMP produce a widespread warm bias over the greatest part of Europe exceeding 2 °C over Alps and France.

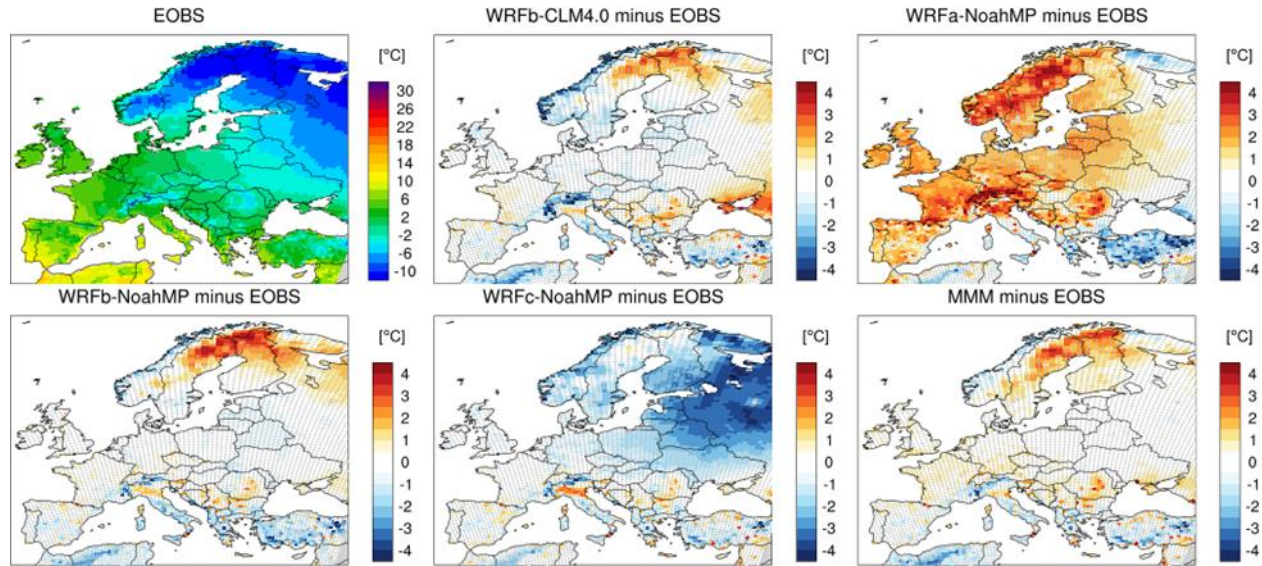


Figure 2.2: Mean 2-meter temperature bias (models minus observations) for winter (DJF) over the 1986-2015 time period. Stippling indicates areas where model bias is within the E-OBS uncertainty range. The  $\pm 1 \times SD$  is used as estimate of the uncertainty range of E-OBS dataset. MMM: multi-model-mean of LUCAS simulations excluding WRF configurations. The characteristics of LUCAS simulations are reported in Table A 4 in Appendix.

Table 4: Mean winter (DJF) 2-meter temperature bias (°C) over the time period 1986-2015, averaged over eight European sub-regions. AL (Alps), BI (British Isles), EA (Eastern Europe), FR (France), IP (Iberian Peninsula), MD (Mediterranean), ME (Mid-Europe), SC (Scandinavia). MMM: multi-model-mean of LUCAS simulations excluding WRF configurations.

	AL	BI	EA	FR	IP	MD	ME	SC
EOBS (°C)	0.2	4.2	-1.4	4.4	6.6	3.2	1.6	-6.6
WRFb-CLM4.0 minus EOBS	-1	-0.2	-0.2	0	-0.2	-0.2	-0.4	-0.2
WRFa-NoahMP minus EOBS	2.6	1.8	1.4	2.2	1.6	0.5	1.9	1.7
WRFb-NoahMP minus EOBS	-0.2	0	-0.3	0	-0.3	-0.4	-0.1	0.3
WRFc-NoahMP minus EOBS	-0.2	-0.5	-1.3	-0.2	-0.1	-0.2	-0.7	-2
MMM minus EOBS	0	0.3	0	0.3	-0.1	-0.2	0.3	0.4

### 2.3.1.2 Mean summer temperature

**Figure 2.3** depicts the mean 2-meter temperature bias (models minus observations) for summer, while the averaged model bias over the subregions of this analysis is presented in **Table 5**.

In summer, the 2-meter temperature regime is strongly controlled by the selection of atmospheric and land surface schemes. WRFb-NoahMP suffers from large warm biases over Alps (2.5 °C), France (2.5 °C), Iberian Peninsula (2.3 °C), Mediterranean (1.1 °C) and Mid-Europe (1.3 °C). These biases are to a great extent alleviated in WRFc-NoahMP, except the remaining warm bias of 1.1 °C over the Mediterranean. WRFb-CLM4 performs well having minor errors over all subregions. WRFa-NoahMP shows an unacceptable performance with extreme warm biases greater than 3 °C across all regions.

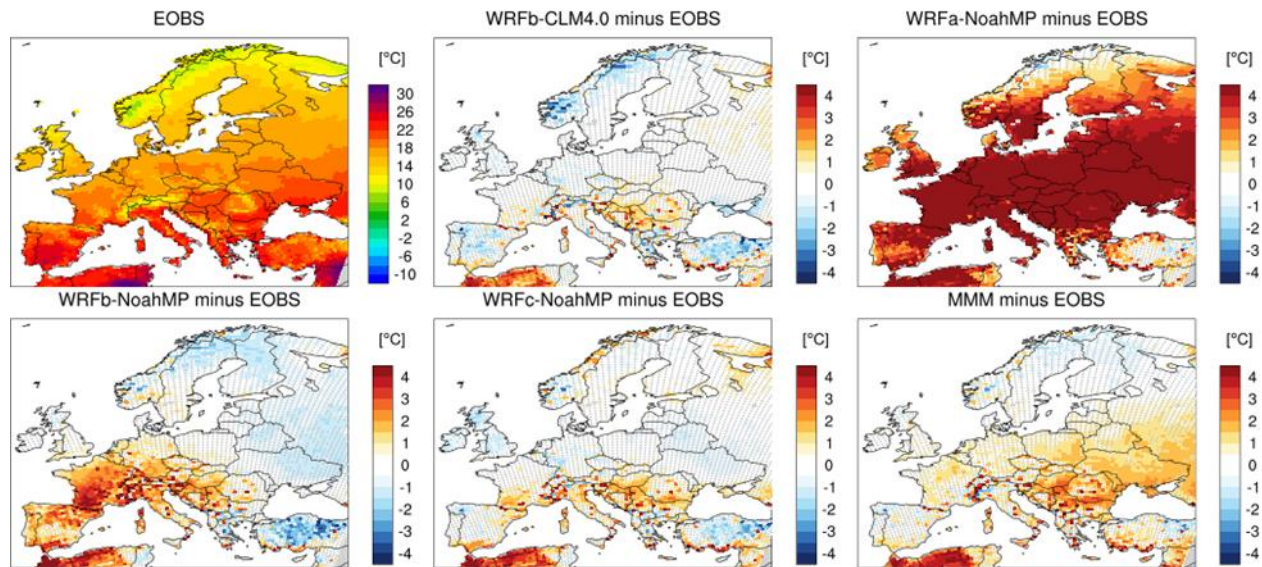


**Figure 2.3:** Mean 2-meter temperature bias (models minus observations) for summer (JJA) over the 1986-2015 time period. Stippling indicates areas where model bias is within the E-OBS uncertainty range. The  $\pm 1 \times SD$  is used as estimate of the uncertainty range of E-OBS dataset. MMM: multi-model-mean of LUCAS simulations excluding WRF configurations.

**Table 5:** Mean summer (JJA) 2-meter temperature bias (°C) over the time period 1986-2015, averaged over eight European subregions. AL (Alps), BI (British Isles), EA (Eastern Europe), FR (France), IP (Iberian Peninsula), MD (Mediterranean), ME (Mid-Europe), SC (Scandinavia). MMM: multi-model-mean of LUCAS simulations excluding WRF configurations.

	AL	BI	EA	FR	IP	MD	ME	SC
EOBS (°C)	16.6	14.8	18.8	18.3	21.4	21.1	17.3	13.2
WRFb-CLM4.0 minus EOBS	0.1	-0.4	0.3	0.1	-0.1	0.6	-0.2	-0.3
WRFa-NoahMP minus EOBS	6.9	3.4	5.2	6.5	4.4	4.8	5.8	2.4
WRFb-NoahMP minus EOBS	2.5	0.2	0.2	2.5	2.3	1.1	1.3	-0.5
WRFc-NoahMP minus EOBS	0.7	-0.7	0.2	0.3	0.6	1.1	-0.1	0
MMM minus EOBS	0.7	0.2	1.4	0.7	0.4	1.5	0.7	-0.1

### 2.3.1.3 Seasonal cycles

Figure 2.4 depicts the mean observed and simulated seasonal cycle of 2-meter temperature over the eight subregions of analysis.

WRFb-CLM4 and WRFc-NoahMP capture adequately the observed seasonal cycle of 2-meter temperature over all the subregions. Their small biases lie within the E-OBS uncertainty range, indicated with the grey shadow. WRFb-NoahMP shows a prominent overestimation of mean temperature during the warm months over the regions of Alps, France and Iberian Peninsula. Last, WRFa-NoahMP exhibits a constant and large overestimation throughout the year over almost all subregions.

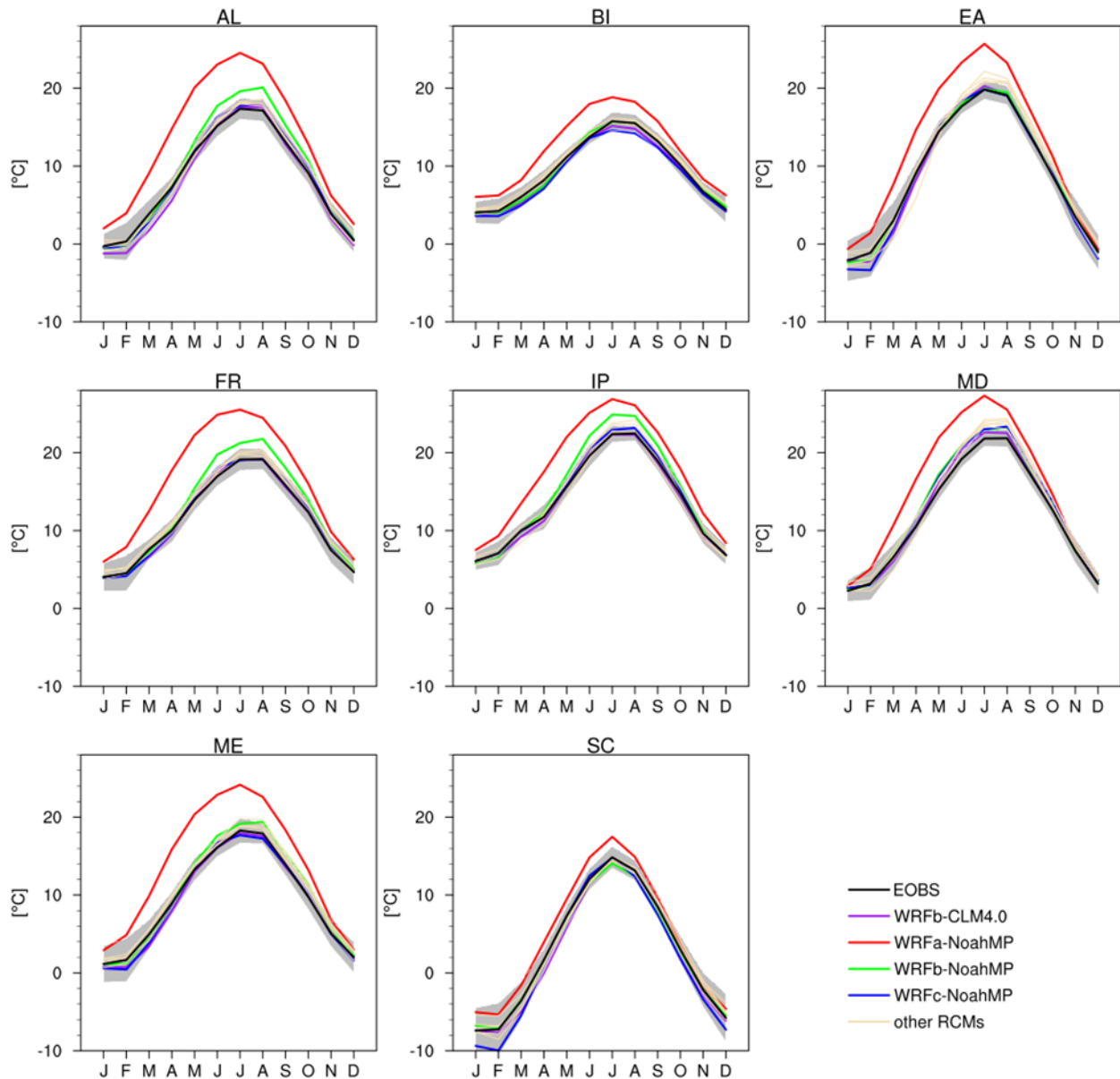
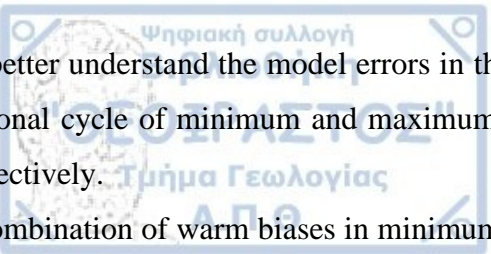


Figure 2.4: Mean seasonal cycle of observed (EOBS) and simulated 2-meter temperature over the eight subregions of analysis: AL (Alps), BI (British Isles), EA (Eastern Europe), FR (France), IP (Iberian Peninsula), MD (Mediterranean), ME (Mid-Europe), SC (Scandinavia). The grey area represents the range of E-OBS uncertainty ( $\pm 1 \times SD$ ).





To better understand the model errors in the estimation of mean temperature, the mean observed and simulated seasonal cycle of minimum and maximum 2-meter temperature is also assessed in **Figure 2.5** and **Figure 2.6** respectively.

A combination of warm biases in minimum and mostly in maximum temperature results in an overestimation of mean temperature over Alps, France, Iberian Peninsula and Mid-Europe for WRFb-NoahMP. The amplification of warm bias in maximum temperature in the late summer is likely associated with positive feedbacks triggered by soil dryness in WRFb-NoahMP and will be checked in the next sessions in combination with other variables, such as the surface heat fluxes and soil moisture. Furthermore, WRFc-NoahMP captures well both the seasonal cycles of minimum and maximum temperature. The maximum temperature is overestimated in late summer over the regions of southern Europe (Iberian Peninsula, Mediterranean) for WRFc-NoahMP, while the minimum and maximum temperatures are underestimated during the cold months over Eastern Europe and mostly in Scandinavia, however these cold biases lie within the E-OBS uncertainty range. Moreover, WRFb-CLM4.0 represents well the observed seasonal cycle of minimum and maximum temperatures in almost all subregions, showing small cold biases during the spring mostly in daytime temperatures over the regions of central and northern Europe (France, Mid-Europe, Alps, Eastern Europe and Scandinavia). This feature could be linked to findings from Daloz et al., 2021, in which WRFb-CLM4.0 was found to have an extended snow-cover period over Eastern Europe and Scandinavia. Last, WRFa-NoahMP fails to capture the seasonal cycle of minimum and mostly maximum temperatures, showing large overestimations in all subregions across seasons.

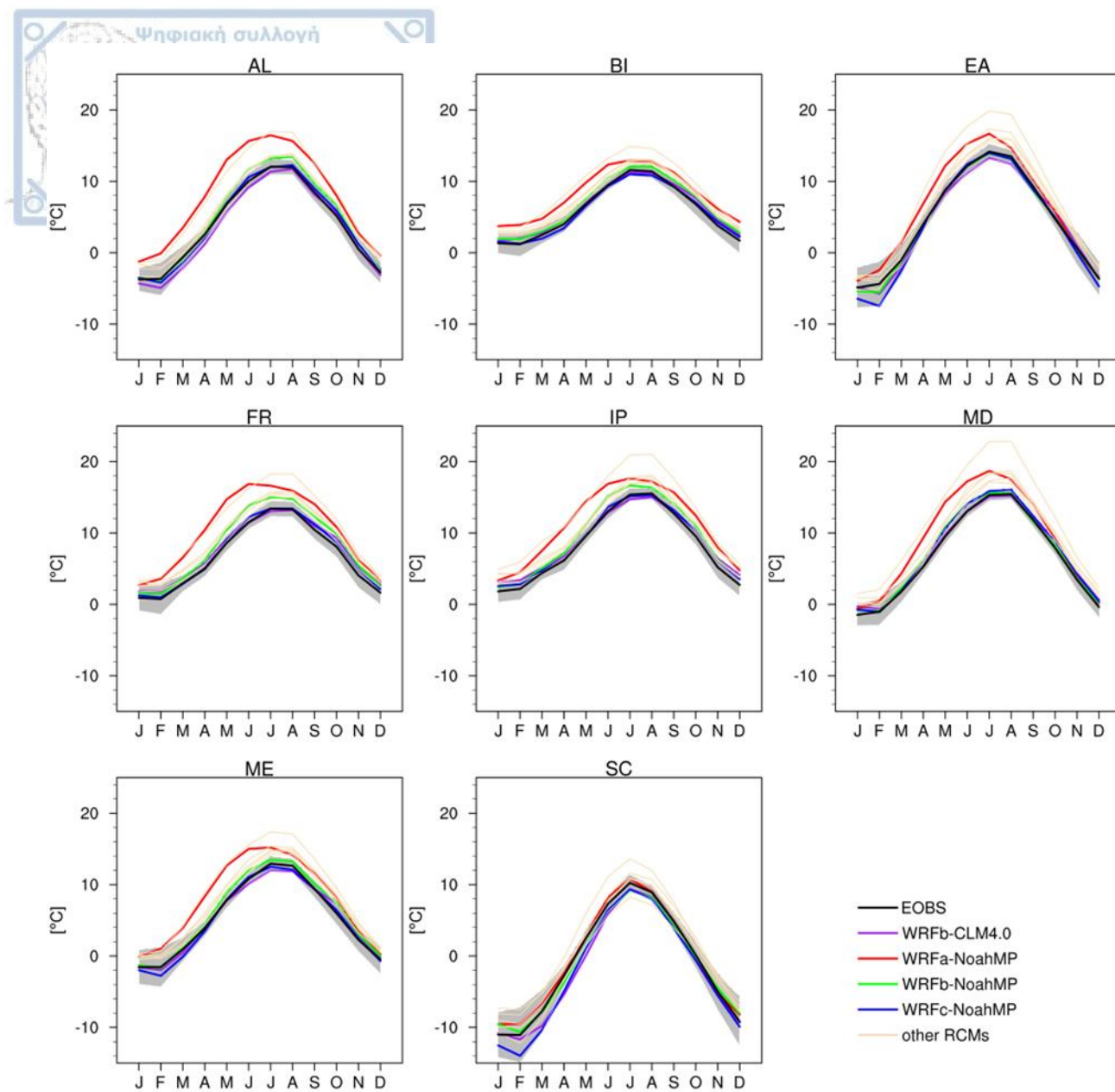


**Figure 2.5: Mean seasonal cycle of observed (EOBS) and simulated 2-meter minimum temperature over the eight subregions of analysis: AL (Alps), BI (British Isles), EA (Eastern Europe), FR (France), IP (Iberian Peninsula), MD (Mediterranean), ME (Mid-Europe), SC (Scandinavia). The grey area represents the range of E-OBS uncertainty ( $\pm 1 \times SD$ ).**

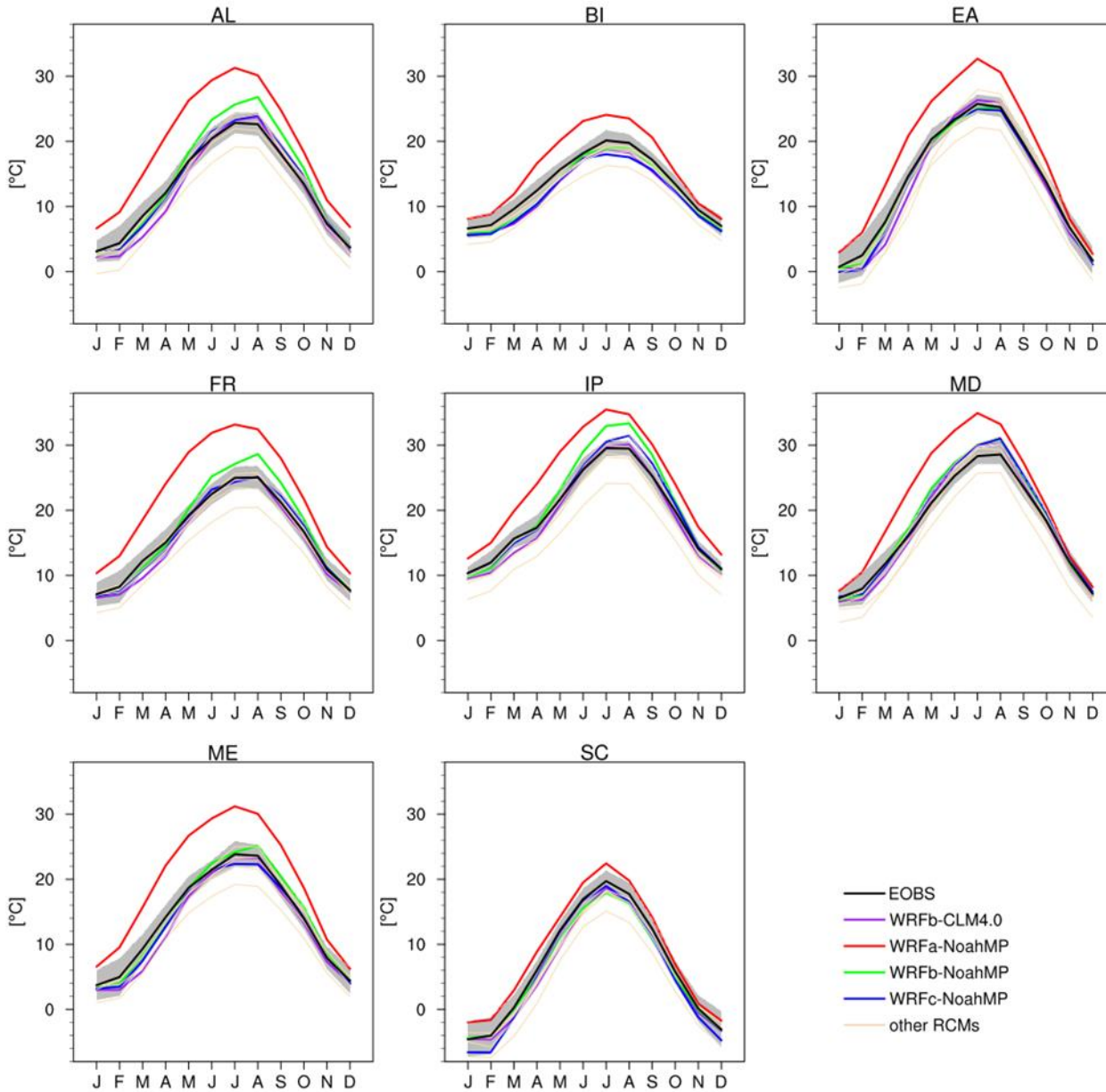


Figure 2.6: Mean seasonal cycle of observed (EOBS) and simulated 2-meter maximum temperature over the eight subregions of analysis: AL (Alps), BI (British Isles), EA (Eastern Europe), FR (France), IP (Iberian Peninsula), MD (Mediterranean), ME (Mid-Europe), SC (Scandinavia). The grey area represents the range of E-OBS uncertainty ( $\pm 1 \times SD$ ).

### 2.3.1.4 Taylor diagrams

Taylor diagrams are used to address the model performances in terms of the amplitude of temperature variability (normalized standard deviation) and correlation with observations on temporal and spatial scale over the European continent. Observed monthly temperature from CRU dataset is considered in addition to EOBS, in order to account for uncertainty in observational data.

In winter (**Figure 2.7**), all WRF configurations except WRFa-NoahMP are found to be in high spatial and temporal agreement with observations in terms of correlation (higher than 0.9). In terms of variability, WRFb-NoahMP somewhat underestimates the spatial temperature variation, while the opposite is true on temporal scale. WRFb-CLM4.0 overestimates the spatial and temporal variability of nighttime temperature but achieves high

performance for daytime temperature. The different atmospheric set-up in WRFc-NoahMP degrades the quality of simulation, producing considerable overestimation of temperature variability, especially for minimum temperature on temporal scale (greater than 1.25). The results are almost the same when comparing either with EOBS or CRU, implying good consistency between the observational datasets.

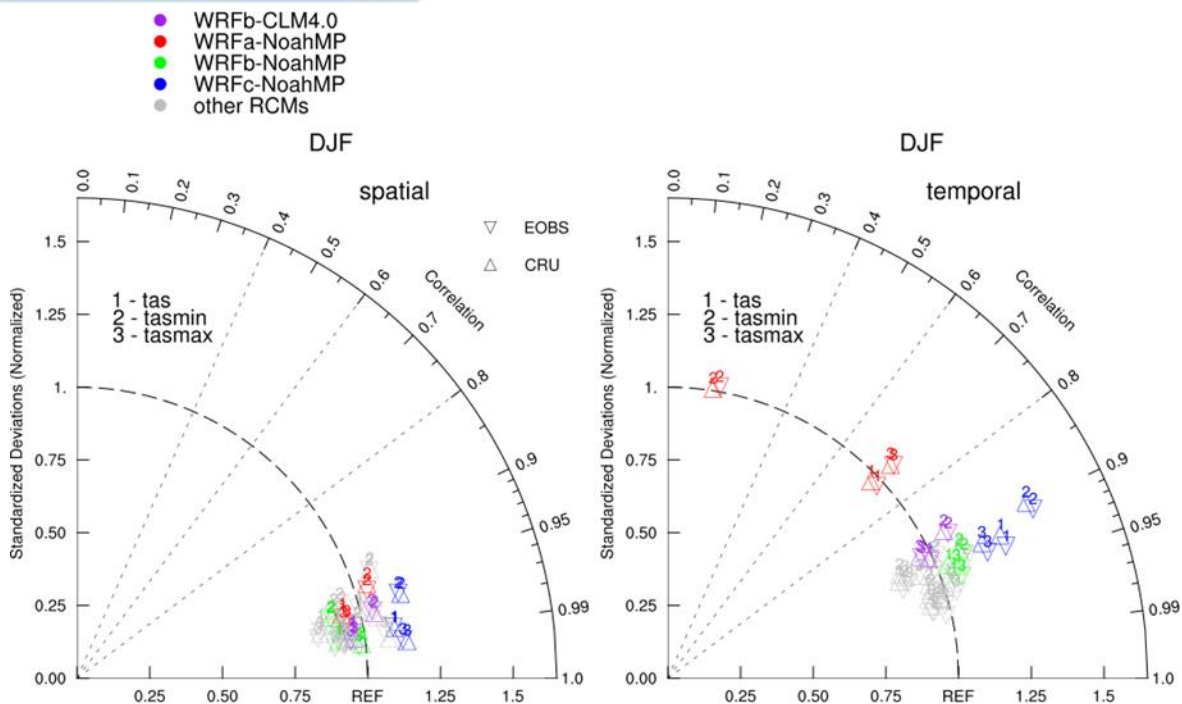


**Figure 2.7:** Taylor diagrams for mean, minimum and maximum winter 2-meter temperature averaged over Europe for 1986-2015 time period. The plots depict the spatial and temporal correlation and ratio of variance (normalized standard deviation) between simulated and observed values from E-OBS and CRU, based on monthly means.

In summer (**Figure 2.8**), the results are more dispersed with respect to winter. It is noticed again a high spatial and temporal correlation between the simulated (except WRFa-NoahMP on temporal scale) and observed values, higher than 0.8. In terms of variability, the different atmospheric set-ups between WRFb-NoahMP and WRFc-NoahMP do not affect the spatiotemporal variability of nighttime temperature (they both underestimate it), although the temporal variation of daytime temperature is clearly improved in WRFc-NoahMP. The switch from NoahMP to CLM4 upgrades the simulation of maximum temperature on spatial scale and changes the sign of bias for minimum temperature variability from negative in WRFb-NoahMP to positive in WRFb-CLM4.0.

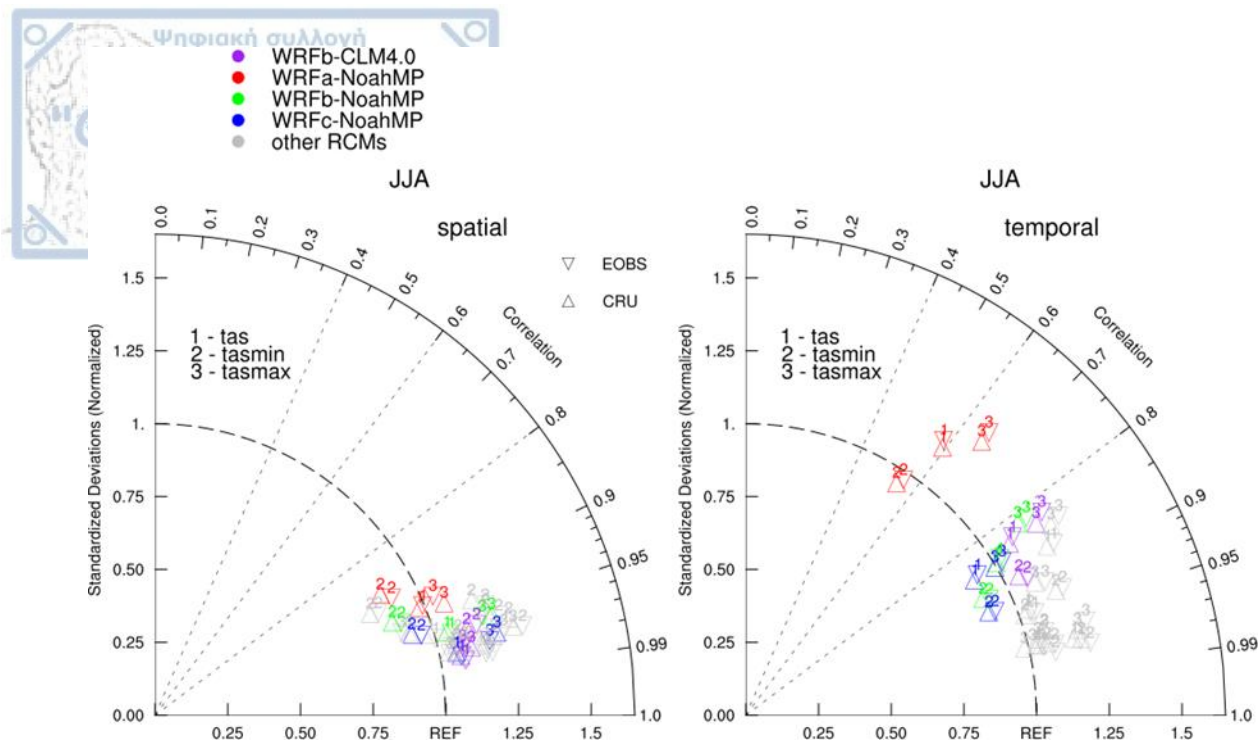


**Figure 2.8:** Taylor diagrams for mean, minimum and maximum summer 2-meter temperature averaged over Europe for 1986-2015 time period. The plots depict the spatial and temporal correlation and ratio of variance (normalized standard deviation) between simulated and observed values from E-OBS and CRU, based on monthly means.

### 2.3.2 Precipitation

In this section, the simulated precipitation is compared to observations (E-OBS) across seasons and regions in Europe over the 1986-2015 time period, following the same methodology applied for temperature.

#### 2.3.2.1 Mean winter precipitation

**Figure 2.9** depicts the mean precipitation bias (models minus observations) for winter, while the averaged model bias over the sub-regions of analysis is presented in **Table 6**.

In winter, all WRF modelling systems, except WRFa-NoahMP, tend to overestimate the mean precipitation in most regions, apart from the area of British Isles. WRFb-NoahMP and WRFc-NoahMP share a similar pattern of precipitation bias, confirming the evidence from Mooney et al., 2013 where the sensitivity of winter precipitation to two different PBL schemes was minor. Only over Eastern Europe, the use of YSU PBL scheme yields somewhat wetter conditions for WRFc-NoahMP compared to WRFb-NoahMP. The wet conditions are also reproduced in WRFb-CLM4.0 which shows larger errors across Europe especially over mountainous regions (60% overestimation over Alps). In Jin et al., 2010, WRF simulations coupled to four different LSMs showed an overestimation of winter precipitation and no close relationship with land surface processes, supporting the general consensus that atmospheric circulation dominates the winter precipitation regime.

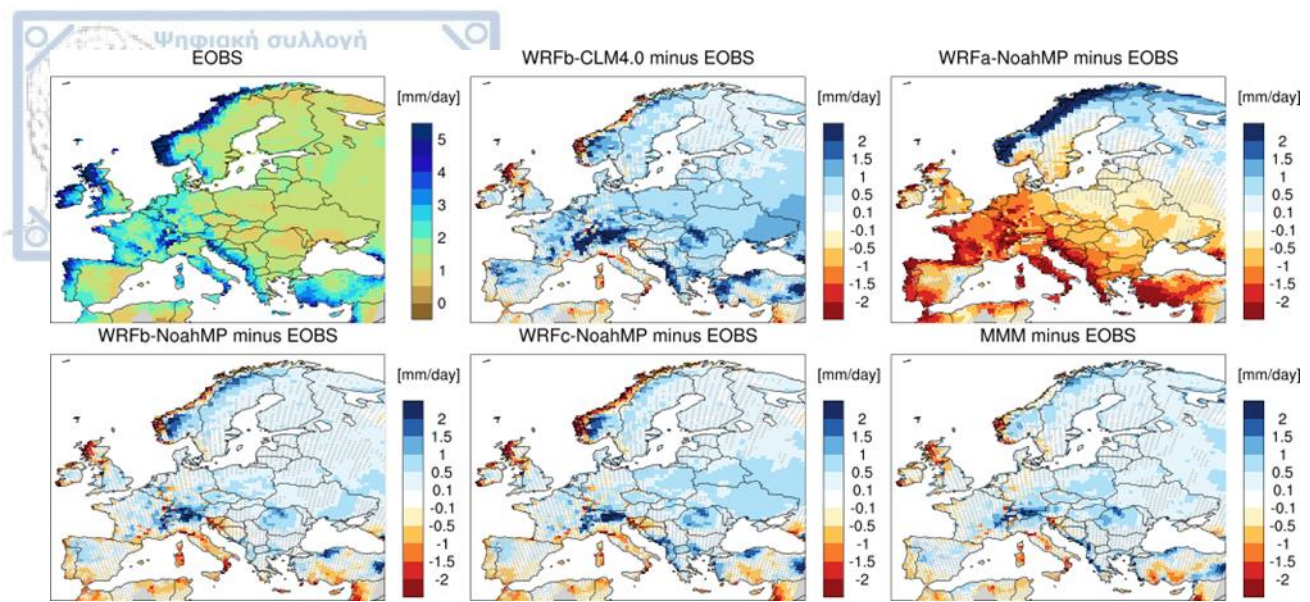


Figure 2.9: Mean precipitation bias (models minus E-OBS) for winter (DJF) over 1986-2015 period. Stippling indicates areas where model bias is within the E-OBS uncertainty range. The  $\pm 1 \times SD$  is used as estimate of the uncertainty range of E-OBS dataset. MMM: multi-model-mean of LUCAS simulations excluding WRF configurations.

Table 6: Mean model relative bias (%) for winter precipitation (mm/day) over 1986-2015 period compared to E-OBS, averaged over eight European subregions. AL (Alps), BI (British Isles), EA (Eastern Europe), FR (France), IP (Iberian Peninsula), MD (Mediterranean), ME (Mid-Europe), SC (Scandinavia). MMM: multi-model-mean of LUCAS simulations excluding WRF configurations.

	AL	BI	EA	FR	IP	MD	ME	SC
EOBS (mm/day)	2.3	3.5	1.2	2.3	2	1.9	1.9	1.9
WRFb-CLM4.0 minus EOBS	60%	-4%	65%	38%	27%	26%	45%	21%
WRFa-NoahMP minus EOBS	-65%	-30%	-47%	-70%	-66%	-76%	-60%	49%
WRFb-NoahMP minus EOBS	30%	-7%	33%	12%	0%	0%	20%	15%
WRFc-NoahMP minus EOBS	30%	-8%	42%	13%	0%	7%	19%	9%
MMM minus EOBS	30%	-10%	39%	13%	7%	0%	19%	14%

### 2.3.2.2 Mean summer precipitation

In summer (Figure 2.10), the precipitation regime is strongly controlled by the selection of atmospheric and land surface schemes. WRFb-CLM4.0 tends to underestimate the summer rainfall over the south-eastern part of Europe, producing a dry bias of -38% of the absolute E-OBS estimate over Mediterranean (Table 7). WRFb-NoahMP yields a largely drier simulation than WRFb-CLM4.0 over regions of central Europe (-58% over Alps, -74% over France, -61% over Mid-Europe), which is consistent with the warm summer bias over these regions.

The better performance of WRFb-CLM4.0 with respect to WRFb-NoahMP highlights the significant role of advanced LSMs in simulating summer climate with higher accuracy than simpler LSMs. Moreover, the different PBL scheme used in WRFc-NoahMP dramatically reduces the dry bias produced by WRFb-NoahMP, however it yields a wet bias over the north-eastern part of the domain which is not visible in WRFb-NoahMP. Last, the selected atmospheric set-up in WRFa-NoahMP results in a widespread dry bias which likely explains the extensive warm summer bias for this model.

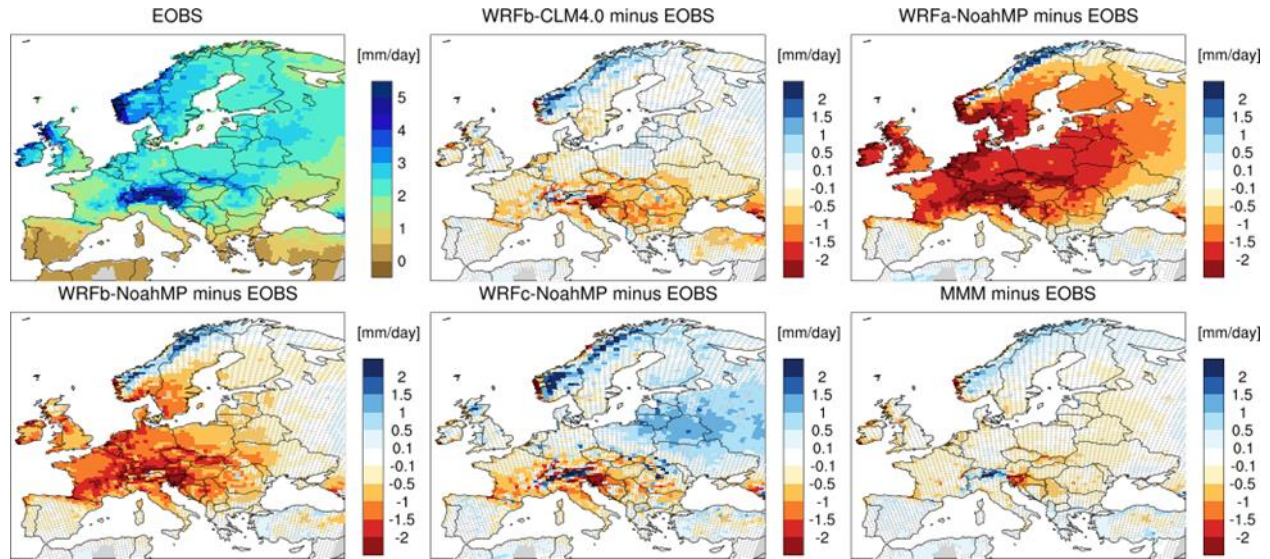


Figure 2.10: Mean precipitation bias (models minus EOBS) for summer (JJA) over 1986-2015 period. Stippling indicates areas where model bias is within the E-OBS uncertainty range. The  $\pm 1 \times SD$  is used as estimate of the uncertainty range of E-OBS dataset. MMM: multi-model-mean of LUCAS simulations excluding WRF configurations.

Table 7: Mean model relative bias (%) for summer precipitation (mm/day) over 1986-2015 period compared to E-OBS, averaged over eight European subregions. AL (Alps), BI (British Isles), EA (Eastern Europe), FR (France), IP (Iberian Peninsula), MD (Mediterranean), ME (Mid-Europe), SC (Scandinavia). MMM: multi-model-mean of LUCAS simulations excluding WRF configurations.

	AL	BI	EA	FR	IP	MD	ME	SC
EOBS (mm/day)	3.2	2.6	2.2	2	0.8	1.3	2.4	2.5
WRFb-CLM4.0 minus EOBS	-16%	-8%	-20%	-18%	-16%	-38%	-11%	8%
WRFa-NoahMP minus EOBS	-76%	-73%	-70%	-84%	-56%	-48%	-82%	-40%
WRFb-NoahMP minus EOBS	-58%	-43%	-39%	-74%	-67%	-48%	-61%	-7%

WRFc-NoahMP minus EOBS	-12%	0%	10%	-26%	-18%	-25%	-6%	22%
MMM minus EOBS	0%	-12%	-13%	-14%	0%	-7%	-7%	4%

Moreover, Katragkou et al., 2015 found that the high summer precipitation rates were overestimated across Europe for an ensemble of WRF modelling systems. The current WRF ensemble does not confirm this finding (**Figure 2.11**). WRFa-NoahMP fails to reproduce the climatological pattern of summer precipitation, showing large deviations from the observed distribution over all subregions. WRFb-CLM4.0 and WRFc-NoahMP perform acceptably in most regions with some exceptions; WRFc-NoahMP overestimates the high rainfall rates in Scandinavia and Eastern Europe, while WRFb-CLM4.0 underestimates the large rainfall amounts in Mediterranean and somewhat overestimates them in Scandinavia. Last, WRFb-NoahMP underestimates the whole range of rainfall rates and mostly the high quantiles over Alps, France, Mid-Europe and Iberian Peninsula.



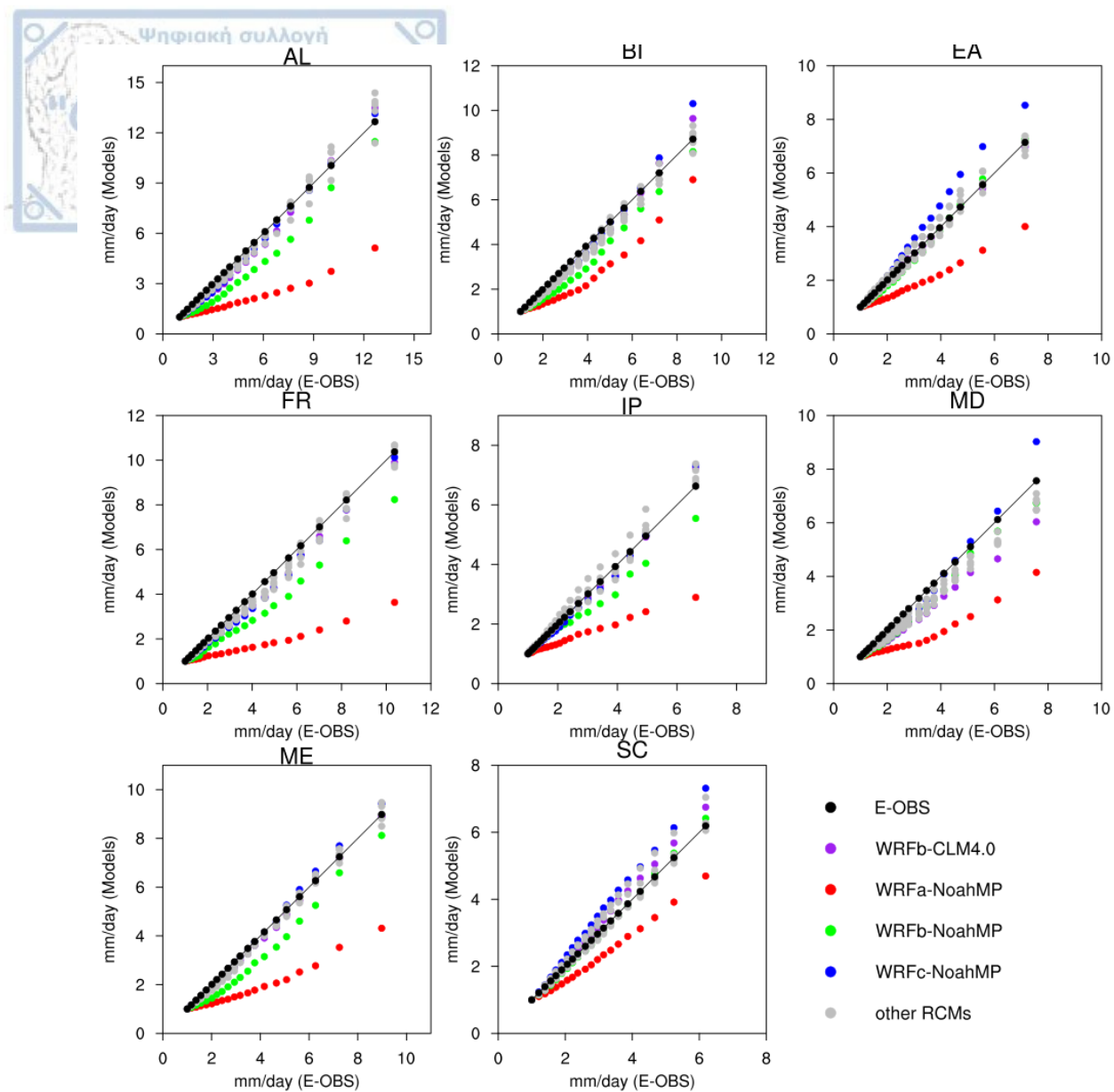


**Figure 2.11: Quantile-quantile plots for mean summer precipitation averaged over eight European sub-regions, based on daily values for 1986-2015 time period. Summer precipitation distribution is divided into 20 quantiles, taking a quantile every 5%. Only daily rainfall amounts greater than 1 mm are considered. AL (Alps), BI (British Isles), EA (Eastern Europe), FR (France), IP (Iberian Peninsula), MD (Mediterranean), ME (Mid-Europe), SC (Scandinavia).**

### 2.3.2.3 Seasonal cycles

**Figure 2.12** depicts the simulated and observed seasonal cycle of mean precipitation over the eight different regions of analysis.

WRFb-CLM4.0 and WRFc-NoahMP capture adequately the observed climatological pattern of precipitation sharing a similar seasonal cycle. They both show a tendency for overestimation during the cold months, which is more pronounced for WRFb-CLM4.0, and small dry biases which lie within the E-OBS uncertainty range during the summer in most regions, apart from Scandinavia where they show a year-round wet bias. Their major difference occurs over Eastern Europe in summer, where WRFb-CLM4.0 exhibits a dry bias in contrast to wet conditions in WRFc-NoahMP. The switch from CLM4.0 to NoahMP or the change of PBL scheme in WRFb-NoahMP, induces a prominent dry bias in summer months across all regions and mostly over Alps, France and

Mid-Europe. WRFa-NoahMP is not agreement with the observed seasonal cycle of precipitation across Europe, showing a constant dry bias throughout the year in most regions.

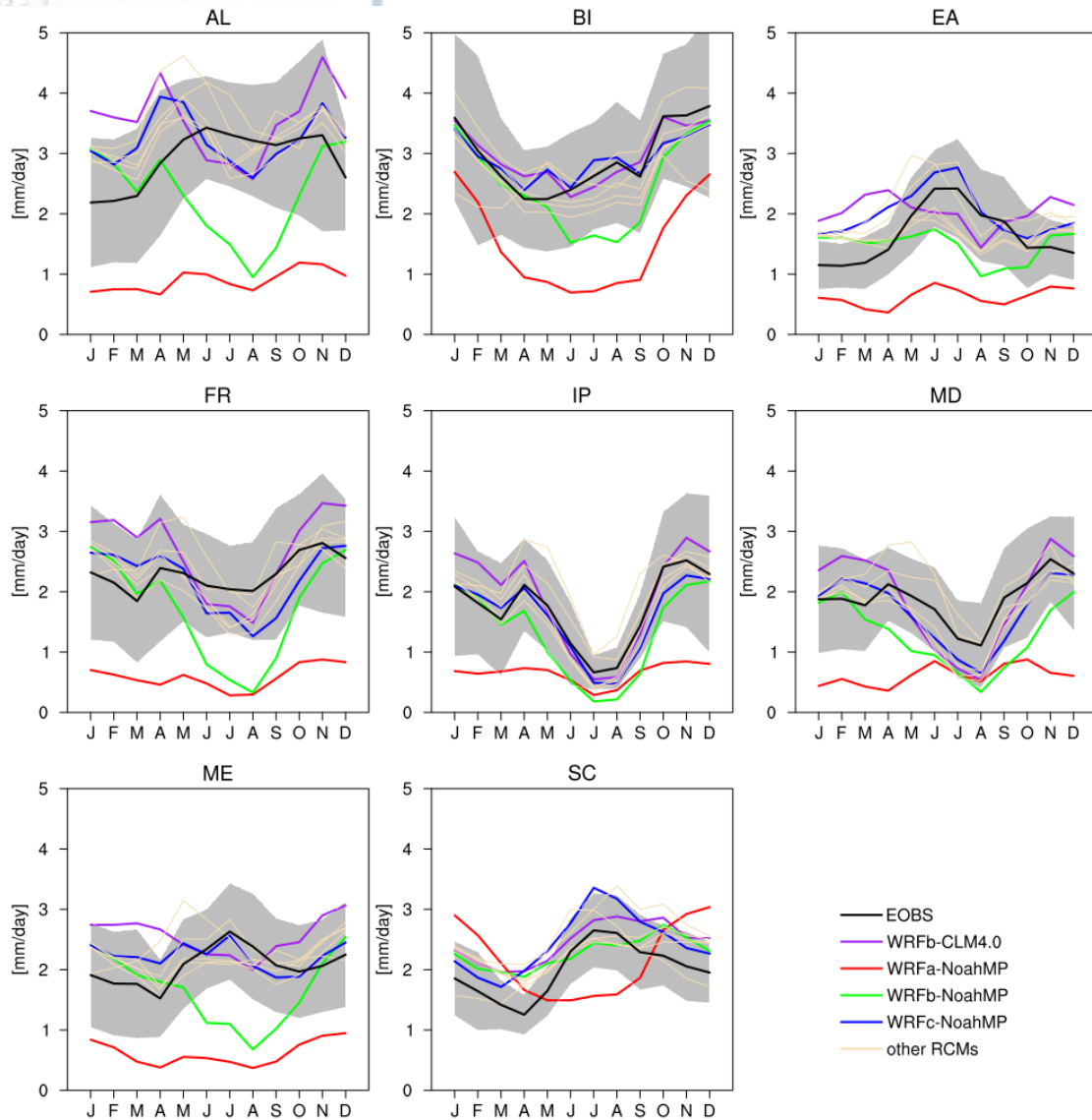


**Figure 2.12: Observed and simulated seasonal cycle of mean precipitation (mm/day) averaged over eight European regions for the period 1986-2015. AL (Alps), BI (British Isles), EA (Eastern Europe), FR (France), IP (Iberian Peninsula), MD (Mediterranean), ME (Mid-Europe), SC (Scandinavia). The grey area represents the range of E-OBS uncertainty ( $\pm 1 \times SD$ ).**

#### 2.3.2.4 Taylor diagrams

Following the same methodology applied for temperature, Taylor diagrams are used to assess the model performances in terms of the variability of precipitation (normalized standard deviation) and correlation with observations on temporal and spatial scale over the European continent.

In winter (**Figure 2.13**), WRFb-NoahMP and WRFc-NoahMP modelling systems exhibit similar performances, indicating the minor effect of PBL scheme selection on winter precipitation. In terms of correlation, they show a high spatial and temporal agreement with observations close to 0.8. When compared to CRU, both modelling systems capture adequately the spatial and temporal variability of winter precipitation, whereas they show a small overestimation on temporal scale in reference to EOBS, revealing a small inconsistency between the observational

datasets. Furthermore, WRFb-CLM4.0 achieves somewhat worse performance than WRFb-NoahMP and WRFc-NoahMP overestimating the spatial and temporal variability of winter precipitation. Last, WRFa-NoahMP does not perform suitably showing low spatial and temporal agreement with observations in terms of correlation and variability.

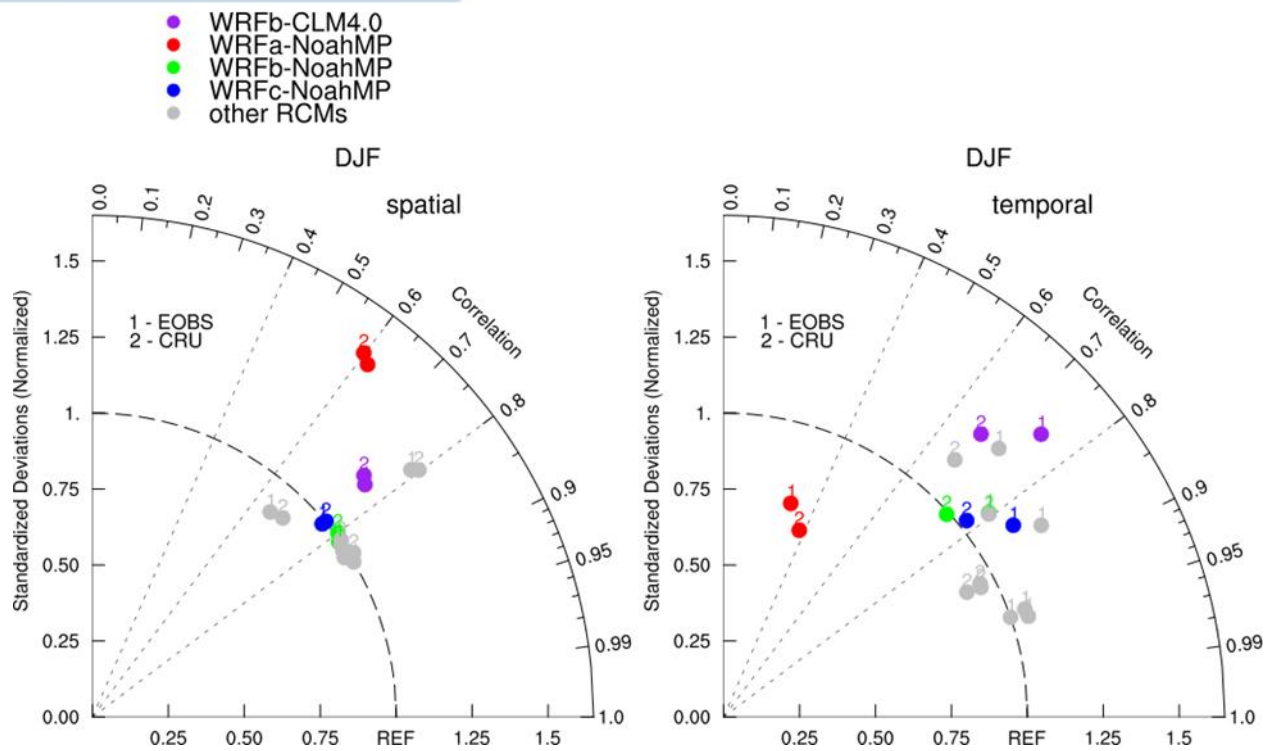


**Figure 2.13: Taylor diagrams for mean winter precipitation (mm/day) averaged over Europe for 1986-2015 time period. The plots depict the spatial and temporal correlation and ratio of variance (normalized standard deviation) between simulated and observed values from E-OBS and CRU, based on monthly means.**

In summer (**Figure 2.14**), the choice of atmospheric and land surface schemes affects the WRF performance for precipitation. With respect to the spatial agreement, WRFb-CLM4.0 outperforms the other WRF modelling systems, showing high correlation with observations around 0.9, and variability close to unity. The change of PBL scheme does not improve the model accuracy, but changes the sign of bias for precipitation variability from negative in WRFb-NoahMP to positive in WRFc-NoahMP. WRFa-NoahMP shows again a bad performance, with large underestimation of precipitation variation and moderate correlation with observational datasets. On temporal scale, all modelling systems exhibit a modest correlation with observations close to 0.6. Excluding WRFa-NoahMP, the WRF configurations overestimate the precipitation variability, with WRFb-NoahMP having the least bias after WRFb-CLM4.0 and WRFc-NoahMP sequentially.

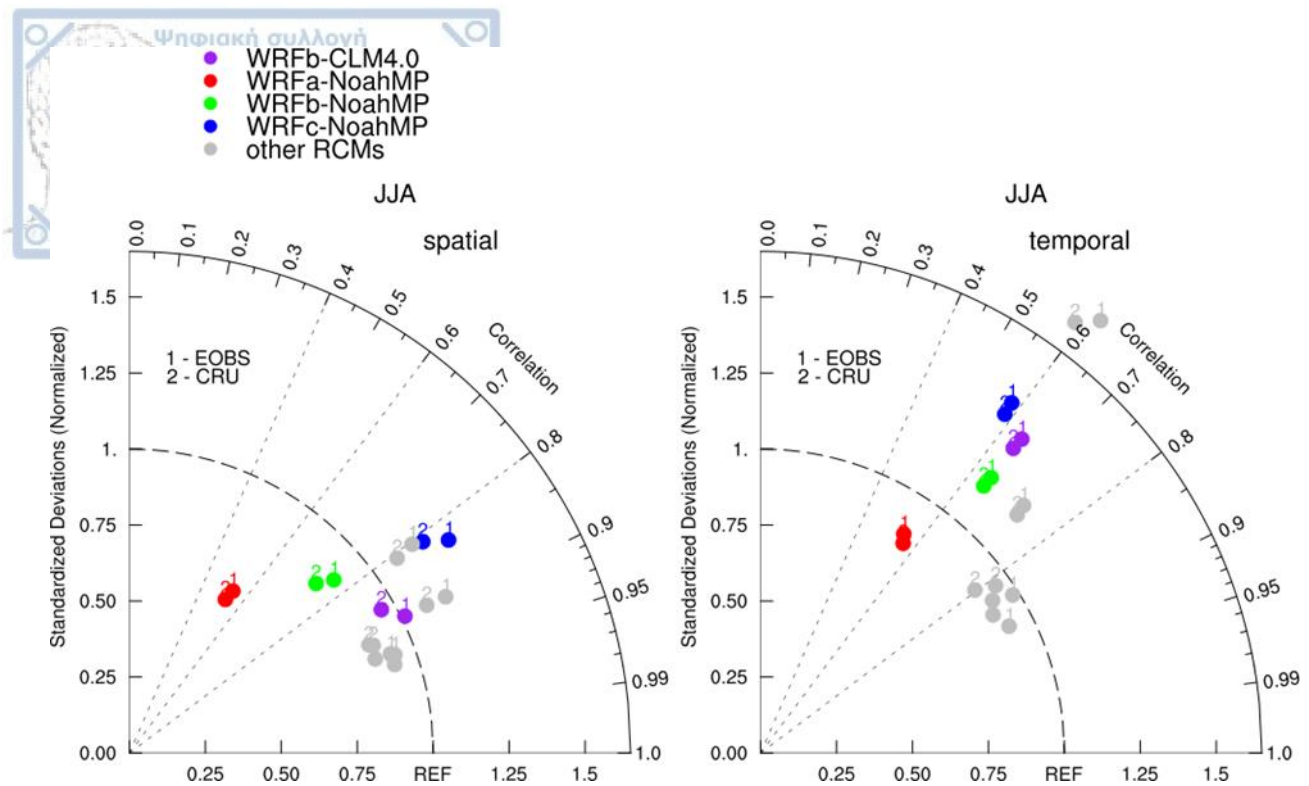


**Figure 2.14:** Taylor diagrams for mean summer precipitation (mm/day) averaged over Europe for 1986-2015 time period. The plots depict the spatial and temporal correlation and ratio of variance (normalized standard deviation) between simulated and observed values from E-OBS and CRU, based on monthly means.

### 2.3.3 Radiation and clouds

The variations of radiation fluxes at surface across seasons and latitude regulate to a great extent the surface climate. In this section, monthly data from CLARA-A2.1 satellite-derived record are used in order to assess the performance of WRF modelling systems in simulating the downwelling shortwave and longwave radiation at surface over Europe. To verify the robustness of results, models are also compared to ERA5 reanalysis data, which combine model data with observations across the world and cover the simulation time period 1986-2015.

#### 2.3.3.1 Winter radiation fluxes

CLARA-A2.1 depict a south-north gradient in the spatial distribution of downwelling shortwave radiation at the surface in winter (**Figure 2.15**). Maximum amounts are observed over Iberian Peninsula around  $91 \text{ W m}^{-2}$  on average (**Table 8**), with values gradually decreasing towards the northern Europe reaching up to  $15 \text{ W m}^{-2}$  on average over Scandinavia.

In winter, all modelling systems tend to overestimate shortwave radiation over the south-eastern part of the domain. The LSM choice has a minor impact on shortwave radiation in winter, since WRFb-CLM4.0 and WRFb-NoahMP exhibit a similar behavior with overestimation over Alps and the south-eastern Europe and an underestimation over British Isles and the west coasts of Iberian Peninsula, France and Benelux. On the other hand, the contribution of atmospheric component on winter radiation bias is considerable. The change of convective and microphysics scheme in WRFa-NoahMP yields a widespread positive bias over central and southern Europe. Also, the change of PBL scheme in WRFc-NoahMP results in a more pronounced and extensive positive bias over the southern and eastern regions, almost doubling the overestimation over Mediterranean (22%

of the absolute CLARA-A2.1 estimate) and Eastern Europe (33%) with respect to WRFb-NoahMP. Moreover, the results seem odd for all modelling systems over the high latitude areas, especially in Scandinavia where the southern part has a negative sign of bias in contrast to the positive bias over the northern part. This feature is probably related to low accuracy of the employed observational dataset over the high latitude areas, where there is a difficulty for satellites to differentiate snow and cloud detection (Babar et al., 2018).

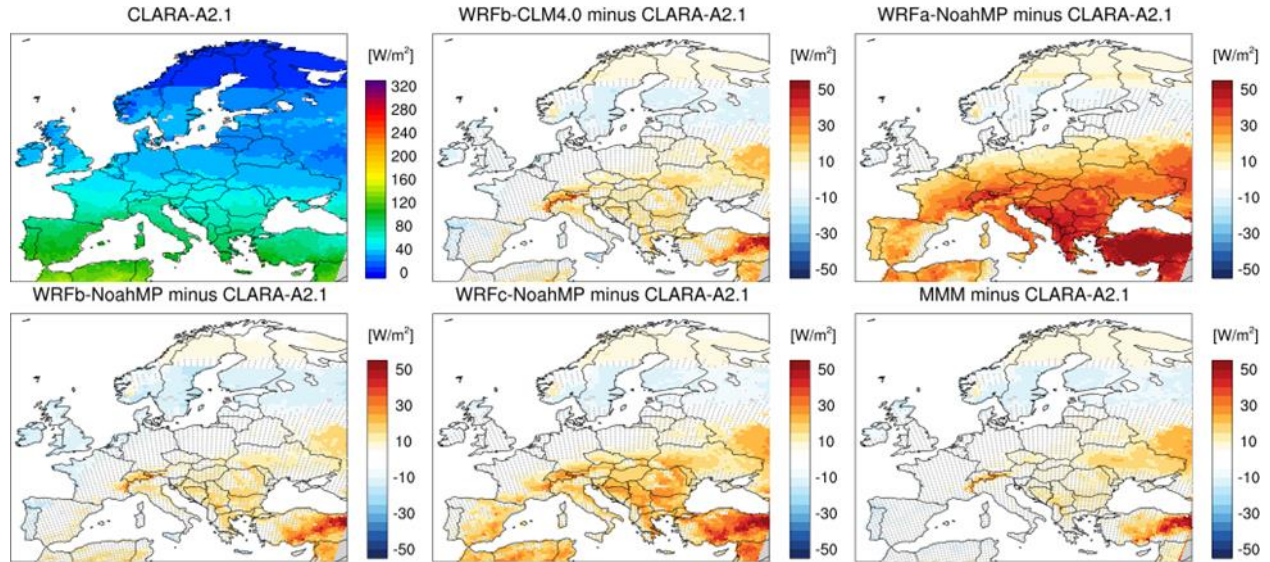


**Figure 2.15:** Mean bias (models minus CLARA-A2.1) for downwelling shortwave radiation at surface in winter (DJF) over 1986-2015 period. Stippling indicates areas where model bias is within the CLARA-A2.1 uncertainty range. The  $\pm 1 \times \text{SD}$  is used as estimate of the uncertainty range of CLARA-A2.1 dataset. MMM: multi-model-mean of LUCAS simulations excluding WRF configurations.

**Table 8:** Mean model relative winter bias for downwelling shortwave radiation at surface over 1986-2015 period compared to CLARA-A2.1, averaged over eight European subregions. AL (Alps), BI (British Isles), EA (Eastern Europe), FR (France), IP (Iberian Peninsula), MD (Mediterranean), ME (Mid-Europe), SC (Scandinavia). MMM: multi-model-mean of LUCAS simulations excluding WRF configurations.

	AL	BI	EA	FR	IP	MD	ME	SC
CLARA-A2.1 ( $\text{W/m}^2$ )	58	36	42	55	91	81	40	15
WRFb-CLM4.0 minus CLARA-A2.1	21%	-17%	24%	-2%	-2%	9%	3%	0%
WRFa-NoahMP minus CLARA-A2.1	57%	0%	64%	44%	24%	46%	50%	13%
WRFb-NoahMP minus CLARA-A2.1	16%	-28%	17%	-4%	0%	11%	-5%	-13%
WRFc-NoahMP minus CLARA-A2.1	28%	-11%	33%	11%	12%	22%	10%	0%
MMM minus CLARA-A2.1	10%	-11%	21%	0%	-4%	5%	5%	-7%

Evidence from comparison of models with ERA5 reanalysis data do not confirm the mixed results over Scandinavia (**Figure 2.16**). Specifically, all WRF configurations perform suitably over Scandinavia when comparing to ERA5. Over the rest domain, the spatial pattern of model biases is somewhat similar when comparing either to CLARA-A2.1 or ERA5, however ERA5 provide larger amounts of shortwave radiation at

surface than CLARA-A2.1. This inconsistency between the datasets largely reduces the model positive biases when comparing to ERA5.

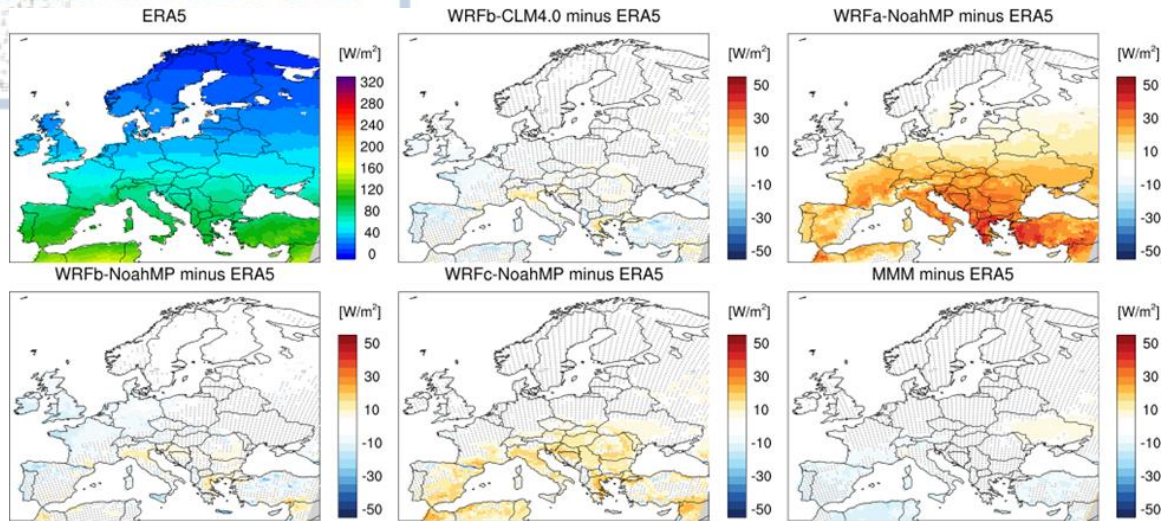


**Figure 2.16: Mean bias (models minus ERA5) for downwelling shortwave radiation at surface in winter (DJF) over 1986-2015 period. Stippling indicates areas where model bias is within the ERA5 uncertainty range. The  $\pm 1 \times SD$  is used as estimate of the uncertainty range of ERA5 dataset. MMM: multi-model-mean of LUCAS simulations excluding WRF configurations.**

The longwave component dominates over shortwave radiation in winter (**Figure 2.17**). The observed longwave amounts range from 250  $W/m^2$  to 290  $W/m^2$  across Europe (**Table 9**) and are minimized over regions of high altitude. All modelling systems generally perform suitably exhibiting minor errors which lie within the range of observational (CLARA-A2.1) uncertainty over the major part of Europe. The LSM choice does not affect the simulation of longwave radiation in winter, since both WRFb-CLM4.0 and WRFb-NoahMP exhibit similar features with slight overestimation across Europe which does not exceed the 5% of the absolute CLARA-A2.1 estimate. The changes in atmospheric set-up do not greatly affect the performance for WRFc-NoahMP compared to WRFb-NoahMP, although have impact on WRFa-NoahMP which yields a spatial dipole in the sign of bias between south-eastern (negative) and north-western (positive) part of the domain, consistent to its temperature bias regime. The results for the longwave component are robust, since the additional comparison to ERA5 produces the same results (Figure A1 in Appendix).

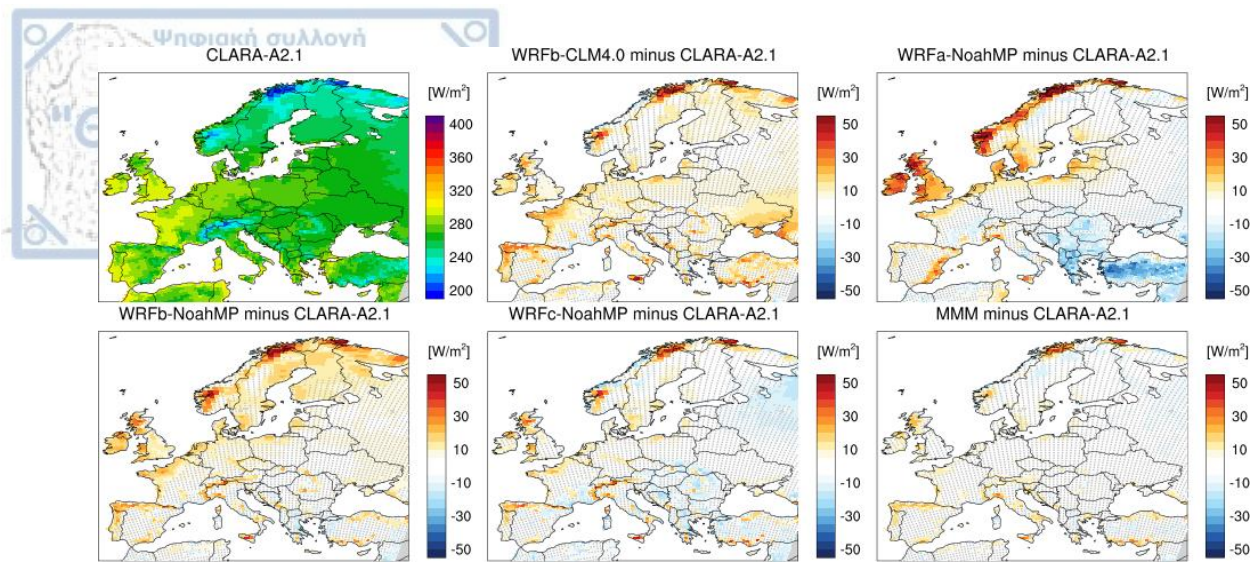


**Figure 2.17:** Mean bias (models minus CLARA-A2.1) for downwelling longwave radiation at surface in winter (DJF) over 1986-2015 period. Stippling indicates areas where model bias is within the CLARA-A2.1 uncertainty range. The  $\pm 1 \times SD$  is used as estimate of the uncertainty range of CLARA-A2.1 dataset. MMM: multi-model-mean of LUCAS simulations excluding WRF configurations.

**Table 9:** Mean model relative winter bias for downwelling longwave radiation at surface over 1986-2015 period compared to CLARA-A2.1, averaged over eight European subregions. AL (Alps), BI (British Isles), EA (Eastern Europe), FR (France), IP (Iberian Peninsula), MD (Mediterranean), ME (Mid-Europe), SC (Scandinavia). MMM: multi-model-mean of LUCAS simulations excluding WRF configurations.

	AL	BI	EA	FR	IP	MD	ME	SC
CLARA-A2.1 ( $W/m^2$ )	257	290	268	286	283	270	281	253
WRFb-CLM4.0 minus CLARA-A2.1	2%	4%	2%	3%	3%	2%	3%	2%
WRFa-NoahMP minus CLARA-A2.1	0%	9%	-1%	0%	1%	-4%	1%	3%
WRFb-NoahMP minus CLARA-A2.1	2%	5%	1%	2%	2%	0%	2%	5%
WRFc-NoahMP minus CLARA-A2.1	1%	3%	-1%	1%	0%	-1%	1%	0%
MMM minus CLARA-A2.1	2%	2%	0%	1%	1%	0%	0%	0%

As a result, the combination of downwelling shortwave and longwave radiation biases produces a radiative surplus at surface in winter for all WRF configurations over the major part of Europe (**Figure 2.18**). The most pronounced and widespread positive bias is noticed in WRFa-NoahMP due to its shortwave component. The rest modelling systems share a similar pattern with positive biases spreading over the southern and eastern regions and maximized over Alps. It's worth noting that the simulated radiative surplus is not in agreement with the winter cold biases. The results for Scandinavia are not considered reliable due to the low accuracy of CLARA-A2.1. The comparison with ERA5 is taken into account, where the models show quite good performance over the specified

areas. The fact that WRFc-NoahMP does not underestimate the incoming radiation at surface supports the view that its cold bias over the north-eastern part of domain has not radiative origins.

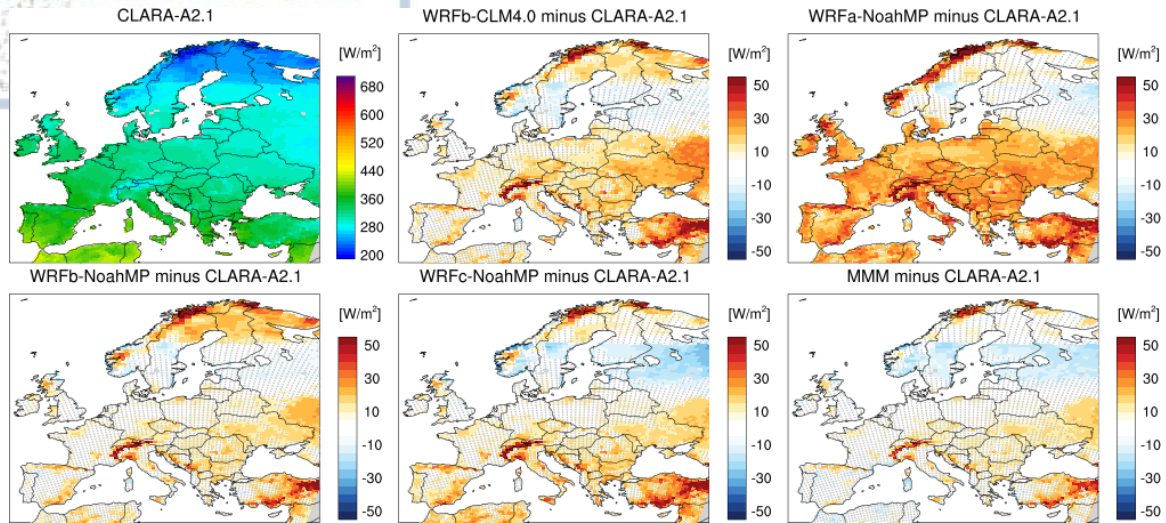


**Figure 2.18:** Mean bias (models minus CLARA-A2.1) for the sum of downwelling shortwave and longwave radiation at surface in winter (DJF) over 1986-2015 period. Stippling indicates areas where model bias is within the CLARA-A2.1 uncertainty range. The  $\pm 1 \times \text{SD}$  is used as estimate of the uncertainty range of CLARA-A2.1 dataset. MMM: multi-model-mean of LUCAS simulations excluding WRF configurations.

### 2.3.3.2 Summer radiation fluxes

In summer, the observed downwelling shortwave radiation is maximized in southern regions (**Figure 2.19**), 283  $\text{W/m}^2$  in Iberian Peninsula on average, and gradually decreases towards the north reaching up to 187  $\text{W/m}^2$  in Scandinavia (**Table 10**). The selection of atmospheric and land surface schemes strongly influences the WRF performance in simulating the summer shortwave radiation. WRFb-CLM4.0 exhibits a south-north dipole in the sign of bias, namely an overestimation close to 10% over Mediterranean, Alps and Eastern Europe and a slight underestimation over British Isles and Scandinavia which does not exceed the -7%. The south-north dipole is also reproduced in WRFb-NoahMP, but it's more extensive and stronger in terms of magnitude with respect to WRFb-CLM4.0. Almost two or three times larger biases are noticed for WRFb-NoahMP over the Alps (23%), France (21%) and Mid-Europe (17%). The change of PBL scheme for WRFc-NoahMP does not alleviate the overestimation of shortwave radiation seen in WRFb-NoahMP, but changes the sign of bias to positive over the northern regions. The atmospheric schemes selected for WRFa-NoahMP result in a bad performance with widespread and large positive biases across Europe reaching almost the 50% of the absolute CLARA-A2.1 estimate over Mid-Europe. ERA5 and CLARA-A2.1 agree well for downwelling shortwave radiation at surface (Figure A2 in Appendix), indicating the robustness of results.



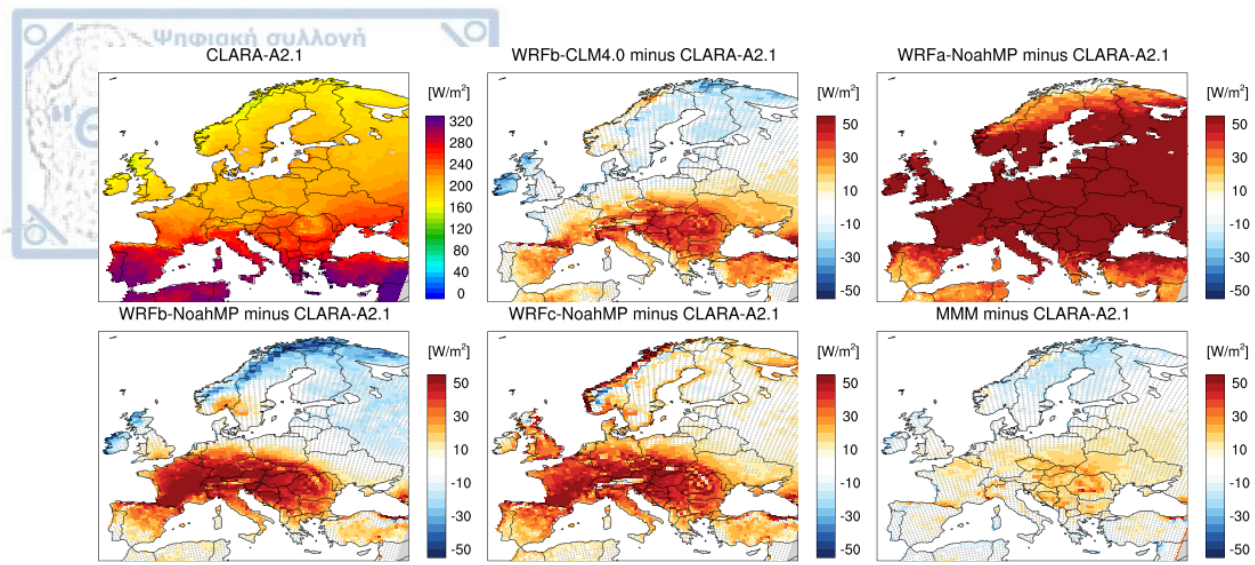


**Figure 2.19:** Mean bias (models minus CLARA-A2.1) for downwelling shortwave radiation at surface in summer (JJA) over 1986-2015 period. Stippling indicates areas where model bias is within the CLARA-A2.1 uncertainty range. The  $\pm 1 \times SD$  is used as estimate of the uncertainty range of CLARA-A2.1 dataset. MMM: multi-model-mean of LUCAS simulations excluding WRF configurations.

**Table 10:** Mean model relative summer bias for downwelling shortwave radiation at surface over 1986-2015 period compared to CLARA-A2.1, averaged over eight European subregions. AL (Alps), BI (British Isles), EA (Eastern Europe), FR (France), IP (Iberian Peninsula), MD (Mediterranean), ME (Mid-Europe), SC (Scandinavia). MMM: multi-model-mean of LUCAS simulations excluding WRF configurations.

	AL	BI	EA	FR	IP	MD	ME	SC
CLARA-A2.1 ( $W/m^2$ )	228	179	223	227	283	273	205	187
WRFb-CLM4.0 minus CLARA-A2.1	12%	-7%	12%	6%	6%	10%	5%	-4%
WRFa-NoahMP minus CLARA-A2.1	36%	46%	38%	40%	16%	19%	49%	27%
WRFb-NoahMP minus CLARA-A2.1	23%	0%	11%	21%	10%	10%	17%	-6%
WRFc-NoahMP minus CLARA-A2.1	19%	12%	13%	20%	11%	11%	18%	4%
MMM minus CLARA-A2.1	4%	0%	7%	4%	0%	3%	5%	-3%

According to CLARA-A2.1, the longwave amounts range from  $320 W/m^2$  to  $350 W/m^2$  (**Table 11**) across Europe in summer, showing minimum values over the high-altitude areas (**Figure 2.20**). All WRF configurations capture adequately the longwave component with biases lower than 3% of the absolute CLARA-A2.1 estimation. The various physics schemes do not cause large differences between the simulations. In short, WRFb-CLM4.0 shows a south-north dipole with underestimation in the southern regions and overestimation over British Isles and Scandinavia. This dipole is reproduced but it's somewhat weaker in the other WRF simulations, while slight positive biases occur over the south-western part of the domain for WRFb-NoahMP and WRFa-NoahMP.

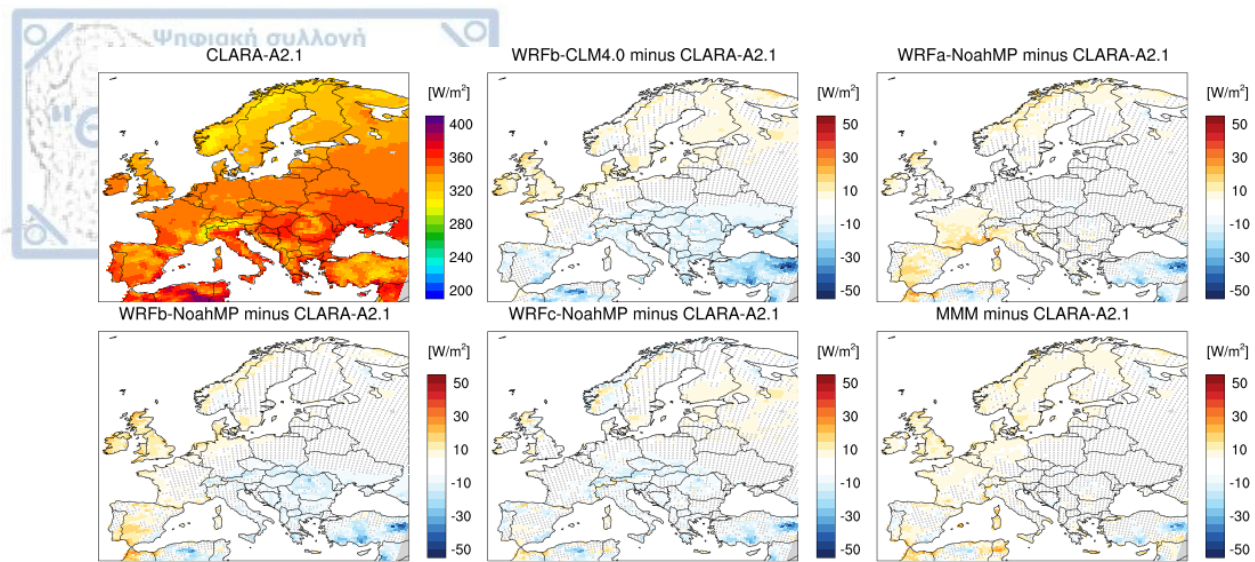
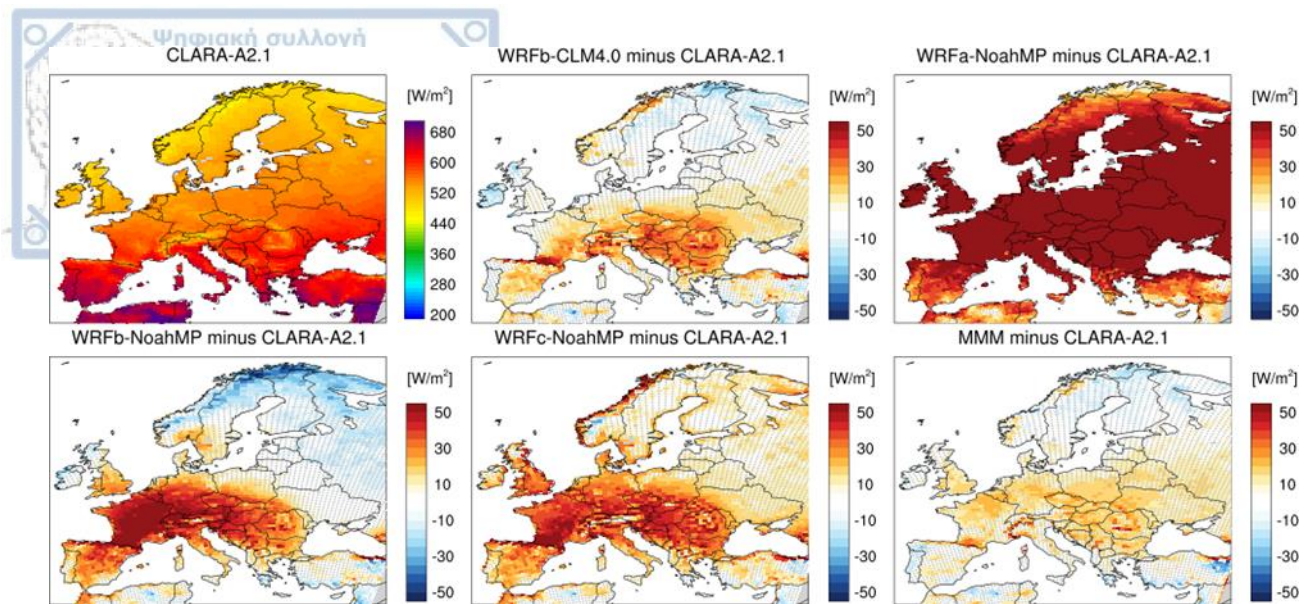


Figure 2.20: Mean bias (models minus CLARA-A2.1) for downwelling longwave radiation at surface in summer (JJA) over 1986-2015 period. Stippling indicates areas where model bias is within the CLARA-A2.1 uncertainty range. The  $\pm 1 \times SD$  is used as estimate of the uncertainty range of CLARA-A2.1 dataset. MMM: multi-model-mean of LUCAS simulations excluding WRF configurations.

Table 11: Mean model relative summer bias for downwelling longwave radiation at surface over 1986-2015 period compared to CLARA-A2.1, averaged over eight European subregions. AL (Alps), BI (British Isles), EA (Eastern Europe), FR (France), IP (Iberian Peninsula), MD (Mediterranean), ME (Mid-Europe), SC (Scandinavia). MMM: multi-model-mean of LUCAS simulations excluding WRF configurations.

	AL	BI	EA	FR	IP	MD	ME	SC
CLARA-A2.1 ( $W/m^2$ )	335	340	349	345	345	348	344	327
WRFb-CLM4.0 minus CLARA-A2.1	-1%	3%	-1%	1%	-1%	-2%	0%	1%
WRFa-NoahMP minus CLARA-A2.1	1%	1%	0%	2%	2%	0%	0%	1%
WRFb-NoahMP minus CLARA-A2.1	-1%	3%	-1%	1%	2%	-1%	0%	1%
WRFc-NoahMP minus CLARA-A2.1	-1%	1%	-1%	-1%	0%	-1%	-1%	0%
MMM minus CLARA-A2.1	1%	2%	0%	1%	1%	0%	1%	2%

Finally, the shortwave bias largely offsets the longwave and regulates the incoming radiation regime at surface in summer (Figure 2.21). That is, WRFb-NoahMP, WRFc-NoahMP and partly WRFb-CLM4.0 suffer from radiative surplus over a major part of Europe which extends from Eastern Europe to Iberian Peninsula. The radiative surplus regime is in agreement with the summer temperature biases in WRFb-NoahMP, which shows prominent overestimation of shortwave radiation over Alps, France and Mid-Europe in correlation with its high maximum temperatures in these regions. Strong radiation-temperature correlation is also noticed for WRFa-NoahMP which largely overestimates the shortwave and consequently the total incoming radiation at surface, in line with its widespread warm summer bias.



**Figure 3: Mean bias (models minus CLARA-A2.1) for the sum of downwelling shortwave and longwave radiation at surface in summer (JJA) over 1986-2015 period. Stippling indicates areas where model bias is within the CLARA-A2.1 uncertainty range. The  $\pm 1 \times SD$  is used as estimate of the uncertainty range of CLARA-A2.1 dataset. MMM: multi-model-mean of LUCAS simulations excluding WRF configurations.**

### 2.3.4 Cloud cover

The representation of cloud cover is a substantial factor for the accurate simulation of radiation fluxes. **Figure 2.22** illustrates the differences in total cloud cover between models and CLARA-A2.1 in winter.

The observed cloud fraction is minimized over the south-western part of the domain and it gradually increases towards the north-eastern regions. The simulation of winter cloudiness is not affected by the land surface processes, as expected. WRFb-CLM4.0 and WRFb-NoahMP show a similar behavior with a general overestimation of cloudiness across Europe, apart from Mediterranean region where they are in very good agreement with CLARA-A2.1. Neither the change of PBL scheme greatly modify the simulation of winter cloud cover in WRFc-NoahMP. Only the different atmospheric set-up of WRFa-NoahMP yields a different cloudiness regime, with strong underestimation over the southern Europe and slight overestimation over British Isles and Scandinavia. In addition, the magnitude of bias is substantially larger mostly over Scandinavia when comparing to CRU dataset (Figure A3 in Appendix), but the sign of bias remains consistent.

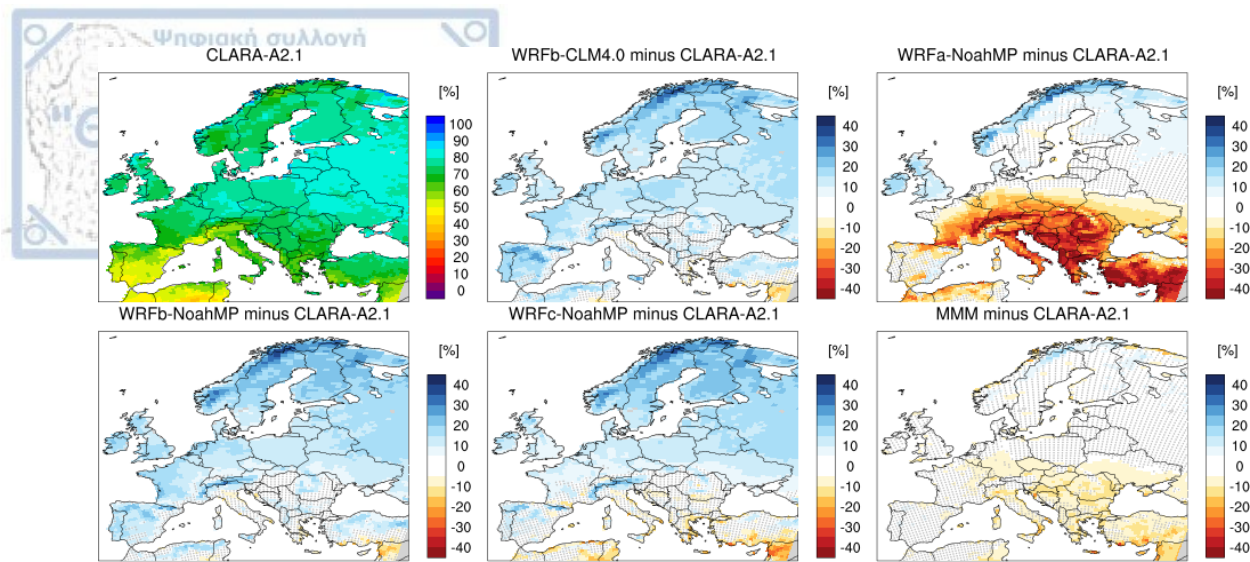


**Figure 4: Mean bias (models minus CLARA-A2.1) for total cloudiness (%) in winter (DJF) over 1986-2015 period. Stippling indicates areas where model bias is within the CLARA-A2.1 uncertainty range. The  $\pm 1 \times SD$  is used as estimate of the uncertainty range of CLARA-A2.1 dataset. MMM: multi-model-mean of LUCAS simulations excluding WRF configurations.**

The underestimation of cloud cover over the southern Europe in WRFa-NoahMP explains the overestimation of winter shortwave radiation over these regions for this model. Also, the excess cloudiness in the other three WRF configurations cause a general overestimation of winter longwave radiation, as discussed above. A corresponding link cloudiness-shortwave radiation is not clearly detected (except from WRFa-NoahMP), for example the overestimation of downwelling shortwave radiation over the south-eastern Europe in WRFb-CLM4.0, WRFb-NoahMP and WRFc-NoahMP is not associated with an underestimation of cloudiness. Such inconsistency can be related to the presence of different types of clouds in models and CLARA-A2.1 and their impact on shortwave radiation. For example, thin cirrus clouds are greatly transparent to shortwave radiation, whereas the low thick clouds largely reflect the incoming solar radiation back to space. Moreover, the consistent overestimation of cloudiness over Scandinavia is not in agreement with the mixed sign of bias for shortwave radiation (or with the almost zero bias when comparing with ERA5). Apart from the low accuracy of satellite data over the high-latitude areas, this discrepancy is probably related to small amounts of incoming solar energy over these regions in winter. Last, note that the current methodology does not differentiate between daytime and nighttime clouds which could has great impact on the link shortwave radiation-cloudiness.

In summer, the observed cloudiness is minimized over the southern Europe and gradually increases towards the north (**Figure 2.23**). Either the land or atmospheric component have an essential role in the simulation of summer cloudiness. WRFb-CLM4.0 exhibits a negative bias over Balkan Peninsula and around Black Sea which becomes positive towards the western coasts and northern part of Europe. The change of LSM in WRFb-NoahMP extends the negative bias from Balkan peninsula to Alps and expands the positive bias over the north-eastern regions, compared to WRFb-CLM4.0. With the change of PBL scheme in WRFc-NoahMP, this dipole remains but it is weakened. The change of atmospheric schemes in WRFa-NoahMP yield a dramatically different summer cloudiness regime with a general negative bias. The bias patterns for summer cloudiness are in good agreement with the results for the downwelling shortwave radiation. That is, regions which show low cloudiness tend to

show excess shortwave radiation. A corresponding link is also detected for summer cloudiness – longwave radiation (not in WRFa-NoahMP), but the representation of summer clouds has generally greater impact on shortwave than longwave radiation.

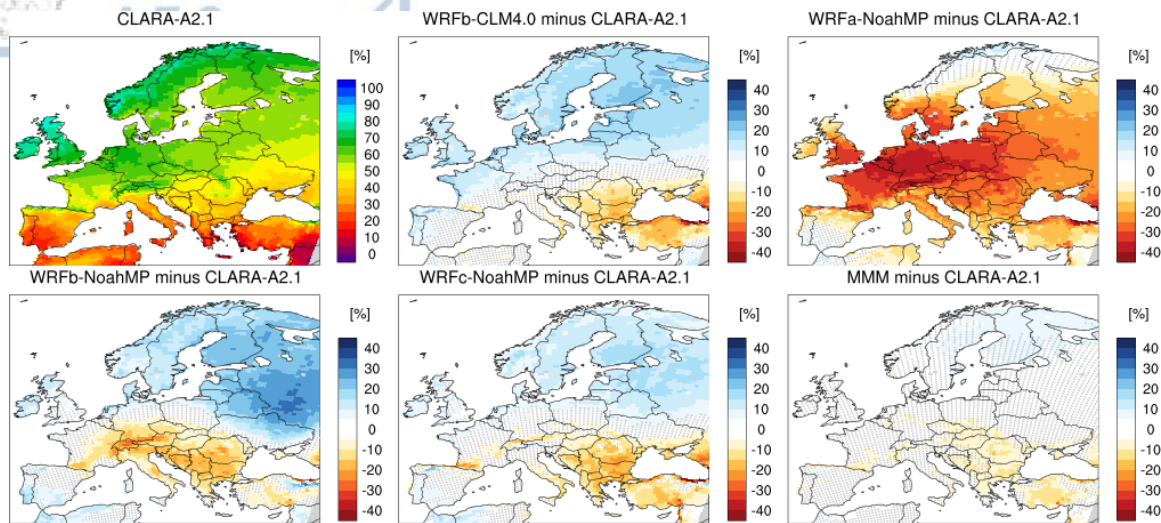


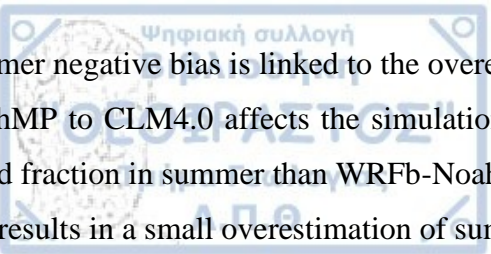
**Figure 5: Mean bias (models minus CLARA-A2.1) for total cloudiness (%) in summer (JJA) over 1986-2015 period. Stippling indicates areas where model bias is within the CLARA-A2.1 uncertainty range. The  $\pm 1 \times SD$  is used as estimate of the uncertainty range of CLARA-A2.1 dataset. MMM: multi-model-mean of LUCAS simulations excluding WRF configurations.**

### 2.3.5 Seasonal cycles

The observed and simulated seasonal cycles of downwelling shortwave (**Figure 2.24**) and longwave radiation (**Figure 2.25**) and total cloud fraction (**Figure 2.26**) are analyzed in order to obtain a comprehensive view on the relationship between radiation fluxes and cloudiness across seasons and regions in Europe.

WRFa-NoahMP shows a year-round overestimation of shortwave radiation which is maximized during the summer months. With the change of atmospheric set-up in WRFb-NoahMP, the shortwave radiation is in better agreement with CLARA-A2.1, although a prominent overestimation remains during the warm months apart from the regions of British Isles and Scandinavia. WRFb-NoahMP and WRFc-NoahMP exhibit a similar seasonal cycle, indicating the small impact of PBL change on the simulation of shortwave radiation. Only over British Isles and Scandinavia, WRFc-NoahMP produces greater radiation amounts than WRFb-NoahMP in summer. Moreover, the switch from NoahMP to CLM4.0 improve the WRF performance over Alps, France, Mid-Europe and Iberian Peninsula.

The various atmospheric and land surface schemes produce a range of behaviors for the seasonal cycle of cloudiness. WRFa-NoahMP shows unrealistically low cloud fraction in most regions across all months, which helps to explain the overestimated seasonal cycle of shortwave radiation. With the change of atmospheric set-up in WRFb-NoahMP, the WRF performance is clearly improved in simulating the cloud fraction. WRFb-NoahMP simulates greater cloud fraction than CLARA-A2.1 during the cold months in all regions, while underestimates the observed values in summer mostly over Alps and Mediterranean. Only over British Isles and Scandinavia it shows a year-round overestimation of cloudiness. The excess cloudiness during the cold months or the year-round overestimation over the northern regions do not correspond to smaller shortwave amounts at surface, whereas the



summer negative bias is linked to the overestimated shortwave radiation over the most regions. The switch from NoahMP to CLM4.0 affects the simulation of cloudiness in summer months. WRFb-CLM4.0 produces larger cloud fraction in summer than WRFb-NoahMP, mostly over Alps, France, Mid-Europe and Mediterranean. This fact results in a small overestimation of summer cloudiness in WRFb-CLM4.0 over France and Mid-Europe, but it's in better agreement with CLARA-A2.1 over Alps and Mediterranean. The LSM-induced differences in summer cloudiness are reflected to the results for shortwave radiation, where WRFb-CLM4.0 achieves higher performance than WRFb-NoahMP over Alps, France and Mid-Europe. The change of PBL scheme in WRFc-NoahMP leads to smaller cloud fraction in winter months in most regions compared to WRFb-NoahMP and consequently to better agreement with CLARA-A2.1. In summer, the selected atmospheric set-up for WRFc-NoahMP improves the WRF performance for cloudiness over Alps, France, Iberian Peninsula and Mediterranean, however without inducing differences in shortwave radiation with respect to WRFb-NoahMP.

The errors in the simulation of cloud fraction have not great impact on the seasonal cycle of longwave component. In all regions except the British Isles, the modelling systems tend to reproduce with high accuracy the observed seasonal variations of downwelling longwave radiation, showing small biases which lie within the CLARA-A2.1 uncertainty range in most cases.

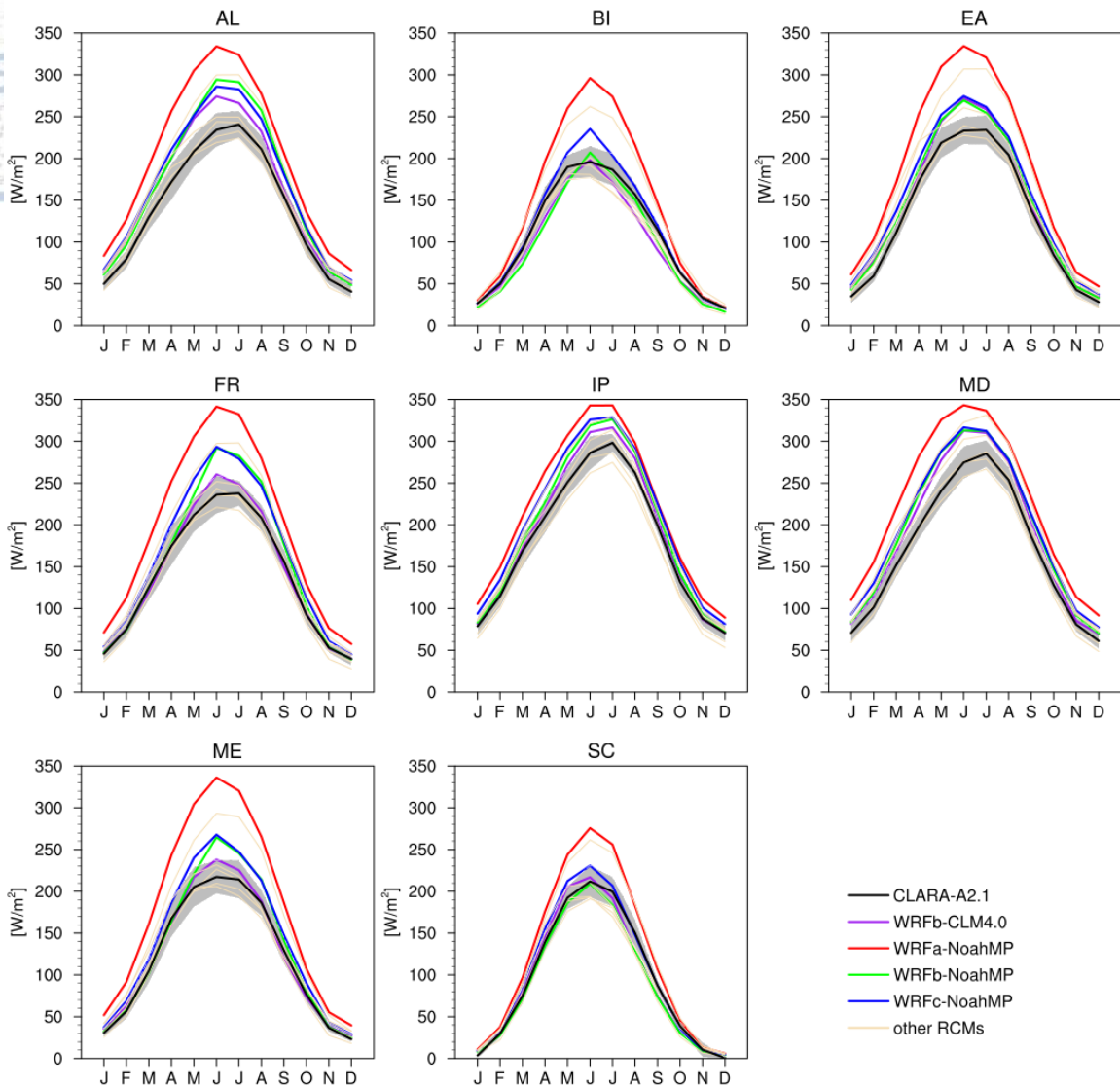


**Figure 6: Observed and simulated seasonal cycle of downwelling shortwave radiation at surface ( $W/m^2$ ) averaged over eight European regions for the period 1986-2015. AL (Alps), BI (British Isles), EA (Eastern Europe), FR (France), IP (Iberian Peninsula), MD (Mediterranean), ME (Mid-Europe), SC (Scandinavia). The grey area represents the range of CLARA-A2.1 uncertainty ( $\pm 1 \times SD$ ).**

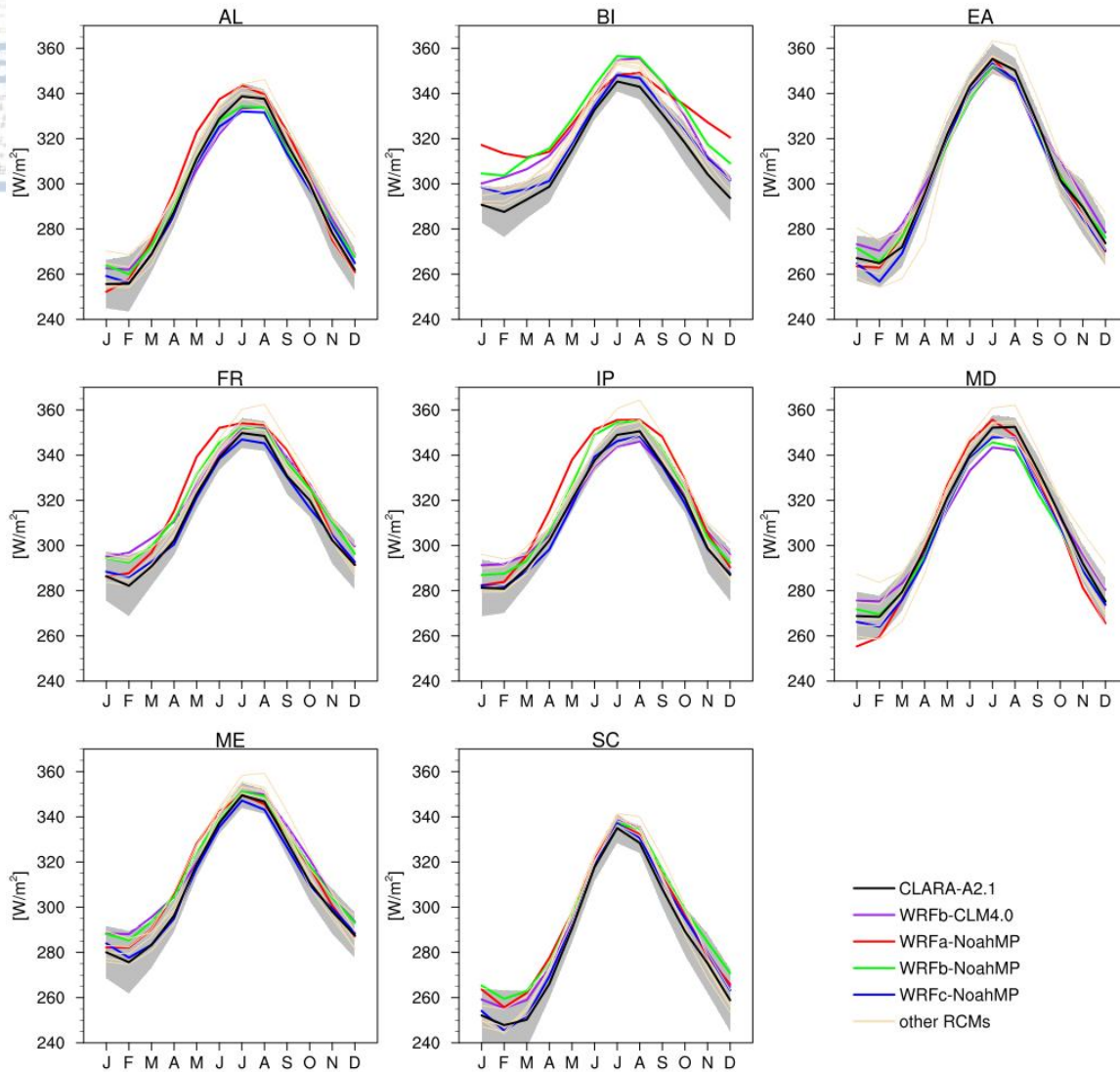
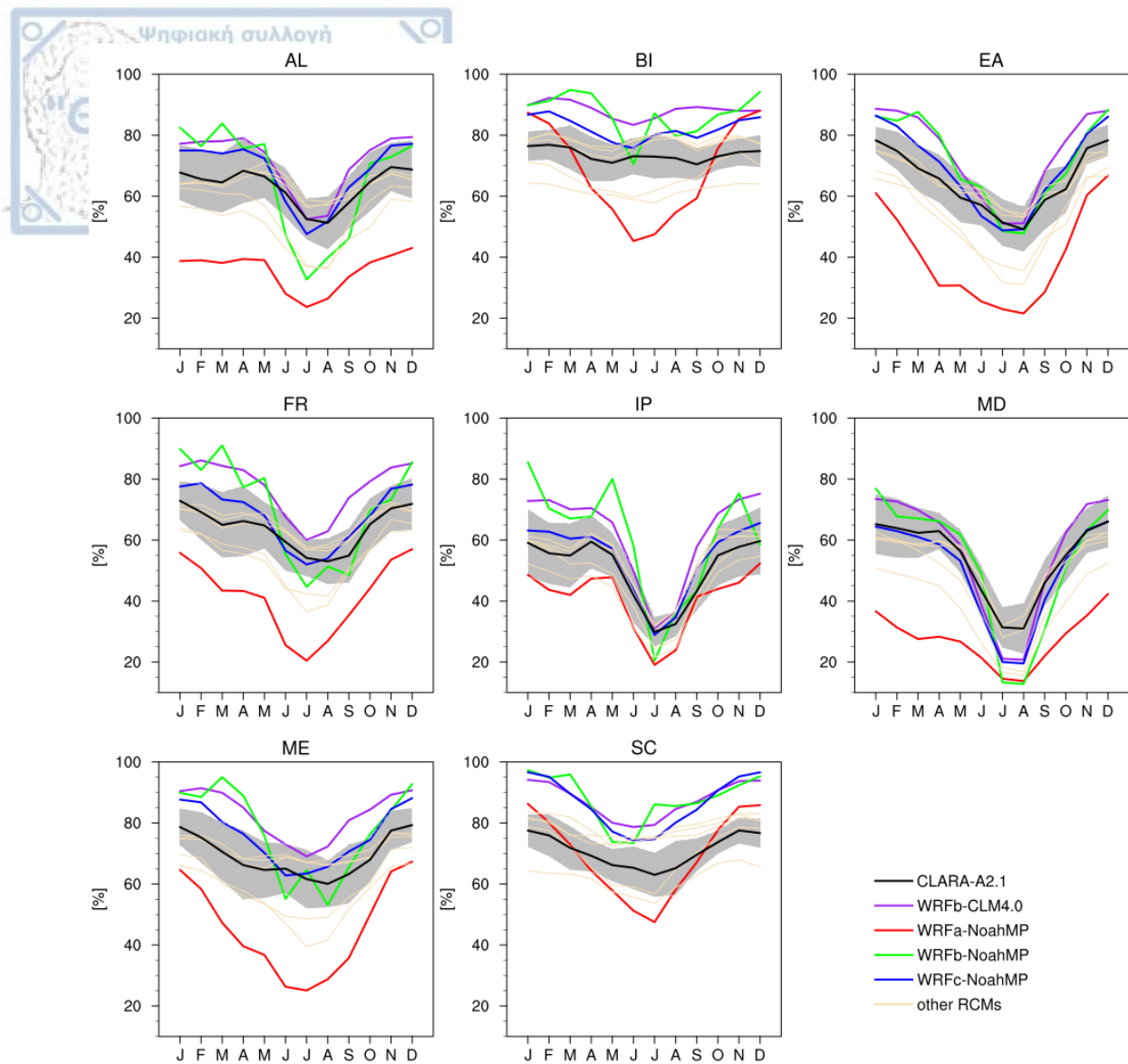


Figure 2.25: Observed and simulated seasonal cycle of downwelling longwave radiation at surface ( $W/m^2$ ) averaged over eight European regions for the period 1986-2015. AL (Alps), BI (British Isles), EA (Eastern Europe), FR (France), IP (Iberian Peninsula), MD (Mediterranean), ME (Mid-Europe), SC (Scandinavia). The grey area represents the range of CLARA-A2.1 uncertainty ( $\pm 1 \times SD$ ).





**Figure 2.26: Observed and simulated seasonal cycle of total cloud fraction (%) averaged over eight European regions for the period 1986-2015. AL (Alps), BI (British Isles), EA (Eastern Europe), FR (France), IP (Iberian Peninsula), MD (Mediterranean), ME (Mid-Europe), SC (Scandinavia). The grey area represents the range of CLARA-A2.1 uncertainty ( $\pm 1 \times SD$ ).**

### 2.3.6 Surface heat fluxes

A large part of radiative energy absorbed by the surface is released to the atmosphere in the form of latent and sensible heat fluxes. These fluxes have an essential role in summer when the solar energy reaching the ground is maximized. This section is focused on the evaluation of summer heat fluxes, comparing models to ERA5 reanalysis data, in order to better interpret the model behaviors with respect to surface climate.

**Figure 2.27** illustrates the mean summer bias for latent heat over the 1986-2015 time period in Europe. ERA5 latent heat amounts range from  $63 \text{ W/m}^2$  in Iberian Peninsula to almost  $90 \text{ W/m}^2$  in Alps and Eastern Europe on average (**Table 12**). All WRF configurations systematically show a negative bias for latent heat in various magnitudes. Between WRFb-CLM4.0 and WRFb-NoahMP are noticed small differences, implying the small impact of LSM change on latent heat simulation. More specifically, the two configurations share a similar and widespread negative bias which is maximized over Mediterranean (greater than  $-30\%$ ). The changes in

atmospheric schemes have greater impact on latent heat. WRFa-NoahMP shows the strongest underestimation with errors exceeding the 50% of the absolute ERA5 estimation over many regions. The change of PBL scheme in WRFc-NoahMP dramatically reduces the negative bias seen in WRFb-NoahMP over the whole Europe. Biases in WRFc-NoahMP lie within the ERA5 uncertainty range over a large part of the domain.

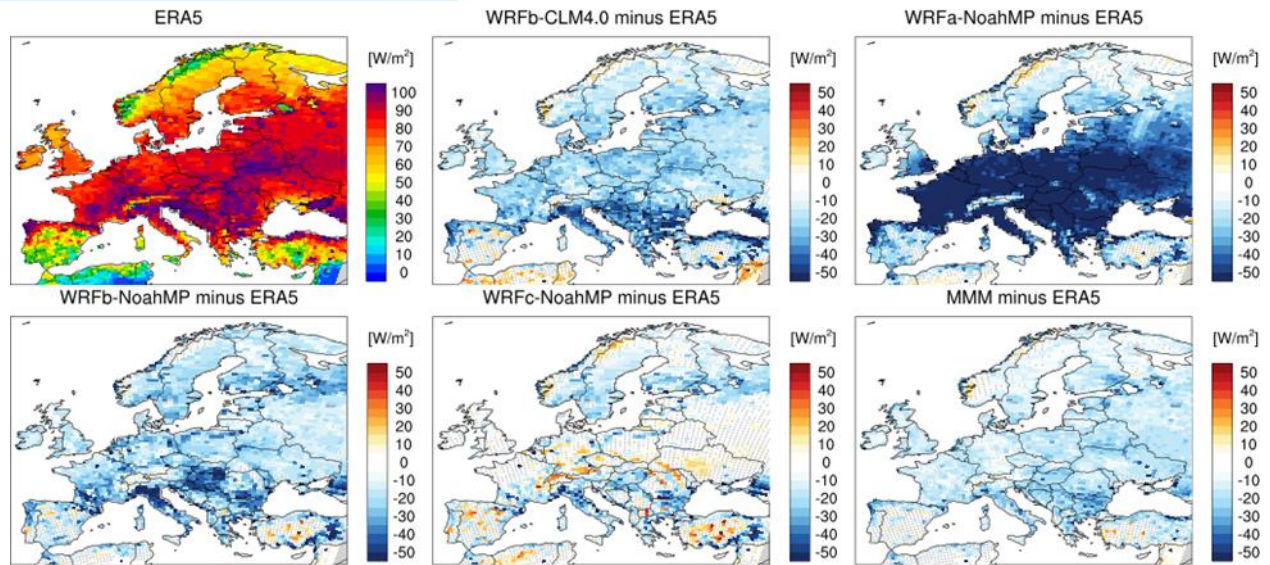
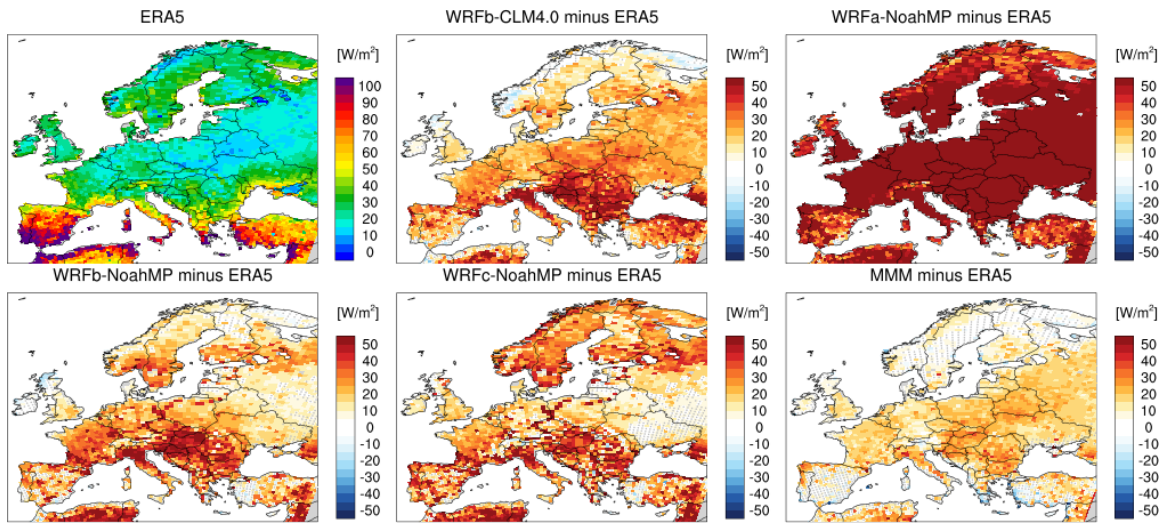


Figure 7: Mean bias (models minus ERA5) for latent heat flux in summer (JJA) over 1986-2015 period. Stippling indicates areas where model bias is within the ERA5 uncertainty range. The  $\pm 1 \times SD$  is used as estimate of the uncertainty range of ERA5 dataset. MMM: multi-model-mean of LUCAS simulations excluding WRF configurations.

Table 12: Mean summer bias for latent heat flux ( $W/m^2$ ) over 1986-2015 period with respect to ERA5, averaged over eight European subregions. AL (Alps), BI (British Isles), EA (Eastern Europe), FR (France), IP (Iberian Peninsula), MD (Mediterranean), ME (Mid-Europe), SC (Scandinavia). MMM: multi-model-mean of LUCAS simulations excluding WRF configurations.

	AL	BI	EA	FR	IP	MD	ME	SC
ERA5 ( $W/m^2$ )	92	75	93	88	63	80	88	70
WRFb-CLM4.0 minus ERA5	-25%	-23%	-27%	-27%	-22%	-35%	-25%	-22%
WRFa-NoahMP minus ERA5	-56%	-38%	-62%	-69%	-57%	-60%	-65%	-27%
WRFb-NoahMP minus ERA5	-22%	-20%	-25%	-27%	-27%	-31%	-24%	-25%
WRFc-NoahMP minus ERA5	-7%	-2%	-5%	-7%	-10%	-15%	-4%	-14%
MMM minus ERA5	-14%	-21%	-20%	-16%	-14%	-25%	-16%	-16%

**Figure 2.28** depicts the mean summer bias for sensible heat over the 1986-2015 time period in Europe. In contrast to latent heat, ERA5 sensible heat is maximized over Iberian Peninsula,  $72 \text{ W/m}^2$  on average (**Table 13**) and reduces towards the north-eastern part of Europe. Widespread positive biases are noticed for all WRF configurations. The different set-ups influence only the magnitude of biases. WRFa-NoahMP shows unrealistically high sensible heat amounts with relative bias reaching the order of 400% of the absolute ERA5 estimation over Mid and Eastern Europe. Note, however, that ERA5 sensible heat amounts are somewhat small mostly over the central and northern regions, so that large relative biases do not necessarily correspond to extremely large absolute errors. Between WRFb-NoahMP and WRFb-CLM4.0 are noticed differences in terms of magnitude of bias over Eastern Europe, where WRFb-CLM4.0 shows a greater overestimation, and over Alps, Mid-Europe and France where WRFb-NoahMP shows larger errors. The PBL change in WRFc-NoahMP yields smaller biases in central and eastern regions of Europe but not in Scandinavia, where the overestimation almost doubles with respect to WRFb-NoahMP.



**Figure 2.28:** Mean bias (models minus ERA5) for sensible heat flux in summer (JJA) over 1986-2015 period. Stippling indicates areas where model bias is within the ERA5 uncertainty range. The  $\pm 1 \times \text{SD}$  is used as estimate of the uncertainty range of ERA5 dataset. MMM: multi-model-mean of LUCAS simulations excluding WRF configurations.

**Table 13:** Mean summer bias for sensible heat flux ( $\text{W/m}^2$ ) over 1986-2015 period with respect to ERA5, averaged over eight European subregions. AL (Alps), BI (British Isles), EA (Eastern Europe), FR (France), IP (Iberian Peninsula), MD (Mediterranean), ME (Mid-Europe), SC (Scandinavia). MMM: multi-model-mean of LUCAS simulations excluding WRF configurations.

	AL	BI	EA	FR	IP	MD	ME	SC
ERA5 ( $\text{W/m}^2$ )	30	23	21	31	72	51	21	24
WRFb-CLM4.0 minus ERA5	94%	53%	164%	90%	33%	74%	117%	57%
WRFa-NoahMP minus ERA5	255%	271%	400%	280%	76%	137%	421%	231%
WRFb-NoahMP minus ERA5	108%	41%	137%	107%	34%	67%	132%	62%
WRFc-NoahMP minus ERA5	91%	66%	107%	96%	42%	62%	107%	99%

The absolute magnitude of the turbulent fluxes is directly affected by radiation biases and thus does not reflect the inherent model skills in simulating these fluxes. It's more informative to analyze turbulent fluxes in terms of their partitioning by examining the evaporation fraction, calculated as the ratio between latent heat and the sum of latent and sensible heat. This metric is relatively independent of radiation biases.

According to ERA5, the evaporation fraction is too weak over the southern Europe in summer and increases towards the north (**Figure 2.29**). All model configurations tend to underestimate the evaporation fraction across Europe. This was expected, since the models underestimate the latent heat and overestimate the sensible heat. In other words, models simulate weaker evapotranspiration and stronger sensible heating than ERA5 in summer. This fact could potentially trigger a physical mechanism which explains the different climate states between the models. For example, less evaporation theoretically implies a decrease of the atmospheric moisture content and subsequently a decrease of cloudiness and precipitation. The reduction of atmospheric humidity and therefore the decrease of cloudiness and precipitation, would lead to an increase of the incoming shortwave radiation and finally to a warming effect on surface temperature. This idealized mechanism of positive feedbacks could explain the climate state as simulated by WRFa-NoahMP, that is, the extremely low evaporation fraction in summer results in dry atmospheric conditions and thus low rainfall rates and cloudiness, in line with unrealistically high shortwave amounts at surface and finally a large warm summer bias. The same idealized mechanism could also explain the warm and dry conditions over the southern regions in summer in the other three WRF simulations, and mostly the high maximum temperatures in late summer over Alps, France and Mid-Europe in WRFb-NoahMP. The summer climate over the northern Europe is not regulated by the partitioning of surface heat fluxes, since the underestimated evaporation fraction is not consistent to the increased cloud fraction and the subsequent decrease of shortwave radiation.

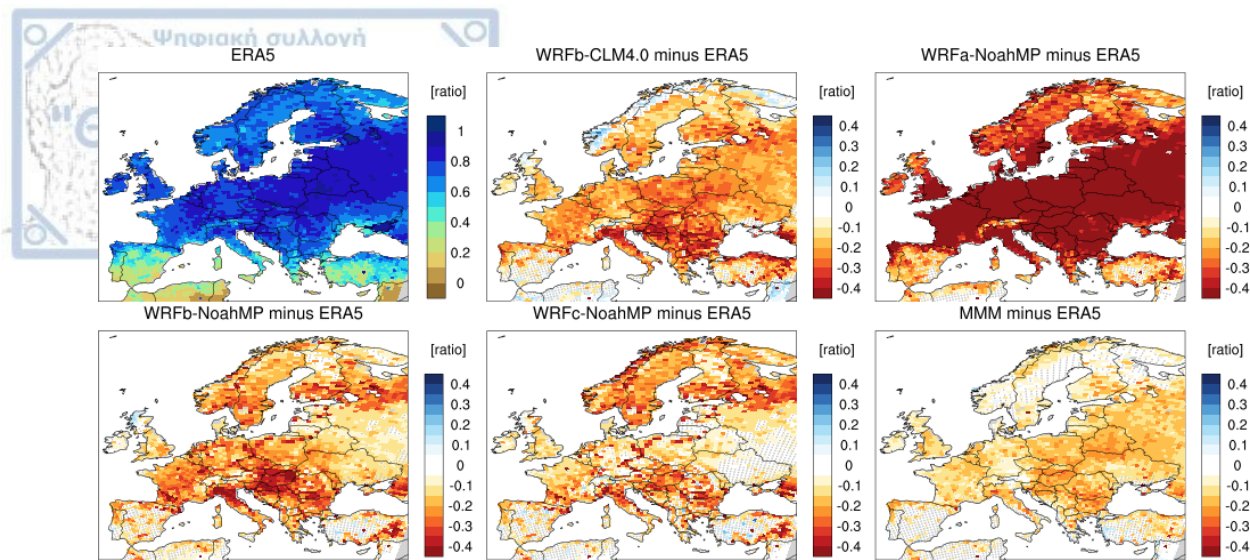


**Figure 2.29:** Mean summer bias (models minus ERA5) for evaporation fraction over 1986-2015 period. Stippling indicates areas where model bias is within the ERA5 uncertainty range. The  $\pm 1 \times SD$  is used as estimate of the uncertainty range of ERA5 dataset. MMM: multi-model-mean of LUCAS simulations excluding WRF configurations.

To complement the results for evaporation fraction, the simulations are also compared to flux measurements at 8 different sites over Europe (**Table 14**). Indeed, the models generally underestimate the evaporation fraction in all selected flux sites (except BE-Vie), confirming the results from the previous comparison to reanalysis data. WRFa-NoahMP again shows the worst performance among the WRF configurations with large negative deviations from measurements. In addition, WRFc-NoahMP does not clearly improve the results with respect to WRFb-NoahMP, as seen in comparison to ERA5.

**Table 14:** Comparison between simulated and measured evaporation fraction at 8 different FLUXNET sites. MMM: multi-model-mean of LUCAS simulations excluding WRF configurations. Evaporation fraction is calculated as the ratio between latent heat and the sum of latent and sensible heat.

	BE-Vie	CH-Fru	DE-Geb	ES-LJu	FI-Hyy	FR-Gri	FR-LBr	IT-Col
FLUXNET (ratio)	0.58	0.8	0.65	0.21	0.6	0.63	0.55	0.56
WRFb-CLM4.0 minus FLUXNET	0.05	-0.19	-0.02	-0.08	-0.07	-0.08	-0.19	-0.14
WRFa-NoahMP minus FLUXNET	-0.26	-0.35	-0.43	-0.15	-0.23	-0.46	-0.46	-0.27
WRFb-NoahMP minus FLUXNET	0.03	-0.21	-0.02	-0.15	-0.13	-0.09	-0.2	-0.02
WRFc-NoahMP minus FLUXNET	0.14	-0.18	-0.07	-0.12	-0.12	-0.02	-0.19	-0.06
MMM minus FLUXNET	-0.14	-0.36	-0.21	-0.22	-0.16	-0.19	-0.11	-0.12

### 2.3.6.1 Seasonal cycles

**Figure 2.30** and **Figure 2.31** show the mean seasonal cycle of latent and sensible heat as represented by models and ERA5, averaged over the eight subregions of analysis.

The ERA5 seasonal cycle of latent heat is a normal distribution with minimum values in the cold months and peak in the summer. The modelled seasonal cycles have smaller amplitude, as they show lower maximum values

than ERA5 in summer, while the winter amounts are equally small. In Scandinavia, it is noticed a great consistency between ERA5 and models which show a small underestimation during the summer. In the other regions, WRFa-NoahMP performs poorly with quite large negative biases. WRFc-NoahMP fits quite well with ERA5 in British Isles, while it shows negative deviations from ERA5 in late summer and autumn mostly over France, Mediterranean and Iberian Peninsula (here also in spring). Even though they share a similar pattern of seasonal cycle, the change of PBL scheme in WRFb-NoahMP degrades the quality of simulation in most regions compared to WRFc-NoahMP. Last, the switch from NoahMP to CLM4.0 results in smaller seasonal variations in latent heat. WRFb-CLM4.0 shows greater underestimation until the mid-summer and better agreement with ERA5 in late summer and autumn compared to WRFb-NoahMP.

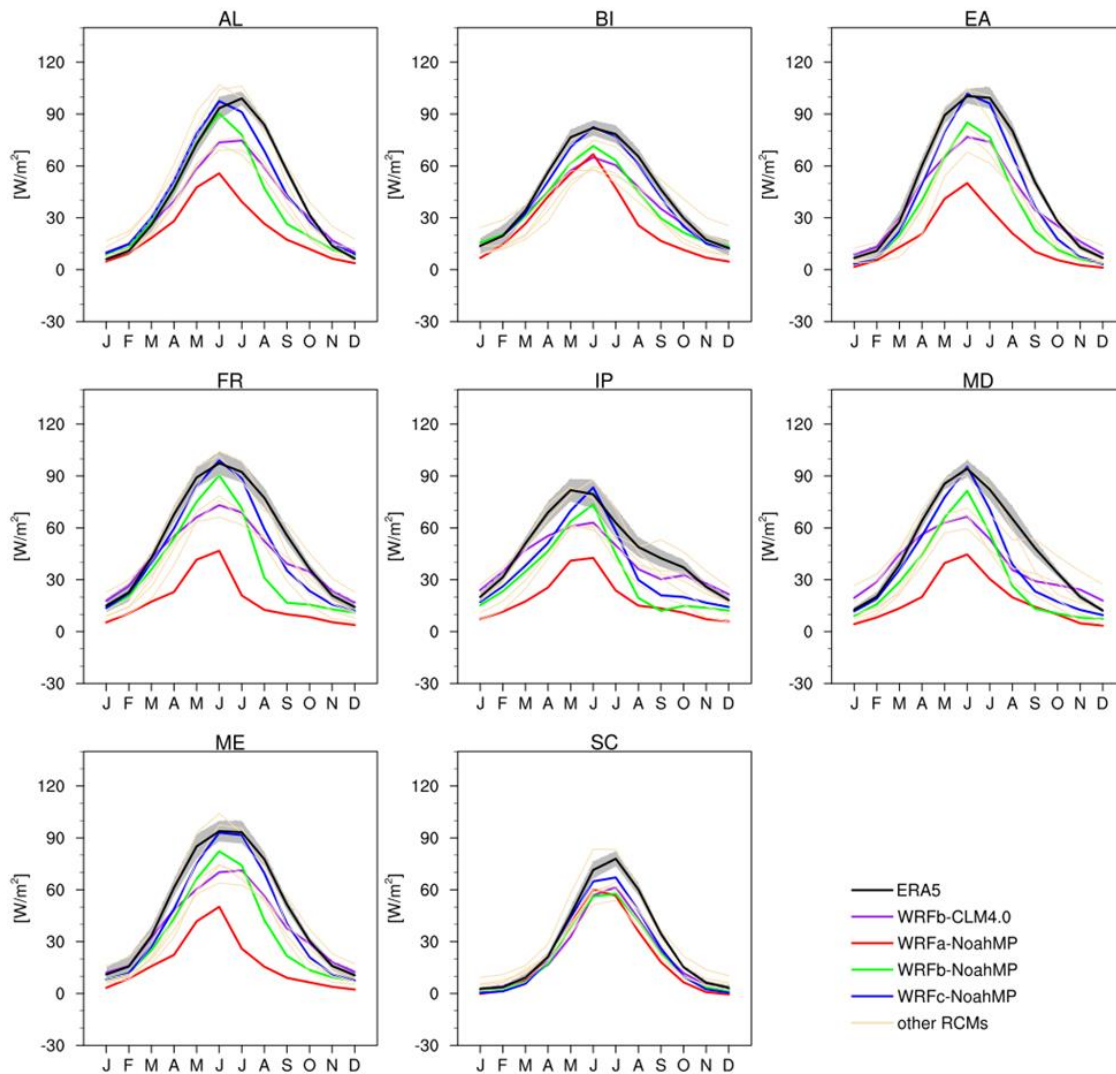


**Figure 2.30: ERA5 and simulated seasonal cycle of latent heat ( $\text{W/m}^2$ ) averaged over eight European regions for the period 1986-2015. AL (Alps), BI (British Isles), EA (Eastern Europe), FR (France), IP (Iberian Peninsula), MD (Mediterranean), ME (Mid-Europe), SC (Scandinavia). The grey area represents the range of ERA5 uncertainty ( $\pm 1 \times \text{SD}$ ).**

The seasonal variation of sensible heat is smaller than that of latent heat in ERA5 over all regions apart from Iberian Peninsula. WRFa-NoahMP stands out again for its poor performance showing a largely overestimated seasonal cycle, which is associated with its poor representation of latent heat. The other WRF configurations also

overestimate sensible heat amounts in summer months showing deviations outside the range of ERA uncertainty in all regions. Despite their different set-ups, they show quite similar behavior over the most regions. The most prominent differences are noticed over Alps, France and Mid-Europe where WRFb-NoahMP shows a pronounced overestimation in the late summer, which is not visible when the LSM (WRFb-CLM4.0) or PBL (WRFc-NoahMP) changes, and is probably the main reason for its high maximum temperature over these regions. The LSM change improved the WRF performance over Iberian Peninsula and Scandinavia in summer, while the different PBL scheme in WRFc-NoahMP yields better agreement with ERA5 over Eastern Europe.

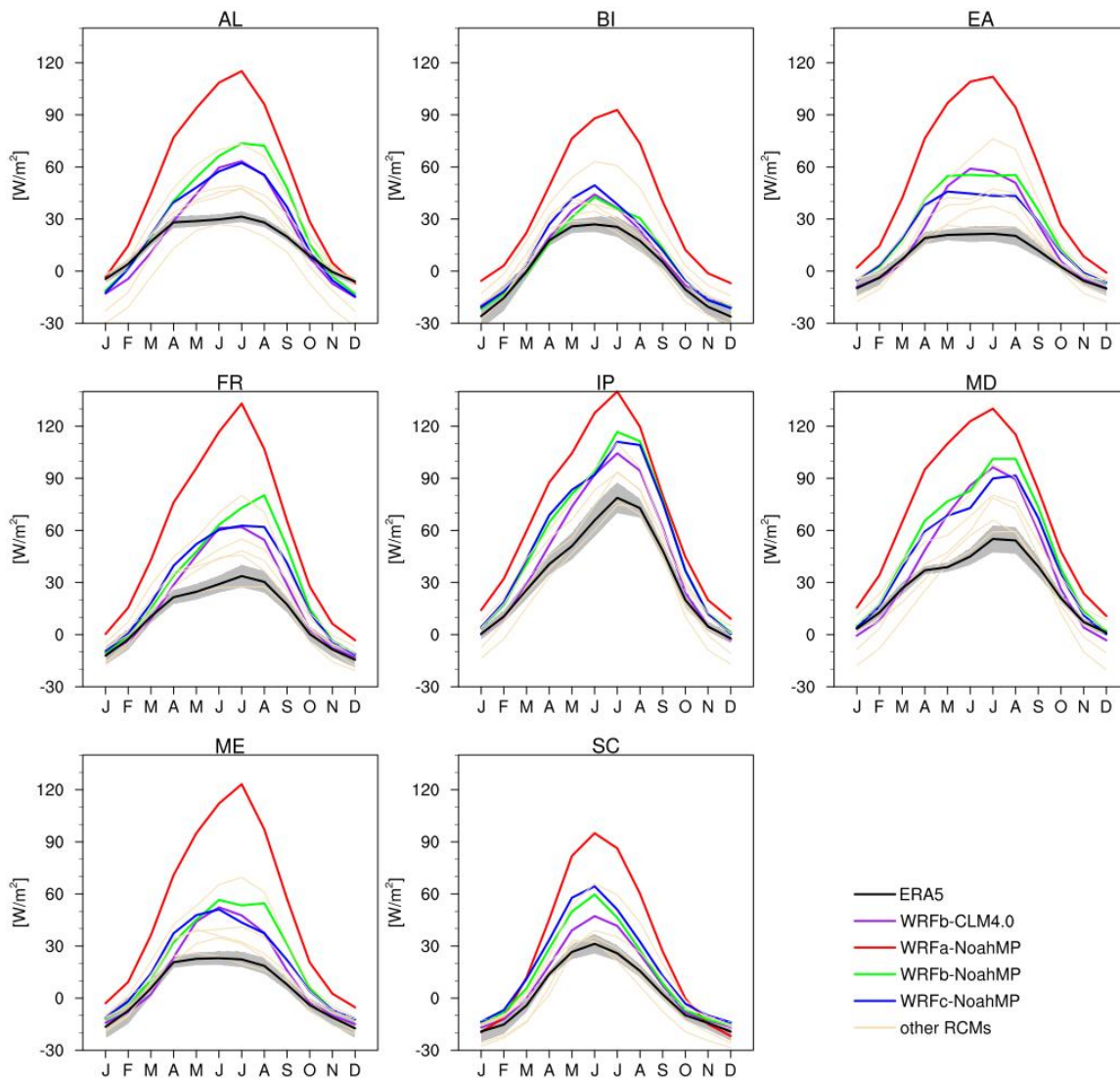


**Figure 2.31:** ERA5 and simulated seasonal cycle of sensible heat ( $\text{W/m}^2$ ) averaged over eight European regions for the period 1986-2015. AL (Alps), BI (British Isles), EA (Eastern Europe), FR (France), IP (Iberian Peninsula), MD (Mediterranean), ME (Mid-Europe), SC (Scandinavia). The grey area represents the range of ERA5 uncertainty ( $\pm 1 \times \text{SD}$ ).

### 2.3.7 Soil moisture

Land hydrology could help to interpret the results for the partitioning of surface heat fluxes. **Figure 2.32** depicts the mean seasonal cycle of soil moisture content of the top 1 m of soil, averaged over eight European regions as

represented by ERA5 and WRF configurations. The results are discussed mainly for summer, as in winter the land-atmosphere interaction is not essential.

The seasonal cycle of ERA5 receives maximum values in the cold months and minimum in the late summer. In Scandinavia, the seasonal variation of soil wetness is small with a secondary maximum in late spring due to snowmelt. WRF configurations follow the pattern of ERA5 seasonal variations although they systematically show drier soils across all seasons and regions, which is consistent with the simulation of less evaporation amounts. A corresponding link between soil dryness and precipitation forcing is also valid mostly in summer, when models tend to underestimate precipitation in most regions. In winter, the higher simulated precipitation amounts do not explain the low soil moisture contents. Also, in Scandinavia the almost year-round overestimation of precipitation (not in WRFa-NoahMP) is not in agreement with the simulated soil dryness. After all, it is not always easy to relate the differences in soil water content to the simulation of surface heat fluxes and precipitation forcing. Such an approach requires a detailed analysis of the hydrological cycle and the examination of all the participating components, such as the leaf area index, surface and subsurface runoff, the recharge of soil column from the underlying aquifer, etc.

The changes of atmospheric and land surface schemes have impact on the simulation of soil water content. WRFb-NoahMP shows quite dry soils in late summer and autumn in almost all regions but mostly over Alps, Mid-Europe and France. The dry soils over these regions are associated with strong sensible heating, less rainfall amounts and finally higher maximum temperatures in WRFb-NoahMP. The results for the soil moisture in the late summer are improved either with the change of LSM in WRFb-CLM4.0 or the change of PBL scheme in WRFc-NoahMP, indicating that both the land and atmospheric processes contribute to soil dryness. Actually, the dry soils remain in WRFb-CLM4.0 and WRFb-NoahMP, but they are closer to ERA5. The better representation of soil moisture by WRFb-CLM4.0 and WRFc-NoahMP compared to WRFb-NoahMP, is consistent to the more accurate results for sensible heating, precipitation and finally for maximum summer temperature in Alps, France and Mid-Europe. The coupling of WRF to CLM4.0 results in a better representation of soil moisture in late summer and autumn over the southern regions (Mediterranean, Iberian Peninsula) and France with respect to NoahMP configurations, which is also reflected to the better partitioning of heat fluxes. This is likely due to a better groundwater management in CLM4.0, which has a larger soil volume discretized in ten layers and generally is more sophisticated than NoahMP. Last, WRFa-NoahMP shows a poor performance by simulating too dry soils across all seasons and regions. Since WRFa-NoahMP differs only in microphysics and convection schemes with WRFb-NoahMP, it could be suggested that the bias in soil wetness has its origins in the representation of atmospheric processes and specifically is caused by the low rainfall amounts, resulting in high sensible heating (or less evaporation) and finally warmer than observed surface climate.



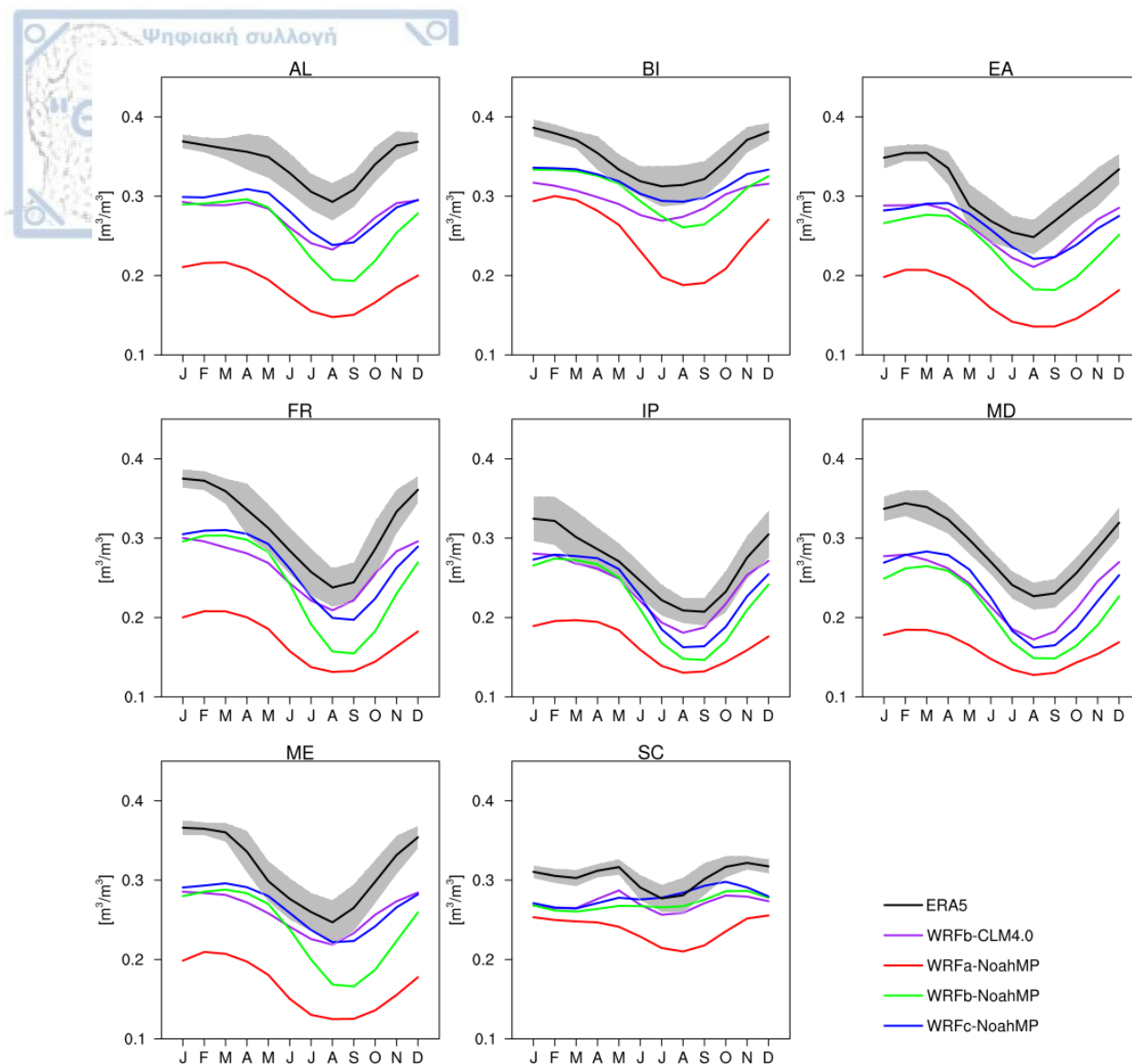
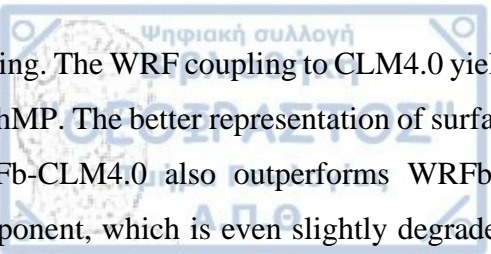


**Figure 2.32: Mean seasonal cycle of integrated soil water content of the top 1 m of the soil for ERA5 and WRF configurations, averaged over eight European subregions for the time period 1986-2015.**

### 2.3.8 Model performances

To obtain a quantitative estimate of the overall RCM performances in simulating the surface climate state, RMSE (root mean squared error) scores are calculated for each modelling system over the 1986-2015 time period in the whole Europe (**Figure 2.33**). As in Davin et al., 2016, RMSE is calculated from the difference between simulated and observed values taken at each land grid cell of the domain and based on monthly means over the entire simulation time period, thus accounting for both spatial and temporal model performance. When possible, two different reference products are employed in order to consider the uncertainty in observational data.

The use of Grell-Freitas (Grell and Freitas, 2014) as convection scheme and WDM6 (Lim and Hong, 2010) as microphysics scheme lead WRFa-NoahMP to the worst performance not only among the WRF configurations but also among the LUCAS simulations. Its bad scores have their origins in the simulation of atmospheric processes, as the atmospheric schemes are those that differ in relation to the simulation from WRFb-NoahMP. In view of the multi-model spread, the other three WRF configurations somewhat cluster together in terms of



ranking. The WRF coupling to CLM4.0 yields better scores for latent and sensible heat fluxes compared to WRFb-NoahMP. The better representation of surface heat fluxes is reflected to the results for shortwave radiation, where WRFb-CLM4.0 also outperforms WRFb-NoahMP. No improvement, however, is seen for the longwave component, which is even slightly degraded. The change of PBL and skin surface schemes in WRFc-NoahMP improve the representation of latent heat and slightly the simulation of sensible heat flux compared to WRFb-NoahMP. Better scores are also noted for longwave radiation in WRFc-NoahMP, but not for the shortwave component. It's worth noting that the models generally reproduce the downwelling longwave radiation more accurately than the downward shortwave radiation at surface, while WRF configurations achieve higher performances for latent than sensible heat. With respect to temperature, WRFb-CLM4.0 again shows better performance than WRFb-NoahMP both in daytime (maximum) and nighttime (minimum) temperatures, outperforming most other LUCAS simulations. Moreover, WRFb-NoahMP and WRFc-NoahMP almost cluster together for temperature in terms of ranking. However, the change of atmospheric set-up in WRFc-NoahMP somewhat degrades the quality of simulation compared to WRFb-NoahMP, not only for temperature but also for precipitation. Last but not least, the poorer performance of WRFb-CLM4.0 for precipitation in comparison to WRFb-NoahMP is in contrast to the better scores for turbulent fluxes. This discrepancy could be associated with the different timestep for model integration between WRFb-CLM4.0 and WRFc-NoahMP.

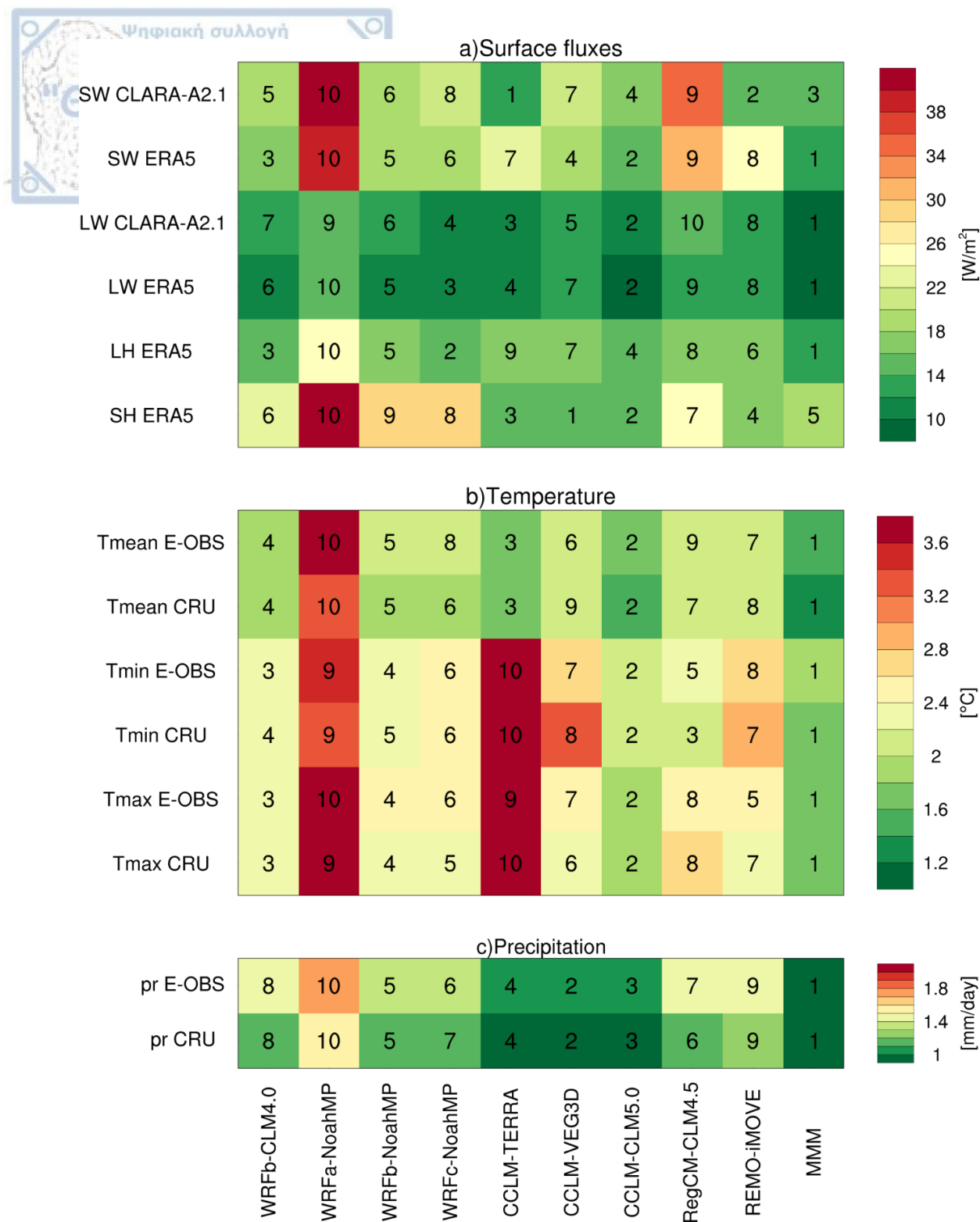
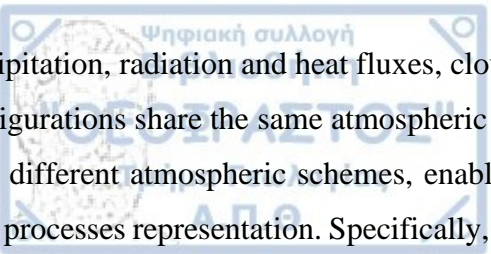


**Figure 2.33: Model performances in simulating a) surface heat fluxes, b) temperature and c) precipitation over the 1986-2015 time period in Europe, described with RMSE scores (colors). As in Davin et al., 2016, RMSE is calculated across all land grid points of the domain based on monthly values over multiple years. Numbers denote model ranking. MMM: multi-model-mean of LUCAS simulations.**

## 2.4 Summary

In chapter 1, the ability of a WRF multi-physics ensemble in simulating surface climate of a 30-year period at 0.44° spatial resolution over Europe is evaluated, in the context of LUCAS FPS. The simulated fields are compared to reference products, either satellite or terrestrial and reanalysis data, for 2-meter temperature,

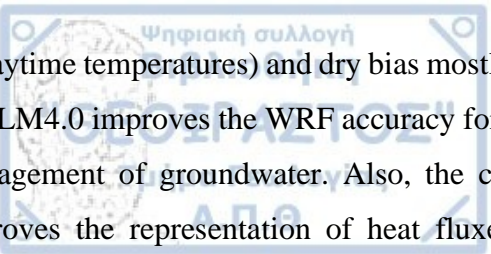


precipitation, radiation and heat fluxes, cloud fraction and soil moisture. Within the LUCAS ensemble, the WRF configurations share the same atmospheric scheme but are coupled to different LSMs or combine the same LSM with different atmospheric schemes, enabling the evaluation of the respective influence of atmospheric versus land processes representation. Specifically, four WRF simulations are involved, three of which share the NoahMP as land surface model; WRFa-NoahMP uses the Grell-Freitas (Grell and Freitas, 2014) and WDM6 (Lim and Hong, 2010) as cumulus and microphysics scheme as opposed to WRFb-NoahMP which is coupled to Kain-Fritsch (Kain, 2004) and Thompson (Thompson et al., 2004) schemes respectively. Also, WRFc-NoahMP differs from WRFb-NoahMP in PBL and skin surface layer schemes, while WRFb-CLM4.0 has the same atmospheric component as WRFb-NoahMP but is coupled to CLM4.0 LSM.

There is no ideal configuration that optimizes WRF performance for all climate variables in all regions across Europe. However, the combination of atmospheric schemes selected for WRFa-NoahMP dramatically degrades WRF performance, achieving the worst scores not only between WRF simulations but within LUCAS ensemble as a whole. Since a similar behavior is not reproduced by WRFb-NoahMP, with which they differ only in cumulus and microphysics schemes, it is concluded that its poor performance originates from the representation of atmospheric processes. WRFa-NoahMP suffers from a general dry bias which leads to extremely dry soils and consequently to strong sensible heating and less evaporation. As a result of the decreased moisture flux to the atmosphere, lower cloudiness is simulated and increased shortwave amounts reach the ground finally producing a largely warmer and drier than observed climate. However, the overall inferior WRF performance caused by the combination of atmospheric schemes in WRFa-NoahMP, contradicts findings from recent literature (Jeworrek et al., 2019; Gao et al., 2017) which identified Grell-Freitas as the best performing cumulus scheme in combination with various microphysics schemes. However, note that these studies were conducted over a different domain with different topography and on higher spatial resolution than the present study.

The other three WRF configurations show a more balanced overall behavior and despite their different set-ups they show similar features. For example, they all underestimate evaporation fraction, overestimate winter cloudiness and precipitation and produce a radiative surplus at surface in winter, resulting from a positive bias for shortwave and longwave radiation. The simulated radiative surplus is not consistent to the winter cloudiness overestimation and in no way explains the general tendency for cold winter bias, which is prominent over the north-eastern part of the domain (around  $-2\text{ }^{\circ}\text{C}$ ) for WRFc-NoahMP and is attributed to the poor performance of MM5, as skin surface layer scheme, over the snow-pack.

In summer, any combination of parameterization schemes yields an overestimation of sensible heat and underestimation of latent heat. The errors in the estimation of the partitioning of heat fluxes result in less atmospheric humidity, therefore less cloudiness and precipitation, producing increased downwelling shortwave amounts and finally a warmer and drier climate over the central and southern regions. However, the partitioning of heat fluxes has different characteristics between models, due to the different representation of atmospheric and land processes. The strong sensible heating in WRFb-NoahMP configuration yields a prominent warm (mainly



in daytime temperatures) and dry bias mostly over Alps, Mid Europe and France in the late summer. The coupling to CLM4.0 improves the WRF accuracy for sensible and latent heat especially in the late summer, due to a better management of groundwater. Also, the change in the combination of PBL and skin surface layer schemes improves the representation of heat fluxes and consequently reduces the warm biases for WRFc-NoahMP compared to WRFb-NoahMP, however it produces wetter conditions over the north-eastern part of the domain. In general, WRF configurations show weaknesses in simulating adequately the heat fluxes, especially sensible heat. The coupling to the advanced CLM4.0 LSM yields higher scores for WRF performance in simulating the summer surface climate with respect to NoahMP simulations.

In this chapter, the systematic errors in model performances and the identification of the underlying physics mechanisms that are responsible for the occurrence of these biases are highlighted. Most models are considered reliable in simulating quite realistically the climate physical processes and thus participate in the next phase of sensitivity experiments, about the forestation effect on surface climate in Europe.



### **3 Afforestation impact on soil temperature in regional climate simulations over Europe**

The published version of these results can be found in Sofiadis et al., 2022 on Geoscientific Model Development (GMD) international scientific journal.

#### **3.1 Introduction**

There is currently a strong policy focus on afforestation as a possible greenhouse gas mitigation strategy to meet ambitious climate targets (Grassi et al., 2017). The biogeochemical effects of afforestation or reforestation are mostly related to increased carbon stocks stored in vegetation and soil, as the total carbon stored in forests is nearly 3 times larger than the carbon stored in croplands (Devaraju et al., 2015). However, understanding the full climate consequences of the large-scale deployment of such a strategy requires to consider also the biophysical effects of afforestation arising from changes in evapotranspiration efficiency, surface roughness and surface albedo (Betts, 2000; Bonan, 2008; Perugini et al., 2017; Duveiller et al., 2018; Davin and Noblet-Ducoudré, 2010).

The crucial need for the assessment of land-use change biophysical impacts on regional scale over Europe is addressed by the Land Use and Climate Across Scales (LUCAS) FPS (Rechid et al., 2017). In the first phase of LUCAS, for the first time, multi-model simulations were performed under a common experimental protocol to address the RCMs sensitivity to theoretical afforestation in Europe, contrasting two idealized land cover scenarios. The first scenario assumed a maximum forest coverage, while the second assumed a maximum grass coverage over Europe.

Up to now, research based on LUCAS ensemble highlighted some robust model responses to theoretical transition from grasslands to forests. First, Davin et al., 2020 suggested that afforestation induce a warming over northern Europe in winter and spring owing to a decrease in surface albedo. They also reported a strong disagreement between models for the signal of summer 2m temperature change, related to uncertainty for turbulent heat fluxes partitioning following afforestation. Moreover, Breil et al., 2020 identified opposing effects of afforestation on surface temperature and temperature at the lowest atmospheric model level. Specifically, they found that afforestation dampened the diurnal surface temperature range and amplified the daily temperature cycle at lowest atmospheric model level. Also, Mooney et al., 2021 indicated changes in snow-albedo effect and snowmelt enhancement due to afforestation in sub-polar and alpine climates.

While the afforestation impact on surface climate has been discussed in previous studies, the changes in soil temperature profile remain unexplored in LUCAS community so far. MacDougall and Beltrami, 2017 suggested that a ground warming remains present for centuries after deforestation. In this chapter, the biophysical impact of afforestation on soil temperature profile across Europe is investigated, as simulated by the suite of 10 RCMs established within FPS LUCAS Phase 1, comparing two idealized scenarios which represent Europe entirely

covered by forest and grass respectively. The soil temperature response to afforestation is investigated through inter-model changes in surface energy balance components and soil moisture. In addition, the simulated impact on soil temperature is compared to observational evidence based on FLUXNET paired sites, classified as forest or open land.

### 3.2 Data & Methods

#### 3.2.1 Regional climate model ensemble

Two idealized land cover change experiments are carried out using an ensemble of 10 RCMs. **Table 16** provides a brief description of the RCM ensemble characteristics, while more information about the land and atmospheric setups can be found in Davin et al., 2020. Compared to Davin et al. (2020), the current model ensemble includes simulations from two additional RCMs (CCLM-CLM5.0 and WRFc-NoahMP), while one of the RCMs (RCA) is not included here because the necessary variables for the analysis were not recorded. Compared to CCLM-CLM4.5, CCLM-CLM5.0 is coupled with a modified version of CLM 5.0 (Lawrence et al., 2019) that includes biomass heat storage (Swenson et al., 2019; Meier, 2019). WRFc-NoahMP shares the same land component as WRFb-NoahMP but differs in the atmospheric setup. Namely, WRFc-NoahMP used the Yonsei University (YSU) scheme (Hong et al., 2006) as planetary boundary layer (PBL) parameterization, as opposed to Mellor–Yamada–Nakanishi–Niino (MYNN) level 2.5 PBL (Nakanishi and Niino, 2009) in WRFb-NoahMP. In addition, new simulations were carried out for WRFb- NoahMP and WRFb-CLM4.0 to address minor bug fixes.

**Table 15: Characteristics of the RCMs participating in the study. JLU – Justus-Liebig-Universität Gießen; BTU: Brandenburgische Technische Universität; KIT – Karlsruhe Institute of Technology; ETH – Eidgenössische Technische Hochschule Zürich; SMHI – Swedish Meteorological and Hydrological Institute; ICTP – International Centre for Theoretical Physics; GERICS – Climate Service Center Germany; IDL – Instituto Amaro Da Costa; UHOH – University of Hohenheim; BCCR – Bjerknes Center for Climate Research; AUTH –Aristotle University of Thessaloniki. The full table including the parameterization schemes and model settings, can be found in Davin et al., 2020.**

Model name	Institute	RCM version	LSM	Soil column
CCLM-TERRA	JLU/BTU/CMCC	COSMO_5.0_clm9	TERRA-ML (Schrodin and Heise, 2001)	10 layers down to 15.3 m. First 9 (8) layers are thermally (hydrologically) active.
CCLM-VEG3D	KIT	COSMO_5.0_clm9	VEG3D (Breil et al., 2018)	10 layers down to 15 m. First 9 (8) layers are thermally (hydrologically) active.
CCLM-CLM4.5	ETH	COSMO_5.0_clm9	CLM4.5 (Oleson et al., 2013)	15 thermally active layers down to 42 m. The first 10 layers are hydrologically active.

CCLM-CLM5.0	ETH	COSMO_5.0_clm9	CLM5.0 (Lawrence et al., 2019)	25 thermally active layers down to 50 m. The first 20 layers are hydrologically active.
RegCM-CLM4.5	ICTP	RegCM4.6.1	CLM4.5	15 thermally active layers down to 42 m. The first 10 layers are hydrologically active.
REMO-iMOVE	GERICS	REMO2009	iMOVE (Wilhelm et al., 2014)	5 thermally active layers down to 9.8 m. One water bucket.
WRFa-NoahMP	IDL	WRF381	NoahMP	4 layers down to 2 m.
WRFb-NoahMP	UHOH	WRF381	NoahMP	4 layers down to 2 m.
WRFc-NoahMP	BCCR	WRF381	NoahMP	4 layers down to 2 m.
WRFb-CLM4.0	AUTH	WRF381	CLM4.0 (Oleson et al., 2010b)	10 thermally and hydrologically active layers down to 3.43 m.

### 3.2.2 Experimental design

In LUCAS, each participating RCM undertook two different simulations, applying the same experimental design. In the first experiment, called FOREST, models are forced with a vegetation map representing a Europe fully covered by trees, where they can realistically grow. Bare lands and water bodies were conserved as in original model maps. In the second experiment, called GRASS, the models integrate the same vegetation map, with the only difference that trees are entirely replaced by grasslands. These maps are shown in Figure S1 in Appendix and a detailed description about creation of maps and the way they are implemented into the respective RCMs can be found in Davin et al. (2020). All simulations are performed over the EURO-CORDEX domain (Jacob et al., 2020) with a spatial resolution of 0.44° (~ 50 km), forced by ERA-Interim reanalysis data (Dee et al., 2011) at their lateral boundaries and at the lower boundary over the sea. The analysis covers the 30-year period of 1986–2015 and focuses on the following eight European subregions as described in Christensen and Christensen (2007): the Alps, the British Isles, eastern Europe, France, the Iberian Peninsula, the Mediterranean, mid-Europe and Scandinavia (**Figure 3.1**).



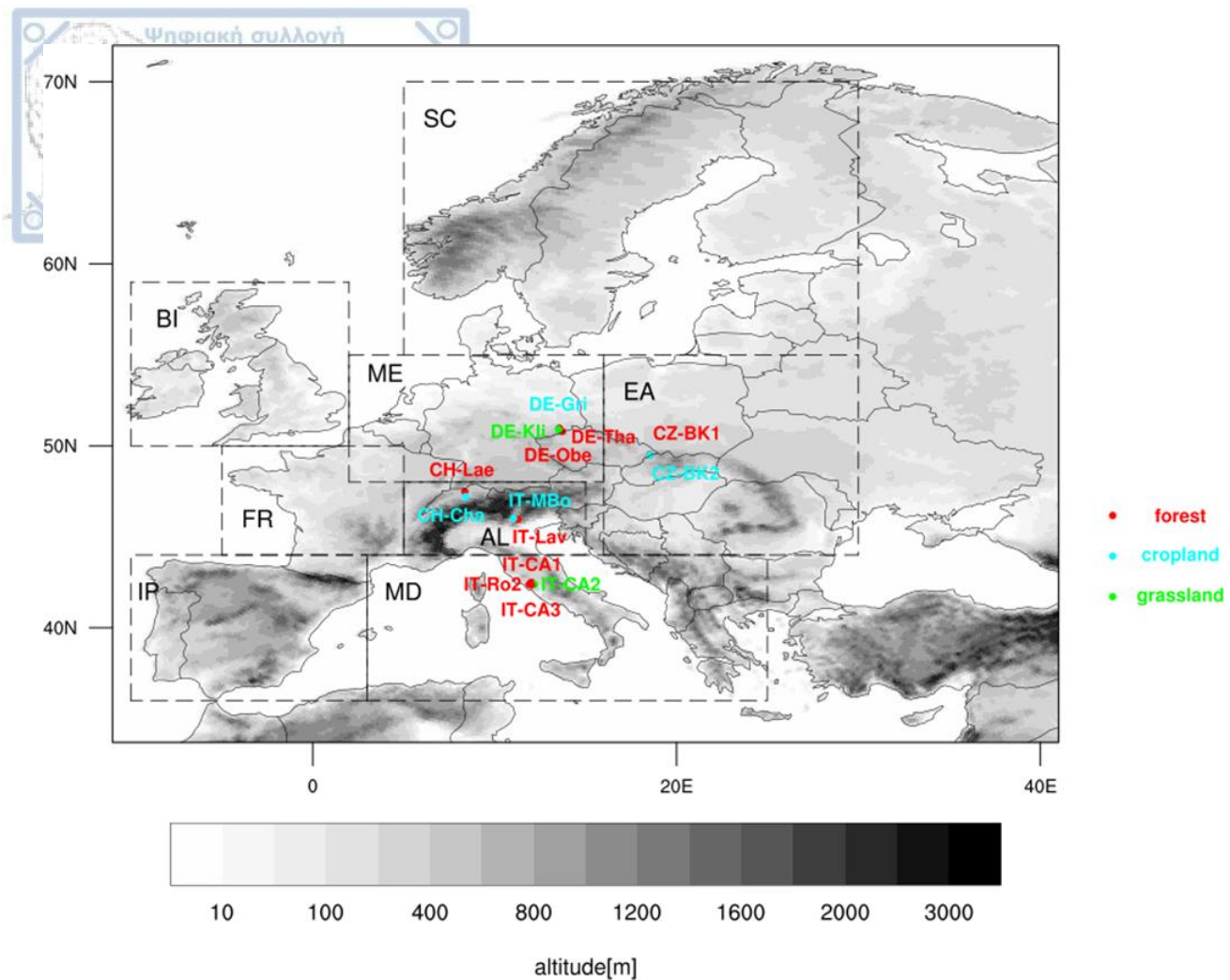


Figure 3.1: Topography of the model domain and location of the observational pairs. The outlined boxes with a dashed line correspond to the eight regions on which the analysis focused: AL (Alps), BI (British Isles), EA (Eastern Europe), FR (France), (IP) Iberian Peninsula, MD (Mediterranean), ME (Mid-Europe), (SC) Scandinavia.

FOREST minus GRASS differences are considered, implying the impact of theoretical maximum afforestation on soil temperature in Europe. Fourier's second law of heat conduction is widely used by land surface models (LSMs) to update temperature in each soil layer (Equation 1):

$$\frac{\partial T}{\partial t} = \frac{\partial}{\partial z} \left[ k * \frac{\partial T}{\partial z} \right]$$

where  $\frac{\partial T}{\partial t}$  is the time rate of soil temperature ( $K s^{-1}$ ) and  $\frac{\partial T}{\partial z}$  is the spatial gradient of soil temperature ( $K m^{-1}$ ) in the vertical direction  $z$  (m). The quantity  $k$  represents the thermal diffusivity ( $m^2 s^{-1}$ ) defined at the layer node depth  $z(m)$  and is equal to the ratio of thermal conductivity to volumetric heat capacity ( $\rho \times c_m$ , where  $\rho$  is mass density and  $c_m$  specific heat capacity per unit mass). In RCMs,  $k$  is time variable and is parameterized depending on soil type and composition (mineral components, organic matter content), on bulk density and soil wetness. In our experiments, soil texture remains unchanged and RCMs do not account for possible occurrence of heat sources or sinks (such as organic matter or carbon decomposition) in the realm where soil heat flow takes place. Thus, the potential changes in soil wetness with afforestation constitute the main driver of differences in soil thermal

diffusivity in our experiments. In this way, we use soil moisture response to afforestation as a potentially explanatory variable of soil temperature variations across RCMs.

Similar to Breil et al., 2020, we employ the residual of energy balance at surface in order to express the surface energy input into the ground. Specifically, we define as energy input into ground the residual energy amount resulting from available radiative energy (net shortwave + incoming longwave radiation) minus the sum of turbulent heat fluxes (latent and sensible heat flux), without accounting for likely deviation of surface energy budget from assumed balance in models (Constantinidou et al., 2020). Our analysis on the changes of surface energy balance components due to afforestation is carried out for summer season, when models disagree both on the sign and magnitude of soil temperature response. Thus, the land surface is assumed to be snow-free. Also, the current RCMs do not account for heat storage into biomass over land surface, apart from CCLM-CLM5.0. A detailed description on the structure of land-atmosphere exchange in the different LSMs is provided in Breil et al., 2020.

### 3.2.3 FLUXNET observational data

We use measured or high-quality gap-filled data of soil temperature on monthly scale from the FLUXNET2015 Tier 2 dataset to complement the model-based analysis. Detailed documentation on data and processing methods can be found in Pastorello et al., 2020.

In order to extract the potential effect of afforestation from observations, we employ a space-for-time analogy by searching for pairs of neighbouring flux towers located over forest (deciduous, evergreen or mixed trees) and open land (grasslands or croplands), respectively. This approach has been used in previous studies aiming to investigate biophysical impacts of local LUC and evaluate LSM performance (Broucke et al., 2015; Chen et al., 2018). In search for site pairs, the following criteria were defined: the two sites have to 1) be located in the Euro-CORDEX domain, 2) differ in the type of vegetation, one site being forested and the other one being either cropland or grassland, 3) have a linear distance within the horizontal resolution of the performed simulations (less than 50 km), 4) have a common measurement period of at least two years, and 5) provide measurements at common depth below the ground surface. In total, we found 14 sites that met our criteria and combined in ten pairs. Their locations are depicted in **Figure 3.1** and their characteristics are reported in **Table 17**. The median linear distance between the paired sites is 11.4 km and their median elevation difference is 125 m.

The close proximity between the flux towers of paired sites ensures almost similar atmospheric conditions, so that differences can be primarily attributed to the different vegetation cover. Applying a simple linear correlation test, the differences either in elevation or separation between the flux towers of paired sites are not the dominant factors in determining the changes in soil temperature ( $r = -0.2$  and  $r = -0.3$ , respectively).

For comparison with the RCMs, we consider the observed mean monthly soil temperature differences (forest minus open land) averaged over all paired sites. This is then compared with the mean of the grid cells matching the locations of the observational pairs in the various RCMs (FOREST minus GRASS). Modelled soil temperature

was linearly interpolated to the common measurement depth that is available for each pair site and averaged over the time period 2003-2014 which covers the observational time span.

Last but not least, the observational setup does not fully resemble the experimental design applied in RCM ensemble. The spatial scale of afforestation applied in models is significantly different from the small forest patches the flux towers are located in. The theoretical maximum afforestation in RCMs has the potential to induce changes in large-scale atmospheric circulation, which can create tele-connections (Swann et al., 2012) that modify the regional cloud cover (Laguë and Swann, 2016) and thus the regional climate conditions. Such feedbacks are not realistic in observations, where most forest measurement locations are located in relatively small forest patches surrounded by open land and is almost unlikely to alter the climate conditions on regional scale.

**Table 16: Characteristics of the sites selected from FLUXNET2015 dataset. DBF – Deciduous Broadleaf Forest; ENF – Evergreen Needleleaf Forest; MF – Mixed Forest; CRO – cropland; GRA – grassland, as described by the International Geosphere-Biosphere Programme (IGBP) classification scheme.**

Pair ID	FLUXNET site ID	(Latitude, Longitude)	Elevation (m)	Land cover type	Distance (km)	Time period	Measurement depth
1	IT-CA1	(42.380,12.026)	200	DBF	0.3	2011-2014	15cm
	IT-CA2	(42.377,12.026)	200	CRO			
2	IT-CA3	(42.380,12.022)	197	DBF	0.4	2011-2014	15cm
	IT-CA2	(42.377,12.026)	200	CRO			
3	IT-Ro2	(42.390,11.920)	160	DBF	8.7	2011-2012	15cm
	IT-CA2	(42.377,12.026)	200	CRO			
4	CZ-BK1	(49.502,18.536)	875	ENF	0.9	2004-2012	5cm
	CZ-BK2	(49.494,18.542)	855	GRA			
5	DE-Tha	(50.962,13.565)	385	ENF	4.1	2004-2014	10cm
	DE-Gri	(50.950,13.512)	385	GRA			
6	DE-Obe	(50.786,13.721)	734	ENF	23.4	2008-2014	10cm
	DE-Gri	(50.950,13.512)	385	GRA			
7	DE-Tha	(50.962,13.565)	385	ENF	8.4	2004-2014	10cm
	DE-Kli	(50.893,13.522)	478	CRO			
8	DE-Obe	(50.786,13.721)	734	ENF	18.4	2008-2014	10cm
	DE-Kli	(50.893,13.522)	478	CRO			
9	IT-Lav	(45.956,11.281)	1353	ENF	19.3	2003-2013	10cm
	IT-Mbo	(46.014,11.045)	1550	GRA			
10	CH-Lae	(47.478,8.364)	689	MF	30	2005-2014	10cm
	CH-Cha	(47.210,8.41)	393	GRA			

### 3.3 Results

#### 3.3.1 Soil temperature response

**Figure 3.2** depicts the afforestation (FOREST minus GRASS) impact on the annual amplitude of soil temperature (AAST) at 1 meter below the ground surface. AAST is calculated as the difference between the warmest and coldest month of an average year, based on the climatology of the 30-year simulation period 1986-2015. In **Figure 3.3**, the mean differences in AAST between FOREST and GRASS are averaged over eight European subregions. The differences are also examined at 2 cm, 20 cm and 50 cm below the ground surface, in order to address the soil temperature response to afforestation across soil column.

Within the ensemble, the sign of AAST response to afforestation is mixed, while the magnitude of AAST change at 1 meter depth ranges from  $-7.1$  °C to  $1.8$  °C across regions. Note that the sign of AAST response does not change with depth in almost all models. The fact that the participating modelling systems share the same atmospheric model coupled to different LSMs or share the same LSM coupled to different atmospheric components, helps to address the respective role of atmospheric and land processes in the AAST response to afforestation. According to the results, the LSM selection drives in a great extent the sign of changes in AAST, while the choice of atmospheric schemes further modulates (dampens/enhances) the magnitude of the signal. The first evidence that confirms this finding derives from the comparison between three WRF modelling systems which utilize the NoahMP LSM coupled to different atmospheric schemes (WRFa-NoahMP, WRFb-NoahMP, WRFc-NoahMP). They all show a similar behavior in terms of the sign of changes, namely an increase of AAST due to afforestation, but they differ in the magnitude of changes. WRFa-NoahMP shows the most intense AAST increase across Europe (close to  $2$  °C in several regions) while the other two configurations show absolute changes less than  $1$  °C. Moreover, the atmospheric models which are coupled to CLM LSM (CCLM-CLM4.5, CCLM-CLM5.0, RegCM-CLM4.5, WRFb-CLM4.0) share a similar pattern of changes showing a tendency for decrease in AAST due to afforestation in most regions, in contrast to NoahMP simulations. Another finding that highlights the dominant role of LSM selection on the AAST response results from the opposite sign of changes between WRFb-NoahMP (positive sign) and WRFb-CLM4.0 (negative sign) mostly over the southern Europe. The role of land processes is also addressed within the sub-ensemble built around the CCLM atmospheric model coupled to three different LSMs (TERRA, VEG3D, CLM 4.5 and 5.0) illustrating diverse results. CCLM-TERRA exhibits strong decreases in AAST exceeding  $-4$  °C in many regions. The CCLM-CLM configurations show similar responses with maximum changes up to  $-2$  °C. Last, CCLM-VEG3D exhibits a distinct behavior with small AAST increase over central Europe and large AAST decrease of more than  $-5$  °C in northern Europe and areas of high-altitude.

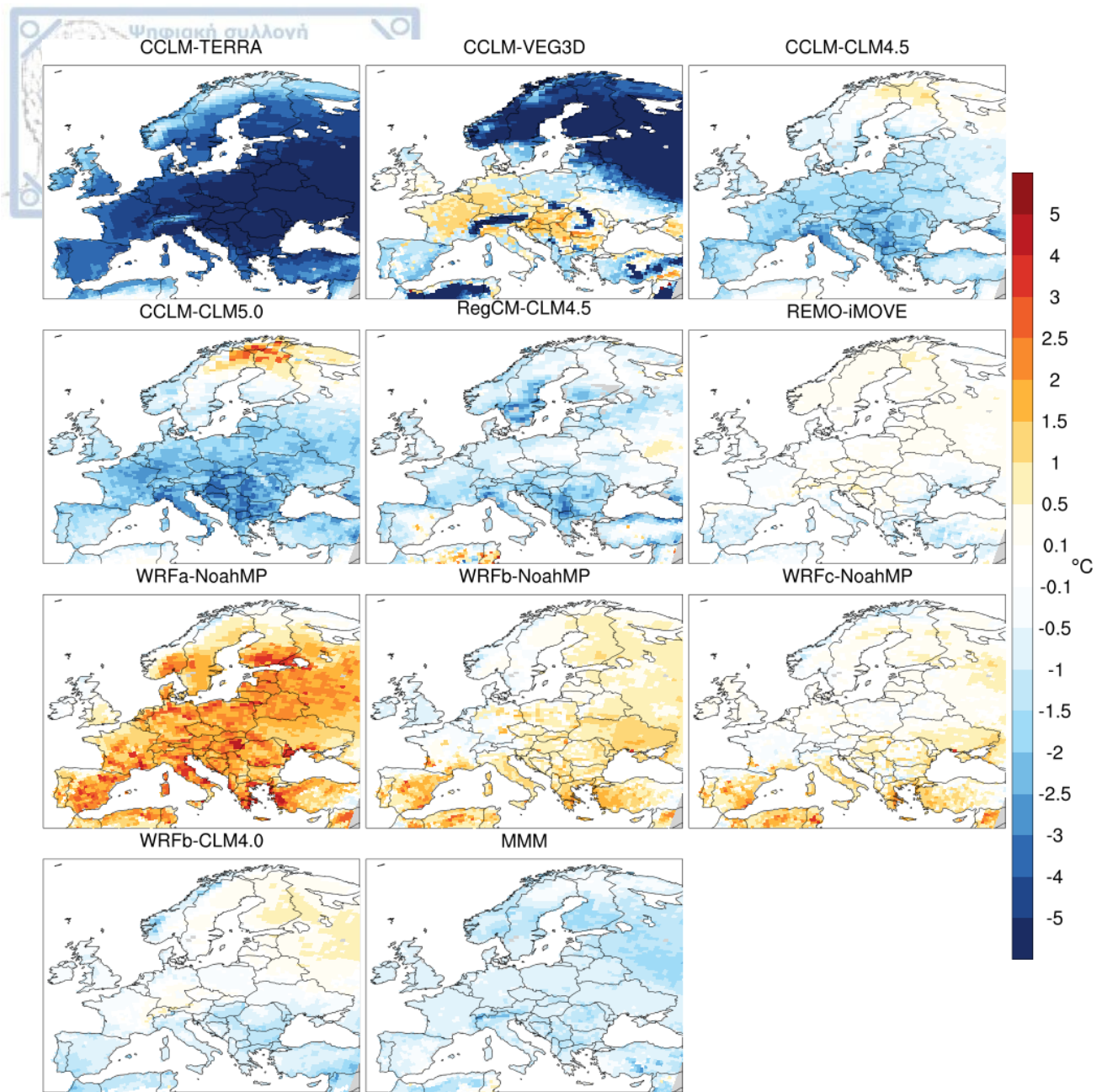


**Figure 3.2: Afforestation (FOREST minus GRASS) impact on the AAST at 1 meter depth. MMM: multi-model-mean of LUCAS simulations. Positive (negative) values indicate an increase (decrease) due to afforestation.**

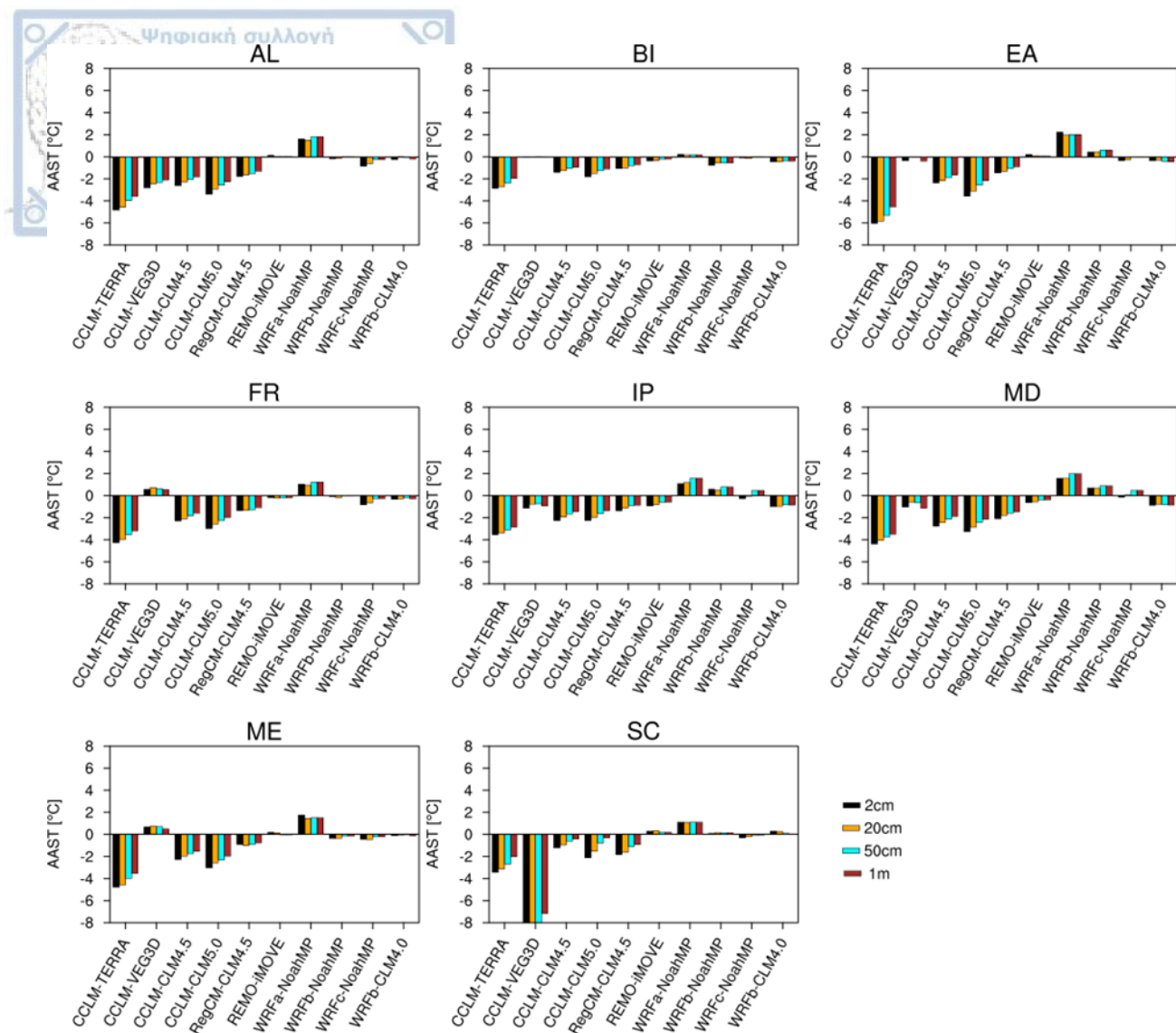


**Figure 3.3:** Afforestation (FOREST minus GRASS) impact on AAST at four different soil depths 2cm, 20cm, 50cm and 1 meter, averaged over eight European subregions.

To better understand the changes in AAST, the mean seasonal differences in soil temperature across soil depths are examined, averaged over Mediterranean (**Figure 3.4**) and Scandinavia (**Figure 3.5**). These two regions are selected as they are representative of southern and northern Europe, while similar figures can be found for all European subregions in Appendix (Figures A 4-9).

Over the Mediterranean region, almost all models respond to afforestation, with REMO-iMOVE exhibiting an almost constant temperature increase of small magnitude at all soil depths and seasons. From the remaining simulations, six out of the nine show that summer (maximum) soil temperatures are higher in the GRASS than in the FOREST experiment. All simulations included in this category include the CLM (coupled to CCLM, RegCM, WRF), TERRA and the VEG3D LSMs. The winter (minimum) soil temperatures in the same modelling systems are not considerably affected by afforestation, thus the decreased AAST, discussed before, is attributed exclusively to the summertime climate processes over the Mediterranean region. Last, the WRF-NoahMP configurations show the opposite behavior with higher forest soil temperatures in summer (this is true only at 1

meter depth for WRFc-NoahMP). Similar to the first group of simulations, the winter soil temperature sensitivity to afforestation is small, and as a result the AAST has a positive sign of change in WRF-NoahMP modelling systems.

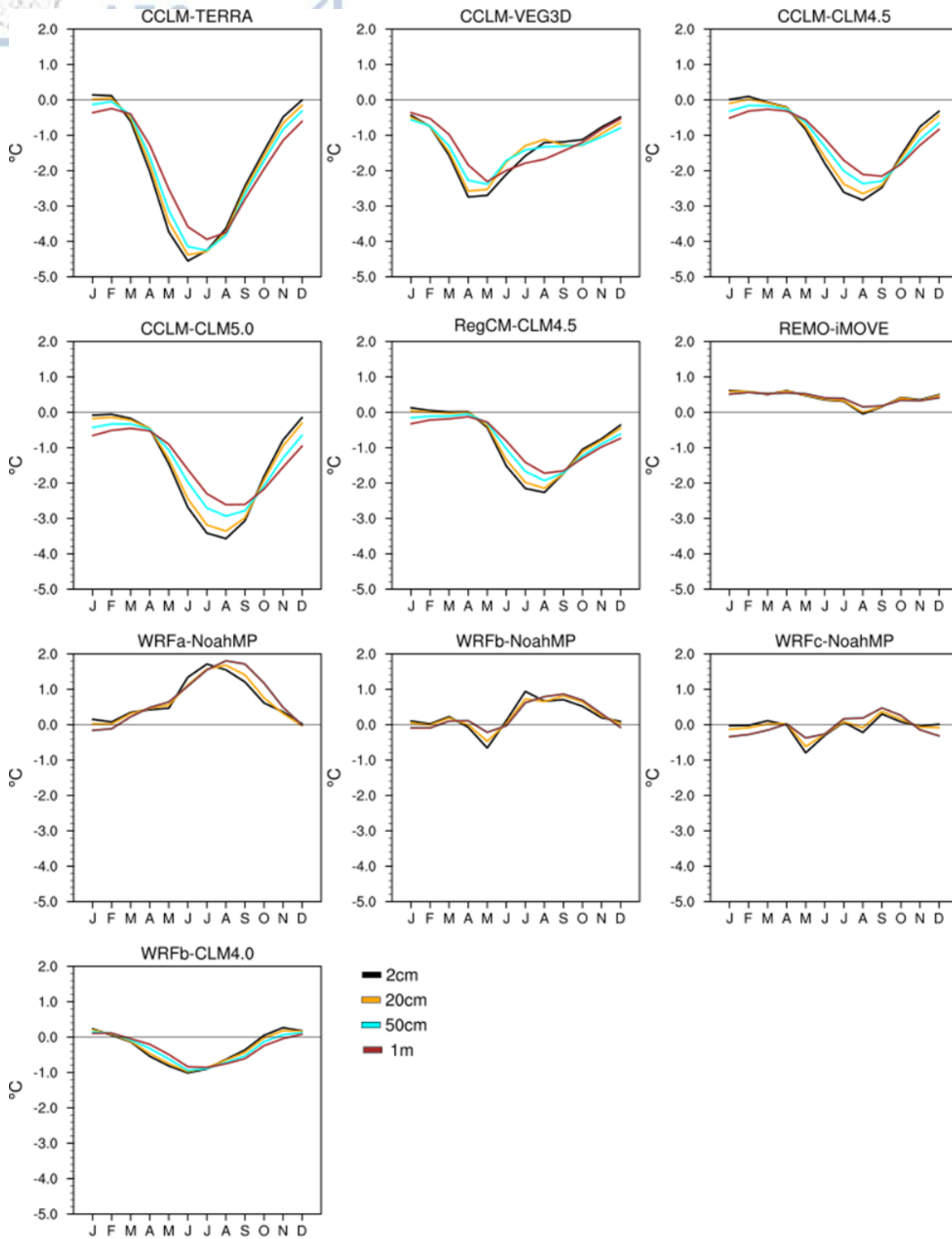
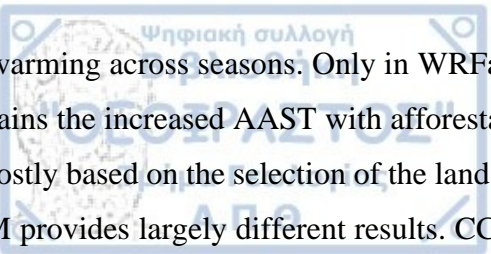


**Figure 3.4: Mean seasonal differences (FOREST minus GRASS) in soil temperature at four different soil depths, averaged over Mediterranean.**

In Scandinavia, a large spread in soil temperature response is simulated across RCMs in summer. Soil temperature is not strongly affected by afforestation in REMO-iMOVE and WRF configurations, which show a small tendency



for warming across seasons. Only in WRFa-NoahMP is noticed an intense warming of 1.5 °C in summer, which explains the increased AAST with afforestation in this model. The response of the rest of the modelling systems is mostly based on the selection of the land component, since the CCLM model coupled to TERRA, VEG3D and CLM provides largely different results. CCLM-TERRA and CCLM-VEG3D show a temperature decrease at all soil depths, with CCLM-VEG3D being the most responsive with changes up to -9 °C in the uppermost soil layer. CCLM-CLM4.5 exhibits small sensitivity across seasons with a tendency towards temperature decrease in summer (similar response from RegCM-CLM4.5), while in CCLM-CLM5.0 the sign of changes switches from negative in upper layers to positive in deeper layers. In winter, the soil temperature differences are small in the majority of simulations and with a tendency for warming.



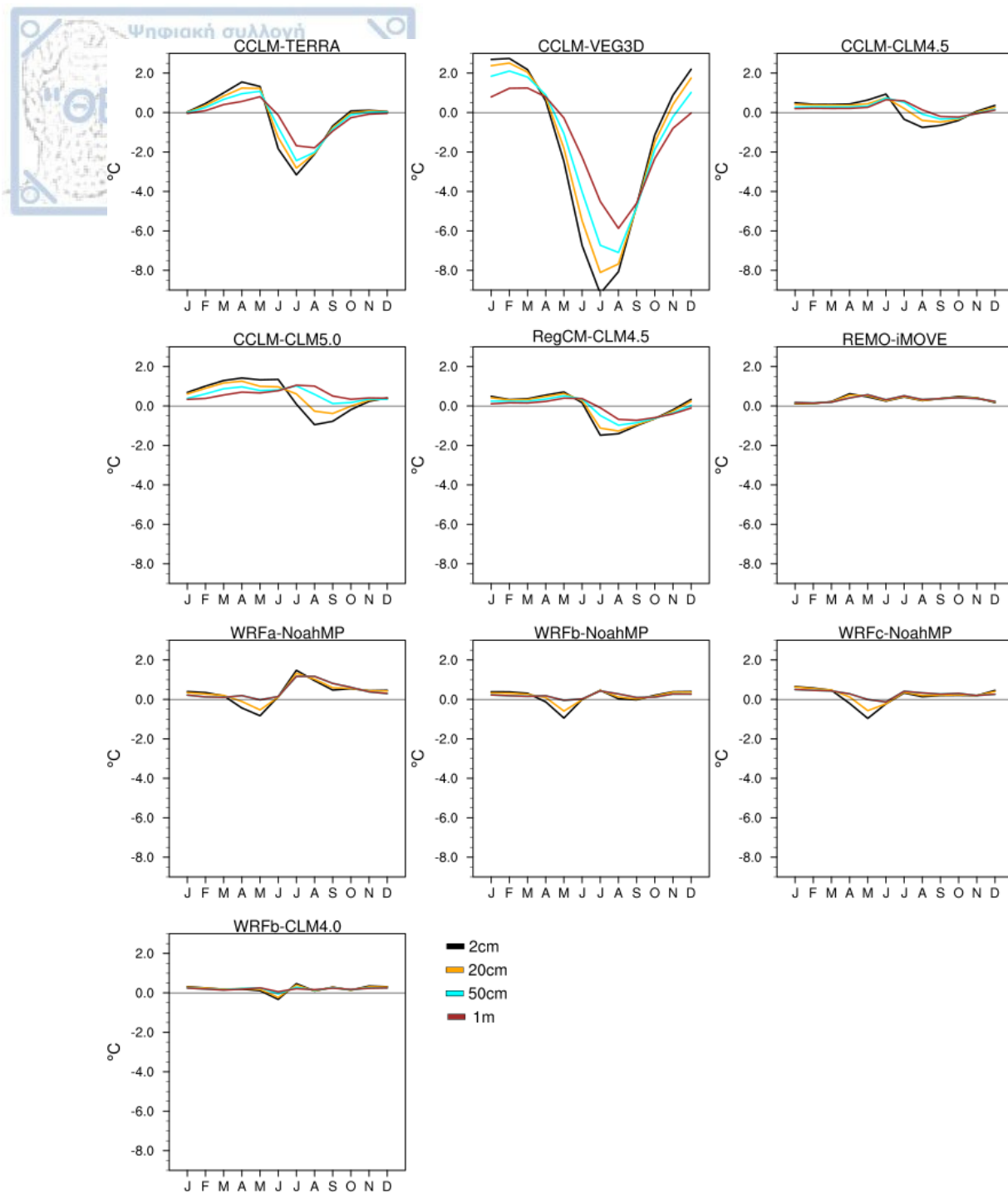


**Figure 3.5: Mean seasonal differences (FOREST minus GRASS) in soil temperature at four different soil depths, averaged over Scandinavia.**

### 3.3.2 Surface energy input

As reported in the previous section, the simulated AAST response exhibits great variability during the summer season, when models disagree both on the sign and magnitude of changes. For this reason, it is essential to examine the afforestation-induced changes in the available energy to warm the ground across RCMs in summer. As available energy to warm the ground or surface energy input into the ground is considered the residual of energy balance at the land surface, as defined in Data & Methodology.

**Figure 3.6** shows maps of the afforestation impact on the surface energy input into the ground in summer. The pattern of changes is largely heterogeneous between the models and correlates well with the spatial pattern of

changes in AAST. The choice of LSM affects the magnitude of changes; different scales of decrease are noticed between the members which share the CCLM atmospheric model, especially between CCLM-VEG3D and CCLM-TERRA in central Europe. CCLM-CLM4.5 and CCLM-CLM5.0 provide similar responses with larger changes in southern Europe (close to  $-10 \text{ W/m}^2$ ). Furthermore, the choice of LSM drives the sign of changes over southern Europe between WRFb-NoahMP and WRFb-CLM4.0. The contribution of atmospheric component is mostly related to the magnitude of changes; between RegCM-CLM4.5 and CCLM-CLM4.5, the latter provides stronger response in southern and central Europe, while between WRF-NoahMP modelling systems, WRFa-NoahMP stands out for its intense increase in surface energy input of more than  $10 \text{ W/m}^2$  in several regions.

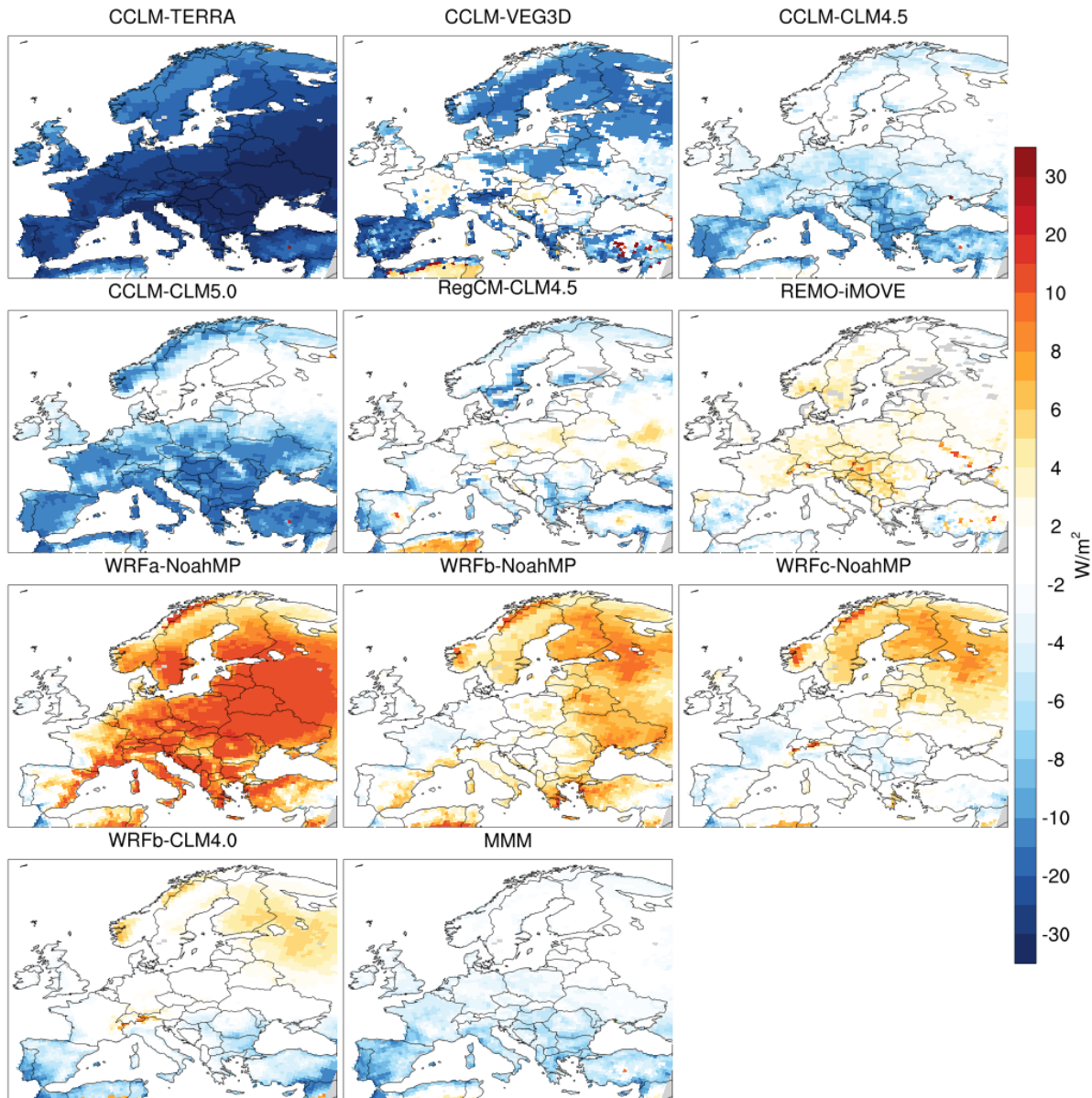


**Figure 8: Afforestation impact (FOREST minus GRASS) on the surface energy input into the ground ( $\text{W/m}^2$ ) in summer. Positive (negative) values indicate an increase (decrease) due to afforestation.**

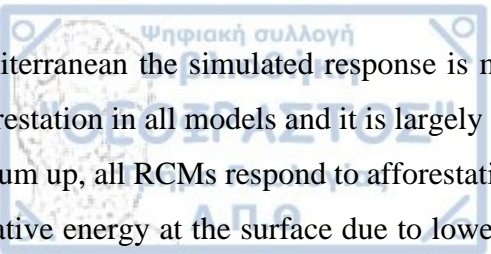
The heterogeneity in the afforestation-induced changes in the available energy to warm the ground is largely consistent to the disagreement for AAST response among RCMs. Thus, it is crucial to explore the origin of large inter-model spread in changes of surface energy balance in summer. Below, the afforestation impact on the

different components of surface energy balance is investigated for each RCM over Mediterranean (**Figure 3.7**) and Scandinavia (**Figure 3.8**). Similar figures can be found for the rest European subregions in the Appendix (Figures A 10–15). The analysis of changes in surface energy balance components is performed with respect to inter-model differences in land-use characteristics, such as leaf area index (LAI), surface roughness and surface albedo.

In both regions, all models (except CCLM-TERRA) consistently show an increase in net shortwave radiation at the surface due to afforestation, which is a result of lower albedo in FOREST compared to the GRASS experiment. The changes vary across RCMs from +5 to +25 W/m<sup>2</sup> over the Mediterranean and from +15 to +35 W/m<sup>2</sup> over Scandinavia. In Scandinavia, the changes in net shortwave radiation are stronger than those in the Mediterranean. This is attributed to the fact that the forests in Scandinavia consist of needleleaf trees, which have lower albedo values compared to broadleaf trees which dominate in Mediterranean. Furthermore, the WRF configurations exhibit more pronounced increases in net shortwave radiation with respect to other RCMs, which is linked to stronger reductions in albedo values in these simulations. Moreover, the albedo effect is further intensified by a reduction in cloud fraction with afforestation over Scandinavia in WRF configurations. In CCLM-TERRA, the reduced net shortwave radiation is due to a pronounced increase in cloud fraction with afforestation triggered by a strong and widespread increase in evaporation rates (Davin et al., 2020). Cloud fraction is also increased with afforestation in the other CCLM members, however the reduced incoming shortwave radiation is offset by the albedo effect, and thus the changes in net shortwave radiation have a positive sign in these simulations.

The increase in available radiative energy at the surface with afforestation is followed by an increase in sensible heat flux, which is another robust feature among simulations. According to Breil et al., 2020, the increase in sensible heat flux with afforestation is attributed to higher surface roughness values in forests compared to grasslands. Generally, the high surface roughness values favor the mixing of atmosphere and enhance the heat exchange between the surface and the upper air. In the current model ensemble, the changes in sensible heat vary across RCMs from +5 to +26 W/m<sup>2</sup> over the Mediterranean and from +16 to +35 W/m<sup>2</sup> over Scandinavia. Again, the only RCM which exhibits a reduction in sensible heat flux is CCLM-TERRA over Scandinavia, because of the pronounced increase in latent heat with afforestation discussed above. Moreover, WRF configurations exhibit the strongest changes in sensible heat flux within ensemble, especially over Scandinavia. As previously shown, afforestation induced an intense increase in net shortwave radiation in these simulations due to strong reductions in albedo in combination with decreases in cloud fraction. Thus, a larger part of radiative energy is available to be transformed into sensible heat flux in these simulations. At the same time, the high surface roughness of needleleaf trees dominating in Scandinavia facilitates the energy exchange between the ground and atmosphere in the form of turbulent heat fluxes.

While RCMs consistently show an increase in sensible heat flux, the agreement is much lower for the response of latent heat flux to afforestation. In Scandinavia, a tendency towards increase in latent heat is noted, but in the



Mediterranean the simulated response is mixed. In general, the sum of turbulent heat fluxes is increased with afforestation in all models and it is largely attributed to an intense and widespread increase in sensible heat flux. To sum up, all RCMs respond to afforestation in the same way. That is, afforestation leads to increased available radiative energy at the surface due to lower albedo values in the FOREST experiment compared to GRASS. In parallel, a large part of this additional radiative energy is transformed into turbulent heat energy due to the mixing-facilitating forest characteristics, such as the high LAI and roughness values, which enhance the heat exchange between the ground and upper atmosphere. The balance between the increased available radiative energy and the increased sum of turbulent heat fluxes will determine if the surface energy input into the soil will be increased or decreased with afforestation in each RCM. Since these processes are differently weighted in each modelling system depending on land-use characteristics, the resulting energy input into the soil varies within the model ensemble in terms of the sign and magnitude of changes. In CCLM-TERRA, CCLM-VEG3D, CCLM-CLM4.5, CCLM-CLM5.0 and RegCM-CLM4.5, the soil heating is decreased with afforestation in summer over the Mediterranean and Scandinavia, because the increased available radiative energy is compensated by the increased sum of turbulent heat fluxes. On the other hand, REMO-iMOVE and the sub-ensemble built around NoahMP LSM exhibit an increase in soil heating with afforestation, since the increase in the sum of turbulent heat fluxes is not enough to compensate their pronounced increase in net shortwave radiation.

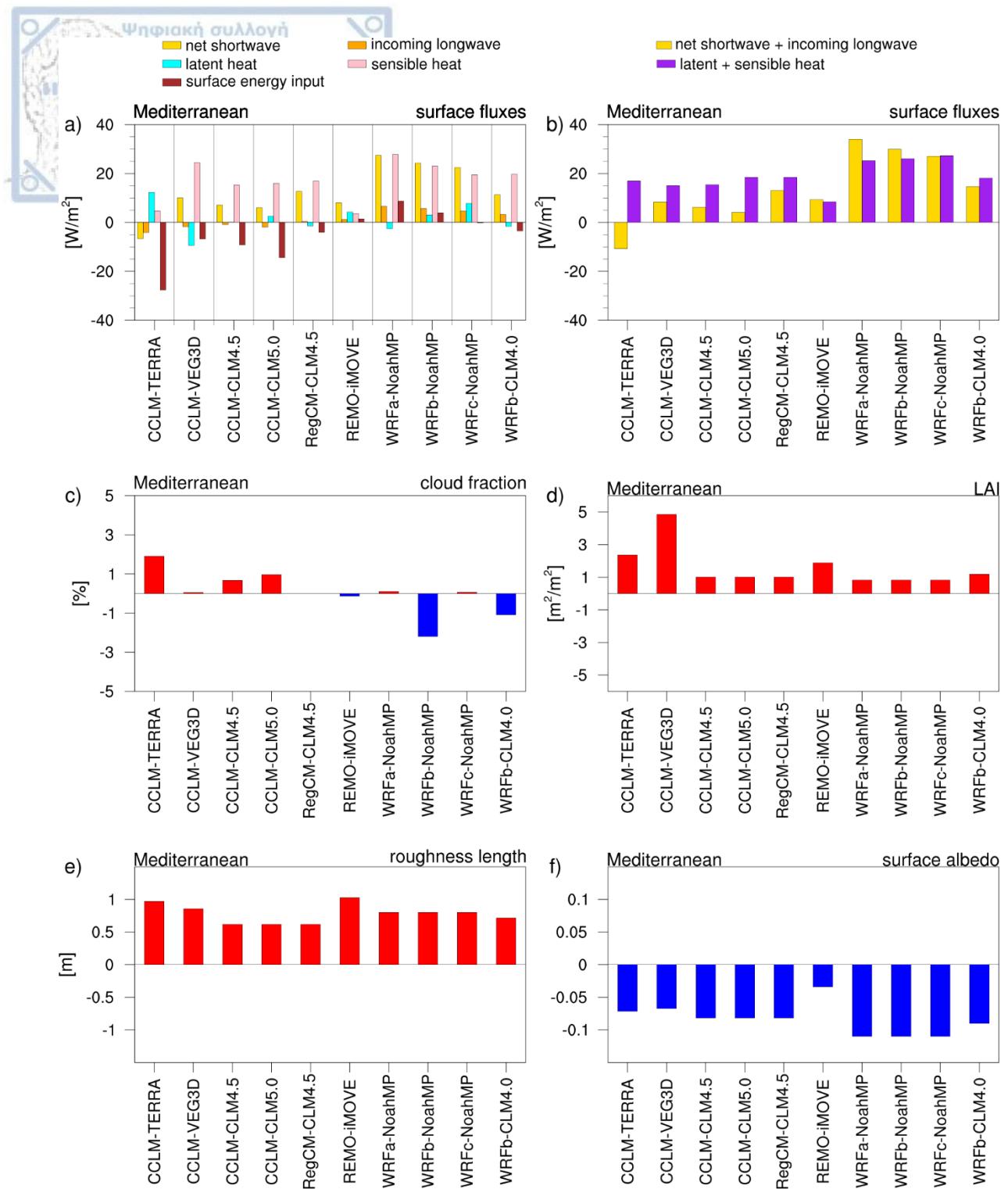


**Figure 3.7: (a) Changes in surface energy balance components (FOREST minus GRASS) averaged over Mediterranean in summer, (b) the changes in available radiative energy at the surface and in the sum of turbulent heat fluxes with afforestation, (c) cloud fraction response to afforestation across models, (d) the inter-model differences in LAI, (e) surface roughness and (f) surface albedo in summer (yearly maximum). Positive (negative) values indicate an increase (decrease) with afforestation.**

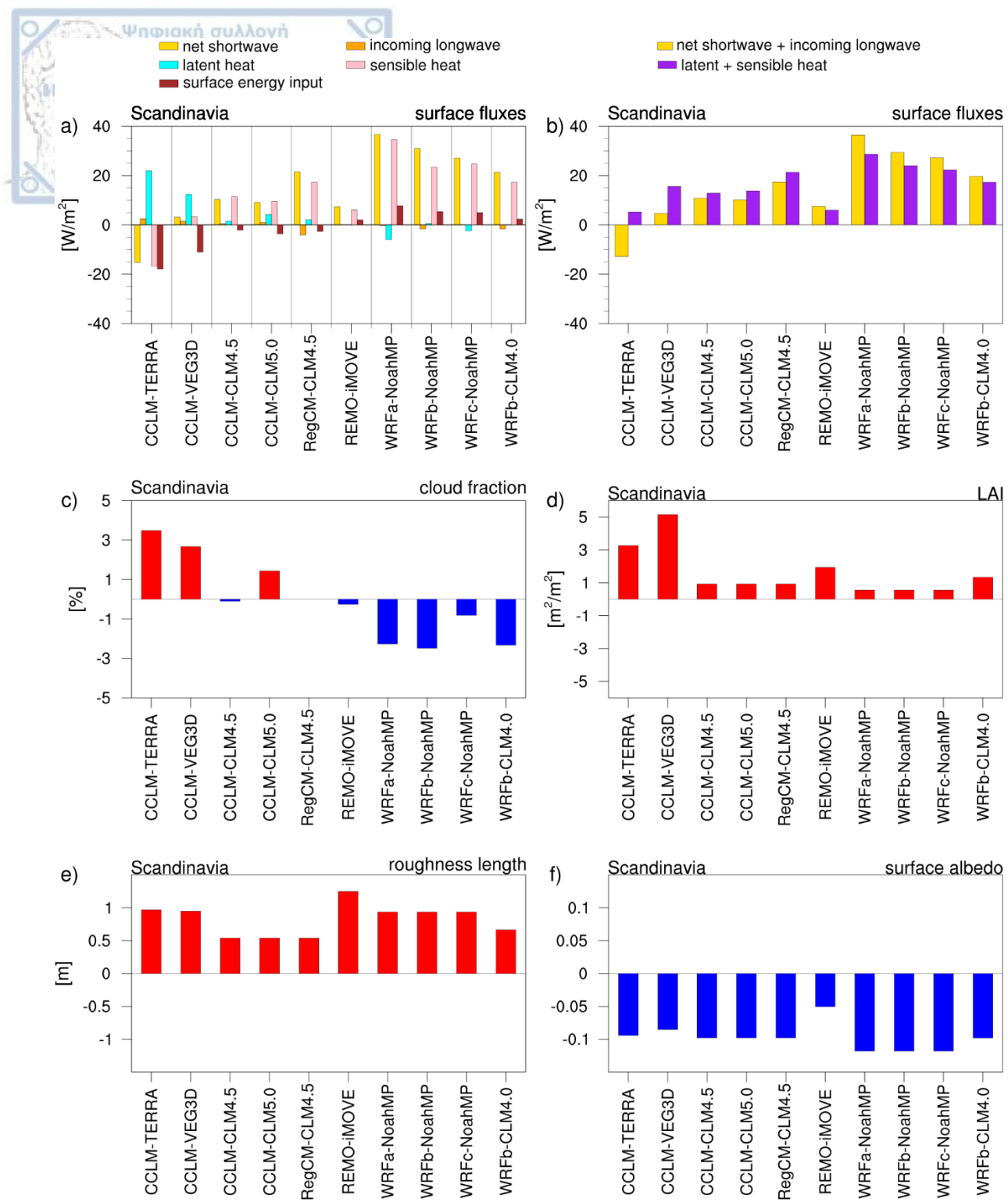


**Figure 3.8: (a) Changes in surface energy balance components (FOREST minus GRASS) averaged over Scandinavia in summer, (b) the changes in available radiative energy at the surface and in the sum of turbulent heat fluxes with afforestation (FOREST minus GRASS), (c) cloud fraction response to afforestation across models, (d) the inter-model differences in LAI, (e) surface roughness and (f) surface albedo in summer (yearly maximum). Positive (negative) values indicate an increase (decrease) with afforestation.**

### 3.3.3 Soil moisture

The changes in soil moisture could also have key role in explaining the simulated soil temperature response to afforestation, because they affect the thermal diffusivity within the soil column. It is expected that a drier (wetter)

soil column would lead to a larger (smaller) AAST due to its smaller (larger) heat capacity, when considering equal soil heat fluxes between the two experiments.

In **Figure 3.9**, the mean summer differences (FOREST minus GRASS) in soil moisture content (SMC) of the top 1m of the soil are mapped over Europe. A widespread soil moisture decrease is simulated over the biggest part of the domain, although with considerable variation in the magnitude of changes across RCMs. The choice of LSM produces a large spread of responses; within the sub-ensemble around CCLM, the SMC change ranges from small decrease of less than  $-10 \text{ kg/m}^2$  in CCLM-CLM4.5 to more than  $-40 \text{ kg/m}^2$  for CCLM-TERRA in several regions. Differences in the magnitude of changes are also noticed between WRFb-NoahMP and WRFb-CLM4.0 because of LSM choice. The atmospheric processes also affect the magnitude of afforestation effect on SMC; among the modelling systems which share the NoahMP LSM, WRFa-NoahMP appears to be the most responsive, with changes exceeding  $-20 \text{ kg/m}^2$  in many regions.

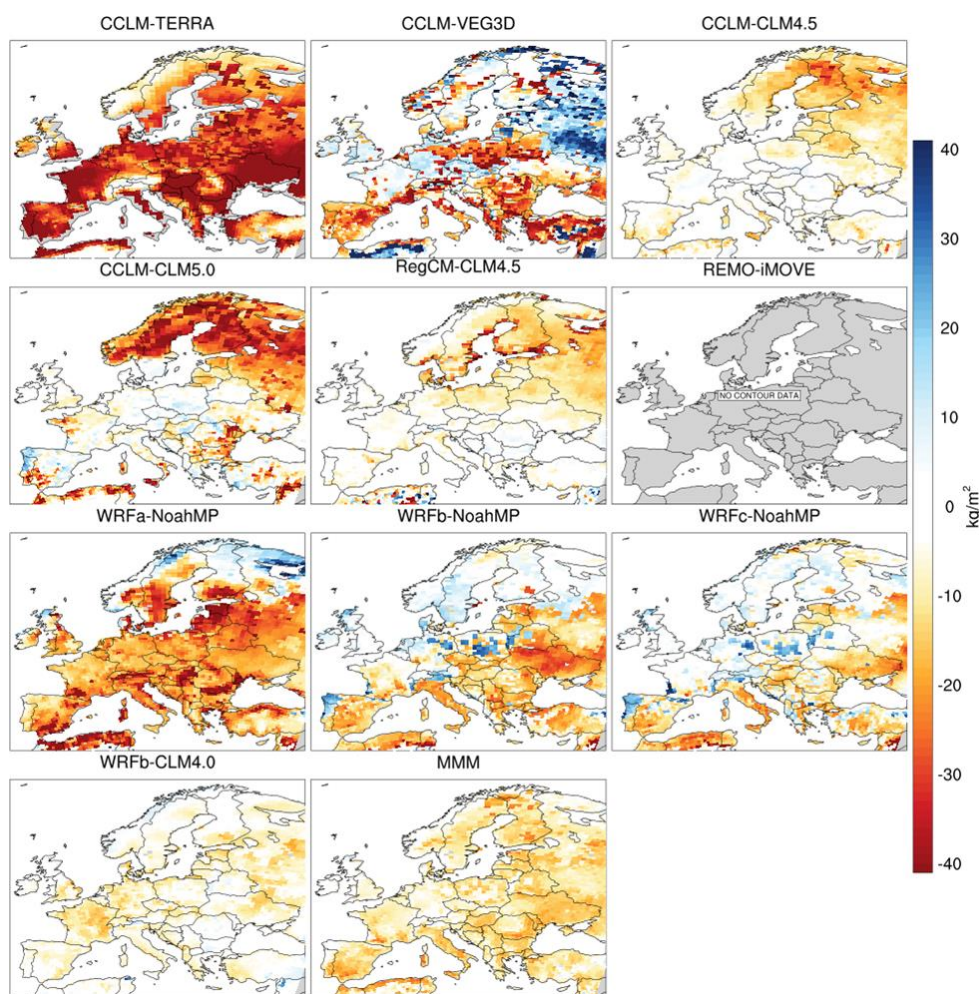
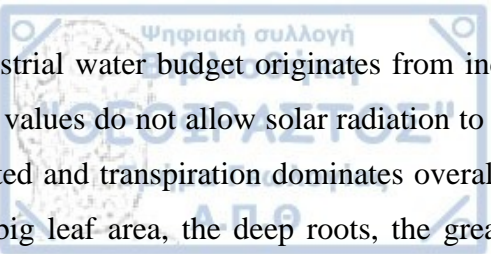


**Figure 3.9: Afforestation (FOREST minus GRASS) impact on soil moisture content ( $\text{kg/m}^2$ ) of the top 1m of the soil in summer. REMO-iMOVE is not included because it employed a bucket scheme for soil hydrology in the LUCAS phase 1 experiments, which does not allow a separation of soil moisture into different layers. Positive (negative) values indicate an increase (decrease) due to afforestation.**

The surface water balance ( $P-E$ ), defined as the difference between precipitation ( $P$ ) and total evapotranspiration ( $E$ ), decreases with afforestation in summer in the majority of models over all regions (Figure A 16 in Appendix). This fact explains the general soil dryness following afforestation. In most simulations, the decrease in the



terrestrial water budget originates from increased evapotranspiration rates with afforestation. In summer, high LAI values do not allow solar radiation to reach the tree-covered ground surface; as a result, soil evaporation is limited and transpiration dominates overall evapotranspiration (Bonan, 2008). Specific characteristics, such as the big leaf area, the deep roots, the great available energy due to low albedo and the mixing of the upper atmospheric boundary layer because of the high surface roughness, enhance the transpiration rate in forests. However, CCLM-VEG3D and WRFa-NoahMP show a positive sign of changes in the water balance in the regions of central and southern Europe, due to decreased evapotranspiration with afforestation. This is linked to low atmospheric demands for hydrates in the FOREST experiment of CCLM-VEG3D (Breil et al., 2021). As for WRFa-NoahMP, its poor performance in simulating correctly the surface climate processes, as shown in chapter 1, does not allow for formulating reliable arguments for its behavior in water balance.

The soil moisture changes with depth would indirectly reveal the afforestation effect on the evapotranspiration process during summer. The water uptake for transpiration occurs in different depths within the soil column for grasslands and forests. In grasslands, the soil water needed for transpiration is extracted from shallow layers, because the large fraction of their roots is located there, depleting the moisture of upper soil. On the other hand, forests have a deeper root distribution, thus consuming water from a bigger soil water reservoir. In **Figure 3.10**, the afforestation-induced soil moisture changes within the top 1m of the soil are averaged over the Mediterranean and Scandinavia. Similar plots for the other subregions can be found in Figure A 17 in Appendix. The heterogeneity of SMC changes with depth is evident in most models, mostly in the Mediterranean. In Scandinavia, the contrast in the sign of changes with depth is not evident and to the opposite a distinct soil drying in the uppermost layers is simulated in most models, especially in CCLM-CLM4.5 and CCLM-CLM5.0, which is probably related to differences in surface runoff of water amounts from snowmelt. The different structures of land models and the various descriptions of physiological characteristics of plants in LSMs, such as the root distributions, differentiate the pattern of SMC changes with depth among the simulations.



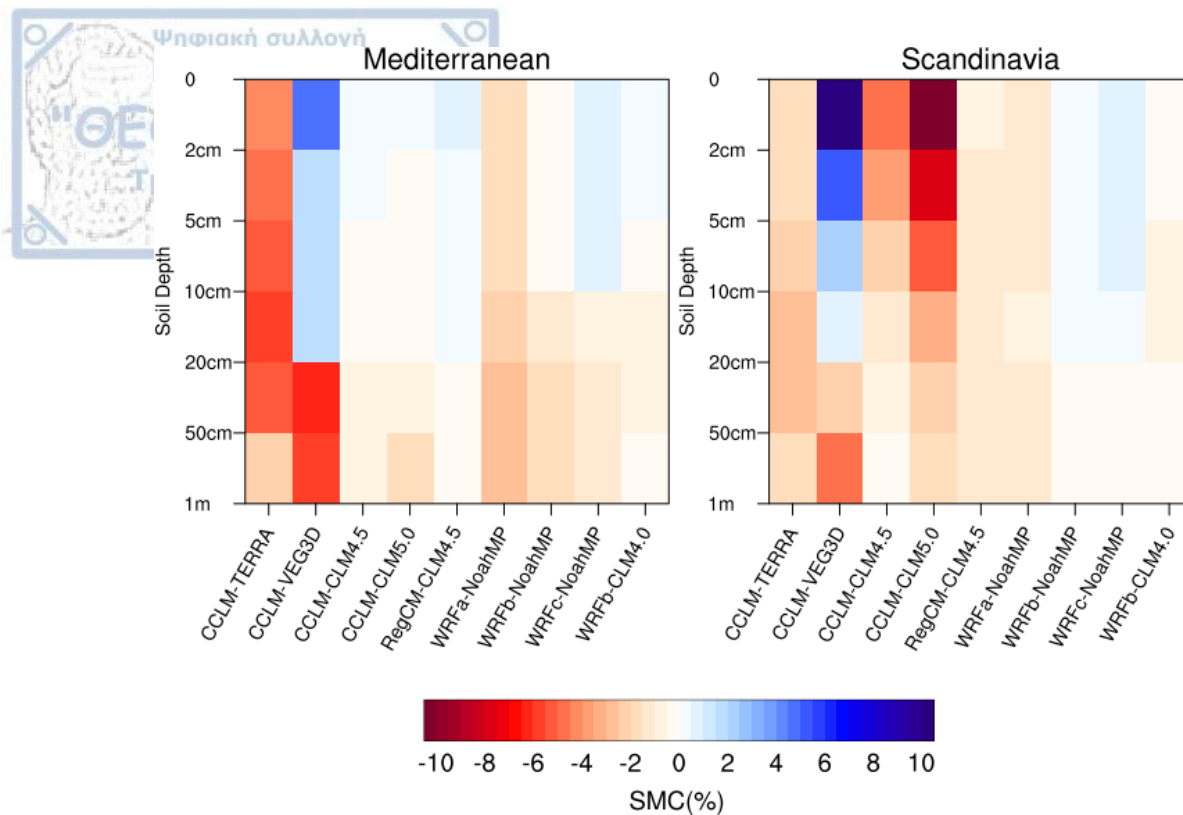


**Figure 3.10: Mean summer differences in soil moisture content (SMC) due to afforestation (FOREST minus GRASS) within the top 1m of the soil, averaged over the Mediterranean and Scandinavia. Positive (negative) values indicate an increase (decrease) due to afforestation.**

### 3.3.4 The origin of inter-model spread in AAST

The widespread and homogeneous soil drying with afforestation, mentioned in the previous section, is not consistent to the mixed AAST response. On the other hand, higher agreement between the pattern of changes in soil heating and in AAST is noted. It has been previously showed that the afforestation impact on radiative processes, such as the decrease in surface albedo, increases the available radiative energy at the surface. In parallel, the afforestation effect on non-radiative processes removes a large part of thermal energy from surface to atmosphere in the form of sensible heat flux. The balance between these processes will determine if the surface energy input into the soil will be increased or decreased with afforestation in each RCM. However, the above biophysical processes are differently weighted across RCMs depending on land-use characteristics, like surface roughness, albedo and LAI, which affect the turbulent mixing and the amount of the absorbed solar energy at the surface. Furthermore, the response of cloud fraction to afforestation is another important factor which affects the soil heating, because of its impact on the incoming shortwave radiation at the surface.

With the aim to quantify the effect of changes in the above-mentioned quantities on the simulated AAST response to afforestation, a linear regression analysis is conducted over all the European subregions. More specifically, the mean summer changes in albedo, LAI, cloud fraction and soil moisture content are used as explanatory (independent) variables to determine to what extent they influence the changes in AAST (dependent variable). When all the explanatory variables are regressed against the simulated AAST response, the coefficient of multiple determination ( $R^2$ ) is found above 80% in all regions, indicating the key role of the selected drivers in shaping

the effect of afforestation on soil temperature (**Figure 3.11**). In southern regions, the Mediterranean and Iberian Peninsula, the albedo effect predicts the largest part of the inter-model spread in AAST response. Over regions of central Europe (mid-Europe, eastern Europe, France, British Isles), the predictive ability of albedo effect remains strong, however the cloud fraction is the dominating factor which effectively explains the inter-model variance over these regions. Soil moisture also contributes to the explanation of the inter-model spread in AAST over the regions of central Europe, although it is not a dominating driver. In Scandinavia, the simulated AAST response is largely explained by differences in LAI across RCMs, with cloud fraction also substantially contributing to the prediction of the inter-model spread. The changes in LAI are potentially connected with the simulated cloud fraction response, since higher LAI values could facilitate the evaporation rates triggering an increase in cloud cover. This interaction effect between two or more physical processes which are used as explanatory variables constitutes a caveat of the used statistical approach, which results in a reduction of the effectiveness of the corresponding drivers in predicting the response of the dependent variable.

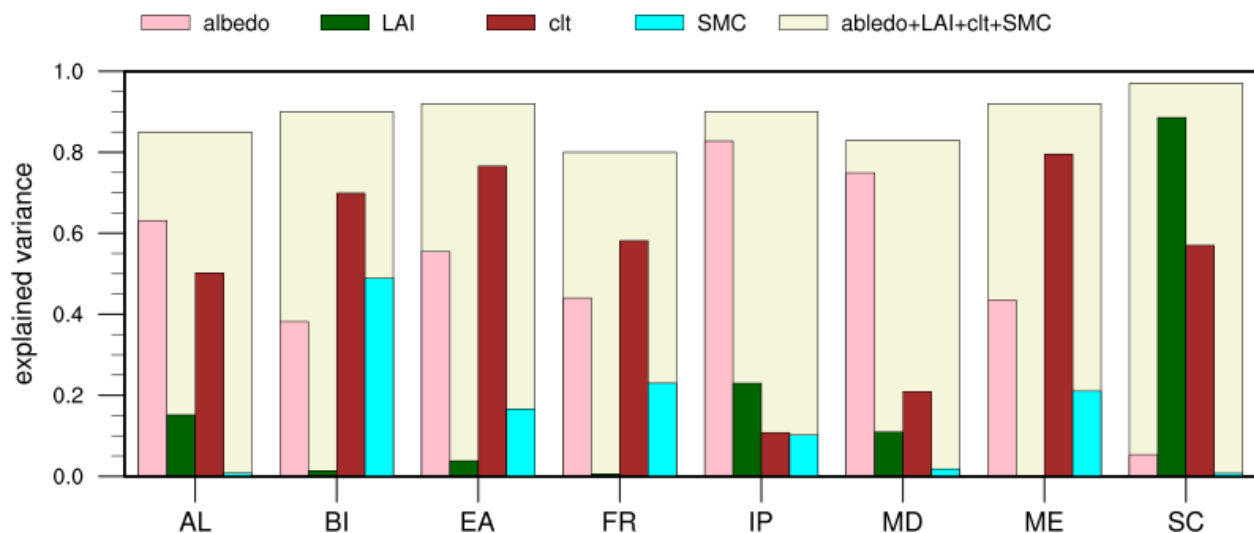


**Figure 3.11: The fraction of inter-model variance in AAST response to afforestation, explained by the mean summer changes in albedo, LAI, cloudiness (clt), soil moisture content (SMC) or all combined (albedo+LAI+clt+SMC). Bars represent the coefficient of determination ( $R^2$ ) derived from linear regression analysis applied over each subregion: Alps (AL), British Isles (BI), eastern Europe (EA), France (FR), Iberian Peninsula (IP), Mediterranean (MD), mid-Europe (ME), Scandinavia (SC).**

### 3.3.5 FLUXNET paired sites

In this section, the simulated impact on AAST is compared to observational evidence of afforestation effect on soil temperature, based on 10 FLUXNET paired sites. In winter, simulations and observations illustrate insignificant changes in soil temperature with afforestation (**Figure 3.12**). The magnitude of afforestation effect in the observations is amplified during summer, revealing a strong cooling up to  $-3$  °C. The majority of models capture the seasonal pattern of changes in soil temperature and particularly the observed summer cooling, albeit with considerable variation in the magnitude of changes. CCLM-TERRA shows the largest changes in summer soil temperature ( $-5$  °C), whereas WRFb-NoahMP and WRFc-NoahMP exhibit subtle summer cooling smaller than  $-1$  °C. On the other hand, WRFa-NoahMP, CCLM-VEG3D and REMO-iMOVE do not capture the observed signal of changes in summer, simulating a warming. Especially REMO-iMOVE shows a yearly warming, in

contrast to the observed cooling throughout the year. According to the observations, afforestation dampens the mean annual soil temperature range by almost  $-3\text{ }^{\circ}\text{C}$ , which is qualitatively consistent with most RCMs, in which the decrease ranges from  $-5\text{ }^{\circ}\text{C}$  for CCLM-TERRA to  $-0.2\text{ }^{\circ}\text{C}$  for REMO-iMOVE. A notable exception is WRFa-NoahMP, which exhibits a distinct increase greater than  $1\text{ }^{\circ}\text{C}$  in contradiction to the observational evidence. Within the sub-ensemble of the CCLM model, the selection of CLM (4.5 or 5.0) as the land component brings the CCLM closer to observations. Also, between the simulations which share the same WRF atmospheric configuration (WRFb), the selection of CLM4.0 against NoahMP LSM improves the WRF performance in simulating the afforestation effect on soil temperature.

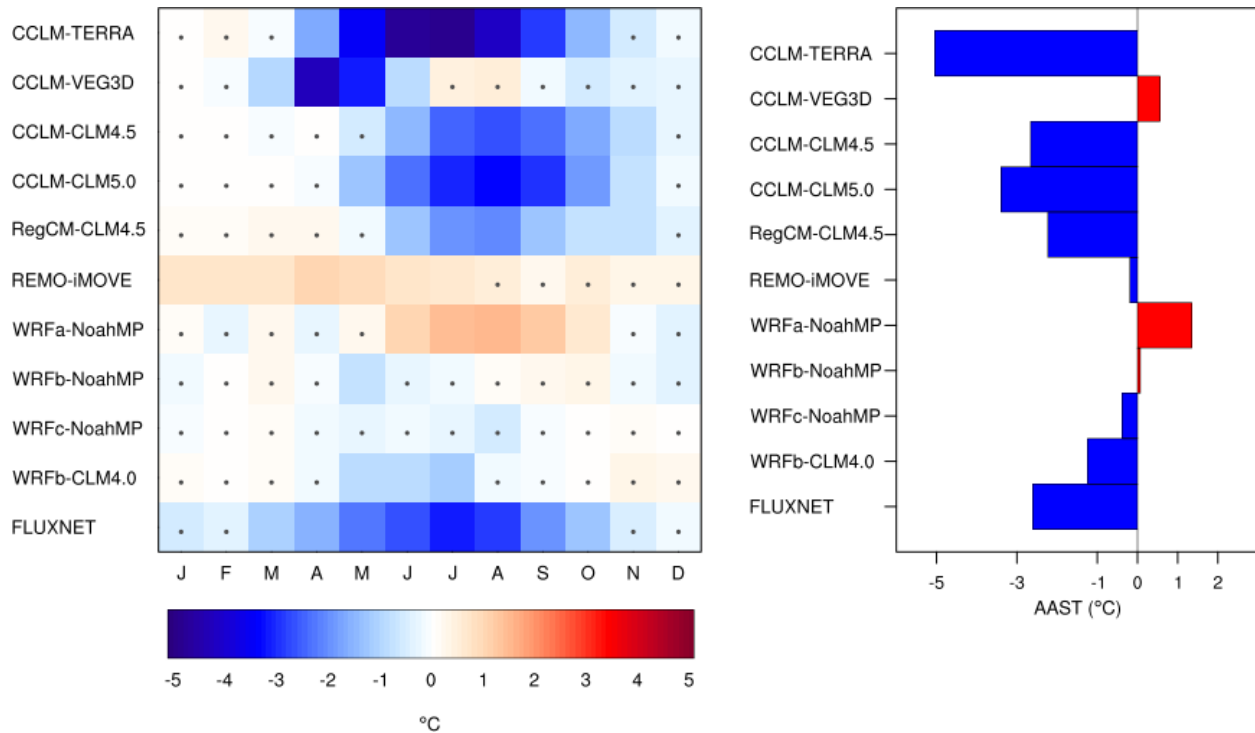


**Figure 3.12: (Left) Observed and simulated impact of afforestation on mean monthly soil temperature. The dots indicate the differences which are insignificantly different from zero in a two-sided t-test at 95% confidence level. (Right) The simulated and observed changes in AAST ( $^{\circ}\text{C}$ ) due to afforestation. The observational differences are averaged over all the paired FLUXNET sites (forest minus open land) and the simulated changes are averaged over the corresponding model grids (FOREST minus GRASS). Positive (negative) values indicate an increase (decrease) with afforestation.**

### 3.4 Summary

In this study, the experimental design established within LUCAS FPS is employed in order to investigate the afforestation impact on soil temperature in Europe. Two idealized land cover change experiments were performed by an ensemble of 10 RCMs, in which the European land surface is represented as fully covered by forest and grass, respectively. The majority of simulations showed a dampening of the annual soil temperature cycle with afforestation, due to changes in summer soil temperature. A large inter-model spread was produced, ranging from  $-7\text{ }^{\circ}\text{C}$  to  $+2\text{ }^{\circ}\text{C}$  depending on model and region.

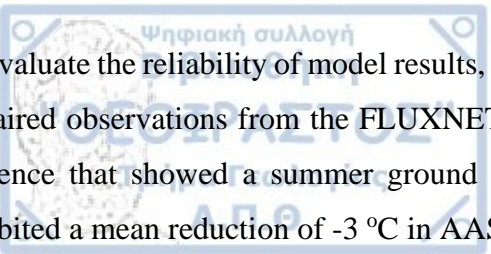
The changes in AAST with afforestation were found to be consistent with summer changes in available energy to warm the ground. In other words, RCMs which showed a ground cooling following afforestation tend to simulate a reduction in surface energy input into the ground, and vice versa. What differentiates the sign of changes in soil

Ψηφιακή συλλογή  
"ΘΕΟΦΡΑΣΤΟΣ"  
Α.Π.Θ.

heating across models is the balance between two biophysical processes, which are greatly affected by afforestation. First, it is the increased available radiative energy at the surface, due to lower albedo in forests, and second it is the increased sum of turbulent heat fluxes (mostly sensible heat flux), due to mixing-facilitating characteristics in forests, such as high LAI and surface roughness values, which enhance the heat exchange between ground and atmosphere. However, these physical processes are differently weighted in LSMs depending on land-use characteristics, such as surface albedo, surface roughness and LAI, while subsequent atmospheric feedbacks, such as the cloud cover changes, can influence the surface fluxes. Thus, the magnitude of afforestation effect on net shortwave radiation and on turbulent heat fluxes is differently pronounced across models. In six out of 10 RCMs of the ensemble, the increased available radiative energy is compensated by the increased sum of turbulent heat fluxes, thus simulating a decrease in soil heating with afforestation and finally a reduction in soil temperature, while the opposite is true for the other four modelling systems. Finally, the changes in albedo, LAI, cloud fraction and soil moisture were found to explain more than 80% of inter-model variance in AAST response in all subregions.

Previous studies which addressed the effects of land-cover changes on soil temperature have reported similar results with the present work. Ni et al., 2019 employed field monitoring on a landscape consisting of tree- and grass-covered ground to investigate the soil temperature effects on root water uptake for a time period from July to November. They found that soil temperature under the grass-covered ground had larger fluctuations and slightly higher values compared to tree-covered ground in summer. Lozano-Parra et al., 2018 studied the combined effect of soil moisture and vegetation cover on soil temperature over three dryland areas of the Iberian Peninsula for two hydrological years. Under dry conditions, they found smaller daily amplitudes of soil temperature below the tree canopies than in grasslands. Longobardi et al., 2016 used a global climate model to investigate the climate sensitivity to various rates of deforestation across the globe. According to their results, deforestation warmed the soils of the midlatitudes because of a reduction in sensible heat fluxes that offset the induced albedo increase. Lastly, MacDougall and Beltrami, 2017 conducted a GCM experiment to study the historical deforestation impact on subsurface temperatures on a global scale. They found that a soil temperature increase remains present for centuries following the deforestation, originating from the reduction of surface energy fluxes towards the atmosphere.

In line with recent findings from observations and model-based studies (Jia et al., 2017; Ren et al., 2018; Zhang et al., 2018; Li et al., 2018b), an afforestation-induced soil drying was detected in summer, implying smaller soil heat capacity. This was also a robust feature among the models, albeit with a considerable inter-model range in the magnitude of responses. Soil moisture decrease with afforestation resulted from large drying of deep layers, related to the fact that forests and grasslands extract soil water for transpiration process from different soil depths. However, the homogeneous soil drying and thus the smaller soil heat capacity is not consistent with the afforestation-induced decrease of soil temperature in the majority of models, explaining only a small part of inter-model variance in AAST response in regions of central Europe.



To evaluate the reliability of model results, the simulated soil temperature response to afforestation was compared to paired observations from the FLUXNET dataset. The vast majority of models agreed with the observational evidence that showed a summer ground cooling in forested areas compared to open land. The paired sites exhibited a mean reduction of -3 °C in AAST, while the simulated response varied from -5 °C to +1 °C.

The structure of the current ensemble helps to address the role of atmospheric and land processes in the representation of biophysical forcing of land cover change, since it involves simulations which share the same atmospheric model coupled to different land components or share the same LSM with different atmospheric setups. The switch from CCLM to RegCM when both were coupled to CLM4.5 did not induce important changes in model results, implying the dominance of land processes in these simulations. Among the suite of models which share the NoahMP LSM, the atmospheric configuration selected for WRFb-NoahMP and WRFc-NoahMP significantly refined the afforestation effect on soil temperature compared to WRFa-NoahMP. Moreover, the results stress the crucial role of LSMs in the simulation of the biophysical effects of afforestation on soil conditions. Among the LSMs coupled to the CCLM model, the choice of CLM significantly improves the representation of afforestation impact on AAST. Also, WRF coupled to CLM4.0 agreed better with observations than WRF coupled to NoahMP. Another issue is the problematic behavior in model performance stemming from unrealistic descriptions of the physical plant functioning in LSMs. Meier et al., 2018 improved the representation of the evapotranspiration with land cover change in CLM4.5, modifying parameters related to transpiration process, such as the root distribution and water uptake formulation.

Research has accounted for the contribution of historical deforestation to present climate conditions. In the last years, governments and non-governmental organizations have been planning (re)afforestation projects around the world with the purpose to mitigate the negative effects of anthropogenic activities on climate. This study aspires to contribute to the deeper understanding of the scientific community on the biophysical effects of afforestation on soil conditions. Future studies focused on the consequences of afforestation from biological or chemical aspects are encouraged to consider these results in order to draw comprehensive conclusions on important climate processes in which afforestation is involved, such as carbon sequestration and microbial respiration.



## 4 Recent land cover changes over Europe could increase the diurnal range of summer temperature at regional scale

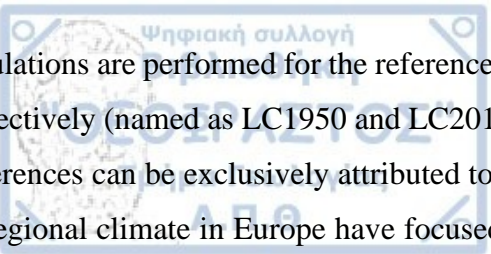
### 4.1 Introduction

Around 15% of the total land cover in Europe has changed over the period 1950-2010, an area similar to France (Fuchs et al., 2013). In recent years, the development of satellite technology enabled the assessment of temporal and spatial dynamics of land cover changes (Song et al., 2018; Hansen et al., 2013). However, the current generation of global land cover datasets, including MODIS-based land cover (Friedl et al., 2010), GLC2000 (Bartholomé and Belward, 2005) and GLOBCOVER (Arino et al., 2008), provide little consistency in terms of time period of observations, spatial resolution, thematic information and accuracy standards (Poulter et al., 2015). Because of these limitations, it is difficult to meet the requirements of earth system models for land cover input, which need high-quality information of the different types of vegetation and their changes over time in order to describe accurately the land cover feedbacks to climate.

To address these challenges, the European Space Agency (ESA) Climate Change Initiative (CCI)-Land Cover project delivered consistent global land cover maps at 300 m spatial resolution on annual basis from 1992 to 2015, based on synthesis of multiple remote sensing products and ground-truth observations (Poulter et al., 2015). Research based on annual ESA-CCI LC maps showed that the global land cover change area from 1992 to 2015 was around 6 million km<sup>2</sup> or 3.5 % of the whole continental area (Li et al., 2018a; Liu et al., 2018). The dominant land cover transition was between croplands and forests. Global forest area decreased fast from 1992 to 2014, mostly over Central and South America and tropical Africa, accompanied by fast increases in croplands. In Europe, the most common land cover transition was from cropland to forest, accounting for 42% of all the transition areas over Europe, mainly distributed in Eastern Europe.

The contribution of historical and future LULCC on climate change signal over Europe is investigated within the framework of FPS LUCAS Phase 2 (Rechid et al., 2017; Jacob et al., 2020), conducting downscaling experiments of CMIP6 results with an ensemble of regional climate models. To cover the need for transient long-term land-use forcing in these model experiments, annual land cover maps of 0.1° spatial resolution which cover the time period 1950-2100 were constructed (Hoffmann et al., 2021). The generation of these maps was based on ESA-CCILC maps and land-use change information from Land Use Harmonization (LUH2) dataset (Hurtt et al., 2020), including information for land management practices, such as irrigated croplands, and accounting for changes in forest types (needleleaf, broadleaf trees) provided by a forest species composition dataset (McGrath et al., 2015).

In this study, the LUCAS LUC dataset is employed in combination with the regional climate model WRF in order to investigate the impact of recent land cover changes on regional climates of Europe. In particular, two WRF



simulations are performed for the reference period 1986-2015, forced with LUCAS maps for 1950 and 2015 year respectively (named as LC1950 and LC2015). The two simulations differ only in their land cover map, thus their differences can be exclusively attributed to land cover change. Previous similar assessments of LULCC impacts on regional climate in Europe have focused on a single variable (Huang et al., 2020) or based on idealized land cover change scenarios (Strandberg and Kjellström, 2019). Here, the effects of realistic land cover changes that recently occurred in Europe on components of surface energy balance and temperature are investigated. It's worthwhile to note that I examine the climate sensitivity of 1986-2015 time period to two different real land cover maps (1950 and 2015) and not the contribution of historical land cover changes on climatic trends between 1986-2015. While acknowledging the limitations of a single model in terms of generalizability and robustness of results, the performance of the specific model configuration has been evaluated (in chapter 1, named as WRFc-NoahMP) and is able to reproduce the observational patterns with good accuracy, adding value to model outputs.

## **4.2 Data & Methodology**

Two climate simulations are performed over Europe for the time period 1986-2015 with the regional climate model WRFv3.8.1 (Skamarock et al., 2008). One simulation is forced with the LUCAS land cover map of 1950 (named as LC1950) and the other with the land cover map of 2015 (named as LC2015). Details about the processing and implementation of these maps into WRF are reported below. Since the two simulations differ only in land cover input, the differences in model outputs can be exclusively attributed to land cover forcing. Here, the LC2015 minus LC1950 differences are considered, which indicate how different the climate of 1986-2015 simulation period would be, if the realistic land cover map of 2015 year instead of the 1950 map is considered as land cover input. The analysis is focused on summer season (June-July-August), since the winter temperature showed a weak sensitivity even to extreme land cover change scenario.

### **4.2.1 Model set-up**

The WRF simulations are carried out over the EURO-CORDEX domain (Jacob et al., 2020) at 0.44° spatial resolution and cover the time period 1985-2015, forced by ERA-Interim reanalysis data at their lateral boundaries and at the lower boundary over the sea (Dee et al., 2011). The first year is used as spin-up period and only the 1986-2015 period is analyzed. Radiative fluxes within the atmosphere are calculated based on Rapid Radiative Transfer Model (RRTMG) (Iacono et al., 2008). Vertical turbulent mixing is parameterized according to Yonsei University PBL scheme (YSU) (Hong et al., 2006), while the fluxes within the lowest atmospheric part of boundary layer are calculated according to revised MM5 surface layer scheme based on Monin-Obhukov similarity theory (Jiménez et al., 2012). For moist convection, the mass flux scheme of Kain-Fritsch (Kain, 2004) is used in combination with Thompson microphysics scheme (Thompson et al., 2004). The present WRF

configuration has been evaluated in chapter 1 (named as WRFc-NoahMP) and achieved good performance in reproducing the observational temporal and spatial patterns.

The atmospheric component of WRF is coupled to NoahMP land surface model in order to represent the key land-atmosphere interaction processes, surface water infiltration and runoff, groundwater transfer and storage as well as soil heat fluxes (Yang et al., 2011). The NoahMP scheme augments the conceptual realism in biophysical and hydrological processes based on the Noah scheme (Chen and Dudhia, 2001) and introduces a framework for multiple options to parameterize selected processes. NoahMP in WRF has a detailed description of land surface, in which the vertical structure includes a single-layer vegetation canopy, a multi-layer snowpack, and a four-layer soil column. The vegetation canopy layer is separated from the combined surface layer, and the two-stream radiation transfer scheme is used to calculate the canopy radiation transfer. Noah-MP contains a multi-layer snow pack with liquid water storage and melt/refreeze capability and a snow-interception model describing loading/unloading, melt/refreeze, and sublimation of the canopy-intercepted snow. A Ball-Berry type stomatal resistance scheme is chosen to consider the difference of sunlit and shaded leaves, while the TOPMODEL scheme is used to parameterize the surface and subsurface water runoff (Niu et al., 2005). NoahMP employs the dominant approach (one vegetation type per grid cell) to represent the land cover, which is classified according to 20 IGBP-MODIS land cover categories that differ in structure and physiology as leaf and stem optical properties, root distribution, aerodynamic and photosynthetic parameters. These parameters are monthly prescribed and daily updated by linearly interpolating monthly values.

#### **4.2.2 Land cover maps**

The LUCAS LUC historical dataset v1.0 (Hoffmann et al., 2021) is used in order to explore the climate effects of recent land cover changes in Europe. The annual LUCAS maps are provided at 0.11° spatial resolution for a period of 65 years, from 1950 to 2015. These maps represent the ground surface using 16 Plant Functional Types (PFTs). The land cover information is provided as PFT fraction per grid cell, where each fraction represents the area covered by the respective PFT within each grid cell (0-1). The LUCAS maps have been generated within the FPS LUCAS Phase 2 in order to be applied as land cover input to downscaling experiments of CMIP6 results over Europe. The new dataset is based on the LANDMATE PFT land cover dataset for Europe (Reinhart et al., 2022), which is derived from the ESA-CCI LC map for 2015. The annual LUCAS maps are also based on land use change information from Land-Use Harmonization Data Set version 2 (LUH2) (Hurtt et al., 2020) in order to derive realistic land use distribution at high spatial resolution from 1950 to 2015. Furthermore, the historical changes in the forest type distributions were adopted from reconstructed forest maps provided by McGrath et al., 2015.



By default, WRF-NoahMP uses a MODIS-based land cover map at a resolution of 30-arc-seconds (around 1 km at 45° latitude) in order to describe the global land cover. This map provides the global distribution of 20 land use categories based on IGBP LC classification system. Thus, specific conversion rules should be applied in order to implement the PFT-based LUCAS maps into WRF-NoahMP. First, the LUCAS LC data were interpolated to model grid with the use of distance weighting method followed by bilinear interpolation. The fractional coverage of land use categories which are present in default MODIS map and are not considered in LUCAS maps (savannas, closed shrublands, cropland/natural vegetation mosaic, mixed forest, wooden and barren tundra) were set to zero. Water, snow and ice are not provided by LUCAS maps therefore these categories were conserved as in the original MODIS maps. Furthermore, the IGBP/MODIS classification system does not distinguish between C3 & C4 grass, irrigated & non-irrigated crops, evergreen & deciduous shrublands, thus the respective PFTs in LUCAS maps were combined into a joint land cover type. In this way, the fractional coverage of C4 grass is added to that of C3 grass in LUCAS maps and then was translated to “Grassland” category in IGBP/MODIS. The fractions of irrigated and non-irrigated crops combined and then translated to IGBP category “Croplands”, while evergreen and deciduous shrublands are added to the IGBP category “Open Shrublands”. The cross-walking table (**Table A 1** in Appendix) describes the conversion of LUCAS PFTs to IGBP classes used as input to WRF.

In order to facilitate the interpretation and visualization of land cover transitions that occurred in Europe, the LUCAS PFTs were aggregated into the generic IPCC land cover classes, according to the cross-walking **Table A 2** in Appendix.

#### 4.2.3 Surface temperature decomposition

An energy balance decomposition method, developed by Juang et al., 2007 and further modified by Luysaert et al., 2014, is employed in order to investigate the processes underlying the surface temperature response to land cover changes. This method enables the quantification of the net impact of changes in each individual term of surface energy balance on surface temperature response.

The energy balance at the surface-atmosphere interface can be written as:

$$SW_{\text{net}} + LW_{\text{net}} = LE + H + G, \quad (1)$$

where  $SW_{\text{net}}$  and  $LW_{\text{net}}$  represent the net shortwave and longwave radiation flux at surface respectively,  $LE$  is the latent heat flux,  $H$  is sensible heat flux and  $G$  is a residual term mainly consisting of soil heat flux. Applying the Stefan-Boltzmann law, the  $LW_{\text{net}}$  can be written as:

$$LW_{\text{net}} = \varepsilon LW_{\text{down}} - LW_{\text{up}} = \varepsilon LW_{\text{down}} - \sigma \varepsilon T_s^4, \quad (2)$$

where  $\varepsilon$  is the surface emissivity (assuming constant  $\varepsilon = 1$ ),  $\sigma$  is the Stefan-Boltzmann constant ( $5.67 \times 10^{-8} \text{ W m}^{-2} \text{ K}^{-4}$ ) and  $T_s$  is the surface temperature. Substituting (2) into (1), we obtain

$$\sigma T_s^4 = SW_{\text{net}} + LW_{\text{down}} - LE - H - G, \quad (3)$$

The change in surface temperature  $\Delta T_s$  is decomposed by calculating the total derivative of equation (3) and solving for  $\Delta T_s$ :

$$\Delta T_s = \frac{1}{4\sigma T_s^3} (\Delta SW_{\text{net}} + \Delta LW_{\text{down}} - \Delta LE - \Delta H - \Delta G) \quad (4)$$

All terms in equation (4) can be computed from the differences in model outputs (LC2015 minus LC1950). In this way, changes of positive sign in  $\Delta SW_{\text{net}}$  and  $\Delta LW_{\text{down}}$  indicate positive changes in  $\Delta T_s$  or a warming, while positive changes in  $\Delta LE$  and  $\Delta H$  heat fluxes induce a cooling. As in Winckler et al., 2017, we omit the residual term  $\Delta G$  in the following analysis, as the multi-year mean ground heat flux is largely unaffected by sparse land cover changes.

Note that the net impact of each term on surface temperature response could arise either from direct biophysical consequences of land cover changes or atmospheric feedbacks triggered by changes in surface properties. For example, the change in net shortwave radiation could arise from changes in surface albedo, which influence the absorption amounts of solar energy from surface, or from changes in cloudiness which regulate the incoming solar radiation at surface.

## 4.3 Results

### 4.3.1 Land cover changes in Europe

The fractional changes in the main IPCC land classes from 1950 to 2015 (LC2015 minus LC1950) are presented in **Figure 4.1**. The PFT-based LUCAS maps were translated to IPCC classification system to facilitate the interpretation of results. A widespread decline in agricultural land is seen in most of Europe, except for the northern coastline of Africa, Albania, Greece, eastern Ukraine and Turkey. The same pattern but with the opposite sign of changes is observed for shrublands. Forest areas increased in Europe, especially around the Alps and Baltic countries. Great urban sprawling also occurred in much of Europe between 1950 and 2015. The spatial pattern of changes in grasslands is heterogeneous, decreasing in much of western Europe and increasing over the eastern part of the domain. Wetlands, bare lands and lands with sparse vegetation have not been significantly affected.

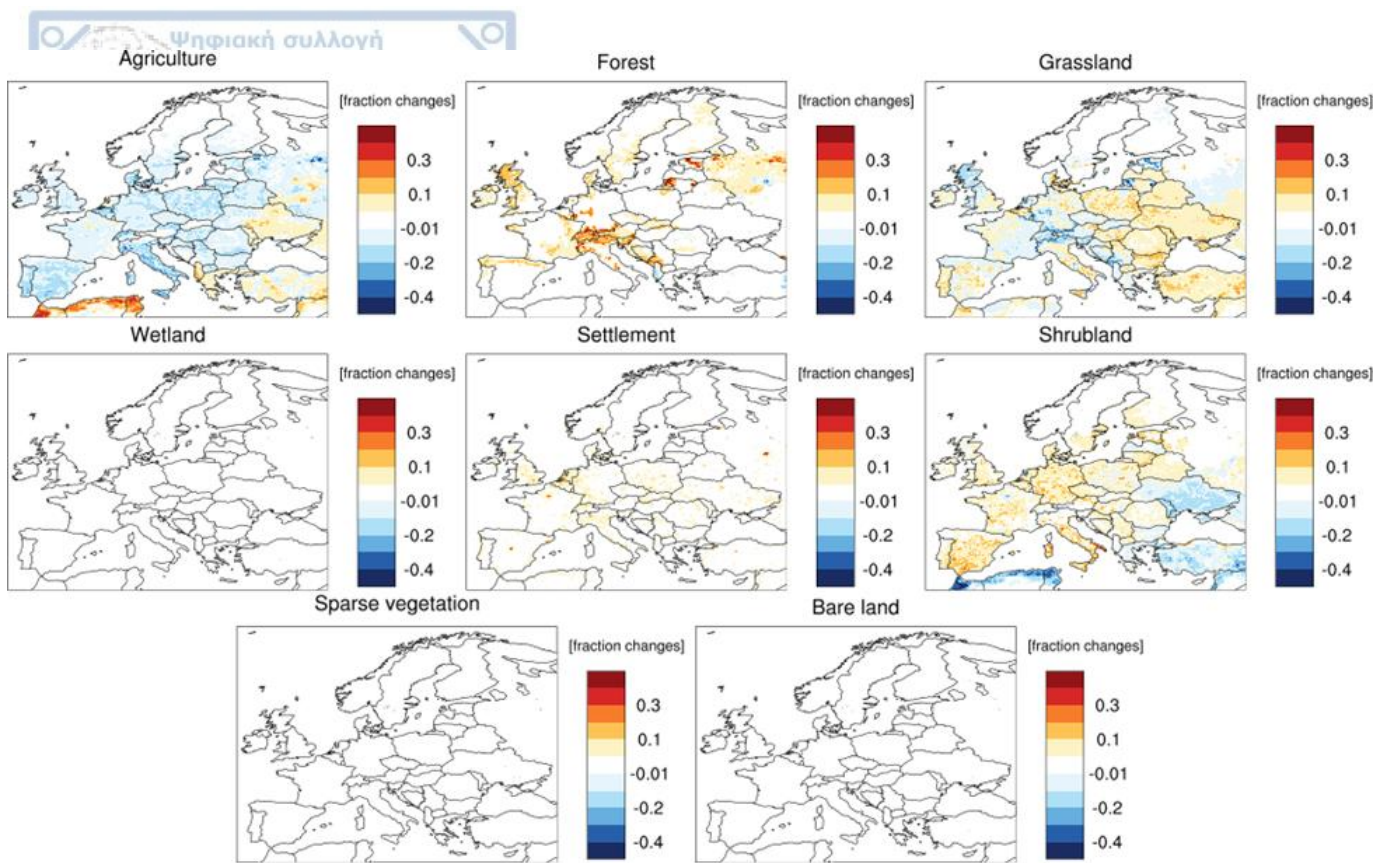


**Figure 4.1:** Changes in grid cell fraction for the main IPCC land classes between 1950 and 2015 based on LUCAS LUC maps (LC2015 minus LC1950). Positive values mean expansion, negative values mean contraction. LUCAS PFT-based maps were converted to IPCC classification system to facilitate interpretation (Table A 2).

In **Figure 4.2**, the land cover fractions are converted into area coverage ( $10^3 \text{ km}^2$ ) for eight European sub-regions. The results show a consistent decline of agricultural lands in all subregions, more pronounced in Eastern Europe where more than 100.000  $\text{km}^2$  of farmlands have been abandoned between 1950 and 2015. Farmland abandonment in Europe has been associated with a combination of socio-economic, political and environmental factors by which formerly cultivated fields are no longer economically viable under existing land-use and socio-economic conditions (Ustaoglu and Collier, 2018; Alcantara et al., 2013; Lesiv et al., 2018). In Eastern Europe, agricultural lands mostly converted into grasslands, but in many areas a great part of croplands was replaced by forests. The conversion of croplands and pasture lands to forests was the dominant land cover transition the last decades in many European regions (Fuchs et al., 2013; McGrath et al., 2015; Kuemmerle et al., 2016; Fuchs et al., 2015). Another major land cover change that occurred in Europe between 1950 and 2015 is the partial conversion of croplands to shrublands. Generally, the type of natural succession after agricultural abandonment depends on soil fertility, local climate and nearby vegetation (Huang et al., 2020; Rey Benayas and Bullock, 2012). Last but not the least, the population and economic growth has led to urban expansion in all subregions at the expense of agricultural areas, especially on the outskirts of mega-cities.

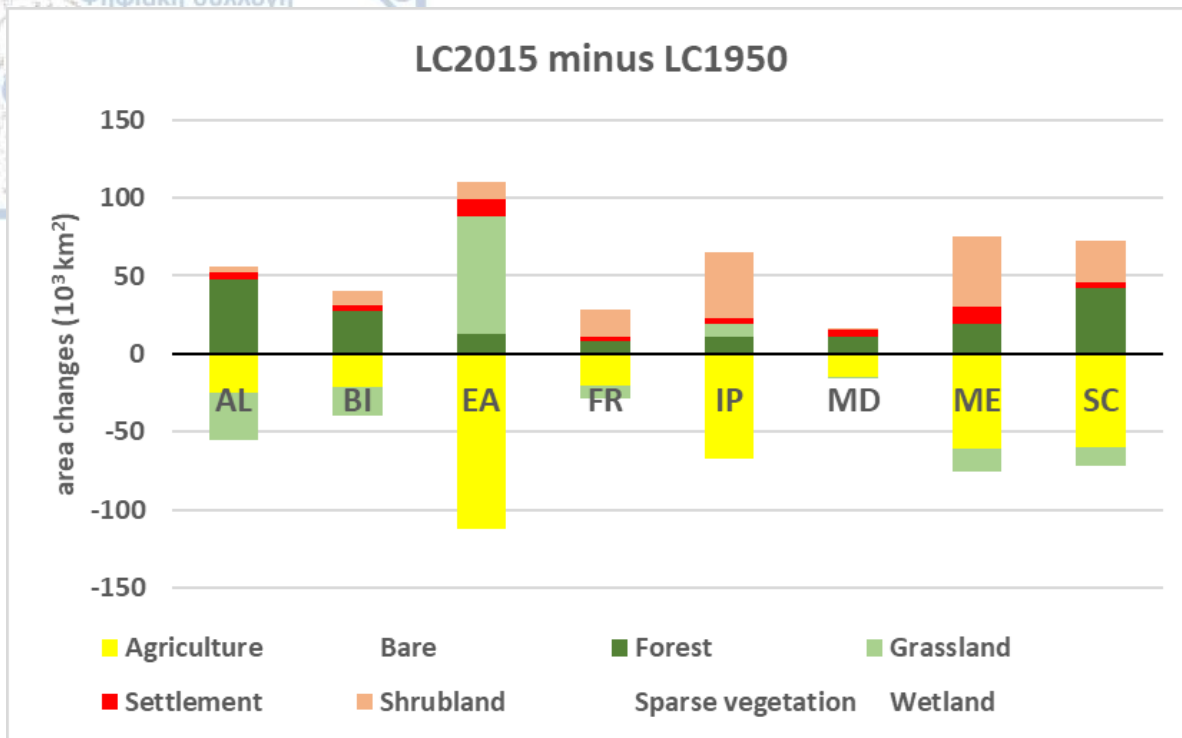


**Figure 9: Area changes (LC2015 minus LC1950) in the main IPCC land classes over eight European subregions. AL (Alps), BI (British Isles), EA (Eastern Europe), FR (France), IP (Iberian Peninsula), MD (Mediterranean), ME (Mid-Europe), SC (Scandinavia).**

### 4.3.2 Land surface properties

The land cover changes have biophysical consequences on land-atmosphere interactions through modifications in land surface characteristics, which regulate the heat and radiation fluxes at surface. **Figure 4.3** depicts the changes in WRF-NoahMP for leaf area index (LAI), surface roughness and albedo due to the recent land cover changes (LC2015 minus LC1950), averaged over eight European subregions.

The transition from open lands to forests and shrublands increased LAI in all subregions, from 0.002 m<sup>2</sup>/m<sup>2</sup> over British Isles to 0.25 m<sup>2</sup>/m<sup>2</sup> in Alps. Also, rougher (from 0.01 m in British Isles to 0.16 m in Alps) and darker (from -0.03 in Eastern Europe to -0.28 in Alps) surfaces are noticed in all subregions. The magnitude of changes in land surface parameters depends not only on the size and type of occurred land cover changes, but also on the magnitude of subregions, as differences (LC2015 minus LC1992) are averaged on regional scale.

Considering the implications from the resulted changes in land surface characteristics and ignoring the possible atmospheric feedbacks triggered by them (e.g. changes in cloudiness), it is expected that the reduction in surface albedo is going to increase the available radiative energy at surface. Also, the greater leaf area could facilitate transpiration due to a greater number of stomata, while the rougher surface is likely to enhance the mixing of atmospheric boundary layer and consequently favor the heat exchange between surface and atmosphere.

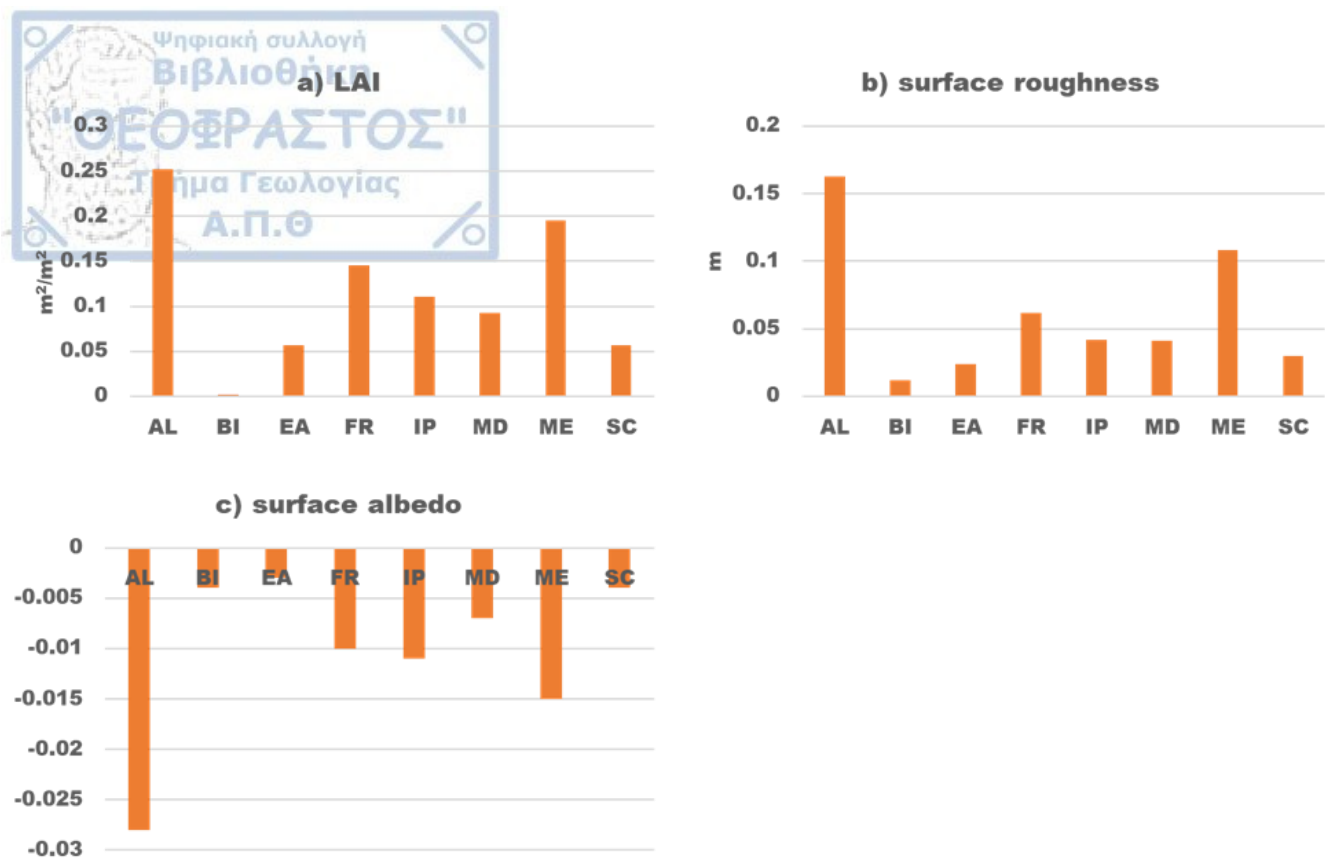
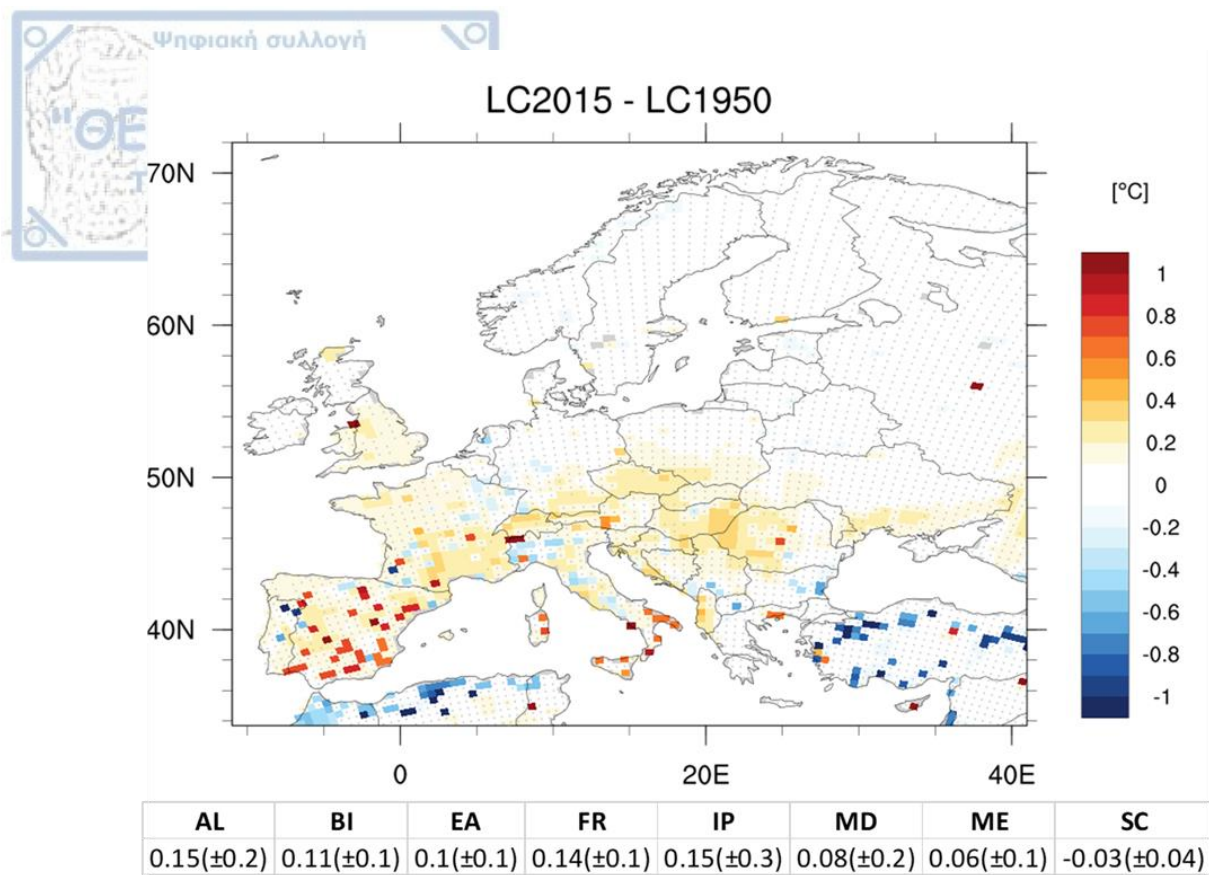


Figure 4.3: Changes in WRF-NoahMP for a) LAI (yearly maximum), b) surface roughness and c) surface albedo due to recent land cover changes (LC2015 minus LC1992) averaged over eight subregions. Surface albedo is calculated for an exemplary leaf/stem ratio.

### 4.3.3 Surface temperature

A method for energy balance decomposition was followed, as described in equation (4), in order to extract the sign of surface temperature change due to the recent land cover changes and quantify the importance of underlying biophysical mechanisms. According to this method, the surface temperature change ( $\Delta T_s$ ) is exclusively attributed to the response of four components of surface energy balance, namely, net shortwave radiation ( $\Delta SW_{net}$ ), incoming longwave radiation ( $\Delta LW_{down}$ ), latent ( $\Delta LE$ ) and sensible heat ( $\Delta H$ ) fluxes.

Figure 4.4 depicts the impact of recent land cover changes (LC2015 minus LC1950) on mean daily surface temperature in summer over Europe for the simulation period 1986-2015. A tendency for warming is shown towards the southern part of Europe, reaching 0.15 °C in Alps and Iberian Peninsula on regional scale. The surface temperature over the northern and eastern part of the domain was not significantly affected by land cover changes.



**Figure 4.4:** The map of differences (LC2015 minus LC1950) in mean daily surface temperature (°C) in summer (JJA) of simulation period (1986-2015) over Europe. The dots indicate the differences which are insignificantly different from zero in a two-sided t-test at 95% confidence level. Below the map, the temperature differences are averaged over eight subregions. The values in parenthesis represent the standard deviation from average. The grid cells with intense red/blue color correspond to grid cells where a land cover change occurs.

In **Figure 4.5**, the temperature decomposition is applied over each subregion, based on spatially averaged daily values for summer. The stacked bars illustrate the contribution of changes in each individual component on surface temperature response to land cover changes.  $\Delta T_s$  arises from the total sum of all individual contributions.

As previously mentioned, the change of land cover induced positive changes in summer temperature (positive  $\Delta T_s$ ) of simulation period 1986-2015, reaching up to 0.15 °C in Alps. The dominant mechanism that explains this warming is the change in net shortwave radiation ( $\Delta SW_{net}$ ) which alone induce a warming from 0.01 °C in Scandinavia to almost 1 °C in Alps. The change in sensible heat ( $\Delta H$ ) is the second major influence, which results in changes of negative sign in surface temperature (from -0.07 °C in Scandinavia to -0.8 °C in Alps) and thus partly offset the warming induced by  $\Delta SW_{net}$ . The influence of latent heat changes ( $\Delta LE$ ) on  $\Delta T_s$  is mixed in terms of sign (from -0.26 °C over Iberian Peninsula to 0.15 °C in British Isles) and has less importance than the corresponding response of sensible heat flux, apart from Iberian Peninsula where  $\Delta LE$  dominates over  $\Delta H$ . Moreover, the changes in downward longwave radiation ( $\Delta LW_{down}$ ) have a minor influence on  $\Delta T_s$ , inducing a range of changes from -0.09 °C in British Isles to 0.15 °C in Iberian Peninsula.

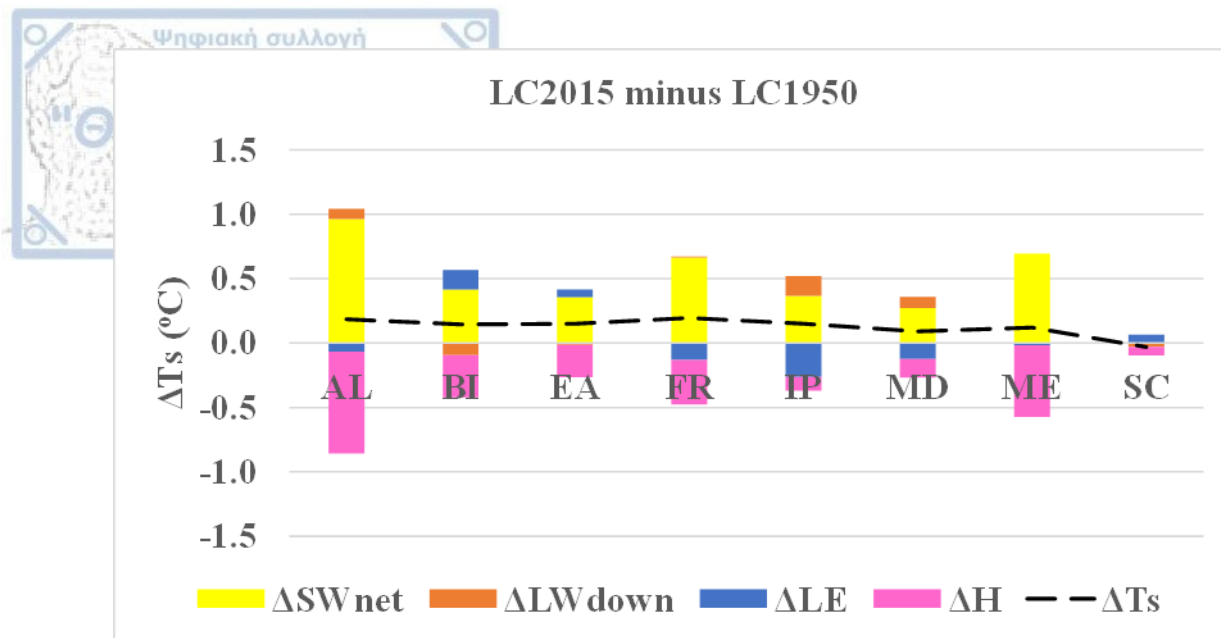


**Figure 4.5: Surface temperature decomposition (equation 4) based on mean daily differences (LC2015 minus LC1950) for summer of simulation period (1986-2015) averaged over eight subregions (over all land pixels). The stacked bars represent the contribution of each component of surface energy balance to temperature response. The black dashed line indicates the net change in surface temperature, which is the sum of individual contributions. In Table A 3 (Appendix),  $\Delta T_s$  as simulated by WRF-NoahMP is compared to  $\Delta T_s$  as estimated from equation 4. Negligible differences are depicted between them, implying the minor contribution of ground heat flux response on surface temperature differences.**

To gain further insights, **Figure 4.6** shows the effect of land cover changes (LC2015 minus LC1950) on mean daily cycle of surface temperature in summer, averaged over eight subregions. The diurnal temperature range increases in all subregions from 0.04 °C in Iberian Peninsula to 0.36 °C in Mid-Europe. In most regions, the increase in diurnal temperature range originates from increased daytime (maximum) temperatures, while the nighttime (minimum) temperature is not considerably affected by land cover changes. Only in Scandinavia the negligible increase of diurnal range results from a small decrease of minimum temperature, while in Iberian Peninsula the hourly temperature is increased all day.

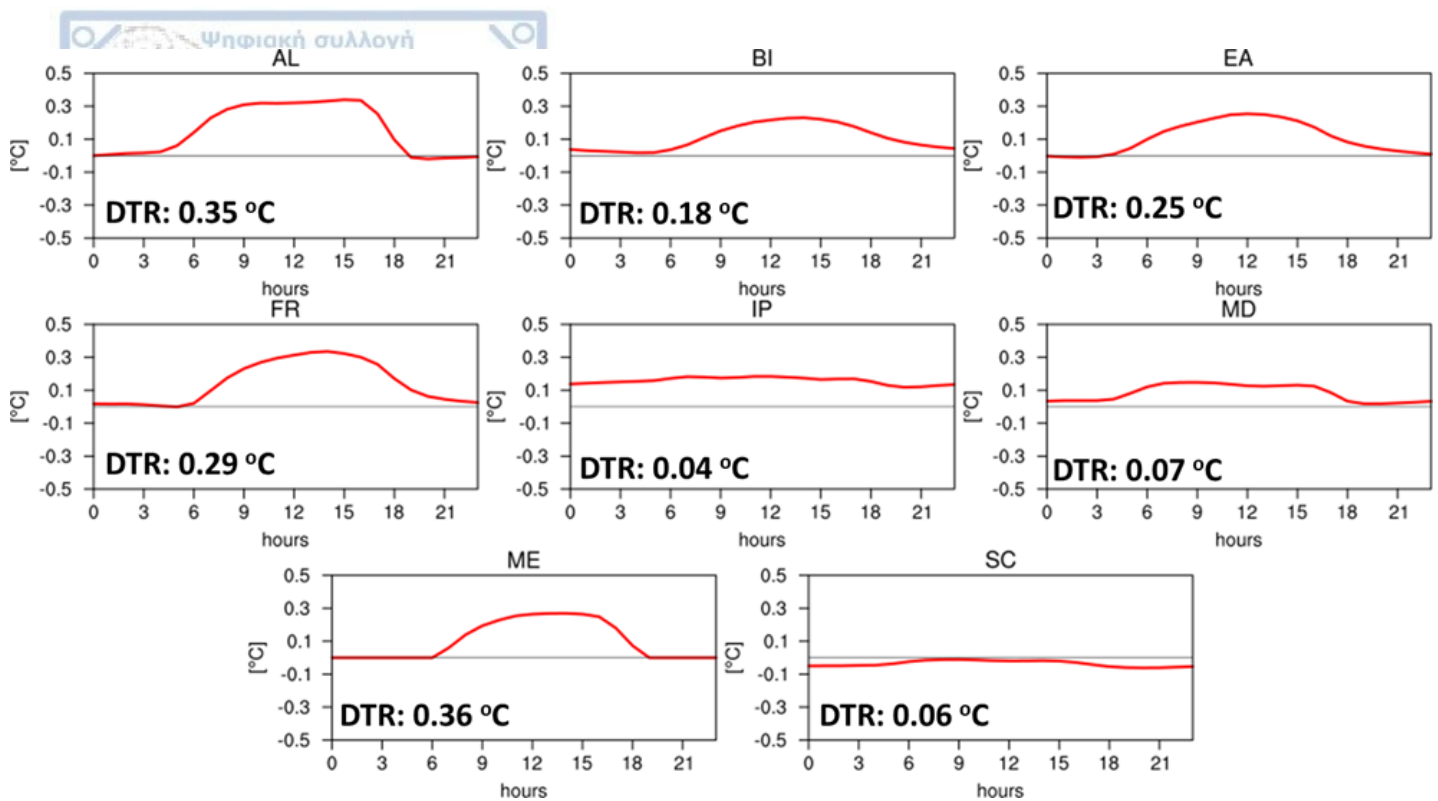


**Figure 4.6:** The impact of recent land cover changes (LC2015 minus LC1950) on daily cycle of surface temperature in summer, averaged over eight subregions. DTR represents the effect on diurnal temperature range, which results from the difference between daily maximum and minimum temperature.

Below, the mean daily summer changes in energy balance components that explain the surface temperature response to land cover changes are investigated.

#### 4.3.4 Shortwave radiation

As previously reported, the change in net shortwave radiation at surface is the dominant mechanism that explains the warming over most of Europe. The changes (LC2015 minus LC1950) in mean daily net shortwave radiation for summer are mapped in **Figure 4.7**. The available net shortwave amounts at surface are increased over the largest part of domain due to land cover changes and maximized over Alps (5.2 W/m<sup>2</sup> on average). Reduced amounts are shown only over Scandinavia (-0.02 W/m<sup>2</sup> on average) which are not statistically significant, in northern African coast and some pixels in Turkey.



LC2015 - LC1950

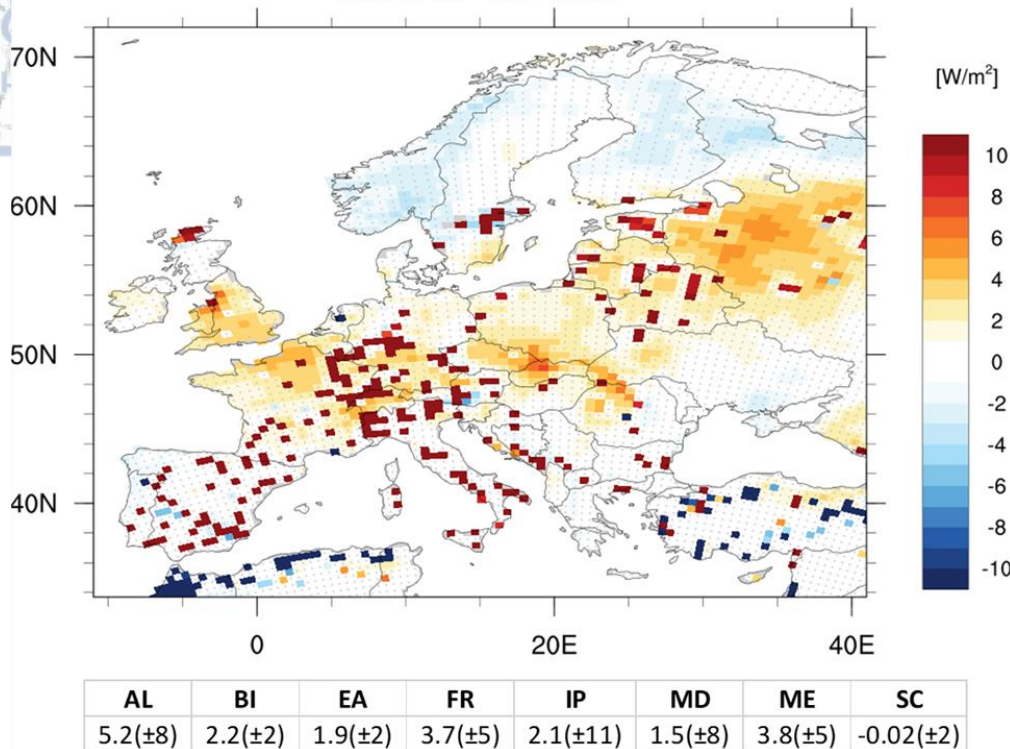


**Figure 4.7:** The impact of land cover changes (LC2015 minus LC1950) on mean daily net shortwave radiation ( $W/m^2$ ) at surface in summer for simulation period 1986-2015. The dots indicate the differences which are insignificantly different from zero in a two-sided t-test at 95% confidence level. Below the map, the differences are averaged over eight subregions. The values in parenthesis represent the standard deviation from average. The grid cells with intense red/blue color correspond to grid cells where a land cover change occurs.

The net shortwave radiation at surface arises from the difference between incoming and outgoing shortwave radiation amounts. The contribution of each component on net change is illustrated in **Figure 4.8a**, averaged on regional scale. The incoming shortwave radiation increased due to land cover changes over regions of central Europe (Alps, British Isles, Eastern Europe, France, Mid-Europe) and decreased in southern regions (Iberian Peninsula, Mediterranean) and Scandinavia. The response of incoming shortwave radiation is explained by the changes in total cloud fraction (**Figure 4.8b**). As shown, the total cloudiness is decreased over Alps, British Isles, Eastern Europe, France, Mid-Europe and increased in Iberian Peninsula, Mediterranean and Scandinavia. On the other hand, the outgoing shortwave radiation is reduced in all regions, leaving more available radiative energy at surface. The reduction of outgoing shortwave radiation is a consequence of darker surface (lower albedo) induced by land cover changes, as discussed in **Figure 4.3**. The decreased outgoing radiation amounts in combination with the increased incoming radiation explain the increased net shortwave radiation amounts in Alps, British Isles, Eastern Europe, France and Mid-Europe. In southern regions (Mediterranean, Iberian Peninsula) the net positive change is attributed to the decreased outgoing radiation amounts which offset the decreased incoming radiation flux. In Scandinavia, the net change is almost zero since the changes in outgoing and incoming radiation offset each other.

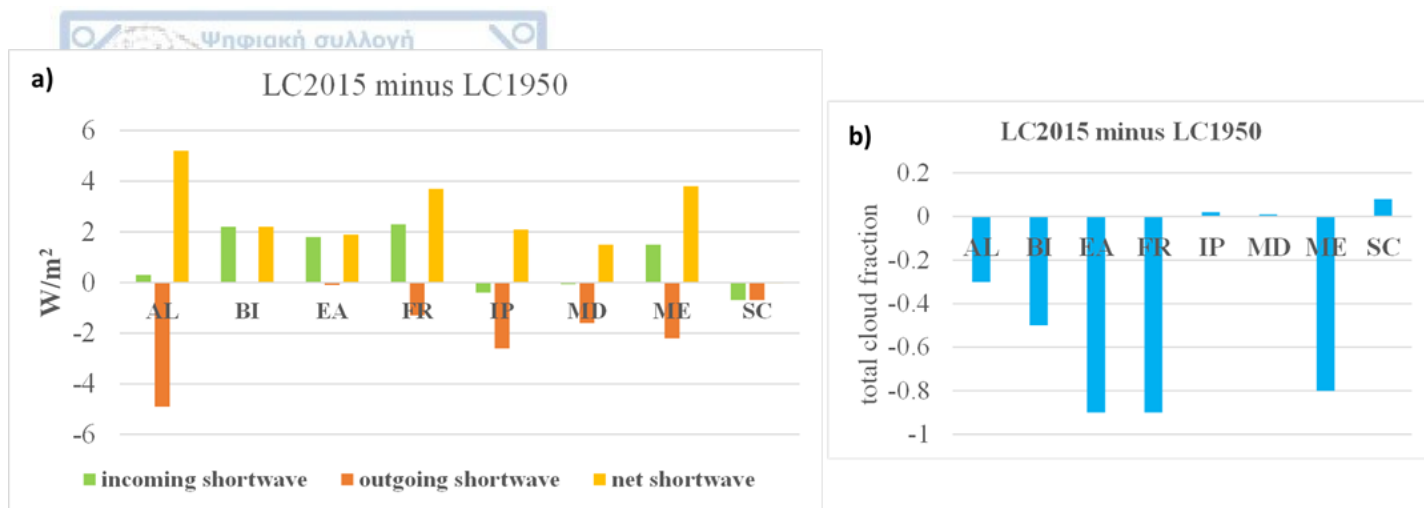


**Figure 4.8:** a) The impact of recent land cover changes (LC2015 minus LC1950) on shortwave radiation components, based on mean daily summer values and averaged over eight subregions. b) The corresponding LCC impact on total cloud fraction.

### 4.3.5 Incoming longwave radiation

The changes in downward longwave radiation have minor influence on surface temperature response to land cover change. The response of incoming longwave radiation to land cover changes (LC2015 minus LC1950) is mapped in **Figure 4.9**. The differences are small and insignificant over the largest part of the domain, ranging from  $-0.14 \text{ W/m}^2$  in Scandinavia to  $0.9 \text{ W/m}^2$  in Iberian Peninsula on average. Longwave radiation and cloudiness responses are not well correlated, in contrast to the strong corresponding link between cloud cover and shortwave radiation.

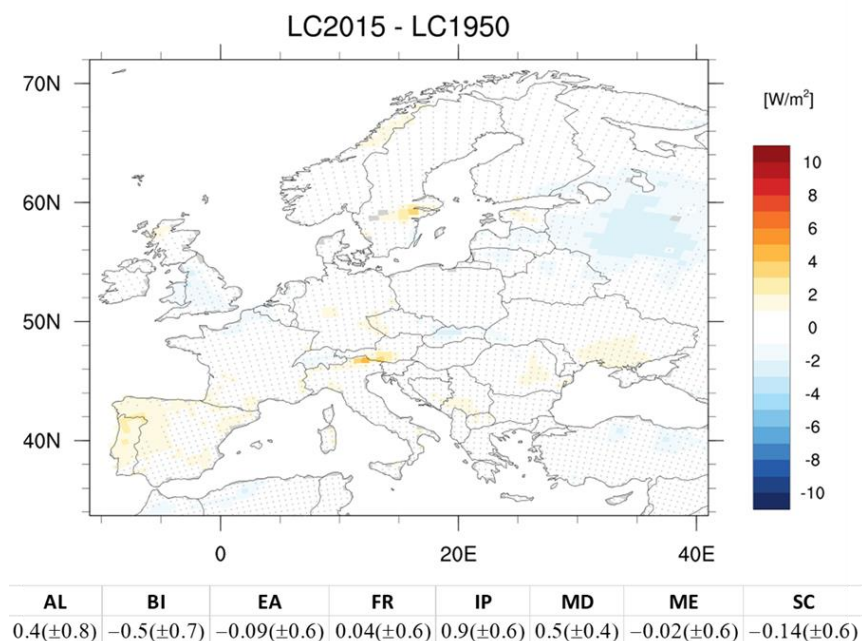


**Figure 10:** The impact of land cover changes (LC2015 minus LC1950) on downwelling longwave radiation at surface ( $\text{W/m}^2$ ) based on mean daily summer values for simulation period 1986-2015. The dots indicate the differences which are insignificantly different from zero in a two-sided t-test at 95% confidence level. Below the map, the differences are averaged over eight subregions. The values in parenthesis represent the standard deviation from average.

#### 4.3.6 Sensible heat

The differences in sensible heat flux due to land cover changes (LC2015 minus LC1950) are mapped in **Figure 4.10**. On regional scale, the sensible heat flux increases from 0.3 W/m<sup>2</sup> in Scandinavia to 4.3 W/m<sup>2</sup> in Alps. The increase of sensible heat flux towards atmosphere removes available energy from surface thus leading to a cooling that partly offset the warming induced by the increased net shortwave radiation. The reason behind the increase of sensible heat flux is likely the increase of roughness length with land cover changes, which favor the turbulent mixing and thus enhance the heat exchange between the ground and atmosphere.

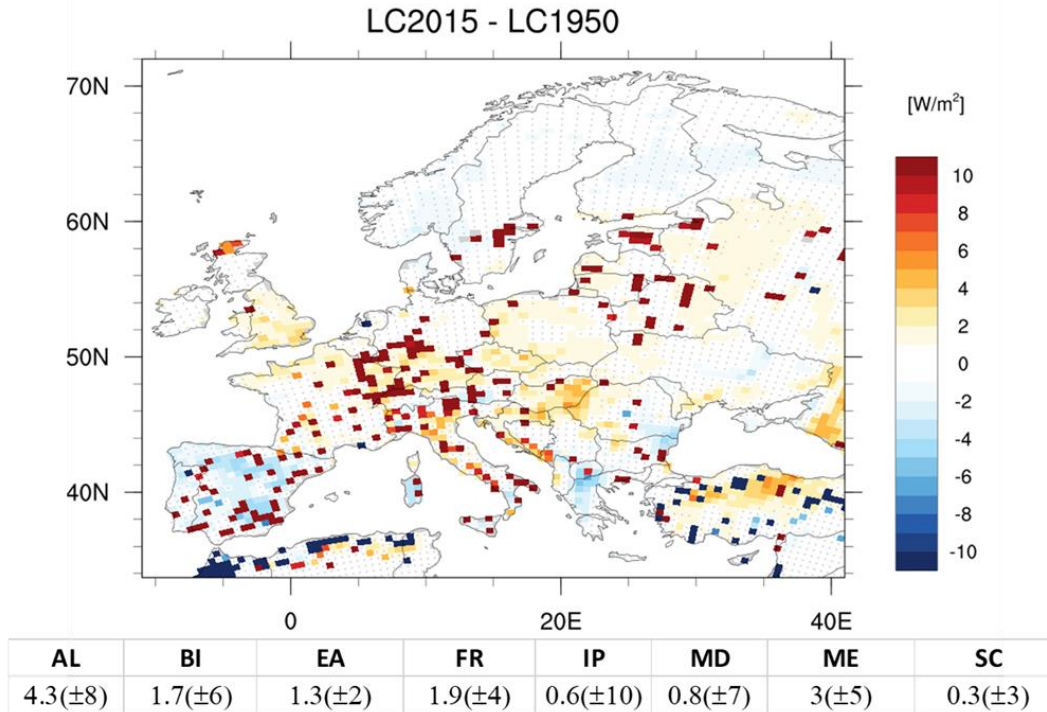


**Figure 4.10:** The impact of land cover changes (LC2015 minus LC1950) on sensible heat flux (W/m<sup>2</sup>) based on mean daily summer values for simulation period 1986-2015. The dots indicate the differences which are insignificantly different from zero in a two-sided t-test at 95% confidence level. Below the map, the differences are averaged over eight subregions. The values in parenthesis represent the standard deviation from average. The grid cells with intense red/blue color correspond to grid cells where a land cover change occurs.

#### 4.3.7 Latent heat

The sign of changes in latent heat flux due to land cover changes is spatially mixed, varying from -0.3 W/m<sup>2</sup> in Eastern Europe and Scandinavia to 1.5 W/m<sup>2</sup> over Iberian Peninsula (**Figure 4.11**). The decrease of latent heat flux in British Isles, Eastern Europe and Scandinavia contributes to the surface warming dominated by increased net shortwave amounts, while the increased latent heat flux over the remaining regions, in combination with the increased sensible heat flux, induce a cooling effect that partly offset the warming of radiative origin. Despite the positive changes in characteristics that facilitate evapotranspiration, such as the increased LAI, roughness length and available radiative energy at surface, the latent heat flux is not increased everywhere as was expected. Other

factors related to evapotranspiration, such as stomatal conductance, saturation deficit between vegetation and atmosphere (Breil et al., 2021) should be investigated in order to unveil the latent heat flux response to land cover change.

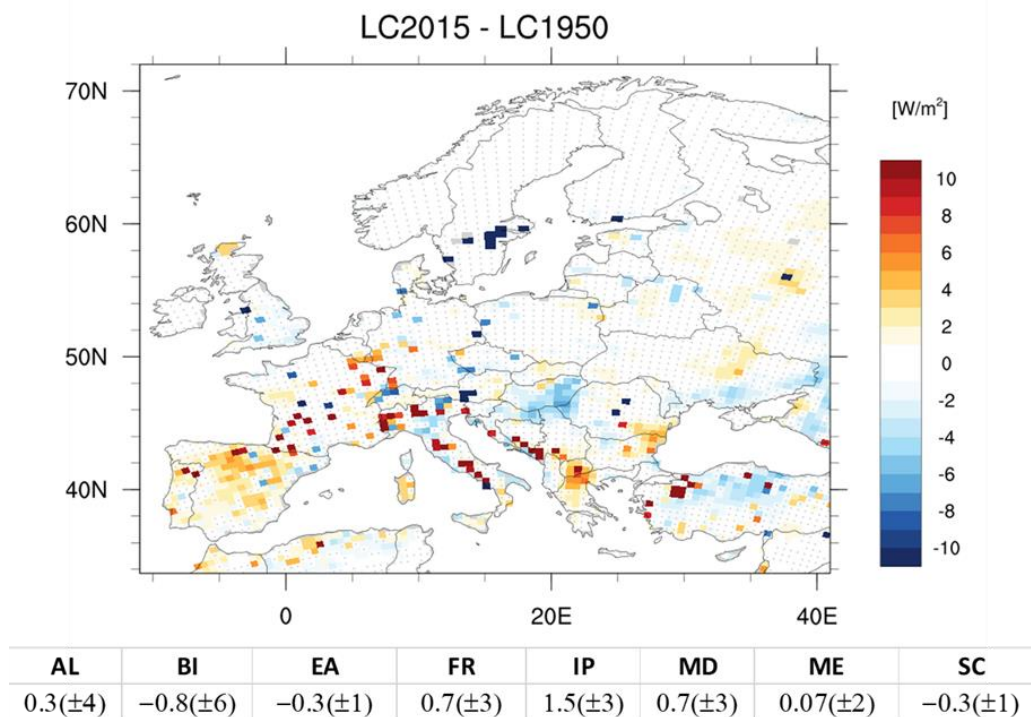
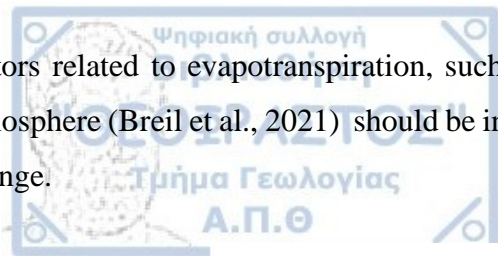


**Figure 4.11:** The impact of land cover changes (LC2015 minus LC1950) on latent heat flux ( $W/m^2$ ) based on mean daily summer values for simulation period 1986-2015. The dots indicate the differences which are insignificantly different from zero in a two-sided t-test at 95% confidence level. Below the map, the differences are averaged over eight subregions. The values in parenthesis represent the standard deviation from average. The grid cells with intense red/blue color correspond to grid cells where a land cover change occurs.

### 4.3.8 Precipitation

The impact of land cover changes on summer precipitation is mapped in **Figure 4.12**. Precipitation does not change dramatically for most of Europe. On regional scale, drier conditions are mostly seen over regions of central Europe (-0.14 mm/day in Alps, -0.12 mm/day in France, -0.14 mm/day in Mid-Europe). Over the remaining areas, the precipitation changes are not considered significant.

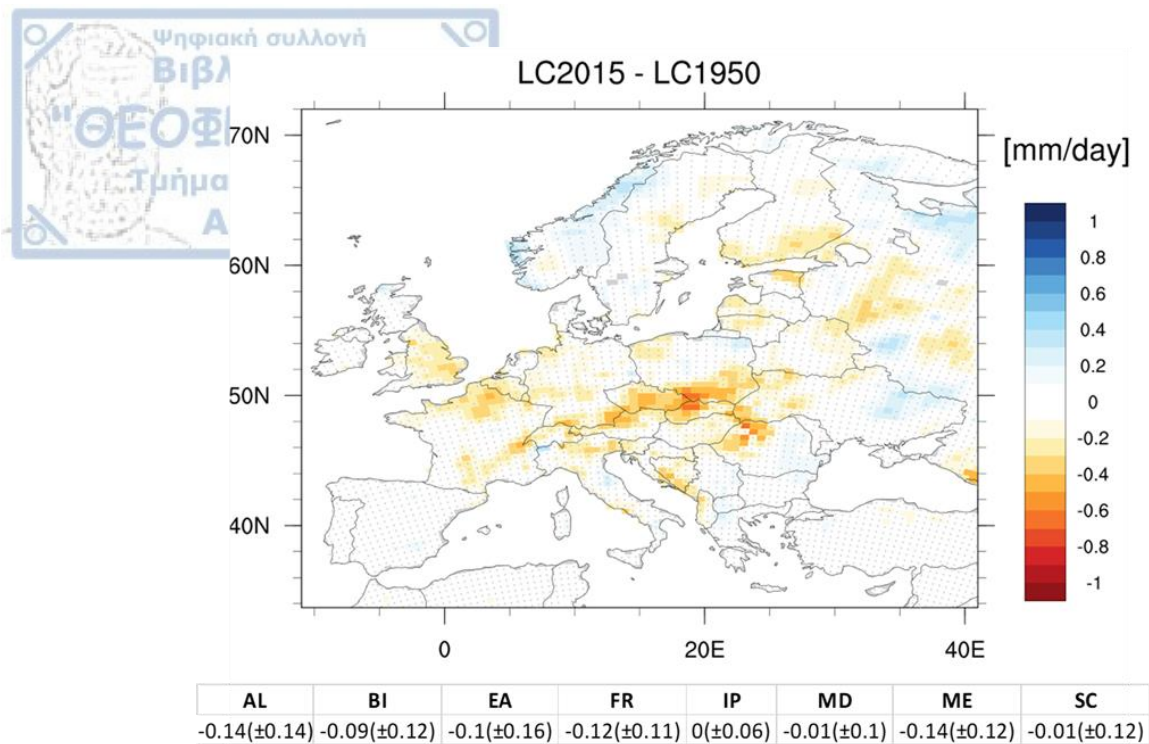


**Figure 4.12: Differences in mean summer precipitation (mm/day) for the simulation period 1986-2015 due to recent land cover changes (LC2015 minus LC1950). The dots indicate the differences which are insignificantly different from zero in a two-sided test at 95% confidence level. Below the map, the differences are averaged over the subregions. The values in parenthesis represent the standard deviation from average.**

The role of turbulent heat fluxes partitioning is probably responsible for the drier conditions over the most of Europe. Indeed, the evaporation fraction, calculated here as the ratio between latent heat and the sum of sensible and latent heat fluxes, is reduced over all subregions due to land cover changes (**Figure 4.13**). This is an implication for reduced water input to the atmosphere and consequently reduced cloudiness and precipitation. The reasons for the reduced evaporative fraction due to land cover change are beyond the scope of this analysis.

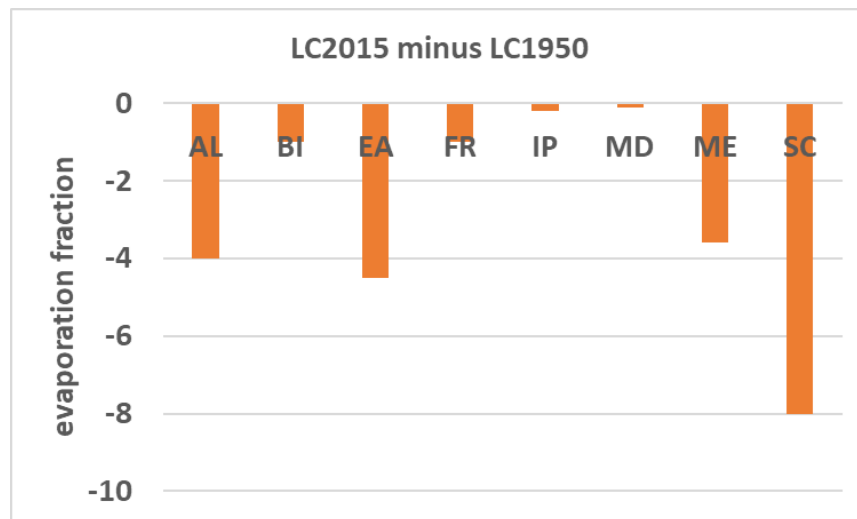


**Figure 4.13: Differences in evaporative fraction due to land cover changes (LC2015 minus LC1950), averaged over eight subregions. Evaporative fraction is calculated as the ratio between latent heat flux and the sum of sensible and latent heat fluxes.**

#### 4.3.9 2m temperature

Compared to changes in surface temperature, changes in 2m temperature may be considered more relevant for human living conditions. 2m temperature is a diagnostic quantity which is estimated at 2 meter above the surface (top of vegetation) and is obtained via a procedure based on Monin-Obhukov similarity theory that uses both the temperatures at the surface and at the lowest atmospheric model level. It could be said that 2m temperature is an interpolation between surface temperature and temperature at the lowest atmospheric model level. Breil et al., 2020 and Winckler et al., 2019 revealed opposing effects of deforestation on the surface and air temperature in climate models, thus the diagnostic calculation and use of 2m temperature in their studies could not reflect the occurring processes near the surface and consequently produced misleading conclusions for temperature response to deforestation. Thus, the sole use of the simulated 2m temperature as a metric to assess the land cover change impact on regional climate is not recommended.

Since the simulated 2m temperature is a diagnostic calculation based on surface and lowest atmospheric model level temperature ( $T_{atm}$ ), the changes in  $T_{atm}$  should be first examined. The impact of land cover changes (LC2015 minus LC1950) on mean daily cycle of  $T_{atm}$  for summer is depicted in **Figure 4.14**, averaged over eight subregions. The diurnal temperature range is increased in all regions, from 0.06 °C in Scandinavia to 0.35 °C in France, owing to increased daytime (maximum) temperature, following the pattern of changes in surface temperature. The warming effect on lowest atmospheric model level results from the increased sensible heat flux from surface towards atmosphere, as a consequence of increased surface roughness, in contrast to surface warming which has radiative origins.

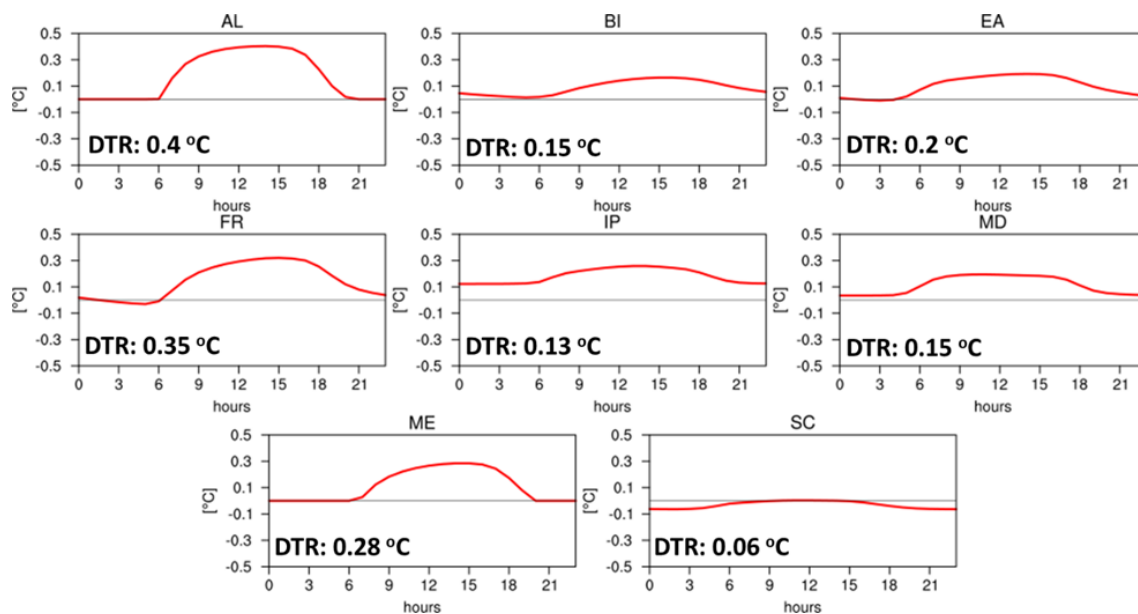


**Figure 4.14:** The impact of recent land cover changes (LC2015 minus LC1950) on daily cycle of summer temperature at the lowest atmospheric model level, averaged over eight subregions. DTR represents the effect on diurnal temperature range, which results from the difference between daily maximum and minimum temperature.

The impact of land cover changes (LC2015 minus LC1950) on daily cycle of summer 2m temperature is depicted in **Figure 4.15**, summarized over eight regions. The diurnal temperature range at 2m is increased over all regions from 0.07 °C in Scandinavia to 0.42 °C in Alps, as a result of warming effects on surface and lowest atmospheric model level.

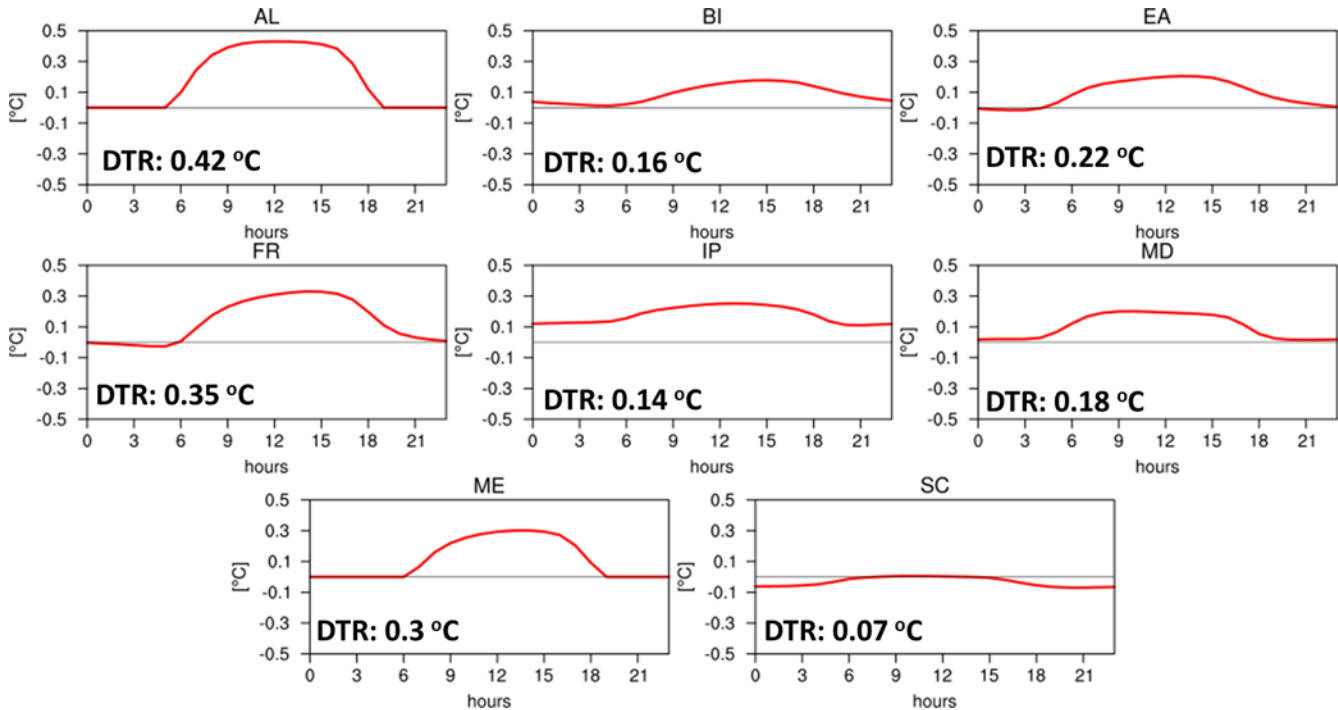
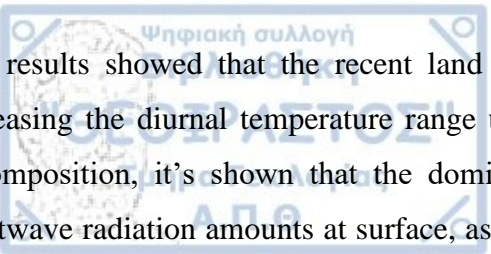


**Figure 4.15:** The impact of recent land cover changes (LC2015 minus LC1950) on daily cycle of summer 2m temperature, averaged over eight subregions. DTR represents the effect on diurnal temperature range, which results from the difference between daily maximum and minimum temperature.

The warming in WRF-NoahMP due to forest cover increase contradicts recent evidence from studies based on models and observations, which suggest that forests cause lower daytime temperatures at surface compared to open lands in mid-latitudes (Alkama and Cescatti, 2016; Breil et al., 2020; Li et al., 2015). In these studies, the temperature over forest was lower than adjacent open lands, because the increased sensible heat flux from ground to atmosphere (roughness effect) offset the radiative gain from decreased forest albedo. The same physical processes take place also in WRF-NoahMP, however the albedo values for forest tiles are somewhat high with respect to other models, as a result the roughness effect is not enough to compensate the albedo effect, leading to an increase of available energy at surface and finally a warming with afforestation.

#### 4.4 Summary

This study addressed the climate change signal in summer on regional scale due to recent land cover changes that occurred in Europe. For this purpose, two climate simulations were performed over the time period 1986-2015, the one forced with a representative land cover map of 1950 year and the other with the land cover map of 2015.



The results showed that the recent land cover changes produce warmer daytime temperatures in summer, increasing the diurnal temperature range up to 0.3 °C on average in most regions. Based on energy balance decomposition, it's shown that the dominant physical mechanism behind this warming was the increased shortwave radiation amounts at surface, as a consequence of lower surface albedo and decreased cloudiness. In parallel, a consistent increase in sensible heat flux from surface to atmosphere, due to increased roughness length, produced a warming at the lowest atmospheric model level and a cooling at surface, that partly offset the warming of radiative origin. Furthermore, summer precipitation was not significantly affected by land cover changes, showing a tendency for drier conditions mostly over regions of central Europe, probably related to a general decrease in evaporation fraction.

The simulated results show a tendency for warmer and drier conditions due to the recent land cover changes, which mostly concern the transition from open lands (croplands/grasslands) to forests and shrublands. This is rather contradictory to the evidence that increased forest cover leads to cooler climate. Observational evidence based on clusters of closely spaced eddy covariance towers located over forested areas and nearby open lands respectively, show that the surface temperature of open land is cooler than forest at night and warmer during the day at temperate zone (Lee et al., 2011; Burakowski et al., 2018). Similar results are reproduced by satellite-driven analyses based on land surface temperature differences between forests and nearby open lands (Li et al., 2015; Tang et al., 2018; Schultz et al., 2017; Alkama and Cescatti, 2016). However, the observational set-up does not resemble the experimental design applied in WRF, thus the observational evidence is not directly comparable to the current model results. The main discrepancy lies in the fact that observations capture only local temperature effects but exclude non-local effects—for example, when measurements of neighboring forests and grasslands are compared, any non-local effects cancel, because advection and atmospheric circulation affect neighboring regions similarly (Pongratz et al., 2021). Winckler et al., 2019b have shown that the non-local effect of forest loss constitutes a cooling across temperate regions, whereas the local biophysical effects lead to a warming. The temperature signal of non-local effect is dominated by changes in albedo (Bright et al., 2017), while the local temperature response is attributed to roughness change (Winckler et al., 2019b).

The present study provides evidence about the impact of recent land cover changes on regional climate, based on results from single model. However, evidence from more models at finer scales is needed in order to deliver reliable information to stakeholders for land management. In the framework of FPS LUCAS Phase 2, simulations driven by GCMs and dynamic land use changes will be performed for past and future in order to quantify the relative contribution of land use changes compared to other forcings in the detection of the past and future climate trends.



## 5 Conclusions

The present dissertation addressed the impact of land cover changes on regional climate in Europe with the use of regional climate simulations performed in the framework of LUCAS FPS. The simulations cover the 1986-2015 time period at ~50 km spatial resolution and follow the Euro-CORDEX protocol for reanalysis-driven simulations. The analysis focused on afforestation impacts, defined as the transition from open lands to forests, as it constitutes a land cover change trend that has recently emerged in developed countries and is frequently proposed as a tool to mitigate anthropogenic greenhouse gas emissions.

The study is divided into three parts. In the first part, WRF simulations within LUCAS ensemble are compared to observational datasets in order to evaluate the WRF performances for correctly simulating the physical processes. In the second part, all the simulations within LUCAS are used in order to investigate the impact of theoretical maximum afforestation across Europe on surface energy balance and soil temperature at regional level. In the last part, land cover maps for 1950 and 2015 are implemented into WRF so as to examine the effect of recent land cover changes on regional climate in Europe for the reference period 1986-2015. Below, the conclusions are reported in detail for each part of the analysis.

### 5.1 Evaluation of WRF simulations

Four WRF simulations within LUCAS ensemble were compared to gridded reference products for 2m temperature, precipitation, radiation and heat surface fluxes, cloud fraction and soil moisture. WRF simulations shared either the same atmospheric set-up coupled to different land surface model (WRFb-NoahMP, WRFb-CLM4.0) or the same land surface model with different combination of parameterization schemes for the representation of atmospheric processes (WRFa-NoahMP, WRFb-NoahMP, WRFc-NoahMP). This fact helped to understand the respective role of atmospheric and land surface processes on the model errors in the estimation of physical processes.

The analysis focused on winter and summer season. In winter, the sign of temperature bias among WRF simulations was mixed. The two WRF simulations with the same land surface model produced minor absolute biases below 1 °C and shared similar spatial bias patterns, indicating the small contribution of land processes on winter temperature simulation. The change of parameterization schemes for the representation of processes which take place within atmospheric boundary layer in WRFc-NoahMP, induced a prominent cold bias of -2 °C in Scandinavia which was attributed to the problematic estimation of skin temperature over snow-covered ground. The change of convection and microphysics scheme in WRFa-NoahMP resulted in a winter temperature overestimation which exceeded 2 °C in many regions. Moreover, winter precipitation was overestimated in all simulations except WRFa-NoahMP confirming a well-known WRF typical behavior. The WRF ensemble produced a positive bias for incoming shortwave radiation at surface in winter mostly towards the southern Europe which ranges from 9% in WRFb-CLM4.0 to 46% in WRFa-NoahMP with respect to the absolute CLARA-A2.1

estimate over Mediterranean. The overestimation of incoming shortwave radiation over the southern regions could not be associated with a general overestimation in total cloud cover in WRF simulations except for the case of WRFa-NoahMP.

In summer, the use of Grell-Freitas scheme for the representation of convection processes in WRFa-NoahMP produced a widespread dry bias across Europe which exceeded the -70 % of EOBS estimate in many regions, in combination with a large underestimation of cloud cover. As a consequence, WRFa-NoahMP overestimated the amounts of incoming shortwave radiation at surface in summer and showed warm biases across Europe which reached the 7 °C over Alps. The switch from Grell-Freitas to Kain-Fritsch scheme strongly improved the results for WRFb-NoahMP, however strong dry biases remained mostly over France, Iberian Peninsula and Alps. The underestimation of summer precipitation over these regions induced dry soils which limited the latent heat flux and enhanced sensible heat and thus reduced water input to the atmosphere and subsequent cloud cover. As a result, WRFb-NoahMP overestimated the incoming shortwave radiation and suffered from warm biases of more than 2 °C in Alps, France and Iberian Peninsula, mostly due to warmer maximum temperatures in late summer. The warm and dry biases are strongly alleviated in WRF coupled to CLM4.0, owing to a better representation of groundwater which improved the heat fluxes partitioning at surface in late summer. The change of PBL scheme in WRFc-NoahMP also improved the heat fluxes partitioning in Alps, France and Mid-Europe resulting in better results for summer temperature and precipitation compared to WRFb-NoahMP, however induced wetter than observed conditions in Eastern Europe. The fact that the overestimation of sensible heat flux and underestimation of latent heat is a robust feature among simulations, despite their different set-ups, highlights the WRF deficiency in estimating the turbulent heat fluxes partitioning across Europe. This fact is probably related to underestimated cloud cover and overestimated incoming shortwave radiation at surface over the southern regions of Europe, which is another robust feature among simulations and finally leads to a tendency for warmer and drier than observed conditions.

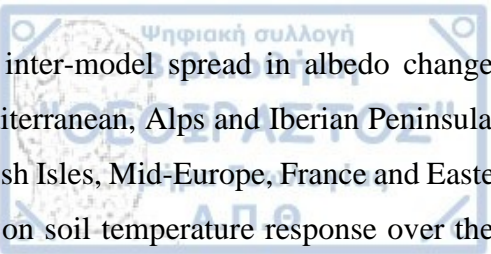
A quantitative estimate of overall performance for all simulations of ensemble based on RMSE scores which account for the entire domain over the full simulation period, showed that there is no ideal configuration that optimizes WRF performance for all climate variables. WRFa-NoahMP configuration achieved the worst performance among WRF simulations and the whole LUCAS ensemble. WRFb-CLM4.0 outperformed WRFb-NoahMP for temperature, shortwave radiation, sensible and latent heat but degraded the quality for longwave component and precipitation. WRFb-NoahMP and WRFc-NoahMP almost cluster together in terms of ranking. WRFb-NoahMP has somewhat better scores than WRFc-NoahMP for temperature, precipitation and shortwave radiation while WRFc-NoahMP outperforms WRFb-NoahMP for heat fluxes and longwave component.

## 5.2 Afforestation impact on soil temperature in Europe

In chapter 2, all LUCAS models performed two simulations with idealized land cover in which Europe is represented as fully covered by forests (FOREST experiment) or grasslands (GRASS experiment) respectively. FOREST minus GRASS differences were considered in order to investigate the impact of theoretical maximum afforestation on surface energy balance and soil temperature across Europe at regional level.

The afforestation impact on annual amplitude of soil temperature (AAST) at 1m below the ground varies from -7 °C to +2 °C across regions depending on model. The choice of land surface model drives in a great extent the sign of change in AAST while the choice of atmospheric component further modulates the magnitude of the signal. The changes in AAST originate from changes in summer temperatures. In winter, the soil temperature differences due to afforestation are small in the majority of simulations and with a tendency towards an increase. Over Mediterranean, the simulations which shared a version of CLM LSM, VEG3D and TERRA-ML showed a decrease in summer soil temperature with afforestation which ranges from -1 °C in WRFb-CLM4.0 to more than -4 °C in CCLM-TERRA. On the other hand, the AAST increased in all WRF-NoahMP simulations, mostly in WRFa-NoahMP where the increase was close to 2 °C. REMO-iMOVE showed a year-round increase smaller than 1 °C. In Scandinavia, REMO-iMOVE together with all WRF modelling systems exhibit a small constant warming in almost all seasons. The ensemble around CCLM model provided largely different results. CCLM-TERRA and CCLM-VEG3D exhibit large soil temperature decreases in summer which are close to -9 °C for CCLM-VEG3D. CCLM-CLM4.5 showed small changes in all seasons with a tendency for decrease in summer, similar to RegCM4.5, while the sign of changes in CCLM-CLM5.0 turns from negative in upper soil layers to positive in deeper layers.

The spatial pattern of changes in AAST correlates well with changes in available energy to warm the ground in summer or the residual of surface energy balance, thus it's considered crucial to explore the origin of inter-model spread in surface energy balance changes. In all regions, models consistently show a systematic increase of net shortwave radiation at surface due to afforestation, as a result of lower albedo of forests compared to grasslands. The increase in available radiative energy at the surface is followed by an increase in sensible heat flux, which is another robust feature among simulations and is attributed to increased roughness length with afforestation which favor the mixing of atmospheric boundary layer and thus enhance the heat exchange between ground and atmosphere. In CCLM simulations and RegCM-CLM4.5, the increase of net shortwave radiation was offset by the increase of sensible heat flux therefore afforestation induced a decrease in available energy to warm the ground and finally a summer cooling in soil temperatures. On the other hand, the increase of net shortwave radiation was more intense in NoahMP simulations due to stronger decreases in surface albedo and partly due to decreased cloud cover in Scandinavia. The increased available radiative energy at surface was stronger than the increased sensible heat and thus NoahMP simulations exhibit an increase of surface energy input into the ground with afforestation and finally a warming of soil temperatures.



The inter-model spread in albedo changes due to afforestation regulate the simulated AAST response over Mediterranean, Alps and Iberian Peninsula. The albedo effect has also strong influence on AAST response over British Isles, Mid-Europe, France and Eastern Europe, however the changes in cloud fraction have the dominating role on soil temperature response over the regions of central Europe. In Scandinavia, the largest part of inter-model variance in AAST response is explained by changes in leaf area index. When the changes in albedo, cloud fraction, leaf area index and soil moisture are all combined into a linear equation and regressed against the simulated AAST response, they explain more than 80% of inter-model variance in all regions. Despite the key role of soil wetness on soil thermal conditions, the changes in soil moisture did not strongly influence the soil temperature response to afforestation. Afforestation induced a widespread soil drying due to transpiration-facilitating forest characteristics, such as big leaf area and deep roots, which remove available water from deeper soil layers.

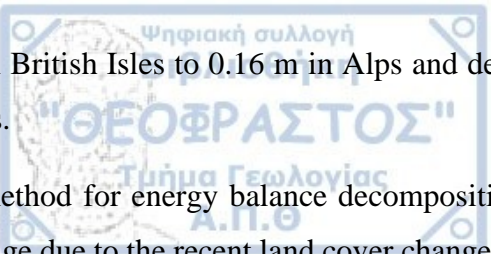
Neighboring sites from FLUXNET network located in forests and open lands paired in order to extract the afforestation effect on soil temperature from observational evidence. Observations showed that the mean annual soil temperature cycle is smaller by almost 3 °C in forests compared to open lands, due to cooler summer temperatures. In line with observational signal, seven out of the ten RCMs showed a mean AAST decrease from -5 °C to -0.2 °C.

### **5.3 The effect of recent land cover changes on regional climate in Europe**

In chapter 3, an evaluated WRF-NoahMP configuration is used to perform two simulations with realistic land cover maps for 1950 (LC1950 experiment) and 2015 (LC2015 experiment) years covering the reference period 1986-2015. LC1950 and LC2015 differ only in land cover input thus the differences LC2015 minus LC1950 imply the potential effect of recent land cover changes on the regional climate of 1986-2015 period in Europe. The analysis focused only on summer season, since the winter climate sensitivity is small even to extreme land cover changes.

A widespread decline of agricultural lands is seen in most of Europe. Especially over Eastern Europe, more than 100,000 km<sup>2</sup> of farmlands abandoned between 1950 and 2015 which is associated with a combination of socio-economic, political and environmental factors. In Eastern Europe the greatest part of croplands was transformed into grasslands, but in many areas a large part of croplands was replaced by forests. Forests generally increased across Europe as did urban areas. Also, the shrublands expanded at the expense of agricultural lands, mostly over Iberian Peninsula, Mid-Europe and France. Wetlands, bare lands and lands with sparse vegetation were not significantly affected.

The recent land cover changes increased the leaf area index across Europe in WRF-NoahMP from 0.002 m<sup>2</sup>/m<sup>2</sup> over British Isles to 0.25 m<sup>2</sup>/m<sup>2</sup> in Alps on average. They also increased the surface roughness length from 0.01



m in British Isles to 0.16 m in Alps and decreased the surface albedo by -0.03 in Eastern Europe up to -0.28 in Alps.

A method for energy balance decomposition was followed in order to extract the sign of surface temperature change due to the recent land cover changes and quantify the importance of underlying biophysical mechanisms. The results exhibited a tendency for summer warming mostly over the southern Europe which was close to 0.15 °C in Alps and Iberian Peninsula at regional level, while the northern Europe was not significantly affected by land cover change. The mean diurnal temperature cycle was increased in all subregions from 0.04 °C in Iberian Peninsula to 0.36 °C in Mid-Europe due to warmer maximum temperatures.

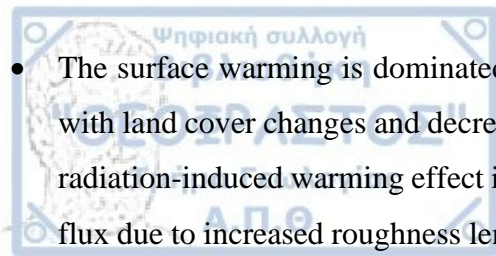
The dominant mechanism that explains the summer warming is the increase of net shortwave radiation which alone induce a surface warming up to 1 °C in Alps. The increase of available radiative energy at surface is attributed to a generally decreased albedo with land cover changes and decreased cloud cover over British Isles, Mid-Europe, France, Eastern Europe and Alps. The radiation-induced warming is partly offset by a cooling effect induced by increased sensible heat flux, which transfers thermal energy from surface to atmosphere and is likely related to increased surface roughness with land cover changes. Furthermore, latent heat flux decreased in British Isles, Eastern Europe and Scandinavia thus contributing to the warming effect of radiative origin, whereas the increased latent heat amounts in the remaining regions contributed to the cooling effect induced by increased sensible heat amounts.

Land cover changes did not dramatically change summer precipitation. A tendency for drier conditions is mostly seen over regions of central Europe reaching up to -0.14 mm/day in Alps and Mid-Europe. The drier conditions are probably related to a general reduced evaporation fraction across Europe, which imply reduced water input to atmosphere and thus less water available for cloud formulation and precipitation.

The increased transmission of thermal energy from ground to atmosphere in the form of sensible heat flux increased the summer temperature at the lowest atmospheric model level, amplifying the diurnal temperature range up to 0.35 °C in France. The diurnal 2m temperature cycle is also increased up to 0.42 °C in Alps due to land cover changes, since it's a diagnostic quantity based on surface and lowest atmospheric model level temperature.

## 5.4 Key remarks

- The use of Grell-Freitas scheme for the representation of convection processes strongly degrades the WRF performance producing large warm and dry biases across Europe.
- The change from Grell-Freitas to Kain-Fritsch scheme improves the quality of simulation, however considerable dry summer biases remain mainly over Alps, France and Mid-Europe in combination with warm biases of more than 2 °C mostly due to overestimated maximum temperatures in late summer. The latter fact is related to excess amounts of sensible heat which suppress the latent heat flux and thus reduce the water input to atmosphere and the subsequent cloud cover, as a result larger than observed amounts of shortwave radiation reach the surface.
- The warm and dry biases in summer are largely alleviated when WRF is coupled to CLM4 LSM due to a better groundwater representation which improves the estimation the turbulent heat fluxes partitioning in late summer.
- The warm and dry summer biases were also reduced over Alps, France and Mid-Europe with the switch from MYNN to YSU PBL scheme, which improved the estimation of turbulent heat fluxes partitioning but produced wetter than observed conditions in Eastern Europe.
- The increased net shortwave radiation at surface, due to lower albedo, and increased sensible heat flux, due to rougher surface, are the most robust model responses to afforestation. The balance between these two biophysical consequences largely depends on LSM choice.
- Simulations with TERRA-ML, VEG3D or version of CLM LSM exhibit cooler soil temperatures due to afforestation in summer, because the increased net shortwave radiation was offset by the increased sensible heat flux, whereas the opposite is true for NoahMP simulations.
- Soil drying with afforestation is another robust models' feature which is attributed to transpiration-facilitating forest characteristics which remove available water from deeper soil layers. However, soil moisture has not a dominating role on soil temperature response to afforestation.
- When changes in surface albedo, cloud fraction, leaf area index and soil moisture are all combined into a linear regression equation, largely explain the inter-model spread in AAST response.
- Evidence from observations showed that ground under forests is cooler by almost 3 °C on average in summer with respect to open lands. This view is supported by seven out the ten ensemble members with a range from -5 °C to -0.2 °C.
- Recent land cover changes in Europe involve widespread abandonment of agricultural lands and expansion of urban areas, shrublands and forests. Among the main biophysical consequences were an increased leaf area index and surface roughness and decreased surface albedo.
- The recent land cover changes amplified the diurnal temperature cycle at surface in summer in all regions reaching up to 0.36 °C in Mid-Europe, due to a warming of maximum temperatures.



- The surface warming is dominated by increased net shortwave radiation at surface due to lower albedo with land cover changes and decreased cloud fraction in British Isles, Mid-Europe, France and Alps. The radiation-induced warming effect is partly offset by a cooling effect resulted from increased sensible heat flux due to increased roughness length. The removal of thermal energy from surface towards atmosphere in the form of sensible heat flux, amplified the diurnal temperature range at the lowest atmospheric model level in summer.
- A tendency for drier atmospheric conditions is seen mostly over regions of central Europe related to reduced evaporation fraction with land cover changes, which implies less water available for cloud formulation and precipitation.



## Abstract

This dissertation addressed the biophysical effects of land cover changes on regional climate in Europe. To this aim, WRF simulations were performed in the framework of FPS LUCAS which covered the 1986-2015 time period at ~ 50 km spatial resolution following the Euro-CORDEX protocol for reanalysis-driven simulations. The analysis focused on afforestation impacts, defined as the transition from open lands to forests, as it constitutes a land cover change trend that has recently emerged in developed countries and is frequently proposed as a tool to mitigate anthropogenic greenhouse gas emissions.

The dissertation divided into three parts. The first part addresses the ability of WRF simulations, which share different configurations for the representation of atmospheric and land surface processes, to correctly simulate the observational spatial and temporal climate patterns. The results showed that there is no ideal configuration that optimizes WRF performance for all climate variables in all regions across Europe. One model configuration was found to dramatically degrade WRF performance, producing extremely warm and dry biases over a large part of the model domain. The other three WRF configurations showed a balanced overall behavior and despite their different set-ups they shared some robust features, such as a wet bias in winter and problematic estimation of turbulent heat fluxes partitioning in summer, which yielded excess sensible heat amounts towards atmosphere. This overestimation was the reason for warmer and drier summer conditions than observed, mostly over regions of central and southern Europe.

In the second part, the LUCAS models are forced with idealized land cover maps which represent Europe as fully covered by forests and grasslands respectively, in order to examine the climatic effect of maximum afforestation on surface energy balance and soil temperature at regional level. Two robust biophysical responses to afforestation were common in all simulations. One was the increased available radiative energy at surface due to lower albedo in forests and second was the increased sensible heat flux from ground towards atmosphere due to rougher forest surface which facilitates the mixing of lower atmospheric layer. The magnitude of the afforestation effect on net radiation and heat flux was differently pronounced across models. In six out of ten RCMs of the ensemble, the increased radiative energy at surface was offset by the increased heat flux towards atmosphere and thus simulated a decrease in available energy to warm the ground with afforestation and finally a reduction in summer soil temperature, while the opposite was true for the other four modelling systems. Observational evidence from paired FLUXNET sites showed that the ground is cooler under forests in summer with respect to open lands, in agreement with the majority of simulations.

In the third part, two realistic land cover maps for 1950 and 2015 years are implemented into WRF in order to investigate the climate change signal from recent land cover changes in Europe. The results revealed a widespread abandonment of croplands in Europe which largely converted to forests and partly to shrublands, in addition to urban sprawling trend. The land cover changes induced an increase in leaf area index and surface roughness and



decreased surface albedo. The decreased albedo induced an increase in net shortwave radiation amounts at surface while the increased roughness resulted in surface energy loss due to increased sensible heat flux from surface to atmosphere. The increase in net shortwave radiation was larger than the increased sensible heat flux and finally the sign of temperature change due to recent land cover changes was positive in most regions. The daily temperature cycle was increased by up to 0.36 °C in Alps and France, due to warmer maximum temperatures. Moreover, the results indicated a tendency for drier summer conditions due to land cover changes, which was attributed to lower evaporation rates and thus reduced water input to atmosphere.

## Περίληψη

Η διδακτορική διατριβή αφορά τις βιοφυσικές επιπτώσεις των αλλαγών κάλυψης γης στο περιοχικό κλίμα της Ευρώπης. Με αυτόν το σκοπό, διεξήχθησαν κλιματικές προσομοιώσεις με το μοντέλο WRF στο πλαίσιο δράσης του πιλοτικού προγράμματος LUCAS, που κάλυψαν την χρονική περίοδο 1986-2015 με χωρική ανάλυση περίπου 50 χλμ ακολουθώντας το πρωτόκολλο του Euro-CORDEX για προσομοιώσεις οδηγούμενες από δεδομένα επανάλυσης. Η εργασία επικεντρώνεται στις επιπτώσεις της δάσωσης/αναδάσωσης, η οποία ορίζεται ως η μετάβαση από εκτάσεις ανοικτής γης σε δάση, καθώς αποτελεί μία τάση που έχει προκύψει πρόσφατα στις αναπτυσσόμενες χώρες και συχνά προτείνεται ως εργαλείο μετριασμού των ανθρωπογενών θερμοκηπιακών αερίων.

Η μελέτη χωρίζεται σε τρεις ενότητες. Στην πρώτη ενότητα, αξιολογείται η ικανότητα των WRF προσομοιώσεων, οι οποίες χρησιμοποιούν διαφορετικά σχήματα παραμετροποίησης για να περιγράψουν τις ατμοσφαιρικές και εδαφικές κλιματικές διεργασίες, να προσομοιώσουν σωστά τα παρατηρούμενα χωρικά και χρονικά κλιματικά μοτίβα. Τα αποτελέσματα έδειξαν δεν υπάρχει ιδανικό σύνολο σχημάτων παραμετροποίησης που να βελτιστοποιεί την επίδοση του WRF για όλες τις μεταβλητές σε όλες τις περιοχές. Μία προσομοίωση βρέθηκε να υποβαθμίζει δραματικά την επίδοση του WRF, παράγοντας υψηλότερες θερμοκρασίες και ξηρότερες συνθήκες από τις πραγματικές σε μεγάλο μέρος της Ευρώπης. Οι υπόλοιπες προσομοιώσεις έδειξαν πιο ισορροπημένη επίδοση και παρά τις διαφορές τους στα σχήματα παραμετροποίησης εμφάνισαν κοινά χαρακτηριστικά, όπως την υπερεκτίμηση βροχής τον χειμώνα και την προβληματική εκτίμηση στον λόγο των θερμικών ροών το καλοκαίρι, που προκάλεσε υπερεκτίμηση στα ποσά μετάδοσης της αισθητής θερμότητας από το έδαφος στην ατμόσφαιρα. Το τελευταίο σφάλμα ήταν η αιτία για την προσομοίωση θερμότερων και ξηρότερων από των πραγματικών καλοκαιρινών συνθηκών, κυρίως πάνω από τις περιοχές της κεντρικής και νότιας Ευρώπης.

Στο δεύτερο μέρος, δύο ιδεατοί χάρτες που απεικονίζουν την Ευρώπη ως πλήρως καλυμμένη είτε από δάση ή από γρασίδι ενσωματώνονται στα μοντέλα του LUCAS, ώστε να εξεταστούν οι επιπτώσεις της μέγιστης θεωρητικής αναδάσωσης στο ενεργειακό ισοζύγιο της επιφάνειας και τη θερμοκρασία εδάφους. Δύο βιοφυσικές συνέπειες προέκυψαν σε όλες τις προσομοιώσεις λόγω της αναδάσωσης. Μία ήταν η αύξηση στη συσσώρευση ενέργειας στην επιφάνεια λόγω της μικρότερης ανακλαστικότητας των δασών στην ηλιακή ακτινοβολία και

δεύτερον η αύξηση στη μετάδοση αισθητής θερμότητας από την επιφάνεια στην ατμόσφαιρα λόγω της τραχείας επιφάνειας των δασών που ευνοεί την ανάμειξη του κατώτερου ατμοσφαιρικού στρώματος. Το μέγεθος της επίδρασης στις δύο αναφερόμενες βιοφυσικές διαδικασίες ήταν διαφορετικό ανάμεσα στα μοντέλα. Σε έξι από τα δέκα μοντέλα, το ενεργειακό απόθεμα στην επιφάνεια λόγω ακτινοβολίας αντισταθμίστηκε από την απώλεια ενέργειας μέσω αισθητής θερμότητας με αποτέλεσμα τη μείωση της διαθέσιμης ενέργειας για τη θέρμανση του εδάφους και συνεπώς τη μείωση της θερμοκρασίας του εδάφους, ενώ τα αντίθετα συνέβησαν στα υπόλοιπα τέσσερα μοντέλα. Ενδείξεις από σταθμούς FLUXNET έδειξαν ότι το έδαφος κάτω από δάση είναι πιο κρύο σε σχέση με το έδαφος καλυμμένο από γρασίδι, σε συμφωνία με την πλειοψηφία των προσομοιώσεων.

Στην τρίτη ενότητα, δύο πραγματικοί χάρτες κάλυψης του εδάφους για τα έτη 1950 και 2015 ενσωματώνονται στο WRF προκειμένου να ερευνηθεί το σήμα της κλιματικής αλλαγής από τις πρόσφατες αλλαγές στις χρήσεις γης στην Ευρώπη. Τα αποτελέσματα έδειξαν μία εκτεταμένη εγκατάλειψη καλλιεργήσιμων και χερσαίων εκτάσεων στην Ευρώπη οι οποίες μετατράπηκαν σε δάση και εν μέρει σε θαμνώδεις εκτάσεις, ενώ παρατηρήθηκε και αστική εξάπλωση. Οι αλλαγές στη χρήση γης προκάλεσαν αύξηση στο δείκτη φυλλικής περιοχής και στην τραχύτητα της επιφάνειας και μείωση στην ανακλαστικότητα της επιφάνειας στην ηλιακή ακτινοβολία (albedo). Η μείωση στην ανακλαστικότητα επέφερε αύξηση στα ποσά ηλιακής ακτινοβολίας στο έδαφος ενώ η αύξηση στην τραχύτητα της επιφάνειας προκάλεσε ενεργειακή απώλεια μέσω της αυξημένης μετάδοσης αισθητής θερμότητας στην ατμόσφαιρα. Ωστόσο, η αύξηση στο ενεργειακό απόθεμα λόγω ακτινοβολίας ήταν μεγαλύτερη από την απώλεια ενέργειας λόγω μετάδοσης της αισθητής θερμότητας με αποτέλεσμα οι αλλαγές στις χρήσεις γης να προκαλέσουν θέρμανση στις περισσότερες περιοχές. Το μέσο ημερήσιο θερμομετρικό εύρος αυξήθηκε μέχρι 0.36 βαθμούς Κελσίου στις Άλπεις και την Γαλλία, το οποίο αποδίδεται στην αύξηση των μέγιστων θερμοκρασιών. Επιπρόσθετα, τα αποτελέσματα αποκάλυψαν μία τάση για ξηρότερες συνθήκες το καλοκαίρι εξαιτίας των αλλαγών στις χρήσεις γης μεταξύ 1950-2015, το οποίο αποδόθηκε στη μείωση του ρυθμού εξάτμισης και συνεπώς της μεταφοράς υδρατμών από το έδαφος στην ατμόσφαιρα.

## Acknowledgements

I must express my gratitude to Dr. Eleni Katragkou, my supervisor, for the patient guidance, encouragement and advice she has provided throughout my time as her student. I have been extremely lucky to have a supervisor who cared so much about my work, and who responded to my questions and queries so promptly. Her guidance and support have been instrumental in helping me achieve so much personal and professional growth during that time.

I would like also to thank Dr. Diana Rechid and Dr. Edouard L. Davin for their contribution to the progress of my doctoral dissertation and our inspiring meetings in the framework of LUCAS FPS. Special thanks to Prof. Edouard L. Davin for the warm hospitality he offered me at Department of Environmental Systems Science, Institute for Atmosphere and Climate at ETH Zurich and his valuable and decisive guidance in my PhD.

I sincerely thank the Seven-Member Committee of the public defense of my doctoral dissertation for the effort and time they devoted to examine my manuscript. I am grateful to Prof. Theodore Karacostas and Prof. Prodromos Zanis for our interaction during my studies in the department of Meteorology & Climatology, School of Geology, at the Aristotle University of Thessaloniki.

My daily life during my doctoral studies would have been very difficult if there were not three wonderful friends and collaborators by my side, Maria, Vasilis and Stergios. I thank them for their support, patience and tolerance.

The author acknowledges the support of the Greek Research and Technology Network (GRNET) High Performance Computing (HPC) infrastructure that provided the computational resources necessary for the model simulations (under project IDs pr005025 and pr007033\_thin). The author also acknowledges the IT center of the Aristotle University of Thessaloniki and its HPC infrastructure.



The research work was supported by the Hellenic Foundation for Research and Innovation (HFRI) under the HFRI PhD Fellowship grant (fellowship no. 1359).

## References

- Alcantara, C., Kuemmerle, T., Baumann, M., Bragina, E. V., Griffiths, P., Hostert, P., Knorn, J., Müller, D., Prishchepov, A. V., Schierhorn, F., Sieber, A., and Radeloff, V. C.: Mapping the extent of abandoned farmland in Central and Eastern Europe using MODIS time series satellite data, *Environ. Res. Lett.*, 8, 035035, <https://doi.org/10.1088/1748-9326/8/3/035035>, 2013.
- Alkama, R. and Cescatti, A.: Biophysical climate impacts of recent changes in global forest cover, *Science*, 351, 600–604, <https://doi.org/10.1126/science.aac8083>, 2016.
- Arino, O., Bicheron, P., Frédéric, A., Latham, J., Witt, R., and Weber, J.-L.: GLOBCOVER: the most detailed portrait of Earth, *European Space Agency Bulletin*, 2008, 24–31, 2008.
- Arora, V. K. and Montenegro, A.: Small temperature benefits provided by realistic afforestation efforts, *Nature Geosci*, 4, 514–518, <https://doi.org/10.1038/ngeo1182>, 2011.
- Babar, B., Graversen, R., and Boström, T.: Evaluating CM-SAF solar radiation CLARA-A1 and CLARA-A2 datasets in Scandinavia, *Solar Energy*, 170, 76–85, <https://doi.org/10.1016/j.solener.2018.05.009>, 2018.
- Bartholomé, E. and Belward, A. S.: GLC2000: a new approach to global land cover mapping from Earth observation data, *International Journal of Remote Sensing*, 26, 1959–1977, <https://doi.org/10.1080/01431160412331291297>, 2005.
- Bastin, J.-F., Finegold, Y., Garcia, C., Mollicone, D., Rezende, M., Routh, D., Zohner, C. M., and Crowther, T. W.: The global tree restoration potential, *Science*, 365, 76–79, <https://doi.org/10.1126/science.aax0848>, 2019.
- Belušić, D., Fuentes-Franco, R., Strandberg, G., and Jukimenko, A.: Afforestation reduces cyclone intensity and precipitation extremes over Europe, *Environ. Res. Lett.*, 14, 074009, <https://doi.org/10.1088/1748-9326/ab23b2>, 2019.
- Betts, R. A.: Offset of the potential carbon sink from boreal forestation by decreases in surface albedo, *Nature*, 408, 187–190, <https://doi.org/10.1038/35041545>, 2000.
- Bonan, G. B.: Forests and Climate Change: Forcings, Feedbacks, and the Climate Benefits of Forests, *Science*, 320, 1444–1449, <https://doi.org/10.1126/science.1155121>, 2008.
- Bonan, G. B.: Forests, Climate, and Public Policy: A 500-Year Interdisciplinary Odyssey, *Annual Review of Ecology, Evolution, and Systematics*, 47, 97–121, <https://doi.org/10.1146/annurev-ecolsys-121415-032359>, 2016.
- Bonan, G. B., Pollard, D., and Thompson, S. L.: Effects of boreal forest vegetation on global climate, *Nature*, 359, 716–718, <https://doi.org/10.1038/359716a0>, 1992.
- Boysen, L. R., Brovkin, V., Pongratz, J., Lawrence, D. M., Lawrence, P., Vuichard, N., Peylin, P., Liddicoat, S., Hajima, T., Zhang, Y., Rocher, M., Delire, C., Séférian, R., Arora, V. K., Nieradzik, L., Anthoni, P., Thiery, W., Laguë, M. M., Lawrence, D., and Lo, M.-H.: Global climate response to idealized deforestation in CMIP6 models, *Biogeosciences*, 17, 5615–5638, <https://doi.org/10.5194/bg-17-5615-2020>, 2020.
- Breil, M., Schädler, G., and Laube, N.: An Improved Soil Moisture Parametrization for Regional Climate Simulations in Europe, *Journal of Geophysical Research: Atmospheres*, 123, 7331–7339, <https://doi.org/10.1029/2018JD028704>, 2018.
- Breil, M., Rechid, D., Davin, E. L., Noblet-Ducoudré, N. de, Katragkou, E., Cardoso, R. M., Hoffmann, P., Jach, L. L., Soares, P. M. M., Sofiadis, G., Strada, S., Strandberg, G., Tölle, M. H., and Warrach-Sagi, K.: The Opposing

Effects of Reforestation and Afforestation on the Diurnal Temperature Cycle at the Surface and in the Lowest Atmospheric Model Level in the European Summer, *Journal of Climate*, 33, 9159–9179, <https://doi.org/10.1175/JCLI-D-19-0624.1>, 2020.

Breil, M., Davin, E. L., and Rechid, D.: What determines the sign of the evapotranspiration response to afforestation in European summer?, *Biogeosciences*, 18, 1499–1510, <https://doi.org/10.5194/bg-18-1499-2021>, 2021.

Bright, R. M., Davin, E., O'Halloran, T., Pongratz, J., Zhao, K., and Cescatti, A.: Local temperature response to land cover and management change driven by non-radiative processes, *Nature Clim Change*, 7, 296–302, <https://doi.org/10.1038/nclimate3250>, 2017.

Broucke, S. V., Luysaert, S., Davin, E. L., Janssens, I., and Lipzig, N. van: New insights in the capability of climate models to simulate the impact of LUC based on temperature decomposition of paired site observations, *Journal of Geophysical Research: Atmospheres*, 120, 5417–5436, <https://doi.org/10.1002/2015JD023095>, 2015.

Bukovsky, M. S., Gao, J., Mearns, L. O., and O'Neill, B. C.: SSP-Based Land-Use Change Scenarios: A Critical Uncertainty in Future Regional Climate Change Projections, *Earth's Future*, 9, e2020EF001782, <https://doi.org/10.1029/2020EF001782>, 2021.

Burakowski, E., Tawfik, A., Ouimette, A., Lepine, L., Novick, K., Ollinger, S., Zarzycki, C., and Bonan, G.: The role of surface roughness, albedo, and Bowen ratio on ecosystem energy balance in the Eastern United States, *Agricultural and Forest Meteorology*, 249, 367–376, <https://doi.org/10.1016/j.agrformet.2017.11.030>, 2018.

Chen, F. and Dudhia, J.: Coupling an Advanced Land Surface–Hydrology Model with the Penn State–NCAR MM5 Modeling System. Part I: Model Implementation and Sensitivity, *Monthly Weather Review*, 129, 569–585, [https://doi.org/10.1175/1520-0493\(2001\)129<0569:CAALSH>2.0.CO;2](https://doi.org/10.1175/1520-0493(2001)129<0569:CAALSH>2.0.CO;2), 2001.

Chen, L., Dirmeyer, P. A., Guo, Z., and Schultz, N. M.: Pairing FLUXNET sites to validate model representations of land-use/land-cover change, *Hydrology and Earth System Sciences*, 22, 111–125, <https://doi.org/10.5194/hess-22-111-2018>, 2018.

Cherubini, F., Huang, B., Hu, X., Tölle, M. H., and Strømman, A. H.: Quantifying the climate response to extreme land cover changes in Europe with a regional model, *Environ. Res. Lett.*, 13, 074002, <https://doi.org/10.1088/1748-9326/aac794>, 2018.

Christensen, J. H. and Christensen, O. B.: A summary of the PRUDENCE model projections of changes in European climate by the end of this century, *Climatic Change*, 81, 7–30, <https://doi.org/10.1007/s10584-006-9210-7>, 2007.

Constantinidou, K., Hadjinicolaou, P., Zittis, G., and Lelieveld, J.: Sensitivity of simulated climate over the MENA region related to different land surface schemes in the WRF model, *Theor Appl Climatol*, 141, 1431–1449, <https://doi.org/10.1007/s00704-020-03258-5>, 2020.

Cornes, R. C., van der Schrier, G., van den Besselaar, E. J. M., and Jones, P. D.: An Ensemble Version of the E-OBS Temperature and Precipitation Data Sets, *Journal of Geophysical Research: Atmospheres*, 123, 9391–9409, <https://doi.org/10.1029/2017JD028200>, 2018.

Crowther, T. W., Glick, H. B., Covey, K. R., Bettigole, C., Maynard, D. S., Thomas, S. M., Smith, J. R., Hintler, G., Duguid, M. C., Amatulli, G., Tuanmu, M.-N., Jetz, W., Salas, C., Stam, C., Piotta, D., Tavani, R., Green, S., Bruce, G., Williams, S. J., Wiser, S. K., Huber, M. O., Hengeveld, G. M., Nabuurs, G.-J., Tikhonova, E., Borchardt, P., Li, C.-F., Powrie, L. W., Fischer, M., Hemp, A., Homeier, J., Cho, P., Vibrans, A. C., Umunay, P.

M., Piao, S. L., Rowe, C. W., Ashton, M. S., Crane, P. R., and Bradford, M. A.: Mapping tree density at a global scale, *Nature*, 525, 201–205, <https://doi.org/10.1038/nature14967>, 2015.

Daloz, A. S., Schwingshackl, C., Mooney, P., Strada, S., Rechid, D., Davin, E. L., Katragkou, E., de Noblet-Ducoudré, N., Belda, M., Halenka, T., Breil, M., Cardoso, R. M., Hoffmann, P., Lima, D. C. A., Meier, R., Soares, P. M. M., Sofiadis, G., Strandberg, G., Toelle, M. H., and Lund, M. T.: Land-atmosphere interactions in sub-polar and alpine climates in the CORDEX FPS LUCAS models: I. Evaluation of the snow-albedo effect, *The Cryosphere Discussions*, 1–33, <https://doi.org/10.5194/tc-2021-290>, 2021.

Davin, E. L. and Noblet-Ducoudré, N. de: Climatic Impact of Global-Scale Deforestation: Radiative versus Nonradiative Processes, *Journal of Climate*, 23, 97–112, <https://doi.org/10.1175/2009JCLI3102.1>, 2010.

Davin, E. L., Maisonnave, E., and Seneviratne, S. I.: Is land surface processes representation a possible weak link in current Regional Climate Models?, *Environ. Res. Lett.*, 11, 074027, <https://doi.org/10.1088/1748-9326/11/7/074027>, 2016.

Davin, E. L., Rechid, D., Breil, M., Cardoso, R. M., Coppola, E., Hoffmann, P., Jach, L. L., Katragkou, E., de Noblet-Ducoudré, N., Radtke, K., Raffa, M., Soares, P. M. M., Sofiadis, G., Strada, S., Strandberg, G., Tölle, M. H., Warrach-Sagi, K., and Wulfmeyer, V.: Biogeophysical impacts of forestation in Europe: first results from the LUCAS (Land Use and Climate Across Scales) regional climate model intercomparison, *Earth System Dynamics*, 11, 183–200, <https://doi.org/10.5194/esd-11-183-2020>, 2020.

Dee, D. P., Uppala, S. M., Simmons, A. J., Berrisford, P., Poli, P., Kobayashi, S., Andrae, U., Balmaseda, M. A., Balsamo, G., Bauer, P., Bechtold, P., Beljaars, A. C. M., Berg, L. van de, Bidlot, J., Bormann, N., Delsol, C., Dragani, R., Fuentes, M., Geer, A. J., Haimberger, L., Healy, S. B., Hersbach, H., Hólm, E. V., Isaksen, I., Kållberg, P., Köhler, M., Matricardi, M., McNally, A. P., Monge-Sanz, B. M., Morcrette, J.-J., Park, B.-K., Peubey, C., Rosnay, P. de, Tavolato, C., Thépaut, J.-N., and Vitart, F.: The ERA-Interim reanalysis: configuration and performance of the data assimilation system, *Quarterly Journal of the Royal Meteorological Society*, 137, 553–597, <https://doi.org/10.1002/qj.828>, 2011.

Devaraju, N., Bala, G., and Nemani, R.: Modelling the influence of land-use changes on biophysical and biochemical interactions at regional and global scales, *Plant, Cell & Environment*, 38, 1931–1946, <https://doi.org/10.1111/pce.12488>, 2015.

Duveiller, G., Hooker, J., and Cescatti, A.: The mark of vegetation change on Earth's surface energy balance, *Nature Communications*, 9, 679, <https://doi.org/10.1038/s41467-017-02810-8>, 2018.

Fowler, L. D., Skamarock, W. C., Grell, G. A., Freitas, S. R., and Duda, M. G.: Analyzing the Grell–Freitas Convection Scheme from Hydrostatic to Nonhydrostatic Scales within a Global Model, *Monthly Weather Review*, 144, 2285–2306, <https://doi.org/10.1175/MWR-D-15-0311.1>, 2016.

Friedl, M. A., Sulla-Menashe, D., Tan, B., Schneider, A., Ramankutty, N., Sibley, A., and Huang, X.: MODIS Collection 5 global land cover: Algorithm refinements and characterization of new datasets, *Remote Sensing of Environment*, 114, 168–182, <https://doi.org/10.1016/j.rse.2009.08.016>, 2010.

Fuchs, R., Herold, M., Verburg, P. H., and Clevers, J. G. P. W.: A high-resolution and harmonized model approach for reconstructing and analysing historic land changes in Europe, *Biogeosciences*, 10, 1543–1559, <https://doi.org/10.5194/bg-10-1543-2013>, 2013.

Fuchs, R., Herold, M., Verburg, P. H., Clevers, J. G. P. W., and Eberle, J.: Gross changes in reconstructions of historic land cover/use for Europe between 1900 and 2010, *Global Change Biology*, 21, 299–313, <https://doi.org/10.1111/gcb.12714>, 2015.

Gao, Y., Leung, L. R., Zhao, C., and Hagos, S.: Sensitivity of U.S. summer precipitation to model resolution and convective parameterizations across gray zone resolutions, *Journal of Geophysical Research: Atmospheres*, 122, 2714–2733, <https://doi.org/10.1002/2016JD025896>, 2017.

García-Díez, M., Fernández, J., Fita, L., and Yagüe, C.: Seasonal dependence of WRF model biases and sensitivity to PBL schemes over Europe, *Quarterly Journal of the Royal Meteorological Society*, 139, 501–514, <https://doi.org/10.1002/qj.1976>, 2013.

García-Díez, M., Fernández, J., and Vautard, R.: An RCM multi-physics ensemble over Europe: multi-variable evaluation to avoid error compensation, *Clim Dyn*, 45, 3141–3156, <https://doi.org/10.1007/s00382-015-2529-x>, 2015.

Grassi, G., House, J., Dentener, F., Federici, S., den Elzen, M., and Penman, J.: The key role of forests in meeting climate targets requires science for credible mitigation, *Nature Climate Change*, 7, 220–226, <https://doi.org/10.1038/nclimate3227>, 2017.

Grell, G. A. and Freitas, S. R.: A scale and aerosol aware stochastic convective parameterization for weather and air quality modeling, *Atmospheric Chemistry and Physics*, 14, 5233–5250, <https://doi.org/10.5194/acp-14-5233-2014>, 2014.

Hansen, M. C., Potapov, P. V., Moore, R., Hancher, M., Turubanova, S. A., Tyukavina, A., Thau, D., Stehman, S. V., Goetz, S. J., Loveland, T. R., Kommareddy, A., Egorov, A., Chini, L., Justice, C. O., and Townshend, J. R. G.: High-Resolution Global Maps of 21st-Century Forest Cover Change, *Science*, 342, 850–853, <https://doi.org/10.1126/science.1244693>, 2013.

Harris, I., Osborn, T. J., Jones, P., and Lister, D.: Version 4 of the CRU TS monthly high-resolution gridded multivariate climate dataset, *Sci Data*, 7, 109, <https://doi.org/10.1038/s41597-020-0453-3>, 2020.

Hassan, R., Scholes, R., Ash, N., Condition, M., and Group, T.: *Ecosystems and Human Well-Being: Current State and Trends: Findings of the Condition and Trends Working Group (Millennium Ecosystem Assessment Series)*, 2005.

Hoffmann, P., Reinhart, V., Rechid, D., de Noblet-Ducoudré, N., Davin, E. L., Asmus, C., Bechtel, B., Böhner, J., Katragkou, E., and Luyssaert, S.: High-resolution land-use land-cover change data for regional climate modelling applications over Europe – Part 2: Historical and future changes, *Antroposphere – Land Cover and Land Use*, <https://doi.org/10.5194/essd-2021-252>, 2021.

Hong, S.-Y., Noh, Y., and Dudhia, J.: A New Vertical Diffusion Package with an Explicit Treatment of Entrainment Processes, *Monthly Weather Review*, 134, 2318–2341, <https://doi.org/10.1175/MWR3199.1>, 2006.

Hong, S.-Y., Park, H., Cheong, H.-B., Kim, J.-E. E., Koo, M.-S., Jang, J., Ham, S., Hwang, S.-O., Park, B.-K., Chang, E.-C., and Li, H.: The Global/Regional Integrated Model system (GRIMs), *Asia-Pacific J Atmos Sci*, 49, 219–243, <https://doi.org/10.1007/s13143-013-0023-0>, 2013.

Huang, B., Hu, X., Fuglstad, G.-A., Zhou, X., Zhao, W., and Cherubini, F.: Predominant regional biophysical cooling from recent land cover changes in Europe, *Nat Commun*, 11, 1066, <https://doi.org/10.1038/s41467-020-14890-0>, 2020.

Hurt, G. C., Chini, L., Sahajpal, R., Frohling, S., Bodirsky, B. L., Calvin, K., Doelman, J. C., Fisk, J., Fujimori, S., Klein Goldewijk, K., Hasegawa, T., Havlik, P., Heinemann, A., Humpenöder, F., Jungclaus, J., Kaplan, J. O., Kennedy, J., Krisztin, T., Lawrence, D., Lawrence, P., Ma, L., Mertz, O., Pongratz, J., Popp, A., Poulter, B., Riahi, K., Shevliakova, E., Stehfest, E., Thornton, P., Tubiello, F. N., van Vuuren, D. P., and Zhang, X.:

Harmonization of global land use change and management for the period 850–2100 (LUH2) for CMIP6, *Geosci. Model Dev.*, 13, 5425–5464, <https://doi.org/10.5194/gmd-13-5425-2020>, 2020.

Iacono, M. J., Delamere, J. S., Mlawer, E. J., Shephard, M. W., Clough, S. A., and Collins, W. D.: Radiative forcing by long-lived greenhouse gases: Calculations with the AER radiative transfer models, *Journal of Geophysical Research: Atmospheres*, 113, <https://doi.org/10.1029/2008JD009944>, 2008.

Intergovernmental Panel on Climate Change: *Climate Change and Land: IPCC Special Report on Climate Change, Desertification, Land Degradation, Sustainable Land Management, Food Security, and Greenhouse Gas Fluxes in Terrestrial Ecosystems*, 1st ed., Cambridge University Press, <https://doi.org/10.1017/9781009157988>, 2022.

Jacob, D., Teichmann, C., Sobolowski, S., Katragkou, E., Anders, I., Belda, M., Benestad, R., Boberg, F., Buonomo, E., Cardoso, R. M., Casanueva, A., Christensen, O. B., Christensen, J. H., Coppola, E., De Cruz, L., Davin, E. L., Dobler, A., Domínguez, M., Fealy, R., Fernandez, J., Gaertner, M. A., García-Díez, M., Giorgi, F., Gobiet, A., Goergen, K., Gómez-Navarro, J. J., Alemán, J. J. G., Gutiérrez, C., Gutiérrez, J. M., Güttler, I., Haensler, A., Halenka, T., Jerez, S., Jiménez-Guerrero, P., Jones, R. G., Keuler, K., Kjellström, E., Knist, S., Kotlarski, S., Maraun, D., van Meijgaard, E., Mercogliano, P., Montávez, J. P., Navarra, A., Nikulin, G., de Noblet-Ducoudré, N., Panitz, H.-J., Pfeifer, S., Piazza, M., Pichelli, E., Pietikäinen, J.-P., Prein, A. F., Preuschmann, S., Rechid, D., Rockel, B., Romera, R., Sánchez, E., Sieck, K., Soares, P. M. M., Somot, S., Srnec, L., Sørland, S. L., Termonia, P., Truhetz, H., Vautard, R., Warrach-Sagi, K., and Wulfmeyer, V.: Regional climate downscaling over Europe: perspectives from the EURO-CORDEX community, *Reg Environ Change*, 20, 51, <https://doi.org/10.1007/s10113-020-01606-9>, 2020.

Jeworrek, J., West, G., and Stull, R.: Evaluation of Cumulus and Microphysics Parameterizations in WRF across the Convective Gray Zone, *Weather and Forecasting*, 34, 1097–1115, <https://doi.org/10.1175/WAF-D-18-0178.1>, 2019.

Jia, X., Shao, M., Zhu, Y., and Luo, Y.: Soil moisture decline due to afforestation across the Loess Plateau, China, *Journal of Hydrology*, 546, 113–122, <https://doi.org/10.1016/j.jhydrol.2017.01.011>, 2017.

Jiménez, P. A., Dudhia, J., González-Rouco, J. F., Navarro, J., Montávez, J. P., and García-Bustamante, E.: A Revised Scheme for the WRF Surface Layer Formulation, *Monthly Weather Review*, 140, 898–918, <https://doi.org/10.1175/MWR-D-11-00056.1>, 2012.

Jin, J., Miller, N. L., and Schlegel, N.: Sensitivity Study of Four Land Surface Schemes in the WRF Model, *Advances in Meteorology*, 2010, 1–11, <https://doi.org/10.1155/2010/167436>, 2010.

Juang, J.-Y., Katul, G., Siqueira, M., Stoy, P., and Novick, K.: Separating the effects of albedo from eco-physiological changes on surface temperature along a successional chronosequence in the southeastern United States, *Geophysical Research Letters*, 34, <https://doi.org/10.1029/2007GL031296>, 2007.

Kain, J. S.: The Kain–Fritsch Convective Parameterization: An Update, *Journal of Applied Meteorology and Climatology*, 43, 170–181, [https://doi.org/10.1175/1520-0450\(2004\)043<0170:TKCPAU>2.0.CO;2](https://doi.org/10.1175/1520-0450(2004)043<0170:TKCPAU>2.0.CO;2), 2004.

Karlsson, K.-G., Anttila, K., Trentmann, J., Stengel, M., Fokke Meirink, J., Devasthale, A., Hanschmann, T., Kothe, S., Jääskeläinen, E., Sedlar, J., Benas, N., van Zadelhoff, G.-J., Schlundt, C., Stein, D., Finkensieper, S., Håkansson, N., and Hollmann, R.: CLARA-A2: the second edition of the CM SAF cloud and radiation data record from 34 years of global AVHRR data, *Atmospheric Chemistry and Physics*, 17, 5809–5828, <https://doi.org/10.5194/acp-17-5809-2017>, 2017.

Katragkou, E., García-Díez, M., Vautard, R., Sobolowski, S., Zanis, P., Alexandri, G., Cardoso, R. M., Colette, A., Fernandez, J., Gobiet, A., Goergen, K., Karacostas, T., Knist, S., Mayer, S., Soares, P. M. M., Pytharoulis, I.,



Tegoulas, I., Tsikerdekis, A., and Jacob, D.: Regional climate hindcast simulations within EURO-CORDEX: evaluation of a WRF multi-physics ensemble, *Geoscientific Model Development*, 8, 603–618, <https://doi.org/10.5194/gmd-8-603-2015>, 2015.

Kotlarski, S., Keuler, K., Christensen, O. B., Colette, A., Déqué, M., Gobiet, A., Goergen, K., Jacob, D., Lüthi, D., van Meijgaard, E., Nikulin, G., Schär, C., Teichmann, C., Vautard, R., Warrach-Sagi, K., and Wulfmeyer, V.: Regional climate modeling on European scales: a joint standard evaluation of the EURO-CORDEX RCM ensemble, *Geoscientific Model Development*, 7, 1297–1333, <https://doi.org/10.5194/gmd-7-1297-2014>, 2014.

Kuemmerle, T., Levers, C., Erb, K., Estel, S., Jepsen, M. R., Müller, D., Plutzer, C., Stürck, J., Verkerk, P. J., Verburg, P. H., and Reenberg, A.: Hotspots of land use change in Europe, *Environ. Res. Lett.*, 11, 064020, <https://doi.org/10.1088/1748-9326/11/6/064020>, 2016.

Kumar, S., Dirmeyer, P. A., Merwade, V., DelSole, T., Adams, J. M., and Niyogi, D.: Land use/cover change impacts in CMIP5 climate simulations: A new methodology and 21st century challenges, *Journal of Geophysical Research: Atmospheres*, 118, 6337–6353, <https://doi.org/10.1002/jgrd.50463>, 2013.

Laguë, M. M. and Swann, A. L. S.: Progressive Midlatitude Afforestation: Impacts on Clouds, Global Energy Transport, and Precipitation, *Journal of Climate*, 29, 5561–5573, <https://doi.org/10.1175/JCLI-D-15-0748.1>, 2016.

Lawrence, D. M., Fisher, R. A., Koven, C. D., Oleson, K. W., Swenson, S. C., Bonan, G., Collier, N., Ghimire, B., Kampenhout, L. van, Kennedy, D., Kluzek, E., Lawrence, P. J., Li, F., Li, H., Lombardozzi, D., Riley, W. J., Sacks, W. J., Shi, M., Vertenstein, M., Wieder, W. R., Xu, C., Ali, A. A., Badger, A. M., Bisht, G., Broeke, M. van den, Brunke, M. A., Burns, S. P., Buzan, J., Clark, M., Craig, A., Dahlin, K., Drewniak, B., Fisher, J. B., Flanner, M., Fox, A. M., Gentine, P., Hoffman, F., Keppel-Aleks, G., Knox, R., Kumar, S., Lenaerts, J., Leung, L. R., Lipscomb, W. H., Lu, Y., Pandey, A., Pelletier, J. D., Perket, J., Randerson, J. T., Ricciuto, D. M., Sanderson, B. M., Slater, A., Subin, Z. M., Tang, J., Thomas, R. Q., Martin, M. V., and Zeng, X.: The Community Land Model Version 5: Description of New Features, Benchmarking, and Impact of Forcing Uncertainty, *Journal of Advances in Modeling Earth Systems*, 11, 4245–4287, <https://doi.org/10.1029/2018MS001583>, 2019.

Lee, X., Goulden, M. L., Hollinger, D. Y., Barr, A., Black, T. A., Bohrer, G., Bracho, R., Drake, B., Goldstein, A., Gu, L., Katul, G., Kolb, T., Law, B. E., Margolis, H., Meyers, T., Monson, R., Munger, W., Oren, R., Paw U, K. T., Richardson, A. D., Schmid, H. P., Staebler, R., Wofsy, S., and Zhao, L.: Observed increase in local cooling effect of deforestation at higher latitudes, *Nature*, 479, 384–387, <https://doi.org/10.1038/nature10588>, 2011.

Lejeune, Q., Davin, E. L., Guillod, B. P., and Seneviratne, S. I.: Influence of Amazonian deforestation on the future evolution of regional surface fluxes, circulation, surface temperature and precipitation, *Clim Dyn*, 44, 2769–2786, <https://doi.org/10.1007/s00382-014-2203-8>, 2015.

Lejeune, Q., Seneviratne, S. I., and Davin, E. L.: Historical Land-Cover Change Impacts on Climate: Comparative Assessment of LUCID and CMIP5 Multimodel Experiments, *Journal of Climate*, 30, 1439–1459, <https://doi.org/10.1175/JCLI-D-16-0213.1>, 2017.

Lesiv, M., Schepaschenko, D., Moltchanova, E., Bun, R., Dürauer, M., Prishchepov, A. V., Schierhorn, F., Estel, S., Kuemmerle, T., Alcántara, C., Kussul, N., Shchepashchenko, M., Kutovaya, O., Martynenko, O., Karminov, V., Shvidenko, A., Havlik, P., Kraxner, F., See, L., and Fritz, S.: Spatial distribution of arable and abandoned land across former Soviet Union countries, *Sci Data*, 5, 180056, <https://doi.org/10.1038/sdata.2018.56>, 2018.

Lewis, S. L., Mitchard, E. T. A., Prentice, C., Maslin, M., and Poulter, B.: Comment on “The global tree restoration potential,” *Science*, 366, eaaz0388, <https://doi.org/10.1126/science.aaz0388>, 2019.

- Li, W., MacBean, N., Ciais, P., Defourny, P., Lamarche, C., Bontemps, S., Houghton, R. A., and Peng, S.: Gross and net land cover changes in the main plant functional types derived from the annual ESA CCI land cover maps (1992–2015), *Earth System Science Data*, 10, 219–234, <https://doi.org/10.5194/essd-10-219-2018>, 2018a.
- Li, Y., Zhao, M., Motesharrei, S., Mu, Q., Kalnay, E., and Li, S.: Local cooling and warming effects of forests based on satellite observations, *Nat Commun*, 6, 6603, <https://doi.org/10.1038/ncomms7603>, 2015.
- Li, Y., De Noblet-Ducoudré, N., Davin, E. L., Motesharrei, S., Zeng, N., Li, S., and Kalnay, E.: The role of spatial scale and background climate in the latitudinal temperature response to deforestation, *Earth Syst. Dynam.*, 7, 167–181, <https://doi.org/10.5194/esd-7-167-2016>, 2016.
- Li, Y., Piao, S., Li, L. Z. X., Chen, A., Wang, X., Ciais, P., Huang, L., Lian, X., Peng, S., Zeng, Z., Wang, K., and Zhou, L.: Divergent hydrological response to large-scale afforestation and vegetation greening in China, *Science Advances*, 4, eaar4182, <https://doi.org/10.1126/sciadv.aar4182>, 2018b.
- Lim, K.-S. S. and Hong, S.-Y.: Development of an Effective Double-Moment Cloud Microphysics Scheme with Prognostic Cloud Condensation Nuclei (CCN) for Weather and Climate Models, *Monthly Weather Review*, 138, 1587–1612, <https://doi.org/10.1175/2009MWR2968.1>, 2010.
- Liu, X., Yu, L., Si, Y., Zhang, C., Lu, H., Yu, C., and Gong, P.: Identifying patterns and hotspots of global land cover transitions using the ESA CCI Land Cover dataset, *Remote Sensing Letters*, 9, 972–981, <https://doi.org/10.1080/2150704X.2018.1500070>, 2018.
- Longobardi, P., Montenegro, A., Beltrami, H., and Eby, M.: Deforestation Induced Climate Change: Effects of Spatial Scale, *PLOS ONE*, 11, e0153357, <https://doi.org/10.1371/journal.pone.0153357>, 2016.
- Lozano-Parra, J., Pulido, M., Lozano-Fondón, C., and Schnabel, S.: How do Soil Moisture and Vegetation Covers Influence Soil Temperature in Drylands of Mediterranean Regions?, *Water*, 10, 1747, <https://doi.org/10.3390/w10121747>, 2018.
- Luysaert, S., Jammet, M., Stoy, P. C., Estel, S., Pongratz, J., Ceschia, E., Churkina, G., Don, A., Erb, K., Ferlicoq, M., Gielen, B., Grünwald, T., Houghton, R. A., Klumpp, K., Knohl, A., Kolb, T., Kuemmerle, T., Laurila, T., Lohila, A., Loustau, D., McGrath, M. J., Meyfroidt, P., Moors, E. J., Naudts, K., Novick, K., Otto, J., Pilegaard, K., Pio, C. A., Rambal, S., Reibmann, C., Ryder, J., Suyker, A. E., Varlagin, A., Wattenbach, M., and Dolman, A. J.: Land management and land-cover change have impacts of similar magnitude on surface temperature, *Nature Clim Change*, 4, 389–393, <https://doi.org/10.1038/nclimate2196>, 2014.
- MacDougall, A. H. and Beltrami, H.: Impact of deforestation on subsurface temperature profiles: implications for the borehole paleoclimate record, *Environ. Res. Lett.*, 12, 074014, <https://doi.org/10.1088/1748-9326/aa7394>, 2017.
- Mass, C: Strange linear features in WRF clouds and precipitation: diagnosis and correction, 2013.
- McGrath, M. J., Luysaert, S., Meyfroidt, P., Kaplan, J. O., Bürgi, M., Chen, Y., Erb, K., Gimmi, U., McInerney, D., Naudts, K., Otto, J., Pasztor, F., Ryder, J., Schelhaas, M.-J., and Valade, A.: Reconstructing European forest management from 1600 to 2010, *Biogeosciences*, 12, 4291–4316, <https://doi.org/10.5194/bg-12-4291-2015>, 2015.
- Meier, R.: Biomass heat storage dampens diurnal temperature variations in forests, *Environ. Res. Lett.*, 21, 2019.
- Meier, R., Davin, E. L., Lejeune, Q., Hauser, M., Li, Y., Martens, B., Schultz, N. M., Sterling, S., and Thiery, W.: Evaluating and improving the Community Land Model's sensitivity to land cover, *Biogeosciences*, 15, 4731–4757, <https://doi.org/10.5194/bg-15-4731-2018>, 2018.

Ψηφιακή συλλογή

Meyfroidt, P., Roy Chowdhury, R., de Bremond, A., Ellis, E. C., Erb, K.-H., Filatova, T., Garrett, R. D., Grove, J. M., Heinemann, A., Kuemmerle, T., Kull, C. A., Lambin, E. F., Landon, Y., le Polain de Waroux, Y., Messerli, P., Müller, D., Nielsen, J. Ø., Peterson, G. D., Rodriguez García, V., Schlüter, M., Turner, B. L., and Verburg, P. H.: Middle-range theories of land system change, *Global Environmental Change*, 53, 52–67, <https://doi.org/10.1016/j.gloenvcha.2018.08.006>, 2018.

Mooney, P. A., Mulligan, F. J., and Fealy, R.: Evaluation of the Sensitivity of the Weather Research and Forecasting Model to Parameterization Schemes for Regional Climates of Europe over the Period 1990–95, *Journal of Climate*, 26, 1002–1017, <https://doi.org/10.1175/JCLI-D-11-00676.1>, 2013.

Mooney, P. A., Rechid, D., Davin, E. L., Katragkou, E., de Noblet-Ducoudré, N., Breil, M., Cardoso, R. M., Daloz, A. S., Hoffmann, P., Lima, D. C. A., Meier, R., Soares, P. M. M., Sofiadis, G., Strada, S., Strandberg, G., Toelle, M. H., and Lund, M. T.: Land-atmosphere interactions in sub-polar and alpine climates in the CORDEX FPS LUCAS models: Part II. The role of changing vegetation, *The Cryosphere Discussions*, 1–22, <https://doi.org/10.5194/tc-2021-291>, 2021.

Muñoz-Sabater, J., Dutra, E., Agustí-Panareda, A., Albergel, C., Arduini, G., Balsamo, G., Boussetta, S., Choulga, M., Harrigan, S., Hersbach, H., Martens, B., Miralles, D. G., Piles, M., Rodríguez-Fernández, N. J., Zsoter, E., Buontempo, C., and Thépaut, J.-N.: ERA5-Land: a state-of-the-art global reanalysis dataset for land applications, *Earth System Science Data*, 13, 4349–4383, <https://doi.org/10.5194/essd-13-4349-2021>, 2021.

Nakanishi, M. and Niino, H.: An Improved Mellor–Yamada Level-3 Model: Its Numerical Stability and Application to a Regional Prediction of Advection Fog, *Boundary-Layer Meteorol*, 119, 397–407, <https://doi.org/10.1007/s10546-005-9030-8>, 2006.

Nakanishi, M. and Niino, H.: Development of an Improved Turbulence Closure Model for the Atmospheric Boundary Layer, *Journal of the Meteorological Society of Japan*, 87, 895–912, <https://doi.org/10.2151/jmsj.87.895>, 2009.

Ni, J., Cheng, Y., Wang, Q., Ng, C. W. W., and Garg, A.: Effects of vegetation on soil temperature and water content: Field monitoring and numerical modelling, *Journal of Hydrology*, 571, 494–502, <https://doi.org/10.1016/j.jhydrol.2019.02.009>, 2019.

Niu, G.-Y., Yang, Z.-L., Dickinson, R. E., and Gulden, L. E.: A simple TOPMODEL-based runoff parameterization (SIMTOP) for use in global climate models, *Journal of Geophysical Research: Atmospheres*, 110, <https://doi.org/10.1029/2005JD006111>, 2005.

Niu, G.-Y., Yang, Z.-L., Mitchell, K. E., Chen, F., Ek, M. B., Barlage, M., Kumar, A., Manning, K., Niyogi, D., Rosero, E., Tewari, M., and Xia, Y.: The community Noah land surface model with multiparameterization options (Noah-MP): 1. Model description and evaluation with local-scale measurements, *Journal of Geophysical Research: Atmospheres*, 116, <https://doi.org/10.1029/2010JD015139>, 2011.

Noblet-Ducoudré, N. de, Boisier, J.-P., Pitman, A., Bonan, G. B., Brovkin, V., Cruz, F., Delire, C., Gayler, V., Hurk, B. J. J. M. van den, Lawrence, P. J., Molen, M. K. van der, Müller, C., Reick, C. H., Strengers, B. J., and Voldoire, A.: Determining Robust Impacts of Land-Use-Induced Land Cover Changes on Surface Climate over North America and Eurasia: Results from the First Set of LUCID Experiments, *Journal of Climate*, 25, 3261–3281, <https://doi.org/10.1175/JCLI-D-11-00338.1>, 2012.

Oleson, K., Lawrence, D., Bonan, G., Flanner, M., Kluzek, E., Lawrence, P., Levis, S., Swenson, S., Thornton, P., Dai, A., Decker, M., Dickinson, R., Feddema, J., Heald, C., Hoffman, F., Lamarque, J.-F., Mahowald, N., Niu, G.-Y., Qian, T., Randerson, J., Running, S., Sakaguchi, K., Slater, A., Stockli, R., Wang, A., Yang, Z.-L., Zeng, X., and Zeng, X.: Technical Description of version 4.0 of the Community Land Model (CLM), UCAR/NCAR, <https://doi.org/10.5065/D6FB50WZ>, 2010a.

Oleson, K., Lawrence, D., Bonan, G., Drewniak, B., Huang, M., Koven, C., Levis, S., Li, F., Riley, W., Subin, Z., Swenson, S., Thornton, P., Bozbiyik, A., Fisher, R., Heald, C., Kluzek, E., Lamarque, J.-F., Lawrence, P., Leung, L., Lipscomb, W., Muszala, S., Ricciuto, D., Sacks, W., Sun, Y., Tang, J., and Yang, Z.-L.: Technical description of version 4.5 of the Community Land Model (CLM), UCAR/NCAR, <https://doi.org/10.5065/D6RR1W7M>, 2013.

Oleson, K. W., Lawrence, D. M., Bonan, G. B., Flanner, M. G., Kluzek, E., Lawrence, P. J., Levis, S., Swenson, S. C., Thornton, P. E., Dai, A., Decker, M., Dickinson, R., Feddema, J., Heald, C. L., Hoffman, F., Lamarque, J.-F., Mahowald, N., Niu, G.-Y., Qian, T., Randerson, J., Running, S., Sakaguchi, K., Slater, A., Stöckli, R., Wang, A., Yang, Z.-L., Zeng, X., and Zeng, X.: Technical Description of version 4.0 of the Community Land Model (CLM), 2010b.

Pan, Y., Birdsey, R. A., Phillips, O. L., and Jackson, R. B.: The Structure, Distribution, and Biomass of the World's Forests, *Annual Review of Ecology, Evolution, and Systematics*, 44, 593–622, <https://doi.org/10.1146/annurev-ecolsys-110512-135914>, 2013.

Pastorello, G., Trotta, C., Canfora, E., Chu, H., Christianson, D., Cheah, Y.-W., Poindexter, C., Chen, J., Elbashandy, A., Humphrey, M., Isaac, P., Polidori, D., Reichstein, M., Ribeca, A., van Ingen, C., Vuichard, N., Zhang, L., Amiro, B., Ammann, C., Arain, M. A., Ardö, J., Arkebauer, T., Arndt, S. K., Arriga, N., Aubinet, M., Aurela, M., Baldocchi, D., Barr, A., Beamesderfer, E., Marchesini, L. B., Bergeron, O., Beringer, J., Bernhofer, C., Berveiller, D., Billesbach, D., Black, T. A., Blanken, P. D., Bohrer, G., Boike, J., Bolstad, P. V., Bonal, D., Bonnefond, J.-M., Bowling, D. R., Bracho, R., Brodeur, J., Brümmer, C., Buchmann, N., Burban, B., Burns, S. P., Buysse, P., Cale, P., Cavagna, M., Cellier, P., Chen, S., Chini, I., Christensen, T. R., Cleverly, J., Collalti, A., Consalvo, C., Cook, B. D., Cook, D., Coursolle, C., Cremonese, E., Curtis, P. S., D'Andrea, E., da Rocha, H., Dai, X., Davis, K. J., Cinti, B. D., Grandcourt, A. de, Ligne, A. D., De Oliveira, R. C., Delpierre, N., Desai, A. R., Di Bella, C. M., Tommasi, P. di, Dolman, H., Domingo, F., Dong, G., Dore, S., Duce, P., Dufrêne, E., Dunn, A., Dušek, J., Eamus, D., Eichelmann, U., ElKhidir, H. A. M., Eugster, W., Ewenz, C. M., Ewers, B., Famulari, D., Fares, S., Feigenwinter, I., Feitz, A., Fensholt, R., Filippa, G., Fischer, M., Frank, J., Galvagno, M., et al.: The FLUXNET2015 dataset and the ONEFlux processing pipeline for eddy covariance data, *Scientific Data*, 7, 225, <https://doi.org/10.1038/s41597-020-0534-3>, 2020.

Perugini, L., Caporaso, L., Marconi, S., Cescatti, A., Quesada, B., Noblet-Ducoudré, N. de, House, J. I., and Arneth, A.: Biophysical effects on temperature and precipitation due to land cover change, *Environ. Res. Lett.*, 12, 053002, <https://doi.org/10.1088/1748-9326/aa6b3f>, 2017.

Pitman, A. J., Noblet-Ducoudré, N. de, Cruz, F. T., Davin, E. L., Bonan, G. B., Brovkin, V., Claussen, M., Delire, C., Ganzeveld, L., Gayler, V., Hurk, B. J. J. M. van den, Lawrence, P. J., Molen, M. K. van der, Müller, C., Reick, C. H., Seneviratne, S. I., Strengers, B. J., and Voldoire, A.: Uncertainties in climate responses to past land cover change: First results from the LUCID intercomparison study, *Geophysical Research Letters*, 36, <https://doi.org/10.1029/2009GL039076>, 2009.

Pongratz, J., Schwingshackl, C., Bultan, S., Obermeier, W., Havermann, F., and Guo, S.: Land Use Effects on Climate: Current State, Recent Progress, and Emerging Topics, *Curr Clim Change Rep*, 7, 99–120, <https://doi.org/10.1007/s40641-021-00178-y>, 2021.

Potapov, P., Yaroshenko, A., Turubanova, S., Dubinin, M., Laestadius, L., Thies, C., Aksenov, D., Egorov, A., Yesipova, Y., Glushkov, I., Karpachevskiy, M., Kostikova, A., Manisha, A., Tsybikova, E., and Zhuravleva, I.: Mapping the World's Intact Forest Landscapes by Remote Sensing, *E&S*, 13, art51, <https://doi.org/10.5751/ES-02670-130251>, 2008.

Poulter, B., MacBean, N., Hartley, A., Khlystova, I., Arino, O., Betts, R., Bontemps, S., Boettcher, M., Brockmann, C., Defourny, P., Hagemann, S., Herold, M., Kirches, G., Lamarche, C., Lederer, D., Otlé, C., Peters, M., and Peylin, P.: Plant functional type classification for earth system models: results from the European Space

Agency's Land Cover Climate Change Initiative, Geoscientific Model Development, 8, 2315–2328, <https://doi.org/10.5194/gmd-8-2315-2015>, 2015.

Rechid, D., Davin, E., de Noblet-Ducoudré, N., and Katragkou, E.: CORDEX Flagship Pilot Study “LUCAS - Land Use & Climate Across Scales” - a new initiative on coordinated regional land use change and climate experiments for Europe, 1, 2017.

Reinhart, V., Hoffmann, P., Rechid, D., Böhner, J., and Bechtel, B.: High-resolution land use and land cover dataset for regional climate modelling: a plant functional type map for Europe 2015, Earth Syst. Sci. Data, 14, 1735–1794, <https://doi.org/10.5194/essd-14-1735-2022>, 2022.

Ren, Z., Li, Z., Liu, X., Li, P., Cheng, S., and Xu, G.: Comparing watershed afforestation and natural revegetation impacts on soil moisture in the semiarid Loess Plateau of China, Scientific Reports, 8, 2972, <https://doi.org/10.1038/s41598-018-21362-5>, 2018.

Rey Benayas, J. M. and Bullock, J. M.: Restoration of Biodiversity and Ecosystem Services on Agricultural Land, Ecosystems, 15, 883–899, <https://doi.org/10.1007/s10021-012-9552-0>, 2012.

Rummukainen, M.: Added value in regional climate modeling, WIREs Climate Change, 7, 145–159, <https://doi.org/10.1002/wcc.378>, 2016.

Schrodin, R. and Heise, E.: COSMO Technical Report No. 2: The Multi-Layer Version of the DWD Soil Model TERRA\_LM, [https://doi.org/10.5676/DWD\\_PUB/NWV/COSMO-TR\\_2](https://doi.org/10.5676/DWD_PUB/NWV/COSMO-TR_2), 2001.

Schultz, N. M., Lawrence, P. J., and Lee, X.: Global satellite data highlights the diurnal asymmetry of the surface temperature response to deforestation, Journal of Geophysical Research: Biogeosciences, 122, 903–917, <https://doi.org/10.1002/2016JG003653>, 2017.

Skamarock, W., Klemp, J., Dudhia, J., Gill, D., Barker, D., Wang, W., Huang, X.-Y., and Duda, M.: A Description of the Advanced Research WRF Version 3, UCAR/NCAR, <https://doi.org/10.5065/D68S4MVH>, 2008.

Sofiadis, G., Katragkou, E., Davin, E. L., Rechid, D., de Noblet-Ducoudre, N., Breil, M., Cardoso, R. M., Hoffmann, P., Jach, L., Meier, R., Mooney, P. A., Soares, P. M. M., Strada, S., Tölle, M. H., and Warrach Sagi, K.: Afforestation impact on soil temperature in regional climate model simulations over Europe, Geoscientific Model Development, 15, 595–616, <https://doi.org/10.5194/gmd-15-595-2022>, 2022.

Song, X.-P., Hansen, M. C., Stehman, S. V., Potapov, P. V., Tyukavina, A., Vermote, E. F., and Townshend, J. R.: Global land change from 1982 to 2016, Nature, 560, 639–643, <https://doi.org/10.1038/s41586-018-0411-9>, 2018.

Strandberg, G. and Kjellström, E.: Climate Impacts from Afforestation and Deforestation in Europe, Earth Interactions, 23, 1–27, <https://doi.org/10.1175/EI-D-17-0033.1>, 2019.

Swann, A. L. S., Fung, I. Y., and Chiang, J. C. H.: Mid-latitude afforestation shifts general circulation and tropical precipitation, Proceedings of the National Academy of Sciences, 109, 712–716, <https://doi.org/10.1073/pnas.1116706108>, 2012.

Swenson, S. C., Burns, S. P., and Lawrence, D. M.: The Impact of Biomass Heat Storage on the Canopy Energy Balance and Atmospheric Stability in the Community Land Model, Journal of Advances in Modeling Earth Systems, 11, 83–98, <https://doi.org/10.1029/2018MS001476>, 2019.

Tang, B., Zhao, X., and Zhao, W.: Local Effects of Forests on Temperatures across Europe, Remote Sensing, 10, 529, <https://doi.org/10.3390/rs10040529>, 2018.

- Tegen, I., Hollrig, P., Chin, M., Fung, I., Jacob, D., and Penner, J.: Contribution of different aerosol species to the global aerosol extinction optical thickness: Estimates from model results, *Journal of Geophysical Research: Atmospheres*, 102, 23895–23915, <https://doi.org/10.1029/97JD01864>, 1997.
- Thompson, G., Rasmussen, R. M., and Manning, K.: Explicit Forecasts of Winter Precipitation Using an Improved Bulk Microphysics Scheme. Part I: Description and Sensitivity Analysis, *Monthly Weather Review*, 132, 519–542, [https://doi.org/10.1175/1520-0493\(2004\)132<0519:EFOWPU>2.0.CO;2](https://doi.org/10.1175/1520-0493(2004)132<0519:EFOWPU>2.0.CO;2), 2004.
- Ustaoglu, E. and Collier, M. J.: Farmland abandonment in Europe: an overview of drivers, consequences, and assessment of the sustainability implications, *Environ. Rev.*, 26, 396–416, <https://doi.org/10.1139/er-2018-0001>, 2018.
- Veldman, J. W., Aleman, J. C., Alvarado, S. T., Anderson, T. M., Archibald, S., Bond, W. J., Boutton, T. W., Buchmann, N., Buisson, E., Canadell, J. G., Dechoum, M. de S., Diaz-Toribio, M. H., Durigan, G., Ewel, J. J., Fernandes, G. W., Fidelis, A., Fleischman, F., Good, S. P., Griffith, D. M., Hermann, J.-M., Hoffmann, W. A., Le Stradic, S., Lehmann, C. E. R., Mahy, G., Nerlekar, A. N., Nippert, J. B., Noss, R. F., Osborne, C. P., Overbeck, G. E., Parr, C. L., Pausas, J. G., Pennington, R. T., Perring, M. P., Putz, F. E., Ratnam, J., Sankaran, M., Schmidt, I. B., Schmitt, C. B., Silveira, F. A. O., Staver, A. C., Stevens, N., Still, C. J., Strömberg, C. A. E., Temperton, V. M., Varner, J. M., and Zaloumis, N. P.: Comment on “The global tree restoration potential,” *Science*, 366, eaay7976, <https://doi.org/10.1126/science.aay7976>, 2019.
- Wilhelm, C., Rechid, D., and Jacob, D.: Interactive coupling of regional atmosphere with biosphere in the new generation regional climate system model REMO-iMOVE, *Geosci. Model Dev.*, 7, 1093–1114, <https://doi.org/10.5194/gmd-7-1093-2014>, 2014.
- Winckler, J., Reick, C. H., and Pongratz, J.: Robust Identification of Local Biogeophysical Effects of Land-Cover Change in a Global Climate Model, *Journal of Climate*, 30, 1159–1176, <https://doi.org/10.1175/JCLI-D-16-0067.1>, 2017.
- Winckler, J., Reick, C. H., Luyssaert, S., Cescatti, A., Stoy, P. C., Lejeune, Q., Raddatz, T., Chlond, A., Heidkamp, M., and Pongratz, J.: Different response of surface temperature and air temperature to deforestation in climate models, *Earth System Dynamics*, 10, 473–484, <https://doi.org/10.5194/esd-10-473-2019>, 2019a.
- Winckler, J., Reick, C. H., Bright, R. M., and Pongratz, J.: Importance of Surface Roughness for the Local Biogeophysical Effects of Deforestation, *Journal of Geophysical Research: Atmospheres*, 124, 8605–8618, <https://doi.org/10.1029/2018JD030127>, 2019b.
- Winckler, J., Lejeune, Q., Reick, C. H., and Pongratz, J.: Nonlocal Effects Dominate the Global Mean Surface Temperature Response to the Biogeophysical Effects of Deforestation, *Geophysical Research Letters*, 46, 745–755, <https://doi.org/10.1029/2018GL080211>, 2019c.
- Yang, Z.-L., Cai, X., Zhang, G., Tavakoly, A. A., Jin, Q., Meyer, L. H., and Guan, X.: The Community Noah Land Surface Model with Multi-Parameterization Options (Noah-MP), 75, n.d.
- Zhang, M., Lee, X., Yu, G., Han, S., Wang, H., Yan, J., Zhang, Y., Li, Y., Ohta, T., Hirano, T., Kim, J., Yoshifuji, N., and Wang, W.: Response of surface air temperature to small-scale land clearing across latitudes, *Environ. Res. Lett.*, 9, 034002, <https://doi.org/10.1088/1748-9326/9/3/034002>, 2014.
- Zhang, S., Yang, D., Yang, Y., Piao, S., Yang, H., Lei, H., and Fu, B.: Excessive Afforestation and Soil Drying on China’s Loess Plateau, *Journal of Geophysical Research: Biogeosciences*, 123, 923–935, <https://doi.org/10.1002/2017JG004038>, 2018.

Zhang, Y., Peng, C., Li, W., Tian, L., Zhu, Q., Chen, H., Fang, X., Zhang, G., Liu, G., Mu, X., Li, Z., Li, S., Yang, Y., Wang, J., and Xiao, X.: Multiple afforestation programs accelerate the greenness in the 'Three North' region of China from 1982 to 2013, *Ecological Indicators*, 61, 404–412, <https://doi.org/10.1016/j.ecolind.2015.09.041>, 2016.

Zhao, K. and Jackson, R. B.: Biophysical forcings of land-use changes from potential forestry activities in North America, *Ecological Monographs*, 84, 329–353, <https://doi.org/10.1890/12-1705.1>, 2014.

## Appendix

### List of Abbreviations

---

AAST	Annual Amplitude of Soil Temperature
clt	Total cloud fraction
ESM	Earth System Model
ET	Evapotranspiration
FPS LUCAS	Land Use Change Across Scales in Europe Flagship Pilot Study
GCM	Global Circulation Model
GHF	Ground Heat Flux
H	Sensible Heat
LAI	Leaf Area Index
LC	Land Cover
LE	Latent Heat
LUC	Land Use Change
LULCC	Land Use Land Cover Change
LSM	Land Surface Model
LST	Land Surface Temperature
LW	Longwave radiation
PBL	Planetary Boundary Layer
RCM	Regional Climate Model
RMSE	Root Mean Squared Error
SMC	Soil moisture content
SW	Shortwave radiation
$T_s$	Surface Temperature
WRF	Weather Research and Forecasting model

---



Supplementary maps and plots

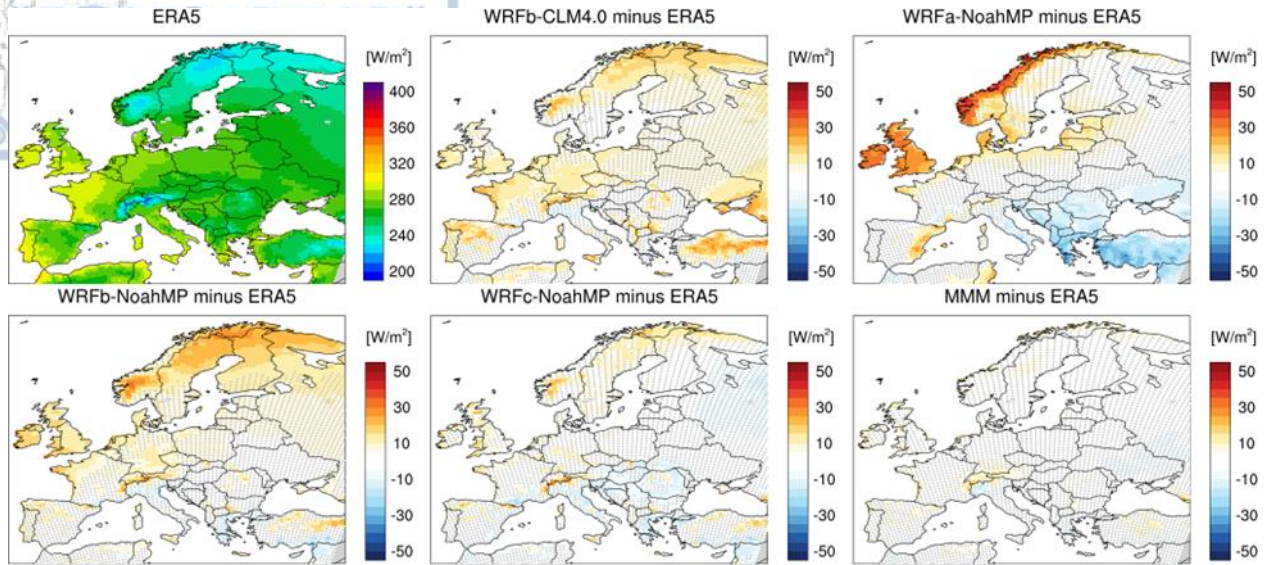


Figure A 1: Mean bias (models minus ERA5) for downwelling longwave radiation at surface in winter (DJF) over 1986-2015 period. Stippling indicates areas where model bias is within ERA5 uncertainty range ( $\pm 1 \times SD$ ). MMM: multi-model-mean of LUCAS simulations excluding WRF configurations.

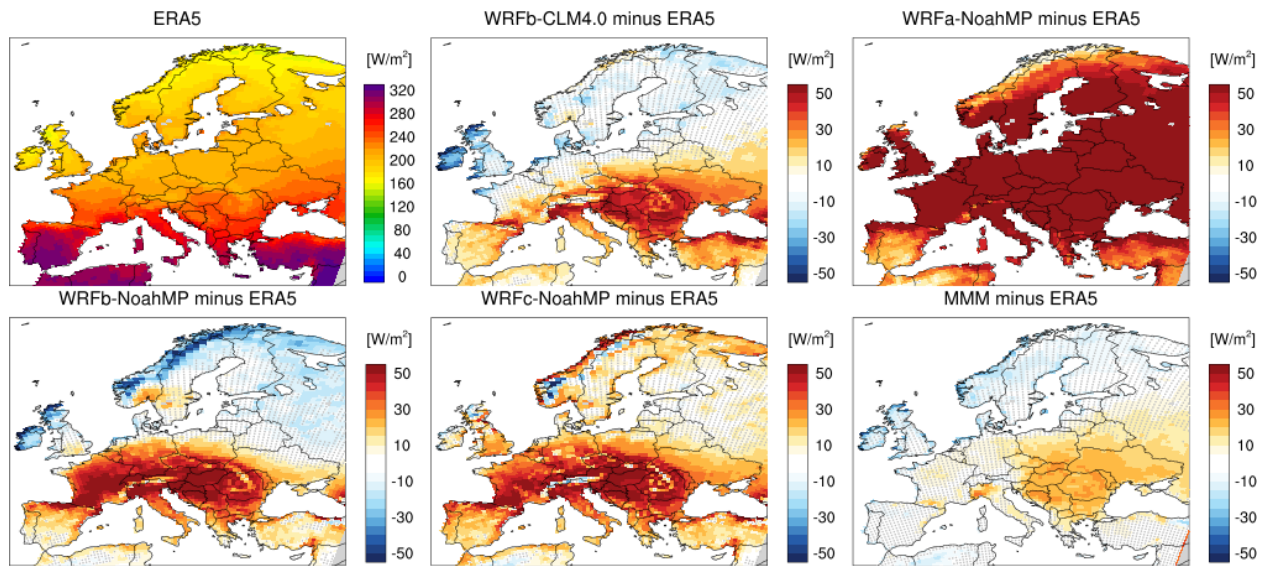
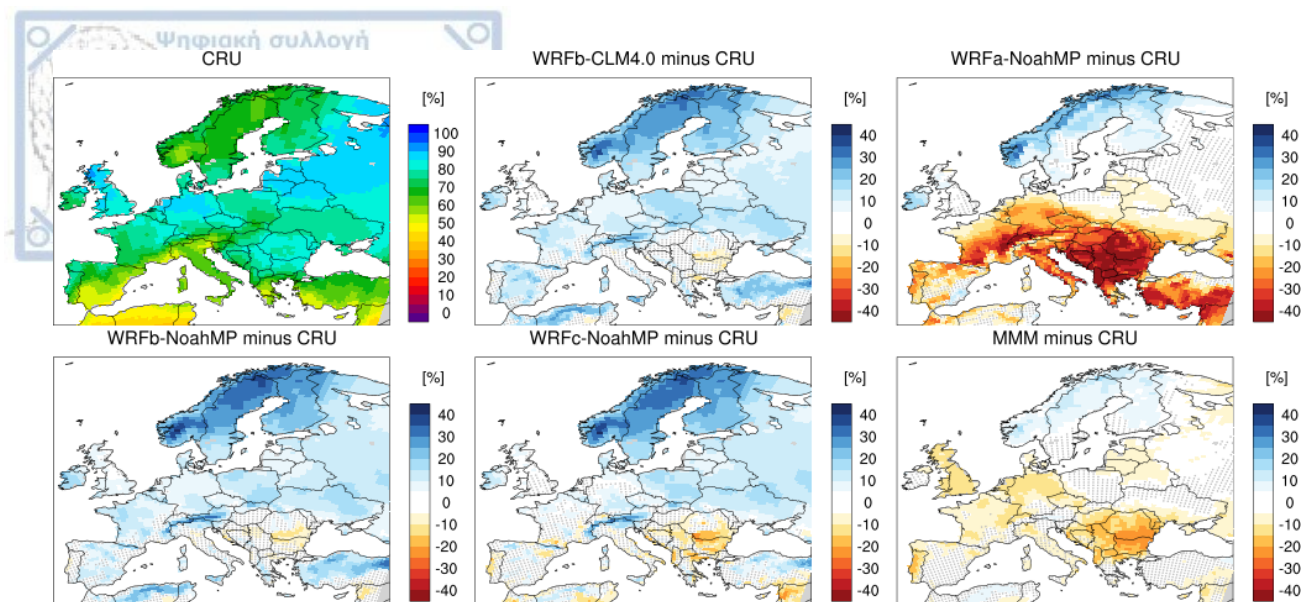
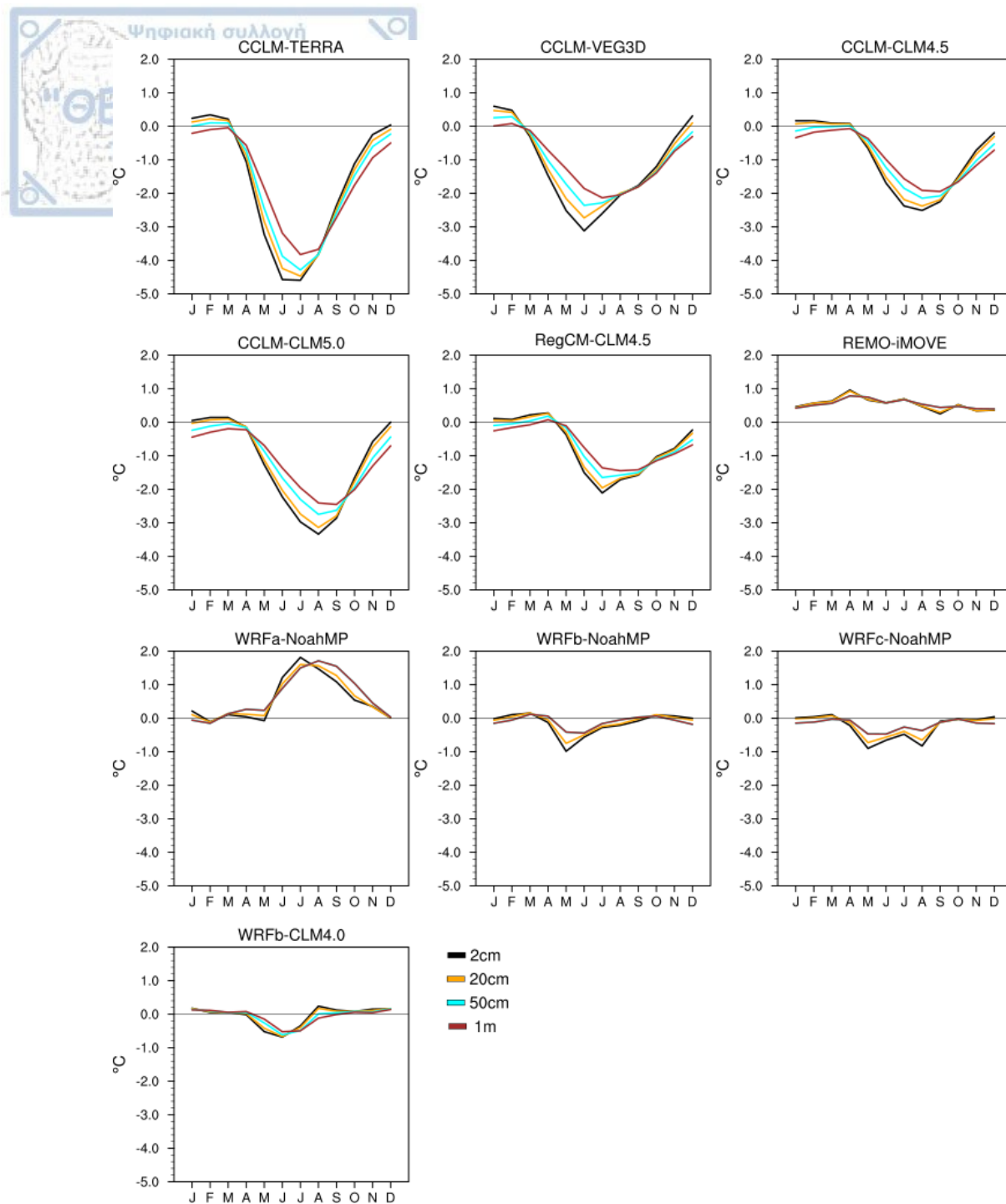


Figure A 2: Mean bias (models minus ERA5) for downwelling shortwave radiation at surface in summer (JJA) over 1986-2015 period. Stippling indicates areas where model bias is within ERA5 uncertainty range ( $\pm 1 \times SD$ ). MMM: multi-model-mean of LUCAS simulations excluding WRF configurations.



**Figure A 3: Mean bias (models minus CRU) for total cloudiness (%) in winter (DJF) over 1986-2015 period. Stippling indicates areas where model bias is within CRU uncertainty range ( $\pm 1 \times SD$ ). MMM: multi-model-mean of LUCAS simulations excluding WRF configurations.**



**Figure A 4: Mean seasonal differences (FOREST minus GRASS) in soil temperature at four different soil depths, averaged over Alps.**

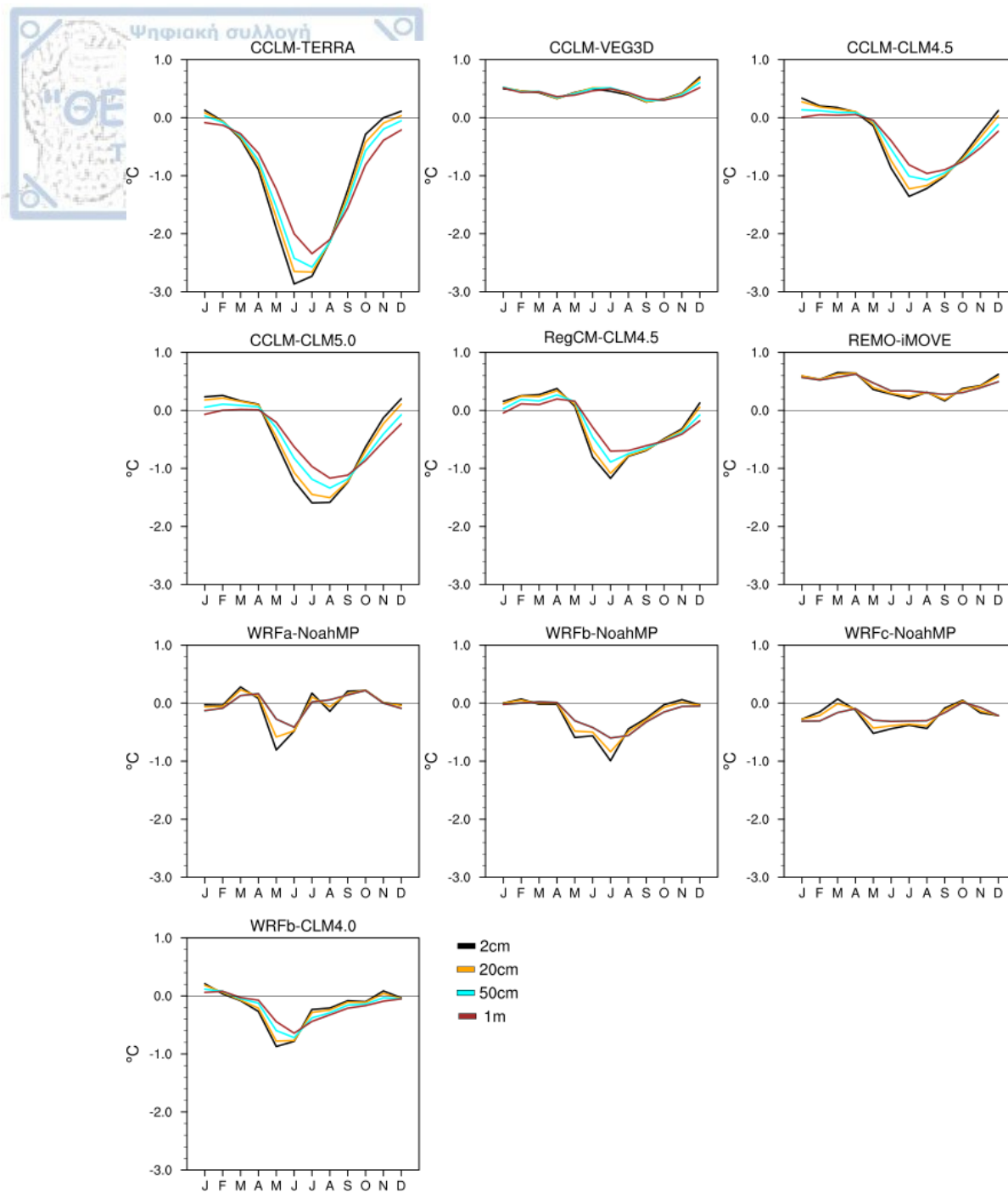


**Figure A 5: Mean seasonal differences (FOREST minus GRASS) in soil temperature at four different soil depths, averaged over British Isles.**

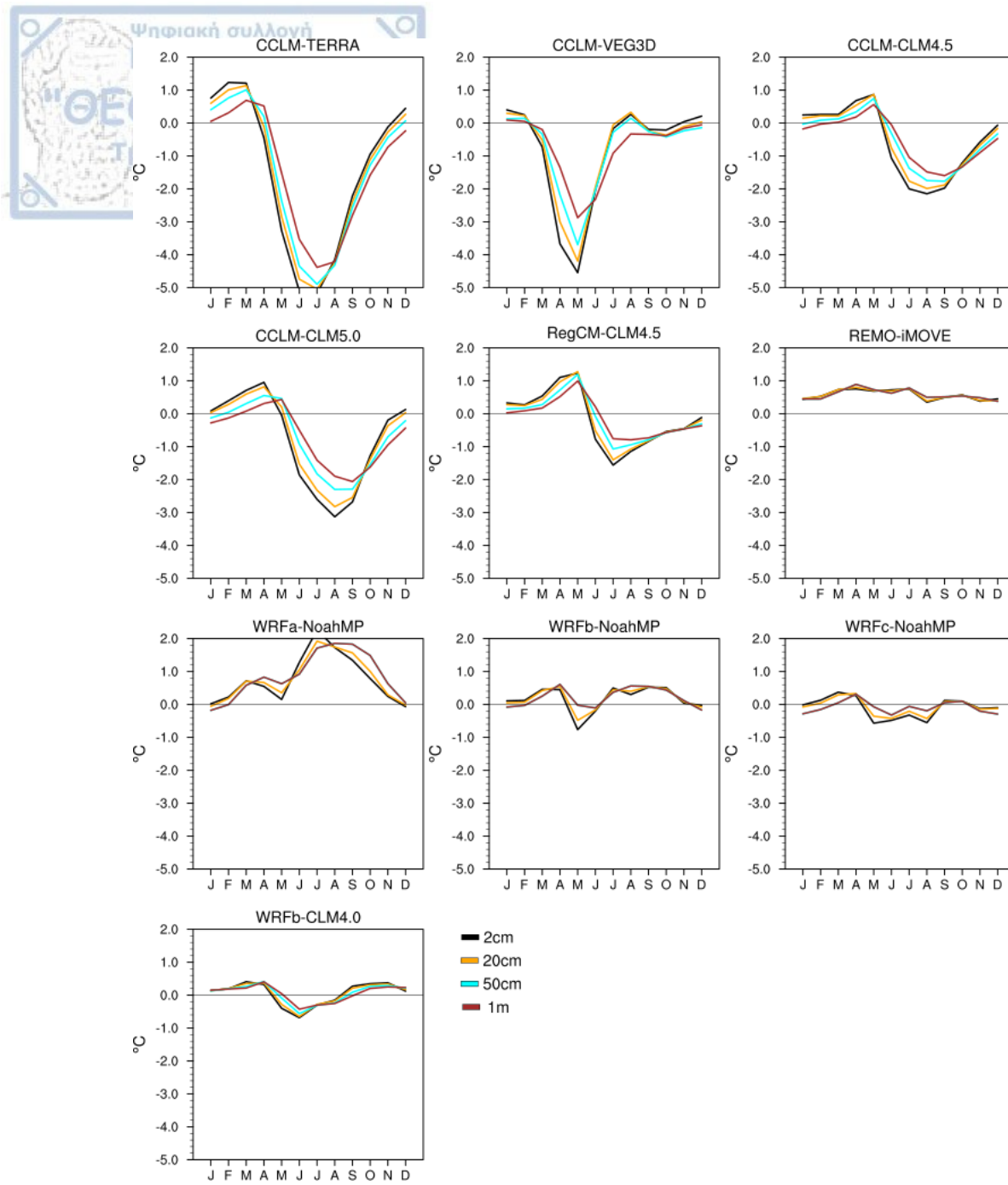


**Figure A 6: Mean seasonal differences (FOREST minus GRASS) in soil temperature at four different soil depths, averaged over Eastern Europe.**

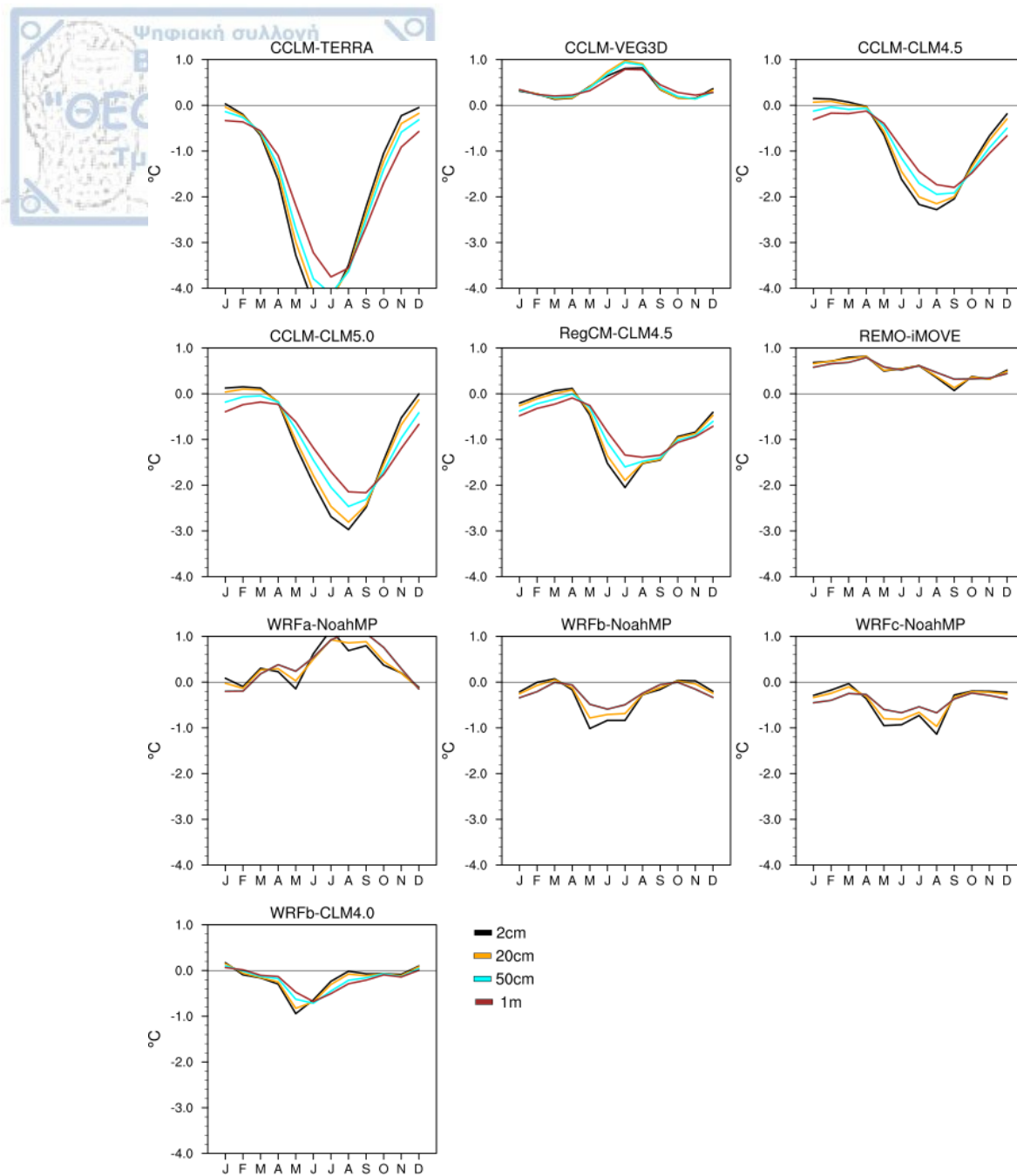


**Figure A 7: Mean seasonal differences (FOREST minus GRASS) in soil temperature at four different soil depths, averaged over France.**

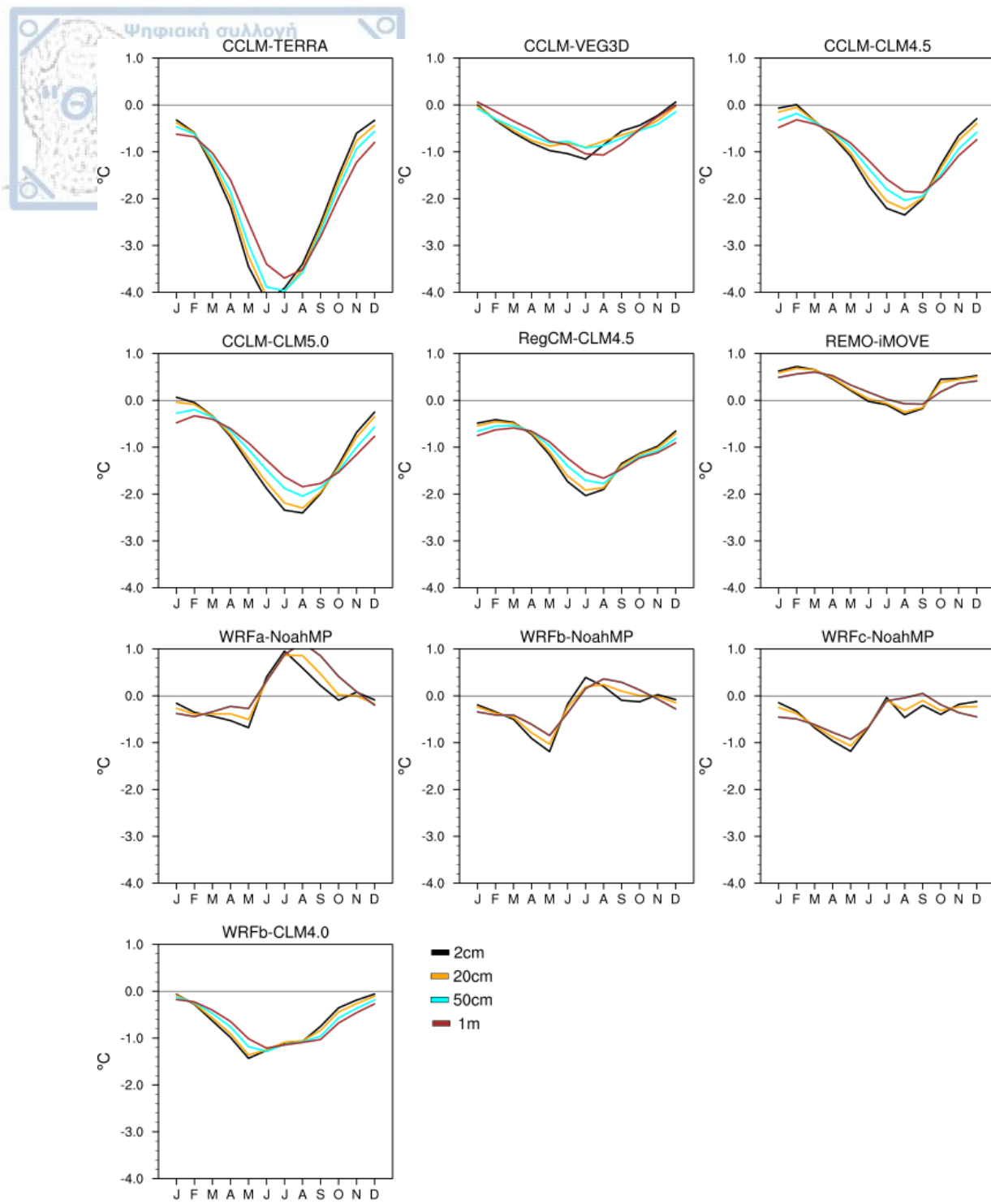


**Figure A 8: Mean seasonal differences (FOREST minus GRASS) in soil temperature at four different soil depths, averaged over Iberian Peninsula.**

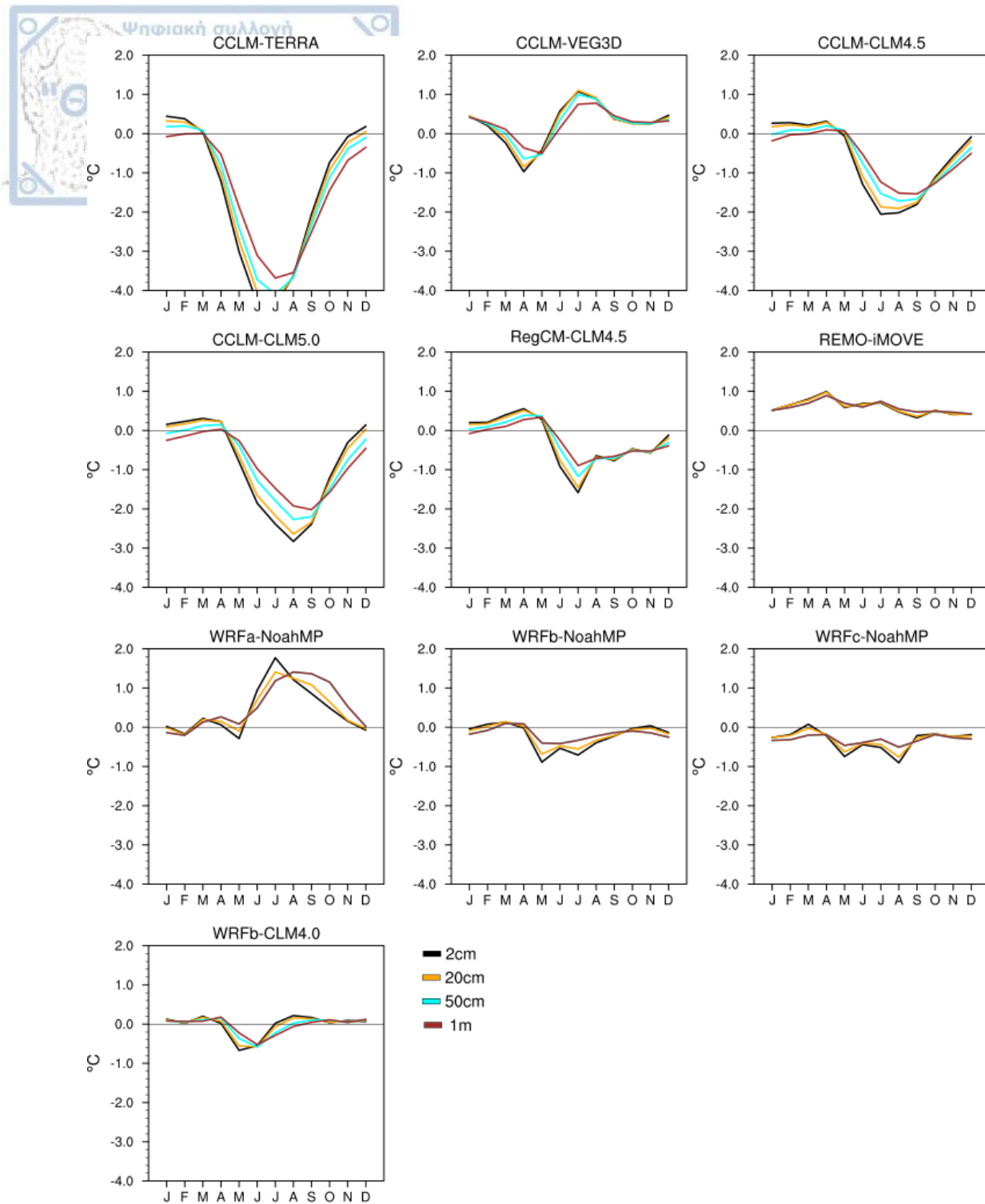


**Figure A 9: Mean seasonal differences (FOREST minus GRASS) in soil temperature at four different soil depths, averaged over Mid-Europe.**



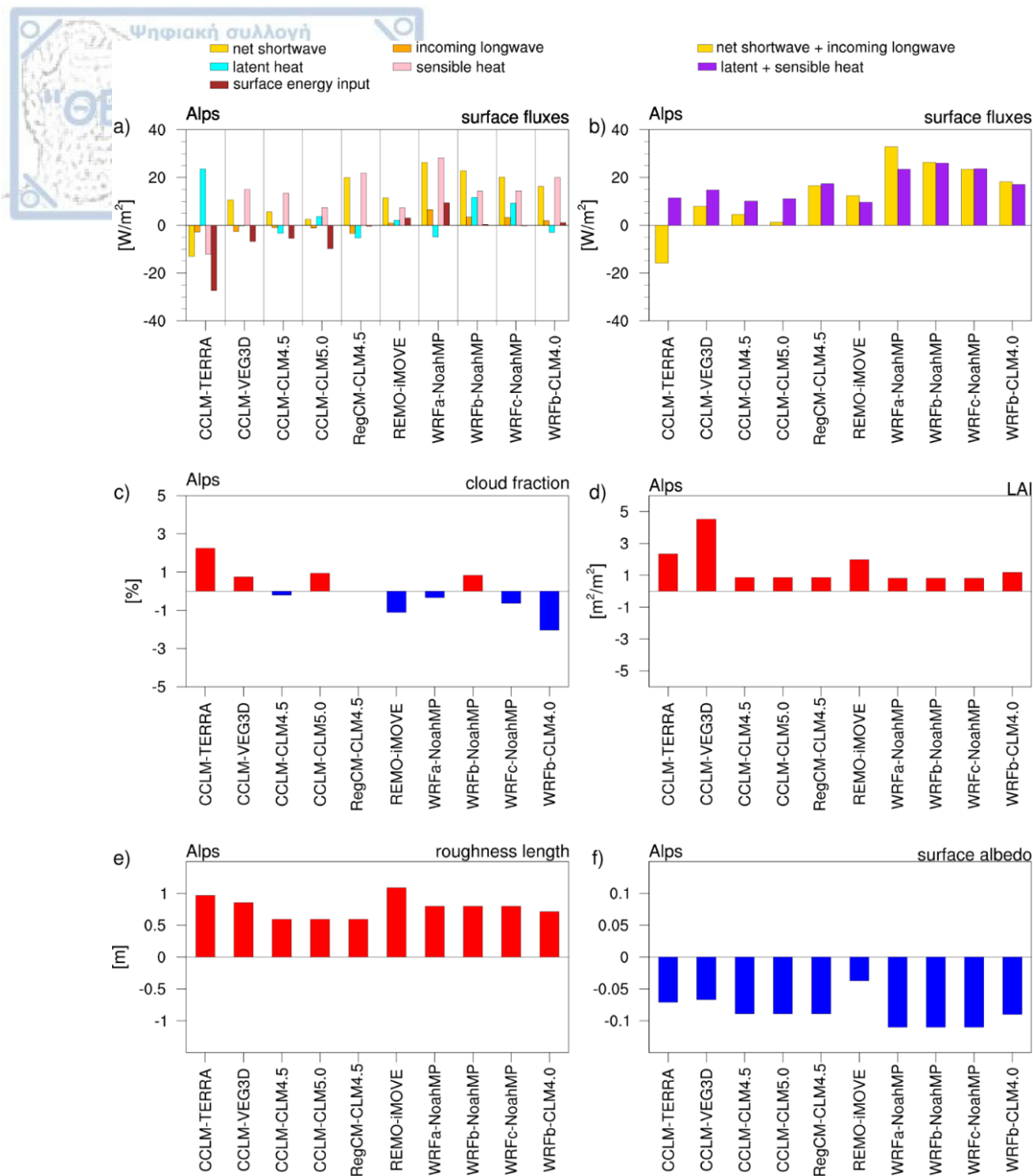


**Figure A 10: (a) Changes in surface energy balance components (FOREST minus GRASS) averaged over Alps in summer, (b) the changes in available radiative energy at the surface and in the sum of turbulent heat fluxes with afforestation, (c) cloud fraction response to afforestation across models, (d) the inter-model differences in LAI, (e) surface roughness and (f) surface albedo in summer (yearly maximum). Positive (negative) values indicate an increase (decrease) with afforestation.**

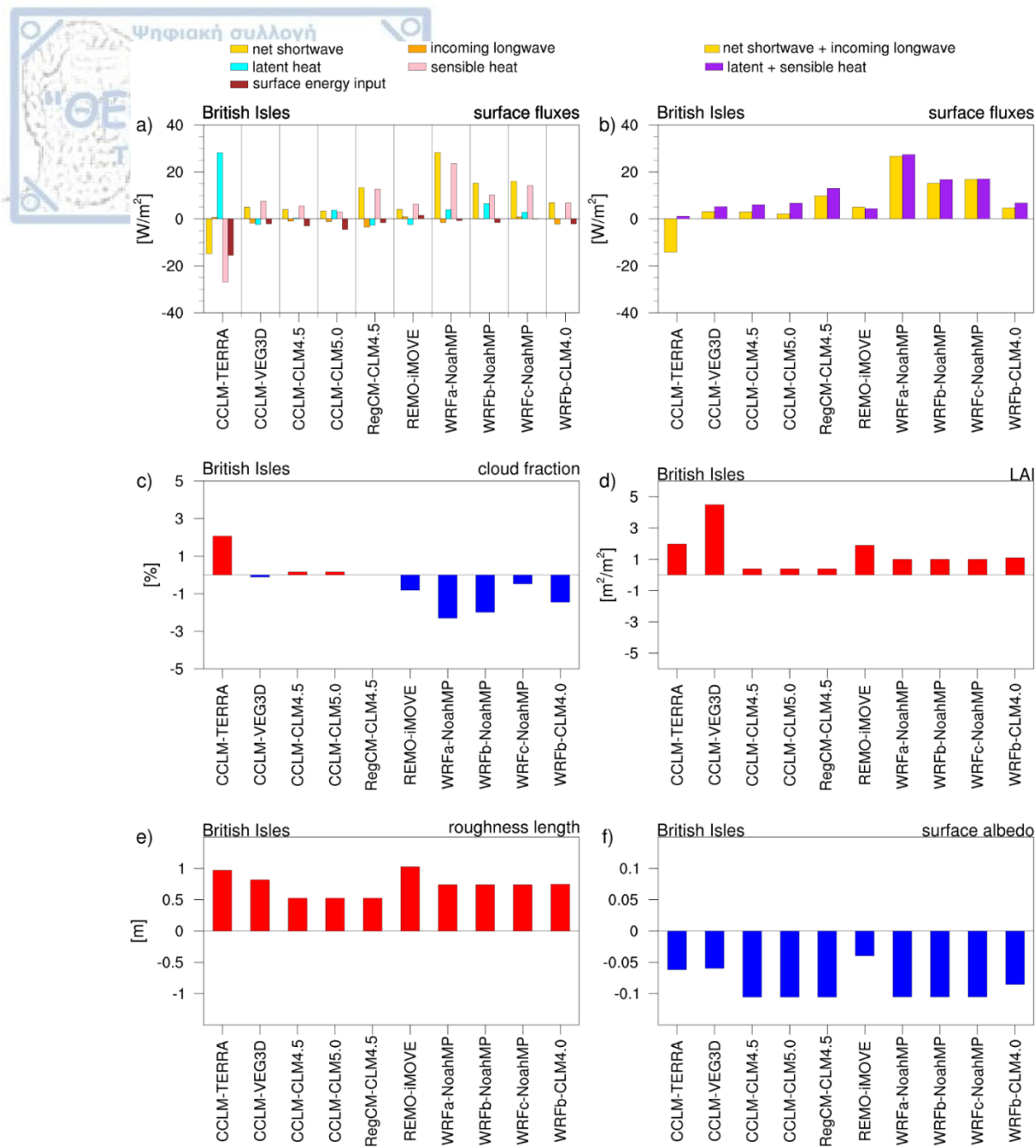
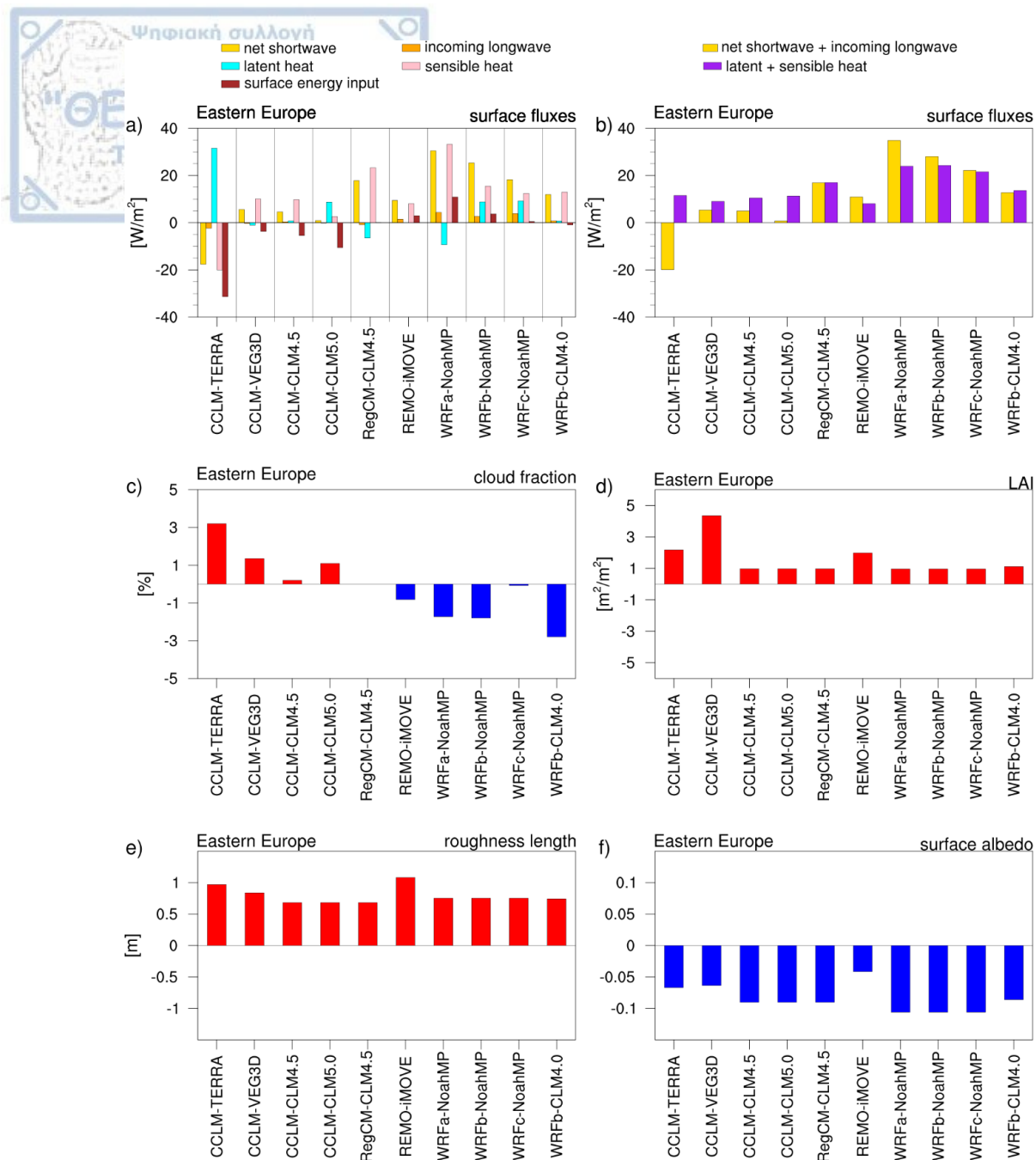
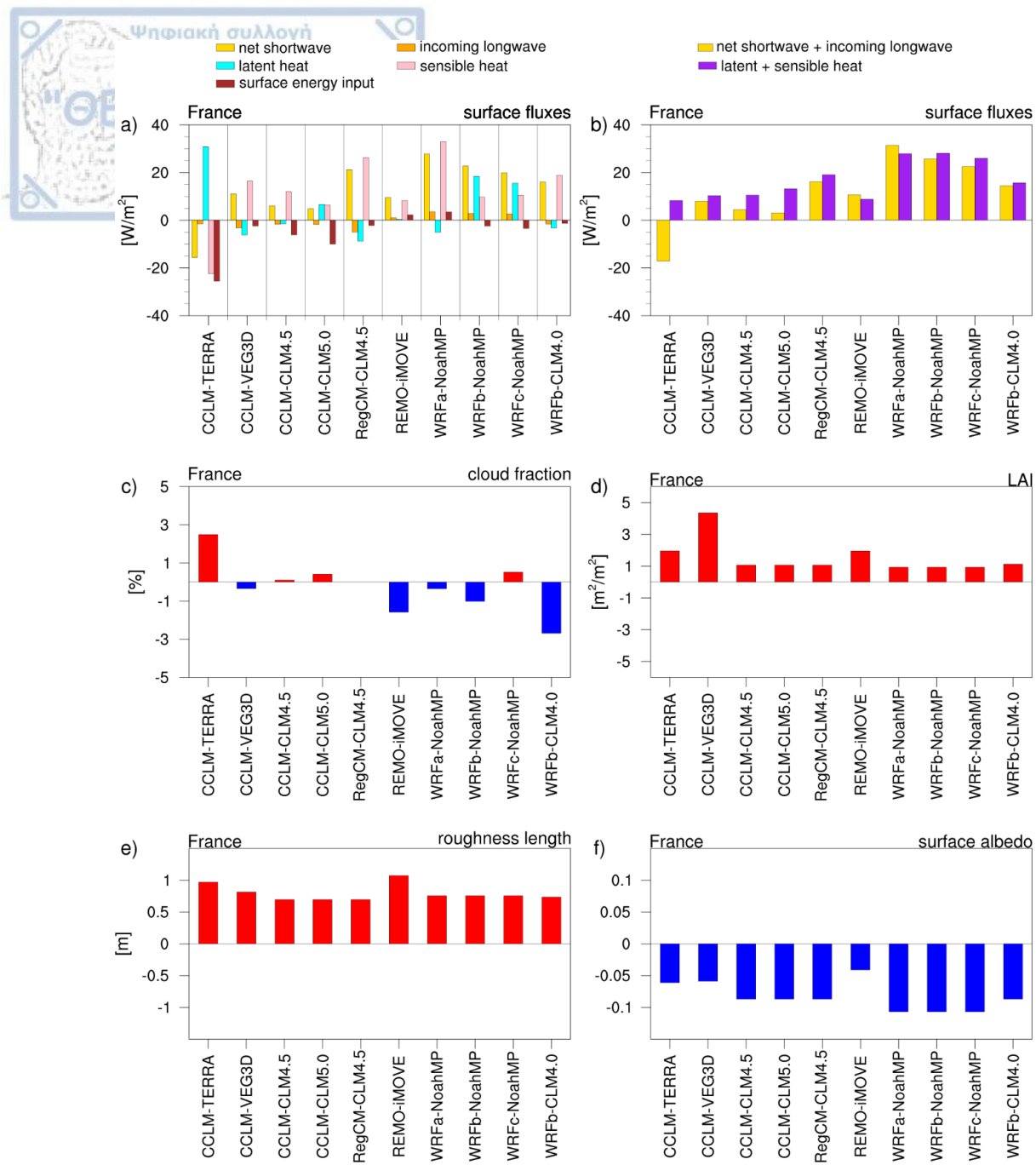


Figure A 11: (a) Changes in surface energy balance components (FOREST minus GRASS) averaged over British Isles in summer, (b) the changes in available radiative energy at the surface and in the sum of turbulent heat fluxes with afforestation, (c) cloud fraction response to afforestation across models, (d) the inter-model differences in LAI, (e) surface roughness and (f) surface albedo in summer (yearly maximum). Positive (negative) values indicate an increase (decrease) with afforestation.



**Figure A 12: (a) Changes in surface energy balance components (FOREST minus GRASS) averaged over Eastern Europe in summer, (b) the changes in available radiative energy at the surface and in the sum of turbulent heat fluxes with afforestation, (c) cloud fraction response to afforestation across models, (d) the inter-model differences in LAI, (e) surface roughness and (f) surface albedo in summer (yearly maximum). Positive (negative) values indicate an increase (decrease) with afforestation.**



**Figure A 13: (a) Changes in surface energy balance components (FOREST minus GRASS) averaged over France in summer, (b) the changes in available radiative energy at the surface and in the sum of turbulent heat fluxes with afforestation, (c) cloud fraction response to afforestation across models, (d) the inter-model differences in LAI, (e) surface roughness and (f) surface albedo in summer (yearly maximum). Positive (negative) values indicate an increase (decrease) with afforestation.**

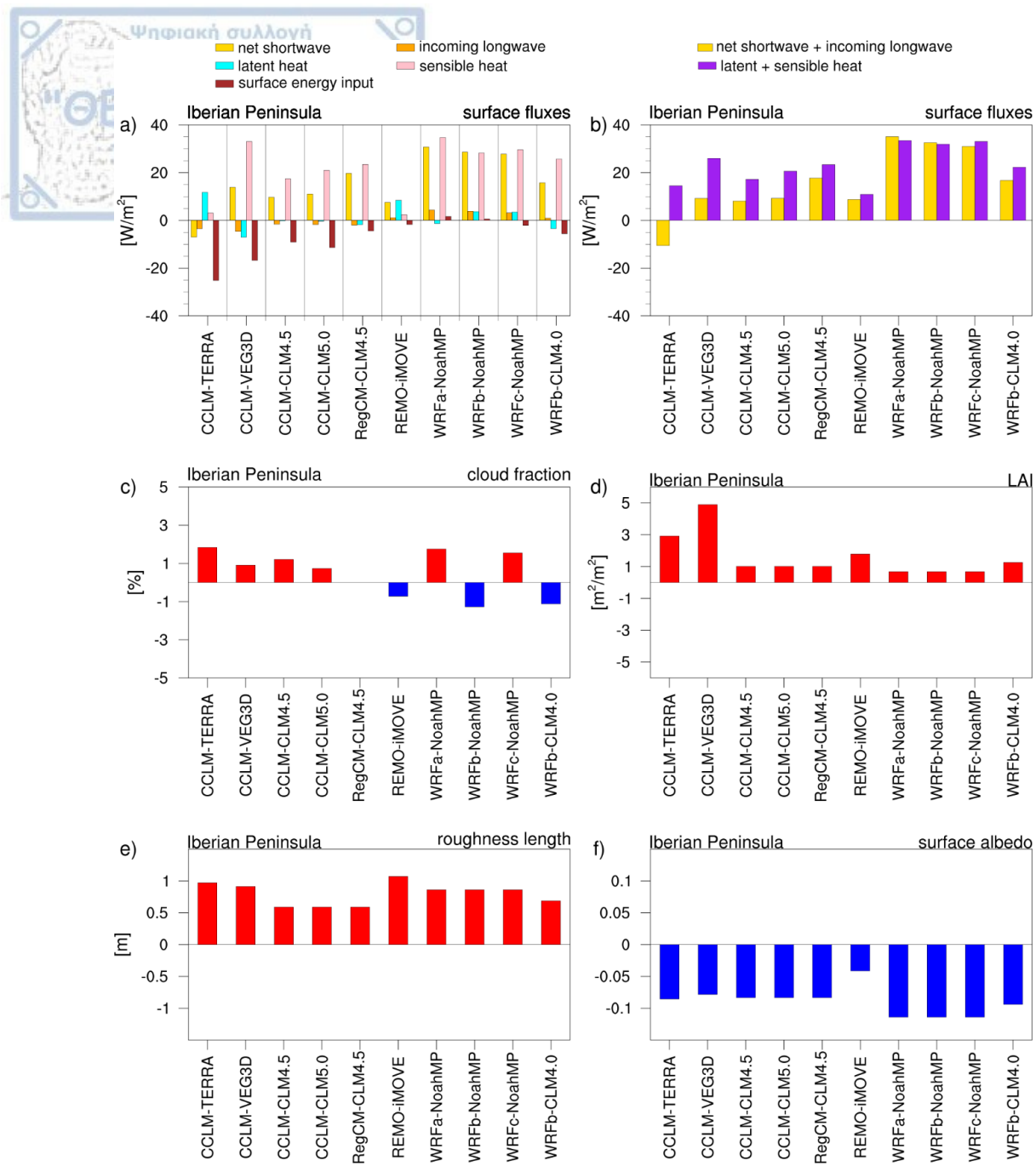


**Figure A 14: (a) Changes in surface energy balance components (FOREST minus GRASS) averaged over Iberian Peninsula in summer, (b) the changes in available radiative energy at the surface and in the sum of turbulent heat fluxes with afforestation, (c) cloud fraction response to afforestation across models, (d) the inter-model differences in LAI, (e) surface roughness and (f) surface albedo in summer (yearly maximum). Positive (negative) values indicate an increase (decrease) with afforestation.**

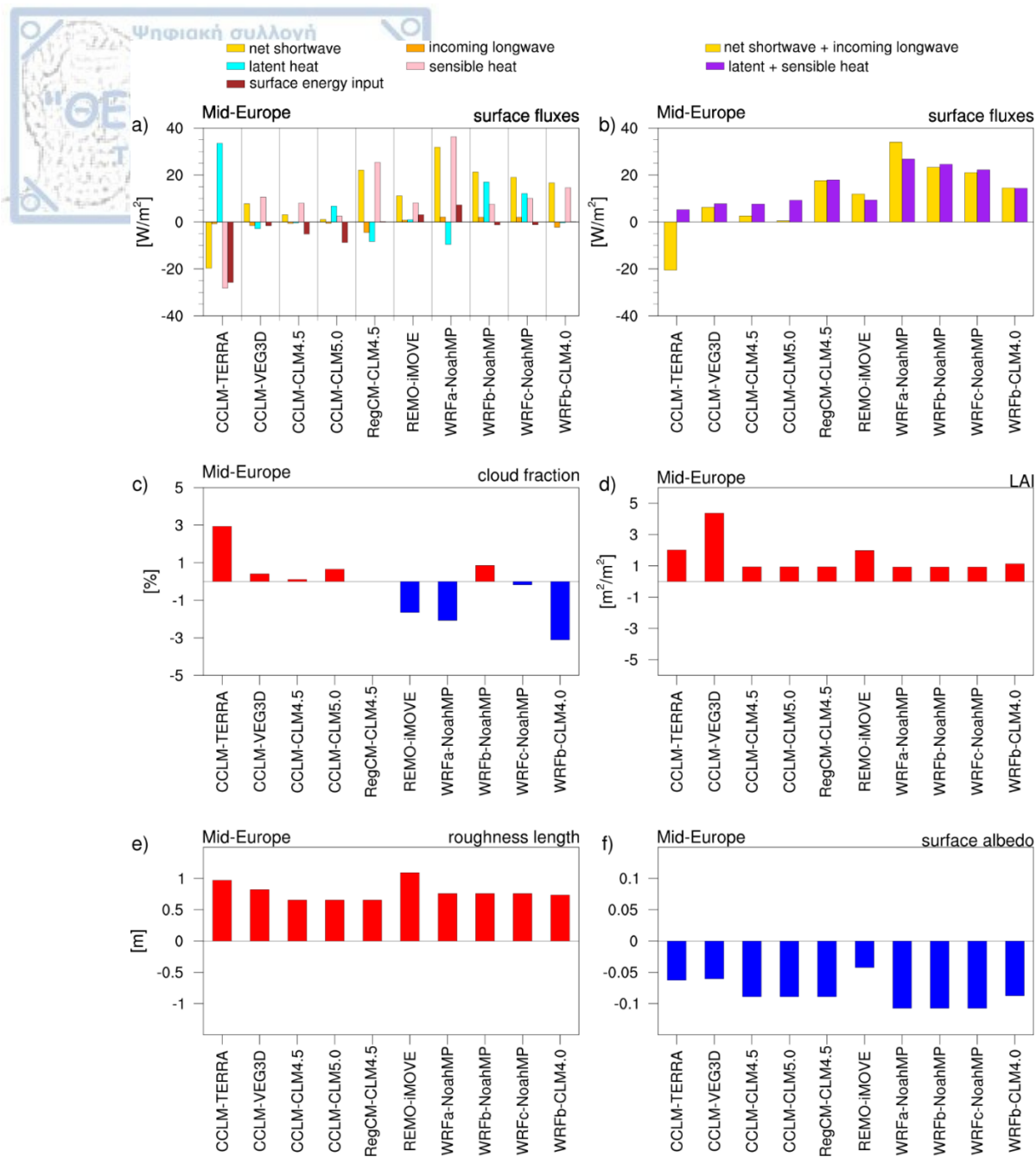


**Figure A 15: (a) Changes in surface energy balance components (FOREST minus GRASS) averaged over Mid-Europe in summer, (b) the changes in available radiative energy at the surface and in the sum of turbulent heat fluxes with afforestation, (c) cloud fraction response to afforestation across models, (d) the inter-model differences in LAI, (e) surface roughness and (f) surface albedo in summer (yearly maximum). Positive (negative) values indicate an increase (decrease) with afforestation.**

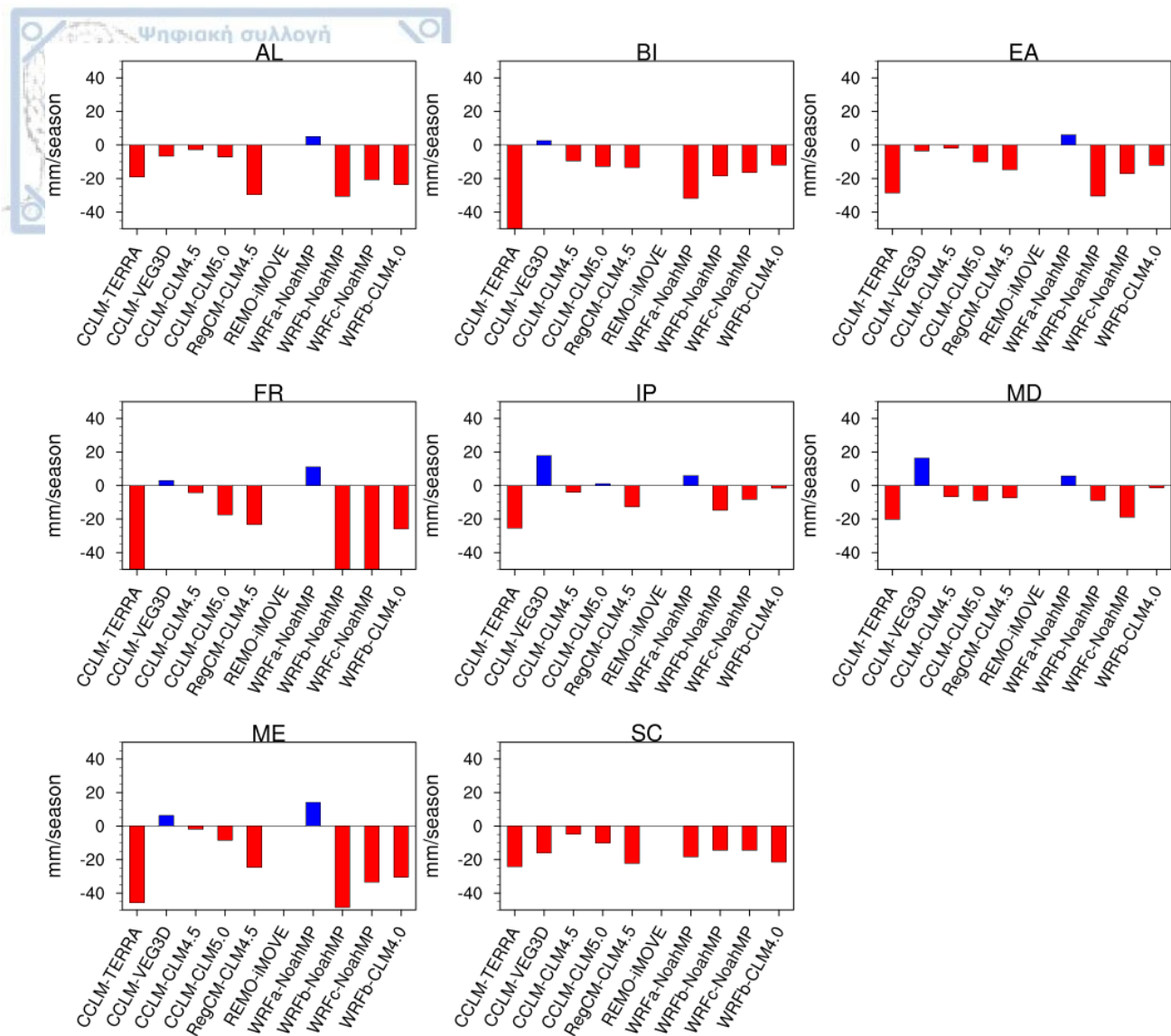


**Figure A 16: Afforestation (FOREST minus GRASS) impact on surface water balance, defined as the difference between precipitation and evapotranspiration in summer, averaged over eight European regions.**

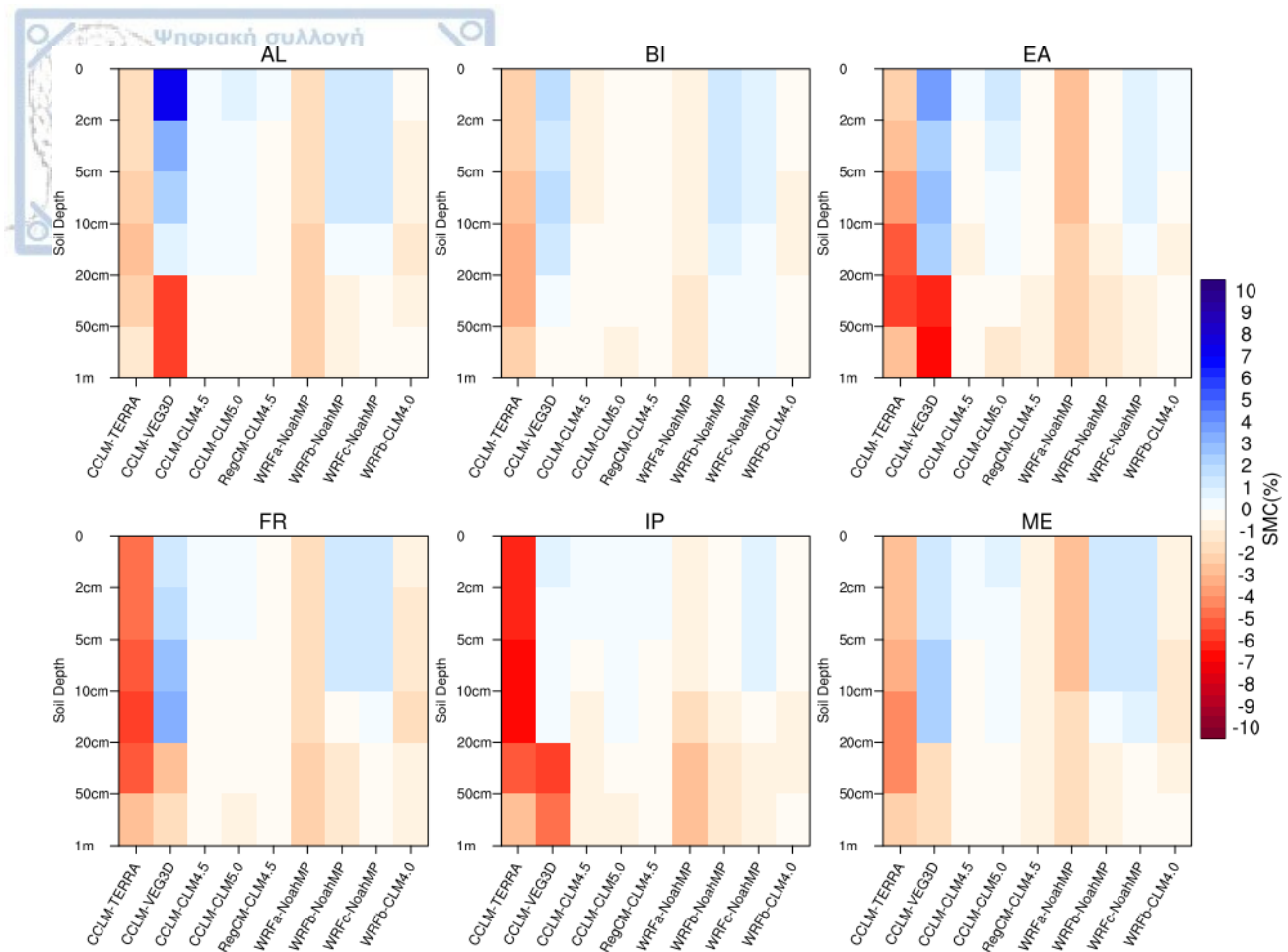


**Figure A 17: Mean summer differences in soil moisture content (SMC) due to afforestation (FOREST minus GRASS) in the top 1m of the soil, averaged over six European regions. Positive (negative) values indicate an increase (decrease) due to afforestation.**



Ψηφιακή συλλογή  
βιβλιοθήκη  
"ΘΕΟΦΡΑΣΤΟΣ"  
Τμήμα Γεωλογίας

Table A 1: Cross-walking table used to convert the LUCAS PFTs to IGBP land cover classes used as input to WRF.

LUCAS PFTs																IGBP	
Temperate Broadleaf Evergreen trees	Tropical Broadleaf Deciduous trees	Temperate Broadleaf Evergreen trees	Temperate Broadleaf Deciduous trees	Coniferous Evergreen trees	Coniferous Deciduous trees	Evergreen shrubs	Deciduous shrubs	Grass C3	Grass C4	Tundra	Swamps	Cropland	Irrigated cropland	Urban	Bare		
				X													Evergreen Needleleaf Forest
X		X															Evergreen Broadleaf Forest
					X												Deciduous Needleleaf Forest
	X		X														Deciduous Broadleaf Forest
						X	X										Open Shrublands
								X	X								Grasslands
											X						Permanent Wetlands
												X	X				Croplands
														X		Urban & Built Up	
															X	Barren or Sparsely Vegetated	
										X						Mixed Tundra	

Table A 2: Cross-walking table to convert the LUCAS PFTs to the standard IPCC classes. This conversion is only used for simplification and visualization purposes of land cover transitions.

LUCAS PFTs	IPCC classification									
	Agriculture	Forest	Grassland	Wetland	Settlement	Shrubland	Lichens & mosses	Sparse vegetation	Bare area	Water
Temperate Broadleaf Evergreen trees		x								
Tropical Broadleaf Deciduous trees		x								
Temperate Broadleaf Evergreen trees		x								
Temperate Broadleaf Deciduous trees		x								
Coniferous Evergreen trees		x								
Coniferous Deciduous trees		x								
Evergreen shrubs						x				
Deciduous shrubs						x				
Grass C3			x							
Grass C4			x							
Tundra								x		
Swamps				x						
Cropland	x									
Irrigated cropland	x									
Urban					x					
Bare									x	

Table A 3: Differences between LC2015 and LC1950 experiments in surface temperature ( $\Delta T_s$ ), when it's estimated according to equation 4 (decomposition method) and when it's taken directly as model output.

	AL	BI	EA	FR	IP	MD	ME	SC
$\Delta T_s$ (estimated)	0.18 °C	0.15 °C	0.15 °C	0.19 °C	0.15 °C	0.09 °C	0.12 °C	-0.03 °C
$\Delta T_s$ (model output)	0.17 °C	0.13 °C	0.14 °C	0.17 °C	0.15 °C	0.08 °C	0.10 °C	-0.03 °C

Table A 4: Characteristics of LUCAS RCM ensemble.

Model name	Institute	RCM version	Land model	Cumulus scheme	PBL scheme
CCLM-TERRA	JLU/BTU	COSMO_5.0_clm9	TERRA-ML	Tiedke (1989)	Mellor-Yamada
CCLM-VEG3D	KIT	COSMO_5.0_clm9	VEG3D	Tiedke (1989)	Mellor-Yamada
CCLM-CLM4.5	ETH	COSMO_5.0_clm9	CLM4.5	Tiedke (1989)	Mellor-Yamada
CCLM-CLM5.0	ETH	COSMO_5.0_clm9	CLM5.0	Tiedke (1989)	Mellor-Yamada
RegCM-CLM4.5	ICTP	RegCM4.6.1	CLM4.5	Tiedke (1989)	Bretherton et al. 2004
REMO-iMOVE	GERICS	REMO2009	iMOVE	Tiedke (1989)	Extended level-2 scheme after Mellor-Yamada
WRFa-NoahMP	IDL	WRFv3.8.1	NoahMP	Grell-Freitas	MYNN 2.5 TKE
WRFb-NoahMP	UHOH	WRFv3.8.1	NoahMP	Kain-Fritsch	MYNN 2.5 TKE
WRFc-NoahMP	BCCR	WRFv3.8.1	NoahMP	Kain-Fritsch	YSU
WRFb-CLM4.0	AUTH	WRFv3.8.1	CLM4.0	Kain-Fritsch	MYNN 2.5 TKE